



HAL
open science

Long range time transfer over optical fiber links and cross-comparison with satellite based methods.

Namneet Kaur

► **To cite this version:**

Namneet Kaur. Long range time transfer over optical fiber links and cross-comparison with satellite based methods.. Physics [physics]. SYRTE, Observatoire de Paris, 2018. English. NNT: . tel-01913286

HAL Id: tel-01913286

<https://hal.science/tel-01913286>

Submitted on 6 Nov 2018

HAL is a multi-disciplinary open access archive for the deposit and dissemination of scientific research documents, whether they are published or not. The documents may come from teaching and research institutions in France or abroad, or from public or private research centers.

L'archive ouverte pluridisciplinaire **HAL**, est destinée au dépôt et à la diffusion de documents scientifiques de niveau recherche, publiés ou non, émanant des établissements d'enseignement et de recherche français ou étrangers, des laboratoires publics ou privés.

THÈSE DE DOCTORAT

de l'Université de recherche Paris Sciences et Lettres
PSL Research University

Préparée à SYRTE, Observatoire de Paris

Transfert de temps à longue distance utilisant des liaisons à fibre optique
et comparaison croisée avec des méthodes par satellite

École doctorale n°127

ASTRONOMIE ET ASTROPHYSIQUE D'ILE-DE-FRANCE

Spécialité ASTRONOMIE ET ASTROPHYSIQUE

Soutenue par **Namneet KAUR**
le 20 Avril 2018

COMPOSITION DU JURY :

Mme Fabienne Casoli, Président
LERMA, Observatoire de Paris

M François Vernotte, Rapporteur
Observatoire de Besançon

Mme Catherine Algani, Rapporteur
CNAM, Paris

M Javier Díaz, Membre du jury
University of Granada, Spain

M Jean Pierre Aubry, Membre du jury
Établissement

M Philip Tuckey, Directeur de thèse
SYRTE, Observatoire de Paris

M Paul-Eric Pottie, Co-supervisor de thèse
SYRTE, Observatoire de Paris

Acknowledgements

I am heartily thankful to my supervisors for their immense help and support. Their enlightening discussions and constant motivation have been the guiding light throughout the journey of my thesis. In addition to the rich professional learning experience that I have gained while working with them, the time spent with them has strengthened and shaped my personality. I wish to express my deep gratitude for their generosity, affection, and understanding. It has been an honor and an absolute pleasure to work with them and I am very grateful for this life-changing opportunity.

I would like to thank Javier Diaz, Rafa Rogriguez, J. Gabriel Ramirez at Seven Solutions and Felipe Torres Gonzalez at University of Granada, Spain for their collaboration and support. I would also like to thank the White Rabbit community for their help by sharing issues through the mailing list and would like to specially thank Javier Serrano, Alessandro Rubini, T. Wlostowski and Mattia Rizzi at CERN for their help and support.

I would also take the opportunity to thank Noel Dimarcq for his stimulating conversations and goodwill. I would specially like to thank the members of SYRTE belonging to Time and Frequency group, Electronics group, Computing group, Fiber link group and administration for their continuous help, support and for their valuable time for urgent matters.

I extend my profound gratitude to my Mom and Dad for being my ever increasing strength and motivation. I would also like to acknowledge my family and all my dearest friends, specially Navnina and Vishnu for being my backbone and for always being there in difficult times. I am truly grateful and I cherish their invaluable friendship.

This work was supported by the LABEX Cluster of Excellence FIRST-TF (ANR-10-LABX-48-01), within the Program d'Investissements d'Avenir and by BPIFrance under the SCP Time project.

I dedicate this thesis to my Mom and Dad.

Contents

Acknowledgements	i
1 Introduction	1
1.1 Time and frequency metrology	1
1.1.1 Accuracy	1
1.1.2 Stability	2
1.2 The Oscillator signal	2
1.3 Noise analysis	3
1.3.1 Frequency domain	3
1.3.2 Time domain	4
1.3.2.1 Allan Variance	4
1.3.2.2 Overlapping Allan Variance	5
1.3.2.3 Modified Allan Variance	5
1.3.2.4 Time Variance	5
1.4 Clocks and timescales	6
1.5 Introduction to time transfer methods	8
1.5.1 One way time transfer method	8
1.5.1.1 GNSS time dissemination	9
1.5.1.2 GNSS time transfer methods	10
1.5.2 Two way time transfer method	11
1.5.3 Two way Satellite Time and Frequency transfer (TWSTFT)	13
1.5.4 Time and frequency transfer over Optical fiber links	15
1.5.5 Time over Internet	16
1.5.5.1 Network Time Protocol (NTP)	16
1.5.5.2 Precision Time Protocol	17
1.5.5.3 SONET and SDH	18
1.5.5.4 White Rabbit PTP (WR-PTP)	18
1.5.6 Performance comparison of some time transfer methods	19
1.6 Implemented and Potential applications of White Rabbit	20
1.6.1 For Scientific experiments	20
1.6.2 Calibration in the RF domain	21
1.6.3 Smart power grids	21
1.6.4 5G mobile networks	21
1.6.5 Financial transactions and timestamping	21
1.7 Outline of the thesis	21

2	Introduction to White Rabbit Precision Time Protocol (WR-PTP)	23
2.1	Introduction to WR project	23
2.2	Introduction to WR-PTP	23
2.2.1	Precision time Protocol (PTP)	23
2.2.2	Synchronous Ethernet	26
2.2.3	Digital Dual Mixer time difference (DDMTD) phase detector	26
2.3	A typical White Rabbit Network	28
2.4	Synchronization in White Rabbit	29
2.4.1	Syntonization	30
2.4.2	Link Delay measurement	30
2.4.3	Link asymmetry evaluation	31
2.4.4	Clock offset evaluation	34
2.5	Unification of White Rabbit into PTP	34
2.6	Components of a White Rabbit Network	35
2.7	White Rabbit equipment	35
2.7.1	The White Rabbit Switch	35
2.7.2	The White Rabbit Nodes	36
2.8	Optical emitters	37
2.9	The transmission medium - Optical fibers	38
2.10	White Rabbit clocking Scheme	41
2.11	The potential performance limitations	42
2.12	Outlook	45
3	Improving the White Rabbit Switch performance	47
3.1	Introduction	47
3.2	The White Rabbit Switch in Grandmaster mode	47
3.2.1	Experimental setup	47
3.2.2	Phase noise power spectral density	48
3.3	Improving the Grandmaster WRS performance	49
3.3.1	Phase noise Power Spectral Density and Allan Deviation	50
3.3.2	Time Stability performance	53
3.4	Performance of a Slave White Rabbit Switch	55
3.4.1	Testing Optical link configurations	55
3.4.2	Experimental setup	55
3.4.3	Effect of Chromatic dispersion	56
3.4.4	Results	58
3.5	Improving the performance of a Slave WRS	60
3.5.1	Phase Locked Loops (PLL)	60
3.5.2	Experimental Setup	62
3.5.3	Phase locked loop Bandwidth variation	62
3.5.4	A mid range White Rabbit link	65
3.5.5	Phase locked loop bandwidth optimization	65

3.5.6	Frequency and Time stability performance	67
3.6	The Local Oscillator performance	68
3.7	Increasing the PTP message exchange rate	70
3.8	Summary	72
4	Towards long range time and frequency dissemination using White Rabbit	74
4.1	Introduction	74
4.2	A realistic Telecommunication network span	74
4.2.1	Experimental Setup	74
4.2.2	Phase locked loop Bandwidth optimization	75
4.2.3	Experimental results	76
4.2.4	Fiber thermal noise	78
4.2.5	Limitations for the time stability performance	81
4.3	Effect of Chromatic Dispersion	82
4.4	Tackling Chromatic Dispersion	84
4.5	Cascaded White Rabbit links using DWDM technique	85
4.5.1	Experimental Setup	85
4.5.2	Phase locked loop Bandwidth optimization for cascaded stages	86
4.5.3	Frequency and time stability performance	90
4.5.4	Extension to a Cascaded 400 km White Rabbit link	91
4.5.4.1	Phase locked loop bandwidth optimization	93
4.5.4.2	Frequency stability performance	93
4.5.4.3	Time stability performance	94
4.6	A long haul telecommunication span White Rabbit link	98
4.6.1	Experimental setup	98
4.6.2	Frequency stability performance	99
4.6.3	Time stability performance	101
4.6.4	Effect of reduced PTP rate	105
4.6.5	Effect of reduced Bandwidth of locking	107
4.7	A multi user 4x125 km White Rabbit link	110
4.7.1	Experimental Setup	110
4.7.2	Frequency and time stability performance	111
4.8	Conclusion	113
5	Deployments	116
5.1	Introduction	116
5.2	A short range in-campus dissemination network	116
5.3	A mid range suburban WR link using dark fiber network	117
6	Time Accuracy	118
6.1	Introduction	118
6.2	Calibration of fiber spools using White Rabbit	119
6.2.1	Calibration: A sensitive task	120

6.2.2	Calibration by forcing asymmetry in a uni-directional link . . .	120
6.3	Wavelength swapping technique	126
6.3.1	Implementation and Results	127
6.4	Fiber swapping technique	128
6.4.1	Implementation and Results	129
6.5	Dual wavelength technique	130
6.5.1	Implementation and Results	134
6.6	Summary	137
7	Conclusion	139
7.1	Summary	139
7.2	Perspectives	141
A		143
	Bibliography	153

List of Figures

1.1	The relationship between accuracy and stability for a frequency standard of nominal frequency f_0 [1].	2
1.2	The time evolution of the uncertainty of Cesium and Optical clocks. Fractional uncertainty of primary Cesium atomic clocks to realize the second in the SI (squares) and optical frequency clocks (dots). Green dots represent optical clocks with estimated standard uncertainties whose optical frequency can be determined only with the accuracy of the frequency comparison with a primary Cesium clock [7].	7
1.3	One way time and frequency transfer.	8
1.4	One way time and frequency transfer.	9
1.5	GPS common-view technique [10].	10
1.6	General schematic of a two way time transfer method.	12
1.7	Two way satellite time and frequency transfer [18].	14
1.8	NTP two way message exchange process.	17
1.9	WR synchronization performance for initial experiments by CERN[42].	19
1.10	Performance comparison of some time transfer methods.	20
2.1	PTP two way message exchange mechanism [39].	25
2.2	Comparison between Standard and Synchronous Ethernet [56].	26
2.3	Schematic of an analog DMTD phase detector [56]	27
2.4	Schematic of a digital DMTD phase detector [56].	28
2.5	A typical White Rabbit Network [42].	29
2.6	A White Rabbit link delay scheme [56].	30
2.7	Delay asymmetries in a White Rabbit link [56].	31
2.8	White Rabbit transceiver PHY calibration scheme [56].	32
2.9	WR-PTP message exchange flow [56].	35
2.10	A White Rabbit Switch (WRS) [59].	36
2.11	SPEC board hosting the five channel FMC card DIO [60].	37
2.12	The White Rabbit Zync embedded node (WR-ZEN) [61].	38
2.13	Types of Small form factor pluggable (SFP) optical transceivers.	38
2.14	Optical attenuation variation with wavelength [63].	39
2.15	Refractive index, group index and material dispersion of silica fibers [63].	40
2.16	Clocking scheme of the White Rabbit switch hardware v3.4v (v3.3 lacks the 10 MHz clock output) [71].	42

2.17	Illustration of a typical Phase noise power spectral density for a free running local oscillator, for the external reference signal and for the locked local oscillator.	43
2.18	A WR Slave system review for studying its potential performance limitations [71].	44
2.19	Pictorial representation of the potential noise sources that could limit the frequency stability performance of a typical Grandmaster and Slave White Rabbit Switch.	45
3.1	Experimental setup for GM switch performance analysis.	48
3.2	Phase noise power spectral density for the Grandmaster WR clock.	48
3.3	Schematic of the external 1 GHz local oscillator box.	49
3.4	Phase noise power spectral density of the 10 MHz output signal of the 1 GHz local oscillator box.	50
3.5	Experimental setup for the "improved" GM switch performance analysis.	51
3.6	Phase noise power spectral density for default and improved Grandmaster WR clock.	51
3.7	Phase noise power spectral density of the improved Grandmaster WR clock for PLL bandwidth optimization.	52
3.8	Allan Deviation (NEQ BW=500 Hz) for default and Improved Grandmaster WR clock (the solid light blue and red lines are their respective noise floors).	52
3.9	Comparison of Allan Deviation (NEQ BW=50 Hz) of our Improved Grandmaster WRS with OPNT enhanced WR.	53
3.10	Phase data for the improved Grandmaster WRS (constant offset has been removed).	53
3.11	Time Deviation for default and Improved Grandmaster switch (Bandwidth of measurement = 1 Hz).	54
3.12	Experimental setup for comparison of uni-directional (Bi-fiber) and bi-directional (Bi-color) 25 km White Rabbit links.	56
3.13	Optical spectrum of the 1310 and 1490 nm (Bi-directional) CWDM SFPs.	57
3.14	Optical spectrum of the 1541 and 1560 nm (Uni-directional) DWDM SFPs.	57
3.15	Phase data for the uni-directional (Bi-fiber) and bi-directional (Bi-color) setups.	59
3.16	Overlapping Allan Deviation (calculated from phase data) for the uni-directional and bidirectional setups (Bandwidth of measurement = 1 Hz).	59
3.17	Time Deviation (calculated from phase data) for the unidirectional and bidirectional setups (Bandwidth of measurement = 1 Hz).	60
3.18	Block diagram of a typical phase locked loop [81].	61

3.19	Experimental setup for a 25 km White Rabbit uni-directional link. . . .	62
3.20	Power spectral density of the Slave clock for different k_p values for a constant $k_i=30$	63
3.21	Power spectral density of the Slave clock for different k_i values for a constant $k_p=800$	64
3.22	Power spectral density of the Slave clock for different k_p values for a constant $k_i=300$	64
3.23	Experimental setup for a 50 km White Rabbit uni-directional link. . . .	65
3.24	Power spectral density of the Slave clock for fine tuning of k_p values for a constant $k_i=300$	66
3.25	Allan deviation (NEQ BW=50 Hz) for the Slave switch for default and optimized gain parameters.	66
3.26	Phase data of the Slave WRS for the 50 km WR link (constant offset has been removed).	67
3.27	Frequency stability for a 50 km White Rabbit link.	67
3.28	Time Deviation for a 50 km White Rabbit link.	68
3.29	Relative frequency noise for the Slave switch, error signal of the Slave switch and for the local oscillator of the WRS.	69
3.30	Relative frequency noise contribution from the 3.3 V and 5 V internal power supply, for the Grandmaster and the Slave switch.	70
3.31	Frequency stability (calculated from phase data) comparison for default and increased PTP rate for the Slave WRS (100 km link).	72
4.1	Experimental setup for a 100 km White Rabbit uni-directional link. . . .	75
4.2	Phase noise power spectral density of the Slave clock for $k_p=4000$ and k_i values.	76
4.3	Allan Deviation of the Slave clock for different k_p and k_i values.	77
4.4	Phase data for the two Slaves (constant offset removed).	77
4.5	Overlapping Allan deviation (calculated from phase data) for the 100 km uni-directional WR link.	78
4.6	Time deviation (calculated from phase data) for the 100 km uni-directional WR link.	79
4.7	Ambient temperature variations experienced and recorded by the time interval counter STS201 and the calculated phase fluctuations. The green trace is the Slave switch data as in Fig. 4.4. We observe a compression factor of about 5 at half a day.	80
4.8	Overlapping Allan deviation (calculated from phase data) for the 100 km uni-directional WR link with evidence of the fiber thermal noise bump.	81
4.9	Limitations for the time stability (calculated from phase data) performance of the 100 km White Rabbit link.	82
4.10	Chromatic dispersion contribution to the time stability performance of the Slave switch (100 km telecom span uni-directional link).	83

4.11	Experimental setup for the cascaded 300 km White Rabbit link.	86
4.12	Phase noise power spectral density of the Second Slave clock for different k_p values with constant $k_i=500$	87
4.13	Phase noise power spectral density of the third Slave clock for default gain values and different k_p values for constant $k_i=500$	87
4.14	Allan Deviation (NEQ BW=5 Hz) for the third Slave clock for default gain values and higher k_p values for constant $k_i=500$	88
4.15	Phase noise power spectral density comparison for the cascaded stages.	89
4.16	Allan Deviation (NEQ BW=500 Hz) for the cascaded stages.	89
4.17	Phase data for the 200 and 300 km cascaded stages (constant offset removed).	90
4.18	Overlapping Allan Deviation (calculated from the phase data) for the 200 and 300 km cascaded stages.	91
4.19	Time Deviation (calculated from the phase data) for the 200 and 300 km cascaded stages.	91
4.20	Experimental setup for the cascaded 400 km White Rabbit link.	92
4.21	Relative frequency deviation for each of the cascaded stages of the 400 km cascaded White Rabbit link.	93
4.22	Overlapping Allan Deviation (calculated from frequency data) for the 400 km cascaded White Rabbit link.	94
4.23	Phase data for the cascaded 300 km stage and for the user end node at 400 km (constant offset removed).	94
4.24	Time Deviation calculated from the phase data for the 300 km cascaded stage and for the user end node at 400 km.	95
4.25	Phase data measurement for the 300 and 400 km cascaded link for the test of short term stability limitation.	96
4.26	Comparison of Overlapping Allan Deviation (calculated from phase data) for the 300 and 400 km cascaded stages for counter swapped case.	96
4.27	Comparison of Time Deviation (calculated from phase data) for the 300 and 400 km cascaded stages for counter swapped case.	97
4.28	Time stability comparison for the frequency data and phase data for the 400 km cascaded link.	97
4.29	Experimental setup for the cascaded 500 km White Rabbit link.	98
4.30	Relative frequency deviation for each of the cascaded stages of the 500 km White Rabbit link with increased PTP rate and increased BW of locking.	100
4.31	Allan Deviation for the 500 km cascaded White Rabbit link and comparison with different GPS receivers. Solid line depicts stability calculated from Frequency data, Dashed line depicts stability calculated from Phase data.	101

4.32	Top: Free running phase fluctuations calculated from the temperature fluctuations of the experimental room (constant offset removed for both), and the Slave ZEN phase fluctuations (blue trace). The blue trace is zoomed in the bottom figure. We observe a compression factor of about 20.	102
4.33	Time stability (calculated from phase data) for the cascaded 500 km White Rabbit link and comparison with infield applications.	103
4.34	Time stability calculated from the frequency data for the cascaded 500 km White Rabbit link.	104
4.35	Wavelength fluctuations for the 1541 nm SFP (constant offset removed).104	
4.36	Relative frequency deviation for each of the cascaded stages of the 500 km White Rabbit link with default PTP rate.	105
4.37	Allan Deviation (calculated from frequency data) for the 500 km cascaded White Rabbit link for default PTP rate.	106
4.38	Time stability calculated from the frequency data for the cascaded 500 km White Rabbit link for default PTP rate.	107
4.39	Relative frequency deviation for each of the cascaded stages of the 500 km White Rabbit link with default bandwidth of locking and default PTP rate.	108
4.40	Allan Deviation (calculated from frequency data) for the 500 km cascaded White Rabbit link for default bandwidth of locking along with default PTP rate.	109
4.41	Time stability calculated from the frequency data for the cascaded 500 km White Rabbit link for default bandwidth of locking along with default PTP rate.	109
4.42	Time stability comparison calculated from phase data for the cascaded 500 km White Rabbit link for default bandwidth of locking along with default PTP rate.	110
4.43	Experimental setup for the multi user 125 km White Rabbit link.	110
4.44	Relative frequency deviation for each of the Slaves at 125 km	111
4.45	Allan Deviation (calculated from frequency data) for the multi-user 4x125 km White Rabbit links.	112
4.46	Time Deviation calculated from frequency data for the multi-user 4x125 km White Rabbit links.	112
4.47	Pictorial representation of the short term and long term limitations for time stability performance of a long haul White Rabbit link.	113
5.1	Experimental setup of the UTC room to Laboratory White Rabbit link.	116
5.2	A 43 km suburban telecommunication network White Rabbit link between SYRTE and LPL (Université Paris 13), Paris.	117
6.1	Experimental setup for the calibration of the fiber spool.	120

6.2	Variation of the delay (offset has been removed) for connecting/disconnecting the fiber link.	121
6.3	Experimental setup of the UTC room to Laboratory White Rabbit link.	127
6.4	A 43 km sub-urban active telecommunication network White Rabbit link between SYRTE and LPL (Université Paris 13), Paris.	129
6.5	The two way PTP scheme for dual wavelength technique.	130
6.6	The two way PTP scheme for dual wavelength technique with Thales theorem representation.	131
6.7	Experimental setup for a 125 km White Rabbit uni-directional link for two Slave WRS.	134
6.8	Round trip time fluctuations for both the Slaves over 16 days of measurement (offset has been removed for both). The trace for Slave 2 has been shifted by 2 ns for clarity.	135
6.9	Fluctuations of the round trip time difference Slave2-Slave1 (offset has been removed).	136
6.10	Fluctuations of β over 16 days of measurement.	136

List of Tables

1.1	Characterization of different noise types for a typical oscillator [2]. PM-Phase modulation, FM- Frequency modulation.	3
1.2	Different noise processes and their dependence on α and τ in the frequency and time domain respectively.	6
3.1	Comparison of the effect of Chromatic Dispersion on stability for commercial SFPs in two setups: a bi-color link using 1490/1310 nm emitters and a single fiber, and a bi-fiber link using the DWDM emitters at 1541 nm and dual fibers.	58
3.2	Summary of the main results.	73
4.1	Allan Deviation (62.5 MHz) at one second of integration time for the Slave clock for different k_p and k_i values.	76
4.2	Comparison of the optimized set of gain parameters for increasing link length.	88
4.3	Summary of the main results. ADEV-Allan Deviation, ODAEV- Overlapping ADEV, TDEV- Time deviation. * the stability is calculated from K+K frequency counter data, else the stability is calculated from time interval counter data.	115
6.1	The measured round trip time (RTT) and bitslide values for Step 1, 2, 3.	122
6.2	The calculated propagation delay for the fiber spool 1 from step 2,3 and the corresponding calculated length of the fiber spool.	123
6.3	Time interval counter readings for Step 1, 2, 3 for Spool 1.	124
6.4	The measured round trip time (RTT) and bitslide values for Step 1, 2, 3 for Spool 2.	125
6.5	The calculated propagation delay for the fiber spool from step 2,3 and the corresponding calculated length of the fiber spool for Spool 2. . . .	125
6.6	Time interval counter readings for Step 1, 2, 3 for Spool 2.	126
6.7	Wavelength swapping of the two links and corresponding variation of δ values.	128

List of Abbreviations

BC	Boundary clock
CWDM	Coarse Wavelength Division Multiplexing
DAC	Digital to Analog Converter
DDMTD	Digital Dual Mixer Time Difference
DFB	Distributed Feedback Laser
DWDM	Dense Wavelength Division Multiplexing
EDFA	Erbium-doped Fiber Amplifier
Fig.	Figure
FMC	FPGA mezzaine card
FPGA	Field-programmable Gate Array
GM	Grandmaster
GNSS	Global Navigation and Satellite System
GPS	Global Positioning System
GTX	Gigabit Transceivers
ITU	International Telecommunication Union
L.O	Local Oscillator
LAN	Local Area Network
NMI	National Metrology Institute
NTP	Network Time Protocol
OADM	Optical Add Drop Multiplexer
OC	Ordinary clock
OSI	Open Systems Interconnection
PLL	Phase Locked Loop

PPS	One Pulse Per Second
PSD	Power Spectral Density
PTP	Precision Time Protocol
RTT	Round Trip Time
SDH	Synchronous Digital Hierarchy
SFP	Small formfactor pluggable optical transceiver
SONET	Synchronous Optical Networking
SPEC	Simple PCI express Carrier board (White Rabbit node)
Sync-E	Synchronous Ethernet
TAI	International Atomic Time
TC	Transparent clock
TIC	Time Interval Counter
TWSTFT	Two Way Satellite Time and Frequency Transfer
UTC	Coordinated Universal Time
VCTCXO	Voltage Controlled Temperature Compensated Crystal Oscillators
WAN	Wide Area Network
WR-PTP	White Rabbit PTP
WR-ZEN	White Rabbit Zync Embedded node
WRPC	White Rabbit PTP core
WRS	White Rabbit Switch

Chapter 1

Introduction

1.1 Time and frequency metrology

Atomic clocks are the most accurate time and frequency standards known, and are used as primary standards for international time distribution services. An atomic frequency standard is a complex system in which the frequency of an oscillator is locked to the frequency of an atomic transition. A timescale is obtained by counting the oscillations of a frequency standard, expressing the number of cycles as a date and time, with some choice of origin. A clock is therefore the combination of a frequency standard and a counter, although frequency standards alone are commonly referred to as clocks.

For metrologists, it is essential to compare the frequency standards and timescales among themselves¹ to assess their accuracy, study possible offsets and measure fine physical effects. These comparisons can measure either time difference or frequency difference, and are referred to as Time or Frequency transfer. The comparison can be done to very high performance over short distances (for instance if in the same laboratory) and the comparison gradually becomes difficult over long distances. This thesis is about Time and Frequency transfer.

First we describe some essential notions and tools. In particular, frequency standards and timescales are metrologically characterized by their accuracy and stability.

1.1.1 Accuracy

For a metrological reference such as a frequency standard, accuracy refers to its offset from its ideal or nominal value. More precisely, since all signals contain statistical fluctuations, it refers to the long-term average value of this offset. Thus accuracy corresponds to the systematic error of the standard.

For a frequency reference, accuracy may be expressed in Hz, or very commonly as a dimensionless value, relative to the nominal frequency.

¹Time/Frequency signals can be transmitted by electrical or electromagnetic signals.

1.1.2 Stability

Stability is defined as the ability of the oscillator to produce the same frequency over time. It doesn't specify if the frequency or time is correct or incorrect, but specifies whether it's constant over time. Fig. 1.1 helps us to understand the relationship between accuracy and stability [1]. A stable oscillator fluctuates little over time but might produce a frequency with a huge offset. An unstable oscillator which fluctuates a lot over time might produce an average frequency close to its nominal value.

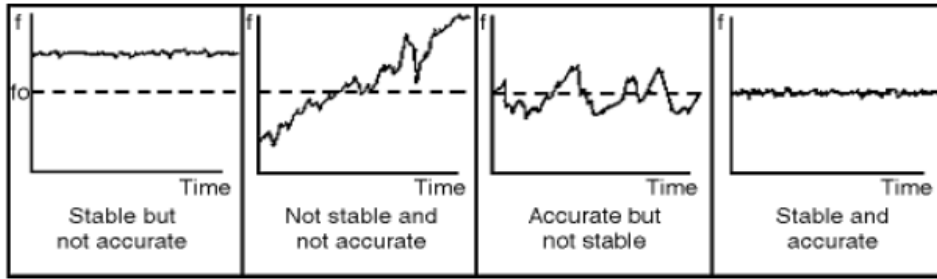


FIGURE 1.1: The relationship between accuracy and stability for a frequency standard of nominal frequency f_0 [1].

1.2 The Oscillator signal

The signal of an oscillator is described by the equation [2]:

$$V(t) = V_0 \sin(2\pi\nu_0 t + \phi(t)) \quad (1.1)$$

where V_0 is the amplitude, ν_0 is the nominal frequency and $\phi(t)$ are the phase fluctuations. The instantaneous frequency is the derivative of the total phase (the term $(2\pi\nu_0 t + \phi(t))$) and is described by the equation [2]:

$$\nu(t) = \nu_0 + \frac{1}{2\pi} \frac{d\phi}{dt} \quad (1.2)$$

and the fractional frequency deviation $y(t)$ is defined as [2]:

$$y(t) = \frac{\nu(t) - \nu_0}{\nu_0} = \frac{1}{2\pi\nu_0} \frac{d\phi}{dt} = \frac{dx}{dt} \quad (1.3)$$

where $x(t)$ are the time fluctuations derived from the phase fluctuations by the relation $x(t) = \phi(t)/2\pi\nu_0$ [2].

1.3 Noise analysis

1.3.1 Frequency domain

In the frequency domain, the power spectral density of the fractional frequency deviation $S_y(f)$ is used to analyze the different noise processes whereas in the time domain, Allan variance $\sigma_y^2(\tau)$ is employed for noise analysis as described in the following section.

The fluctuations of an oscillator are characterized by a power law spectrum [2]:

$$S_y(f) = \sum_{\alpha=-2}^{\alpha=2} h_{\alpha} f^{\alpha} \quad (1.4)$$

where f is the Fourier frequency in Hertz, h_{α} is the intensity coefficient and α is the power law exponent. The different noise types are characterized as follows:

Noise type	α
White PM	2
Flicker PM	1
White FM	0
Flicker FM	-1
Random walk	-2

TABLE 1.1: Characterization of different noise types for a typical oscillator [2]. PM-Phase modulation, FM- Frequency modulation.

The power spectral density of the phase fluctuations $S_{\phi}(f)$ in units of rad^2/Hz is related to the power spectral density of the fractional frequency fluctuations $S_y(f)$ in units of $1/Hz$ by the equation [2]:

$$S_{\phi}(f) = \left(\frac{v_0}{f} \right)^2 S_y(f) \quad (1.5)$$

where v_0 is the carrier frequency and f is the Fourier frequency. The single side band phase noise (SSB phase noise) $\mathcal{L}(f)$ is its logarithmic equivalent and is commonly used to specify phase noise [2]:

$$\mathcal{L}(f) = 10 \cdot \log \left[\frac{1}{2} S_{\phi}(f) \right] \quad (1.6)$$

with units of dBc/Hz.

The Allan Variance is calculated from the power spectral density of the fractional frequency deviation $S_y(f)$ by the following integral [3, 4]:

$$\begin{aligned}\sigma_y^2(\tau) &= 2 \times \int_0^\infty S_y(f) \times \frac{\sin^4(\pi \times \tau \times f)}{(\pi \times \tau \times f)^2} \times df \\ &= 2 \times \sum_{\alpha=-2}^{\alpha=2} \times \int_0^\infty f^\alpha \times h_\alpha \times \frac{\sin^4(\pi \times \tau \times f)}{(\pi \times \tau \times f)^2} \times df\end{aligned}\quad (1.7)$$

where f is the Fourier frequency, τ is the integration time. The above integral for each of the noise types described by α can be written in terms of power of τ [3, 4]:

$$\begin{aligned}\sigma_y^2(\tau) &= h_{-2} \times \frac{(2\pi)^2}{6} \tau + h_{-1} \times 2 \times \ln(2) + h_0 \times \frac{1}{2\tau} \\ &+ \frac{h_1 \times 1.038 + 3\ln(2 \times \pi \times f_h \times \tau)}{(2\pi)^2 \tau^2} + h_2 \times \frac{3f_h}{(2\pi)^2 \tau^2}\end{aligned}\quad (1.8)$$

An interested reader can find details of the above equation in [3, 4].

1.3.2 Time domain

1.3.2.1 Allan Variance

Statistical methods are used to estimate the frequency or time fluctuations of a signal over time. One of the most widely used statistical estimator is Allan Variance for the measure of frequency stability. The utilized statistic is the Allan Deviation ($\sigma_y(\tau)$) which is the square root of Allan variance and is given by the equation [2]:

$$\sigma_y^2(\tau) = \frac{1}{2(M-1)} \sum_{i=1}^{M-1} [y_{i+1} - y_i]^2 \quad (1.9)$$

where y_i is a set of relative frequency variation measurements (see Equation 1.3), and M is the number of measurements and the measurement data are equally spaced by the measurement interval τ . The y_i may be expressed in Hz or as dimensionless values relative to the nominal frequency. It can also be calculated from phase measurements i.e. time measurements as [2]:

$$\sigma_y^2(\tau) = \frac{1}{2(N-2)\tau^2} \sum_{i=1}^{N-2} [x_{i+2} - 2x_{i+1} + x_i]^2 \quad (1.10)$$

where x_i is a set of phase measurements in time units, N is the number of measurements and the data are equally spaced by the measurement interval τ .

Note that $\sigma_y(\tau)$ expresses the stability as a function of τ . The interpretation of this is that $\sigma_y(\tau)$ gives the noise contribution of the reference to a measurement which is averaged over a duration of τ .

1.3.2.2 Overlapping Allan Variance

Another statistical estimator is the Overlapping Allan variance which utilizes overlapping samples for calculations. The calculation is performed by utilizing all possible combinations of the recorded data set at each averaging time τ . It can be determined from a set of M frequency measurements for averaging time $\tau = m\tau_0$, where m is the averaging factor and τ_0 is the basic measurement interval. It is expressed as [2]:

$$\sigma_y^2(\tau) = \frac{1}{2m^2(M-2m+1)} \sum_{j=1}^{M-2m+1} \left\{ \sum_{i=j}^{j+m-1} [y_{i+m} - y_i] \right\}^2 \quad (1.11)$$

In terms of set of $N = M + 1$ phase measurements, it is expressed as [2]:

$$\sigma_y^2(\tau) = \frac{1}{2(N-2m)\tau^2} \sum_{i=1}^{N-2m} [x_{i+2m} - 2x_{i+m} + x_i]^2 \quad (1.12)$$

The use of the overlapping samples improves the confidence of the stability estimate [2].

1.3.2.3 Modified Allan Variance

The modified Allan Variance Mod $\sigma_y^2(\tau)$, is estimated from a set of M frequency measurements for averaging time $\tau = m\tau_0$, where m is the averaging factor and τ_0 is the basic measurement interval. It is expressed as [2]:

$$\text{Mod } \sigma_y^2(\tau) = \frac{1}{2m^4(M-3m+2)} \sum_{j=1}^{M-3m+2} \left\{ \sum_{i=j}^{j+m-1} \left(\sum_{k=i}^{i+m-1} [y_{k+m} - y_k] \right) \right\}^2 \quad (1.13)$$

In terms of set of $N = M + 1$ phase measurements, it is expressed as [2]:

$$\text{Mod } \sigma_y^2(\tau) = \frac{1}{2m^2\tau^2(N-3m+1)} \sum_{j=1}^{N-3m+1} \left(\sum_{i=j}^{j+m-1} [x_{i+2m} - 2x_{i+m} + x_i] \right)^2 \quad (1.14)$$

The Modified Allan Deviation Mod $\sigma_y(\tau)$ has an advantage of distinguishing between the white and flicker phase modulation noise. The Table also depicts the different τ dependence of Allan Deviation and Modified Allan deviation for White and Flicker PM noise. The following table summarizes the different noise processes with α and τ dependence in the frequency and time domain respectively.

1.3.2.4 Time Variance

The Time Variance with square root as the Time deviation is derived from Modified Allan Variance. It is a measure of the time stability and is widely used for time

Noise type	α	$\sigma_y(\tau)$	$Mod\sigma_y(\tau)$
White PM	2	τ^{-1}	$\tau^{-3/2}$
Flicker PM	1	τ^{-1}	τ^{-1}
White FM	0	$\tau^{-1/2}$	$\tau^{-1/2}$
Flicker FM	-1	τ^0	τ^0
Random walk	-2	$\tau^{+1/2}$	$\tau^{+1/2}$

TABLE 1.2: Different noise processes and their dependence on α and τ in the frequency and time domain respectively.

distribution networks. It is defined as [2]:

$$\sigma_x^2(\tau) = \left(\frac{\tau^2}{3}\right) \cdot Mod \sigma_y^2(\tau) \quad (1.15)$$

1.4 Clocks and timescales

Time is one of the seven fundamental physical quantities and the second is one of the seven base units described in the International System of Units (SI). The former definition of second was based on the astronomical event such as the Earth rotation. Motivated by the advances of quantum physics and with the advent of atomic frequency standards providing superior stability and accuracy, the second was redefined in 1967 to the present atomic definition: *the second is the duration of 9,192,631,770 periods of the radiation corresponding to the transition between the two hyperfine levels of the ground state of the Cesium-133 atom.*

Cesium clocks are primary frequency standards. Presently, Cesium fountains exhibit best performance with typical accuracy of a few parts in 10^{-16} and short term stability of 1.6×10^{-14} averaging down to 10^{-16} after one to a few days [5]. Optical clocks are a new generation of clocks, based on optical transitions in various atoms and ions. An optical lattice clock with accuracy and stability performances at the level of 10^{-18} [6] has been demonstrated. Note that this level of uncertainty refers to the clock's own reference transition, not to its capability of realizing the second as currently defined by the Cesium atom. With such remarkable performance, the redefinition of the SI second in terms of an optical transition is expected in the coming decade [7].

The National Metrology Institutes (NMI) realize and maintain timescales based on the highest precision atomic clocks such as cesium fountains, hydrogen masers and optical clocks. All the NMIs over the world compare their time and frequency standards regularly and report the measurement data to the Bureau International des Poids et Mesures (BIPM). The BIPM combines the collected data and generates two timescales, International Atomic Time (TAI) and Coordinated Universal Time (UTC), which is obtained from TAI by addition of leap seconds for synchronization

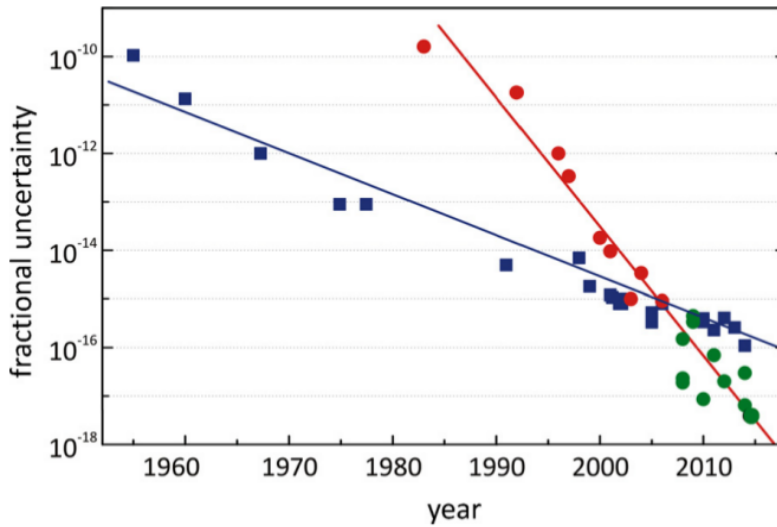


FIGURE 1.2: The time evolution of the uncertainty of Cesium and Optical clocks. Fractional uncertainty of primary Cesium atomic clocks to realize the second in the SI (squares) and optical frequency clocks (dots). Green dots represent optical clocks with estimated standard uncertainties whose optical frequency can be determined only with the accuracy of the frequency comparison with a primary Cesium clock [7].

with Earth rotation. UTC is recognized as an international reference timescale, and it is the basis of legal time in many countries (with the addition of the appropriate offset). Because UTC is calculated in post-processing with some delay, many NMIs maintain their own timescale, known as UTC(k), which is an approximation to UTC in real time, for practical purposes.

The realization of industrial atomic frequency standards allow a wide dissemination of atomic time for syntonization and synchronization in many fields of industry and research: communications, navigation, space, defense, energy and astronomy. Such systems can also provide atomic time. Among them, Global Navigation and Satellite System (GNSS) time services (GPS, GLONASS, Galileo) are widely used and provide good performances, even if care must be taken to ensure traceability to national or international standards.

The improvements of atomic frequency standards actually impose improvements of the whole metrology chain. Applications are becoming more and more demanding over time. The synchronization of de-localized systems turns to be critical in our modern society and alternative methods to GNSS time distribution are needed, either for redundancy and security issues, or to compare and improve the quality of the synchronization.

1.5 Introduction to time transfer methods

The clock systems used to realize and maintain timescales are very complex and non transportable systems with restricted access thus giving rise to the development of different techniques to disseminate timescales such as UTC to users. Typically, this is based on a comparison, then the user clock is steered to correct its time offset. The main time and frequency transfer methods are as follows:

- Satellite-based methods such as GNSS and TWSTFT are adequate for comparison of Cesium clocks.
- Optical fiber link methods for very high performance comparison of Optical clocks.
- Packet-based network protocols used for local and wide area network synchronization.

For discussion on different time and frequency transfer methods, let us consider two clocks, A and B, which are linked by a propagation channel. Let us consider Clock A as the reference clock and Clock B as the local clock of a user. For any time transfer method, different type of delays need to be evaluated in order to synchronize the local clock to the reference clock. Fig. 1.3 presents the various types of delays associated with a time transfer method. One needs to evaluate the instrumental delays such as the transmission and reception delays of the clocks and associated equipment, the propagation delay arising due to the propagation channel, including all relevant contributions such as atmospheric effects, Sagnac effects [8, 9], etc depending on the medium.

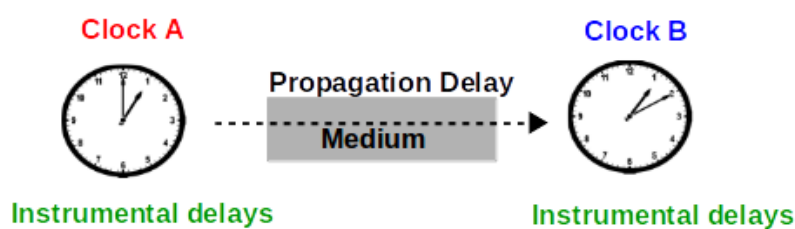


FIGURE 1.3: One way time and frequency transfer.

Two general classes of time and frequency transfer methods are called as "One way" and "Two way". They are described in the following sections. Note that we will not give the relativistic definitions of the time transfer equations, as it will not be needed in this thesis.

1.5.1 One way time transfer method

Fig. 1.4 displays the general scheme of the one way time transfer method. In this method, Clock A sends a time signal to Clock B through the propagation medium.

Clock B uses this signal to synchronize itself to A. For best accuracy, B must take into account the propagation delay. The propagation delay may be determined from the knowledge of factors such as celerity of the waves, modelling of the propagation medium and spatial co-ordinates. The measurement uncertainty is due to the error in determining the one way delay.

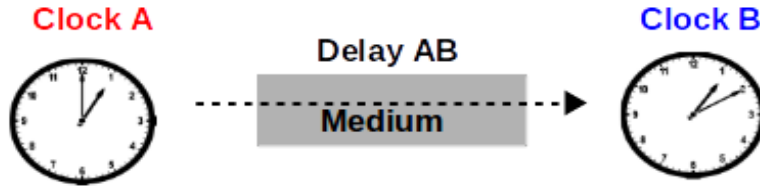


FIGURE 1.4: One way time and frequency transfer.

Clock A and B are associated with equipment delays (measurement and transmission and reception). Let us consider ΔT as the offset between the two clocks, which we aim to measure. Let us denote t_1 as the time at which the signal leaves the reference point of clock A, as measured by A. The time t_2 is the time at which the signal arrives at the reference point of Clock B, as measured by B. The transmission delay of Clock A is denoted by Δ_{txA} , which is the time delay between the reference point of A and the point where the signal is injected into the medium (antenna, optical emitters). The reception delay for Clock B is denoted by Δ_{rxB} , which is the time delay between the arrival of the signal at the receiving point of Clock B (antenna, photodetector) and the reference point of B.

The propagation time in the medium (between the emitter and receiver) is given by δ_{AB} . With these definitions we have:

$$t_2 = t_1 + \Delta_{txA} + \delta_{AB} + \Delta_{rxB} + \Delta T \quad (1.16)$$

thus ΔT is calculated as:

$$\Delta T = t_2 - t_1 - \Delta_{txA} - \delta_{AB} - \Delta_{rxB} \quad (1.17)$$

1.5.1.1 GNSS time dissemination

The one way time transfer method is the basis of *Global Positioning System (GPS)* and more generally GNSS time transfer. GPS is a navigation system operated by the U.S. Department of Defense (DoD) comprising of 24 satellites orbiting the Earth. The GPS satellites transmit time signals to the receivers on the Earth. The GPS satellites transmit signals at 1.5 GHz (L1) and 1.2 GHz (L2) (and now also at L5) and the signals are modulated with pseudo-random noise (PRN) code sequences. There are two types of PRN codes. The first is the coarse/acquisition (C/A) codes with 1023 bits per millisecond rate which are available to all users and the second is the precise

(P) encrypted code with a bit rate of 10230 bits per millisecond [1] reserved for the military. In addition to this, a navigation message is also modulated onto both the carriers, containing satellite orbit data (ephemeris) and other necessary data for the receiver to determine its position and the time. The GPS reception is line-of-sight and requires a clear view of the sky.

For GNSS time dissemination, the simplest case is when the position of the receiver is fixed and known. In this case, it is a one-way time transfer from satellite to receiver. On the other hand, if the position of the receiver is unknown, then the process is more complex because transmission from at least four satellites are required by the receiver to determine both position and time. GPS time service is widely used for dissemination of time and frequency. The signals are available almost anywhere on Earth. It serves various applications such as telecommunications, calibration and testing laboratories and scientific experiments.

1.5.1.2 GNSS time transfer methods

GNSS time dissemination is a simple one way time transfer (where the transfer from the satellite to the receiver is a standard one way) whereas GNSS time transfer as practiced by time and frequency metrology laboratories is a pair of two one way time transfers using the GPS time as "pivot".

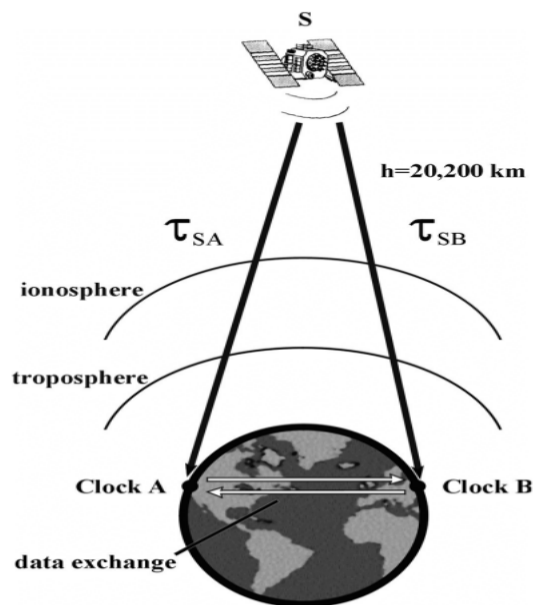


FIGURE 1.5: GPS common-view technique [10].

GPS time transfer can be further categorized as the *Common-view* and *All-in-view* methods. Fig. 1.5 shows the common-view GPS technique [10]. This method uses the GNSS time transfer between two clocks on the ground. In this method, the two

Clocks A and B are measured against two GPS receivers. A GPS satellite is in common view for both the receivers. The transmitted signal is received simultaneously by both the receivers. respectively. Each receiver station compares the received signal to its clock to measure offset from GPS time, Clock A - GPS time and Clock B - GPS time. Then the two sites exchange data to compute their difference. The GPS time cancels out as it is common mode with the final result as (Clock A - Clock B).

The measurement uncertainty is limited by the factors such as the ephemeris errors, ionospheric and tropospheric delay errors, hardware delays and multipath reflections [11, 12]. If the sites are separated by short distance, then the receiving conditions tend to be same at both the locations and same errors tend to cancel as they are common to the two propagation paths. But if they are far apart then the receiving conditions tend to differ resulting in less errors canceling out during the subtraction of the data. Dual frequency GNSS time dissemination can compensate for the effect of ionospheric delay [13].

The *All-in-view* method (also known as the melting pot method) is a variant of above method particularly useful for long distances. In this method, the receiver station receives signals from all the satellites in view. It has an advantage that it is more robust and users can continuously compare standards with no gaps in their measurements. This method is a way of accomplishing global coverage by utilizing multiple satellite transmitters whose signals are synchronized to a common reference [11].

High performance GPS time transfer is achieved by the *GPS-Precise Point Positioning (PPP)*, which is one form of Carrier-Phase GPS technique. This technique utilizes both the time codes transmitted by the GPS satellite along with the phase of the carrier. Utilization of the carrier frequency which is a thousand times higher than the C/A code results in the improvement of the measurement resolution [10]. GPS carrier phase measurements are two orders of magnitude more precise than the GPS code data and a better estimate of the atmospheric effects can be done [14]. This method uses the precise satellite orbit data provided by the International GPS service (IGS) [15]. This technique is used for international comparisons between primary frequency standards [16, 17] and for TAI computation [14]. Table 1.3 shows the typical uncertainties (instabilities) of GPS measurement techniques [10].

1.5.2 Two way time transfer method

Fig. 1.6 shows a general schematic of the two way time transfer. In this method, both the clocks Clock A and B transmit time signals. Each of the Clocks measure the arrival time of the signal of the other clock.

Technique	Timing Uncertainty 24 h, 2σ	Frequency Uncertainty 24 h, 2σ
One-Way	< 20 ns	< 2×10^{-13}
Single-Channel Common-View	≈ 10 ns	$\approx 1 \times 10^{-13}$
Multi-Channel Common-View	< 5 ns	< 5×10^{-14}
Carrier-Phase Common-view	< 500 ps	< 5×10^{-15}

TABLE 1.3: Typical uncertainties of GPS measurement techniques [10].

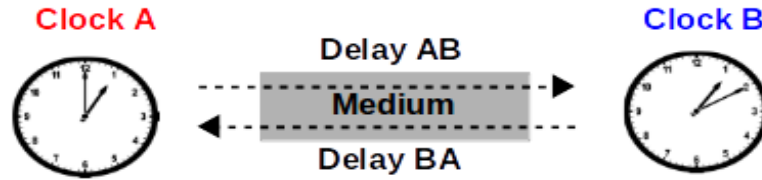


FIGURE 1.6: General schematic of a two way time transfer method.

Let us consider ΔT as the offset between the two clocks, which we aim to measure. Let us denote t_1 as the time at which the signal leaves the reference point of Clock A, as measured by A. The time t_2 is the time at which the signal arrives at the reference point of Clock B, as measured by B. Similarly t_3 is the time at which the signal leaves the reference point of Clock B, as measured by B and t_4 is the time at which the signal arrives at the reference point of Clock A, as measured by A.

The transmission delay of Clock A is denoted by Δ_{txA} , which is the time delay between the reference point of A and the point where the signal is injected into the medium (antenna, optical emitters). The reception delay for Clock B is denoted by Δ_{rxB} , which is the time delay between the arrival of the signal at the receiving point of Clock B (antenna, photodiode) and the reference point of B. Similarly, the transmission delay for Clock B is denoted as Δ_{txB} and the reception delay for Clock A is denoted as Δ_{rxA} . The propagation time from A to B and B to A in the medium is denoted by δ_{AB} and δ_{BA} respectively. With these definitions we have:

$$t_2 = t_1 + \Delta_{txA} + \delta_{AB} + \Delta_{rxB} + \Delta T \quad (1.18)$$

$$t_4 = t_3 + \Delta_{txB} + \delta_{BA} + \Delta_{rxA} - \Delta T \quad (1.19)$$

thus ΔT can be calculated as:

$$\Delta T = \frac{(t_2 - t_1) - (t_4 - t_3)}{2} - \frac{(\delta_{AB} - \delta_{BA})}{2} - \frac{(\Delta_{txA} - \Delta_{rxA})}{2} - \frac{(\Delta_{txB} - \Delta_{rxB})}{2} \quad (1.20)$$

In case of symmetric propagation delays $\delta_{AB} = \delta_{BA}$, the second term reduces to zero. In general the propagation delays are asymmetric and this term may be needed to achieve the required accuracy. The same is true for instrumental delays. Defining the round-trip time, RTT, as

$$\begin{aligned} RTT &= \Delta_{txA} + \delta_{AB} + \Delta_{rxB} + \Delta_{txB} + \delta_{BA} + \Delta_{rxA} \\ &= (t_2 - t_1) + (t_4 - t_3) \end{aligned} \quad (1.21)$$

and the time transfer equation can be rewritten as

$$\Delta T = (t_2 - t_1) - \frac{RTT}{2} - \frac{(\delta_{AB} - \delta_{BA})}{2} - \frac{(\Delta_{txA} - \Delta_{rxA})}{2} - \frac{(\Delta_{txB} - \Delta_{rxB})}{2} \quad (1.22)$$

This is similar to the one-way time transfer equation 1.17. $RTT/2$ can be considered as a first approximation to the sum of the instrumental and propagation delays from A to B, but in general be corrected for the asymmetries of these delays. The disadvantage of the two way method is that the technique is full duplex, for which both the stations should be able to transmit and receive signals.

1.5.3 Two way Satellite Time and Frequency transfer (TWSTFT)

One of the most precise and accurate techniques for comparison of frequency standards located at remote sites is the Two way Satellite Time and Frequency transfer [16, 17]. This is an implementation of the principle described above with signal transmission as follows [11]:

1. The metrology signal is carried at high frequencies in free space. The method utilizes a modem to generate a pseudo random code synchronized to the local clock and this code is used to modulate a microwave signal of about 14 GHz. This modulated signal is transmitted to a geostationary telecommunication satellite from the Earth station and is referred to as the *uplink*.
2. The satellite re-transmits this modulation on a *downlink* at a frequency of 12 GHz which is received at the remote site. The signal is demodulated by a modem and the received pseudo random code is cross correlated with the locally generated pseudo random code.

The scheme for TWSTFT is illustrated in Fig. 1.7 [18]. At Clock A station, a time interval counter measures the time difference (T_A) between the Clock A (C_A) signal and the received signal from Clock B (delayed by the propagation and instrumental delays). Similarly, at the Clock B station, a time interval counter measures the time

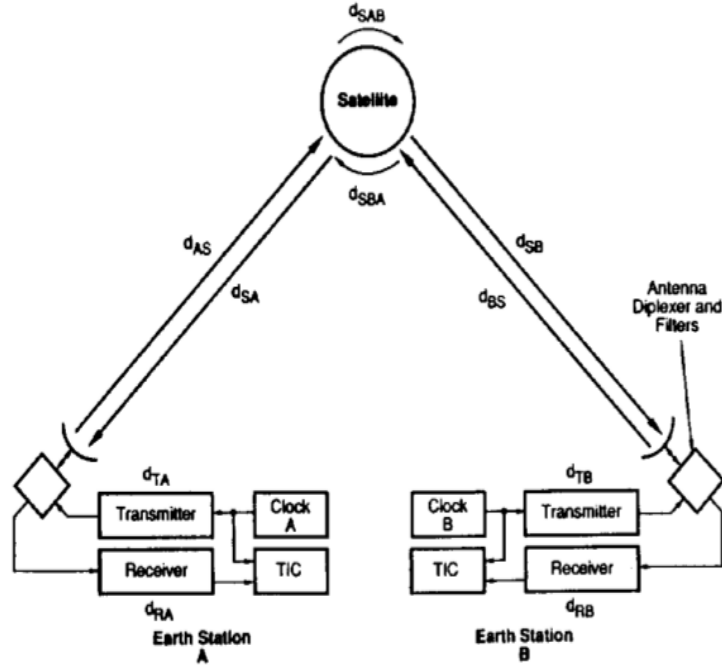


FIGURE 1.7: Two way satellite time and frequency transfer [18].

difference (T_B) between the Clock B (C_B) signal and the received signal from Clock A. The time difference between the clock stations (ΔT) is given by the following equation [18]:

$$T_A = C_A - (C_B + d_{TB} + d_{BS} + d_{SBA} + d_{SA} + d_{RA} + 2\omega A/c^2) \quad (1.23)$$

$$T_B = C_B - (C_A + d_{TA} + d_{AS} + d_{SAB} + d_{SB} + d_{RB} + 2\omega A/c^2) \quad (1.24)$$

where the clock offset $\Delta T = C_A - C_B$ is obtained by subtracting the above two equations:

$$\begin{aligned} \Delta T = (T_A - T_B)/2 - (d_{TB} - d_{RB})/2 + (d_{TA} - d_{RA})/2 + (d_{AS} - d_{SA})/2 \\ - (d_{BS} - d_{SB})/2 + (d_{SAB} - d_{SBA})/2 - 2\omega A/c^2 \end{aligned} \quad (1.25)$$

where d depicts the different delays associated with the time transfer as illustrated in Fig. 1.7. The second the third terms present the difference in the transmission and reception delays of each of the clock stations respectively, the fourth and fifth terms present the difference in the uplink/downlink propagation delays for clock stations A and B respectively; these terms almost cancel out with the assumption that the signals traverse symmetric paths. The sixth term is the difference in delay due to the satellite. The last term is due to Sagnac effect [8, 9]. It arises due to the effect of Earth's rotation, A is the area defined by the equatorial plane by the line segments connecting the satellite and the center of the Earth to the two clock stations. These terms are computed from the positions of the ground stations and the geostationary

satellite.

This method provides high accuracy due to the high frequency signals used for transmission and the nearly symmetric path delays. The high operational cost of this method is a disadvantage.

1.5.4 Time and frequency transfer over Optical fiber links

Over the last fifteen years, optical fiber links have been intensively studied for frequency dissemination. They have demonstrated frequency transfer with uncertainties below 10^{-19} over several hundred km [19, 20]. It allows comparison of optical signals with accuracy and stability down to 10^{-20} level, comparison of remote clocks with unprecedented uncertainty [21, 22] opening doors to new stringent tests of fundamental physics and relativity [23] and chronometric geodesy [24]. In the RF and time domain, the link from AOS to GUM in Poland is running almost continuously from 2013 with state of the art time uncertainty [25]. Applications to VLBI were explored in the RF and optical domain [26, 27, 28, 29, 30].

Time transfer was by comparison less intensively studied. A seminal experiment was carried out by imprinting a modulation on the optical carrier as in [31, 32] and an absolute time accuracy of 250 ps and long-term timing stability of 20 ps was achieved for a 540 km public telecommunication optical fiber network [31]. Another significant time transfer experiment was carried out by transferring a femto-second laser over a 159 km installed fiber network [33]. They achieved a time deviation of 300 fs at 5 s and an accuracy at the 100 ps level.

One of the most mature technique is the active stabilization of the propagation delay for joint time and frequency transfer, also referred as the ELSTAB technique [34, 35]. They extend and test this system up to 600 km long fibers installed in an urban Polish telecommunication network [36]. They demonstrate a time stability below 1 ps for averaging time up to 10^3 seconds which increases to about 3 ps for longer averaging times and a time calibration with accuracy well below 50 ps [36].

Two configurations are possible for optical fiber links. The first is a bi-directional setup which utilizes single fiber for propagation of forward and backward signals. The second configuration is a uni-directional setup which utilizes two separate fibers for propagation of forward and backward signals. Such high performance experiments utilize fully bi-directional architecture (same wavelength, same frequency, same fiber) and fit to point-to-point network architecture or point-to-a few network architecture.

1.5.5 Time over Internet

At the other extreme of fiber based synchronization solutions, there are also packet-based protocols over Ethernet and Internet, including their optical fiber implementations.

1.5.5.1 Network Time Protocol (NTP)

NTP was developed by David Mills [37] and is the most widely utilized Internet protocol. It uses only the highest OSI layer [38] of telecommunication, which is the software layer. NTP is a client-server service. There is no modification at all of the telecommunication backbone and it only requires software installation at the end user. Any computer with commonly used operating system can run NTP daemon and synchronize its clock to the time reference. It works on a wide area network (WAN). The use of NTP is for free. For these reasons, it is extremely popular. But this service may not be traceable and accurate, as the propagation delay is not constant and is not precisely known, and depends on the data traffic.

NTP is a two way technique based on packet exchange process between the Client (local time) and the Server (reference time). Fig. 1.8 displays the NTP packet exchange process. The Client initiates the message exchange process by sending a packet including the value of time t_1 , which is the time at which the message was sent. This message is received by the Server at a time t_2 in its timescale. Then this process is reversed, the Server sends a packet timestamped with t_3 along with the t_1 , t_2 values, which is received at time t_4 by the Client. The Client thus has the knowledge of the timestamps needed to evaluate the time offset between the Client and Server timescales.

With these four timestamps value, one can calculate the round trip time as the sum of the one way delays δ_1 (from Client to Server) and δ_2 (Server to Client). The round trip time (RTT) is given by the equation assuming $\delta_1 = \delta_2 = \delta$:

$$RTT = \delta_1 + \delta_2 \quad (1.26)$$

and assuming $\delta_1 = \delta_2 = \delta$ and ignoring the instrumental delays, then we have

$$\delta = RTT/2 \quad (1.27)$$

the clock offset (ΔT) is calculated:

$$\Delta T = t_2 - t_1 - \delta \quad (1.28)$$

The source of inaccuracy is the above assumption because the path delays for both the directions are never same due to routing and switching in a network (cf Two-way time transfer method). With this method, the achievable time accuracy is typically

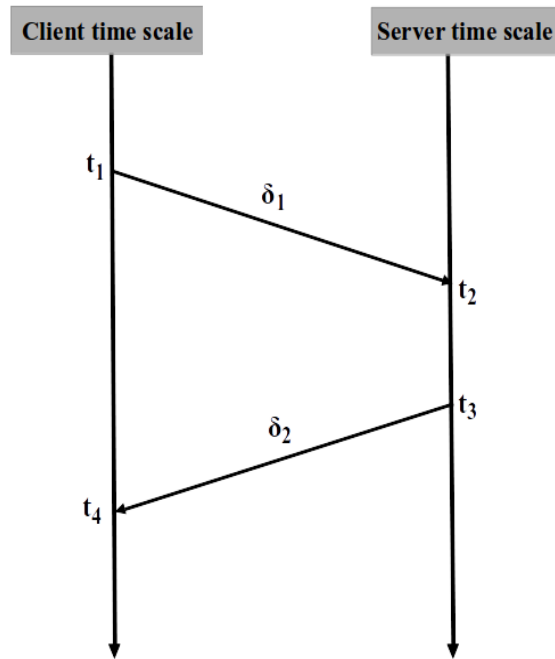


FIGURE 1.8: NTP two way message exchange process.

in the ms to a few hundred of ms range over WANs.

NTP includes different algorithms for selecting the best time servers among all available and to turn down the unreliable ones. One of the main advantages of NTP is that it doesn't require expensive complex hardware, and the timestamps are generated in software. It is easy to implement, robust and cost effective.

1.5.5.2 Precision Time Protocol

Precision Time Protocol (PTP) also known as the IEEE-1588 standard [39] was developed to provide better synchronization for network measurements and control systems. Despite the advantages of NTP, its performance is limited because the timestamps are generated in software and because congestion causes asymmetries in network nodes such as switches and routers. PTP improves over NTP in that hardware timestamping is implemented in PTP technology. Furthermore, PTP provides the solution to node asymmetries by utilizing special switches and routers called transparent clocks or boundary clocks [39]. PTP is able to achieve accuracy in the range of microseconds. Its synchronization is strictly dependent on routing through the network and thus PTP is a suitable synchronization solution for devices in a local area network (LAN). PTP is described in detail in the next chapter.

1.5.5.3 SONET and SDH

Seminal work was done by Jefferts *et al.* in the early 90's on time and frequency over Synchronous Ethernet, using SONET/SDH frames [40]. Their SONET two way time transfer system demonstrated stabilities less than 10 ps over short distances (km).

Relatively few experiments were carried out over the following decade as Global Navigation Satellite System (GNSS) solutions fulfilled most needs and covered wide area (the free space advantage). In 2010, significant work was done on two way optical passive time transfer based on packet over SONET/SDH utilizing the Swedish telecommunication network. This work performed long distance time transfer over a 560 km fiber link with precision (relative to the GPS link) less than 1 ns for over several months of measurement[41].

1.5.5.4 White Rabbit PTP (WR-PTP)

White Rabbit (WR) is an extension of PTP with Synchronous Ethernet and digital phase measurements to achieve much higher performance [42]. White Rabbit was developed by CERN and other scientific laboratories as a successor of their dedicated timing system for CERN's accelerators. It integrates synchronization with the scalability and flexibility of regular Ethernet networks.

The initial White Rabbit experiment by the CERN team was a short range synchronization between a WR Master and three WR Slaves in a daisy chain configuration [42]. Each Slave was synchronized by a 5 km fiber spool to the previous stage. The accuracy and precision of the synchronization between the Master and each of the Slave is displayed in Fig. 1.9. The histogram depicts the master to slave offset below 1 ns for each of the Slaves. The accuracy is within ± 200 ps and standard deviation for each of the Slaves is in the order of 6 ps.

Such impressive results led metrology laboratories to consider White Rabbit PTP for precise time and frequency dissemination. It was initially developed for synchronization of thousands of nodes up to 10 km range. Two seminal experiments were carried out to show that the technique is extensible to long distances over a telecommunication network. The first experiment by the Finnish metrology laboratory VTT, is a dual fiber 950 km link between Espoo and Kajaani in Finland, where WR is carried over an active Dense Wavelength Division Multiplexing (DWDM) network of Finnish University and Research network FUNET (uni-directional, including chromatic dispersion compensation spools). They demonstrated time stability as low as 20 ps at 1000 seconds of integration time [43]. They utilized an external method of

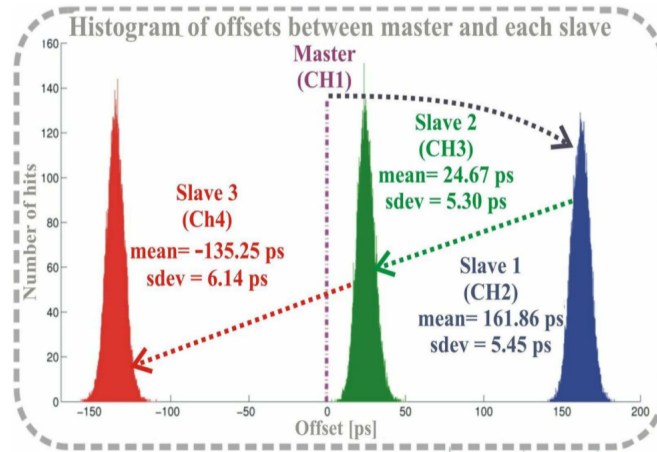


FIGURE 1.9: WR synchronization performance for initial experiments by CERN[42].

GPS calibration and reported that the WR transfer agrees with GPS PPP measurements within ± 2 ns.

The second time transfer experiment was performed on active telecommunication networks almost at the same time as the Finnish experiment. It is a 2×137 km link between VSL and Nikhef, The Netherlands. WR is carried by SURFnet on their active telecommunication network on a Coarse Wavelength Division Multiplexing band. They achieved a time stability of 10 ps at 1000 seconds of integration time [43]. They reported an accuracy budget of 8 ns. With such results, White Rabbit PTP appears to be a very promising technology for long haul time and frequency dissemination. The reader can find more details on WR-PTP in the next Chapter.

Interested readers can find more information in the last review paper [19], recent work at the working group for advanced time and frequency transfer methods at BIPM [44], and the list of projects using or developing White Rabbit on the CERN web page [45, 46]. I simply conclude this section by stating that several studies are nowadays being undertaken all over the world, especially in Europe and Asia. Time and frequency transfer over optical fiber links has emerged as an excellent alternative to GNSS based methods for large scale time dissemination.

1.5.6 Performance comparison of some time transfer methods

In this section we categorize the described time transfer methods according to their performances. The three categories are displayed in Fig. 1.10. The first category is the very high performance time transfer by optical fiber links providing accuracy in the range of hundreds of picoseconds to a few nanoseconds covering national or continental scale. The second category includes the two way satellite time and frequency transfer and the GNSS common view method. This category provides accuracy in the range of few ns and covers long distances (1000 km) with GNSS

covering the Global scale. The last category in the performance comparison is the time over Internet providing synchronization accuracy in milliseconds for NTP, in microseconds for PTP and in nanoseconds range for White Rabbit PTP.

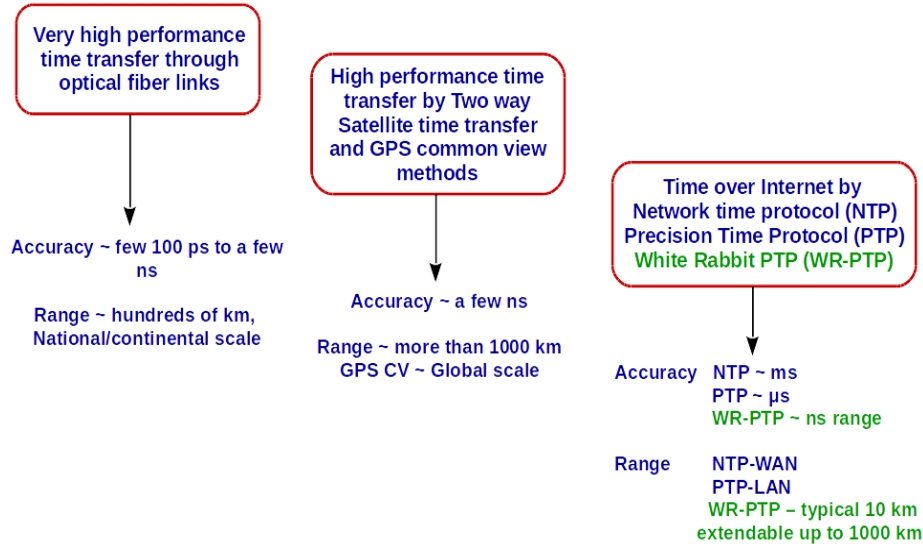


FIGURE 1.10: Performance comparison of some time transfer methods.

Our work falls in the third category of performance providing synchronization to many sectors such as telecommunication, industries and power grids and focuses on the implementation of White Rabbit PTP for precise time and frequency dissemination over long haul links.

1.6 Implemented and Potential applications of White Rabbit

We describe briefly the current and future applications of White Rabbit in various areas.

1.6.1 For Scientific experiments

With its promising timing capabilities and high performance, it is being utilized for many scientific experiments ranging from time synchronization for particle detectors such as LHAASO, HiSCORE, KM3net, CSNS, for Radioastronomy, for trigger distribution systems, Seismic measurements at CERN and their details can be found at [46]. A lot of other scientific projects such as SKA (Square Kilometer array), CTA (Cherenkov Telescope array) and others are evaluating WR for their time applications.

1.6.2 Calibration in the RF domain

White Rabbit signals can be used as reference for calibration. The users can calibrate their local oscillators with respect to the WR signals.

1.6.3 Smart power grids

Precision timing is one of the fundamental elements for optimal wide area monitoring, control and protection in the power industry. Last year, the National Institute of Standards and Technology (NIST) addressed the issue of precision timing needs in power systems. In this regard, they established a Smart Grid Testbed, which includes the Precision Timing module to support the IEEE 1588 Power Profile efforts. A detailed study on the timing needs and challenges in Smart grid can be found in [47]. In this regard, a White Rabbit High-availability Seamless Redundancy (WR-HSR) protocol has been developed to conform a leading-edge deterministic and reliable ultra-accurate timing system with high-availability data features for industrial facilities [48].

1.6.4 5G mobile networks

The journey towards the fifth generation of mobile communication has began. Synchronization is prime in cellular networks and the future networks require nanosecond and picosecond time error [49]. White Rabbit appears to be a potential candidate for network operators for future 5G mobile networks.

1.6.5 Financial transactions and timestamping

According to the new regulations introduced in 2018 by the European Securities Market Authority (ESMA), all the trading deals need to be timestamped within one microsecond [50], which leads to a stringent time traceability for the finance sector. For instance, in the UK, NPLTime provides 'time-over-fiber' service to the financial sector in partnership with network infrastructure providers and overcomes the weaknesses of GPS time service[51].

In France, a new commercial service SCPTIME, is being made available for precise and secure time for a wide range of applications. White Rabbit is likely to be used for the highest performance applications.

1.7 Outline of the thesis

Time and frequency dissemination service from an NMI to an ensemble of highly demanding users at reasonable cost is motivated by the deprecation of other services such as time over phone, radio signals and Loran-C and also by the increasing

need in performance beyond the usual fiber based services but beneath the ultra-high performance of point to point methods. A technology gap emerges between the software based application such as NTP and the high performance optical fiber techniques. Thus, a question arises is there a method compatible with the telecommunication network and potentially multi user which can meet the performances of GNSS signals?

This is the central question of my thesis.

If so, a novel time and frequency service could be developed which would allow interesting comparison studies of the different time and frequency methods for instance fiber based methods vs GNSS techniques.

In view of the impressive timing capabilities of WR-PTP, it appears as a good candidate to bridge the gap between performance, competitive cost and scalability.

The following chapters describe the work under taken. In the next chapter, we give an overview of the White Rabbit PTP. The third chapter describes our initial laboratory experiments with White Rabbit in order to determine its strengths and weaknesses for our applications. Then, we further concentrate on improving its performance, for which a collaboration with the White Rabbit manufacturer Seven Solutions [52] was established and performances of mid range White Rabbit links of 25 km and 50 km were studied. In the fourth chapter, we perform a careful and detailed noise analysis for various situations, extending the range of our laboratory experiments gradually from 100 km to 500 km. In the fifth chapter, we describe two deployments of White Rabbit links. Finally, in chapter 6 we present some initial investigations of methods for calibration of time delays of White Rabbit links. We focused on methods which would not require any external method of calibration and focused on methods that would involve measurements using the optical fiber network and equipment.

Chapter 2

Introduction to White Rabbit Precision Time Protocol (WR-PTP)

2.1 Introduction to WR project

The White Rabbit (WR) project [42] is a multi-laboratory and multi-company collaboration for the development of a deterministic, accurate timing solution based on existing network standards serving thousands of nodes. White Rabbit was initiated at the European Organization for Nuclear Research (CERN) in 2008 as a potential successor for their General Machine Timing (GMT) system. It was developed to provide accurate timing synchronization for CERN's accelerator complex consisting of particle detectors such as ATLAS, ALICE and others. White Rabbit is an open hardware and software project providing a novel and flexible environment for collaboration among research laboratories, public institutes and companies [45]. The White Rabbit community being an open community greatly benefits the users through exchange of ideas and solutions over an active project mailing list.

2.2 Introduction to WR-PTP

White Rabbit is an Ethernet-based network providing deterministic packet delivery and an accurate clock synchronization mechanism. It is based on Precision Time Protocol (PTP), Synchronous Ethernet (Sync-E) and Digital Dual mixer Time difference (DDMTD) phase detection to achieve high performance [53]. It demonstrates sub-nanosecond time stability for the synchronization of arrays over 10 km scale networks. Work has been done and is ongoing on extending it to long haul links of up to 1000 km [43]. The following subsections describe the building technologies for White Rabbit.

2.2.1 Precision time Protocol (PTP)

The IEEE Standard 1588 [39] defines a Precision Clock Synchronization Protocol for networks and measurement and control systems applicable to local area networks. PTP was developed in order to address the growing demands from military, industrial automation, utility power generation and telecommunication users for accurate

timing. Compared to NTP (Network Time Protocol), PTP provides microsecond level synchronization accuracy and utilizes hardware-based timestamping as well as compensating for asymmetries in network node equipment to achieve high performance. There are three types of PTP clocks defined in the IEEE 1588 standard as follows:

- **Ordinary clock (OC)** is a single port device which can be configured as a Master (the reference for synchronization) or as a Slave synchronized to the Master.
- **Boundary clock (BC)** is a multi-port device that can be configured as a Slave synchronized to the Master and it may also serve as a reference for the adjacent nodes.
- **Transparent clock (TC)** is a multi-port PTP node which passes the PTP packets through and inserts in them a record of the transiting delay value. It cannot serve as a Master or a Slave because it does not contain a servo controlled local oscillator.

The PTP standard is based on a master-slave hierarchy mechanism where the free running local oscillator of the Slave node is locked to the reference oscillator of the Master node. The protocol describes a method to evaluate the clock offset between the Master and the Slave through exchange of timestamped Ethernet packets. Fig. 2.1 illustrates the PTP two way message exchange technique. The message exchange consists of two types of messages: the timestamped *event messages* which are used for clock offset calculation (depicted in red in Fig. 2.1) and the *general messages* which are used for PTP node identification, clock hierarchy establishment and for management purposes. The Master sends the first general *Announce* message for clock hierarchy establishment. Afterwards, the Master sends an event message *Sync* at time t_1 , which is received at the Slave timescale at time t_2 . This process is then reversed, the Slave sends an event message *Delay_Req* at time t_3 , which is received at the Master timescale at time t_4 . For synchronization process, the Slave requires the values of t_1 and t_4 timestamps which are measured in the Master timescale. The t_1 value is either embedded in the *Sync* message directly (One step clock) or is transferred by a discrete message *Follow_up* (Two step clock). The t_4 value is transferred in a similar manner.

Let us denote δ_{MS} as the one way delay propagation from Master to Slave and δ_{SM} as the one way propagation delay from Slave to Master. Similar to the two way time transfer equations described in the last Chapter (Section 1.3.2), the clock offset between the Master and the Slave can be calculated as:

$$\text{clock offset} = \frac{(t_2 - t_1) - (t_4 - t_3)}{2} - \frac{(\delta_{MS} - \delta_{SM})}{2} - \frac{(\Delta_{txm} - \Delta_{rxm})}{2} - \frac{(\Delta_{txs} - \Delta_{rxs})}{2} \quad (2.1)$$

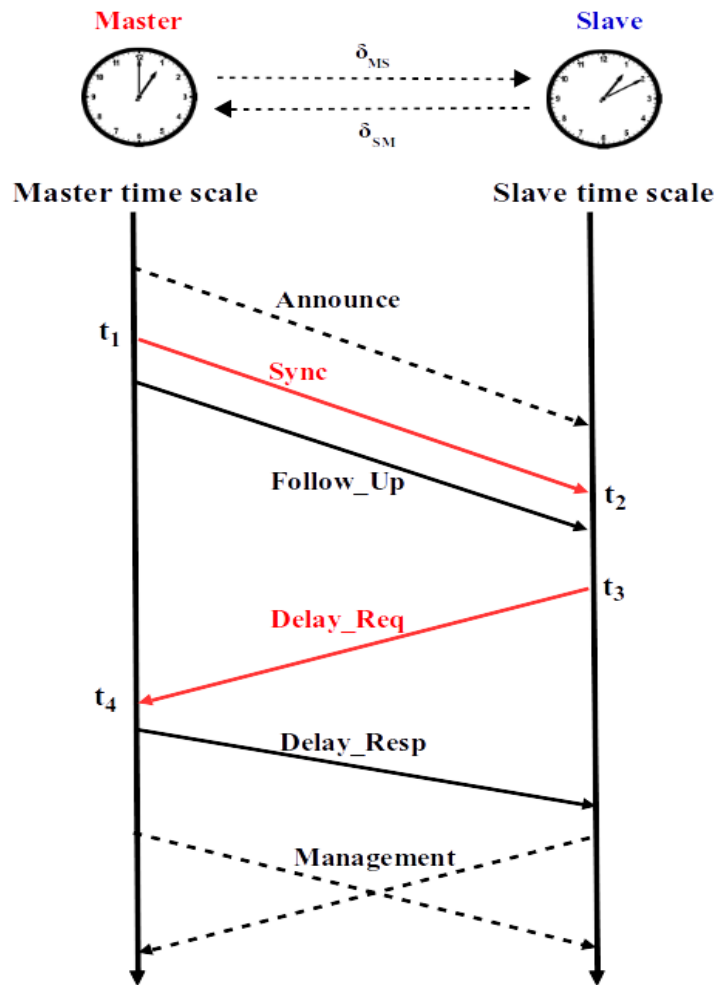


FIGURE 2.1: PTP two way message exchange mechanism [39].

where $\delta_{MS} = \delta_{SM}$ for symmetric path delays and the other terms represent the difference in instrumental delays (transmission ($\Delta_{txm/s}$) and reception ($\Delta_{rxm/s}$) of the Master and the Slave.

The messages are exchanged often to maintain synchronization depending upon user requirements. One of the limitations of typical PTP implementations is that it utilizes free-running oscillators in each node, which leads to an increasing time drift between the Master and Slave unless the message exchange and calculation of δ happen repeatedly. PTP does support frequency transfer between the nodes but is dependent on the *Sync* message rate. Even if there is such a continuous exchange of messages, the time bases will drift during the time interval between two calculations of δ . Thus the ideal case would be to synchronize the Slave clock to the Master clock in order to eliminate the error arising due to the different clock rates of the Master and the Slave. Another limitation is that the minimal attainable clock offset is limited by the resolution of the timestamps.

2.2.2 Synchronous Ethernet

Synchronous Ethernet (Sync-E) is an ITU-T (Telecommunication Standardization Sector of the International Telecommunications Union) standard for computer networking used for physical layer syntonization [54, 55]. This Layer-1 syntonization mechanism uses a common reference frequency for all the nodes in a network. In standard Ethernet, each node utilizes its own free running local oscillator to encode the data it sends to the other nodes of the network, as depicted in Fig. 2.2. Whereas, in Synchronous Ethernet, a clocking hierarchy is established with a system timing master as the primary reference (such as atomic clock or a GPS receiver) for the entire network. The system timing master encodes the data on its output frequency. All the other Slave nodes use Phase locked loops (PLLs) to recover the reference clock from the incoming data. Then the recovered clock is used to encode the outgoing data for the nodes being lower in the network hierarchy and for the data sent back to the Master. Thus, all the nodes end up beating at the same rate. White Rabbit combines PTP with Sync-E thus eliminating the drift problem present in typical PTP implementations as described above. With Sync-E performing the syntonization process, PTP solely handles the synchronization process.

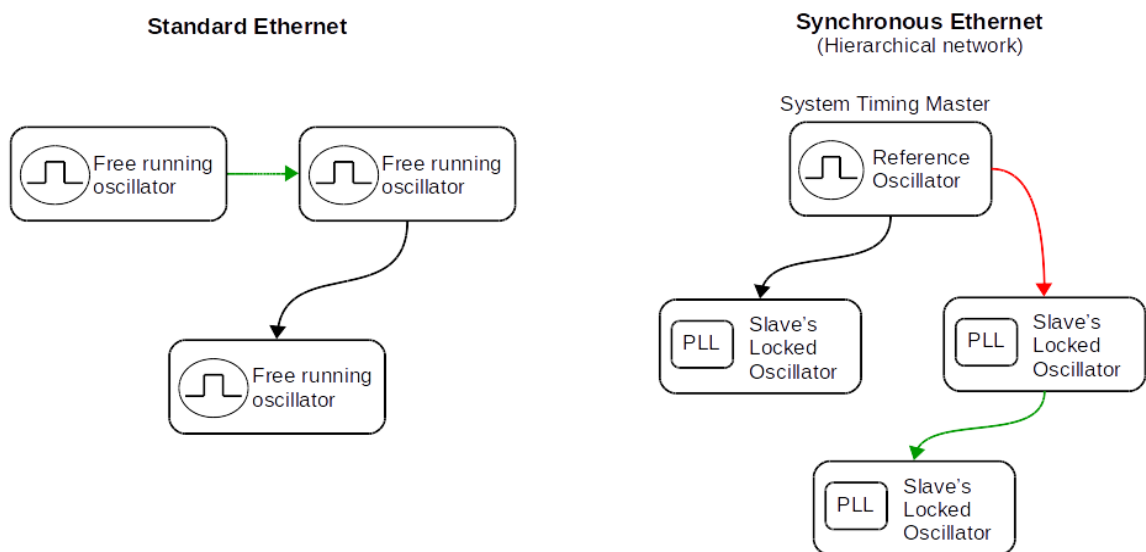


FIGURE 2.2: Comparison between Standard and Synchronous Ethernet [56].

2.2.3 Digital Dual Mixer time difference (DDMTD) phase detector

White Rabbit PTP utilizes the Digital Dual Mixer time difference technique for precise phase measurements. Fig. 2.3 illustrates the basic principle of Dual Mixer time difference method in analog domain [4]. This technique involves a frequency down conversion of the input signals into low frequency signals by utilizing mixers, and the phase difference of the down converted signals is measured by a time interval

counter.

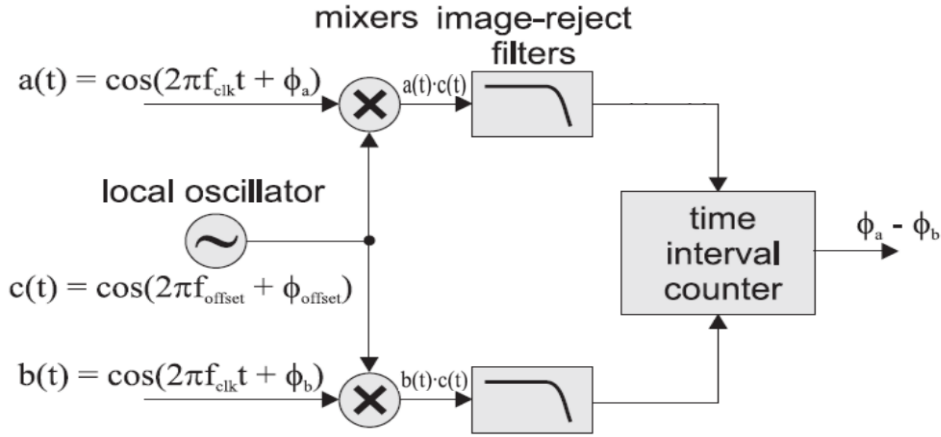


FIGURE 2.3: Schematic of an analog DMTD phase detector [56]

Let's consider two input clock signals with similar amplitude and frequency f_{clk} as:

$$a(t) = \cos(2\pi f_{clk} t + \phi_a) \quad (2.2)$$

$$b(t) = \cos(2\pi f_{clk} t + \phi_b) \quad (2.3)$$

where ϕ_a and ϕ_b are the phases of the two clocks respectively. Both the clocks are multiplied separately with the signal $c(t) = \cos(2\pi f_{offset} t + \phi_{offset})$. The f_{offset} is chosen such that it is very close to the frequency of the input signals f_{clk} . The output of the first mixer presented in Fig. 2.3 is given by the following equation:

$$a(t) \cdot c(t) = \cos(2\pi f_{clk} t + \phi_a) \cdot \cos(2\pi f_{offset} t + \phi_{offset}) \quad (2.4)$$

$$= \frac{1}{2} \cos(2\pi (f_{clk} + f_{offset}) t + \phi_a + \phi_{offset}) + \frac{1}{2} \cos(2\pi (f_{clk} - f_{offset}) t + \phi_a - \phi_{offset}) \quad (2.5)$$

A similar equation can be written for the second mixer output. The first term with a higher frequency is filtered out by the low pass filter and the other term with lower frequency ($f_{clk} - f_{offset}$) is preserved. The frequency down-conversion process alters the frequency but retains the original phase (ϕ_a, ϕ_b) of each of the input signals. Hence, the phase difference between the two input clock signals is estimated as the phase difference of the two down-converted clocks as measured by a time interval counter. For instance, we consider a reference clock of 125 MHz and an offset clock of 124.99 MHz, then the down-conversion process will result in an output signal at 10 kHz, which allows the phase difference to be easily measured by employing a

time interval counter.

This analog downconversion process can be converted into digital domain presented in Fig. 2.4 [56]. The flip flops replace the mixers in analog domain, and perform the sampling operation. A phase locked loop (PLL) is utilized to generate the offset clock from one of the input signals. The frequency of the offset clock is very close to the input signals and the flip flops sample the input signals with this offset clock, thus producing low frequency output signals. The deglitcher removes the glitches and the phase difference between the input signals is measured as a time interval by a time interval counter. The Digital DMTD provides good resolution and linearity and can be easily implemented inside an FPGA with only one external component - the oscillator for generating the offset frequency.

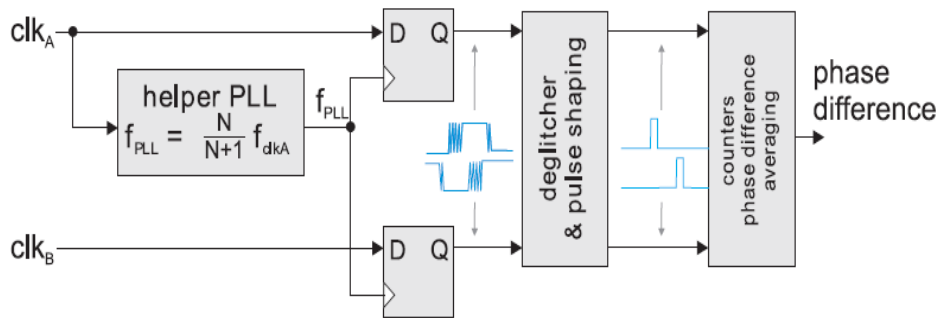


FIGURE 2.4: Schematic of a digital DMTD phase detector [56].

2.3 A typical White Rabbit Network

A typical White Rabbit network consists of White Rabbit switches and White Rabbit nodes interconnected by fiber or copper links supporting coexistence of regular and timing data, as displayed in Fig. 2.5. It can be visualized into layers. A White Rabbit network is hierarchical for synchronization with a tree topology, with the top most layer consisting of the System timing master or the Grandmaster White Rabbit Switch as it is referenced to external clock signals from an atomic clock or a GPS receiver. The second layer consists of Slave White Rabbit switches configured as a PTP Boundary clock. And the last layer consists of the single port White Rabbit nodes analogous to PTP ordinary clock. Each of the switches/nodes synchronize their local oscillators to the reference timescale.

A White rabbit network is a standard Ethernet network for regular data following a flat structure (whereas it is strictly hierarchical for timing data). Any node can send and receive packets from other nodes.

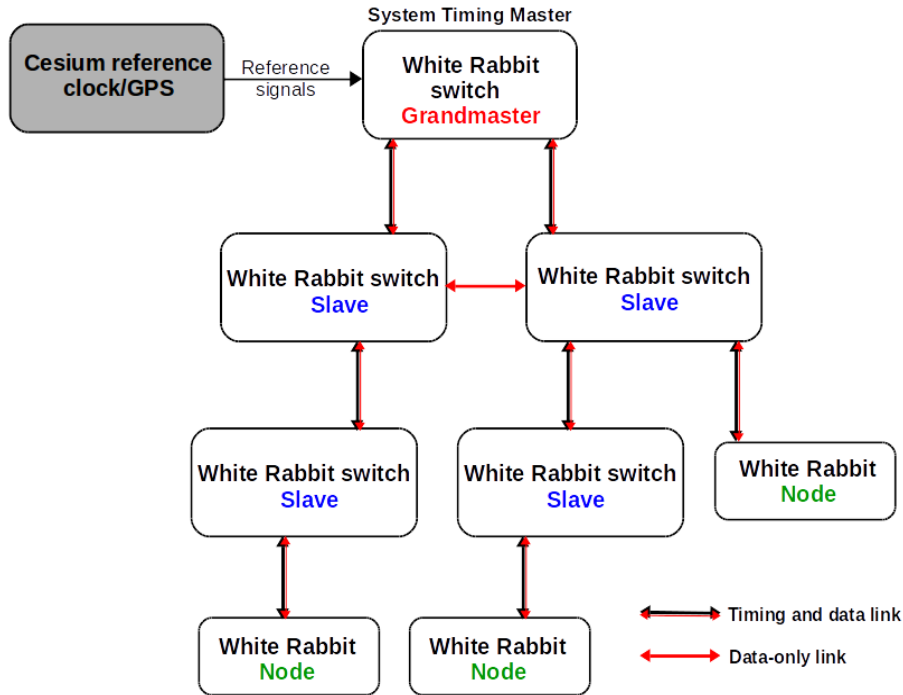


FIGURE 2.5: A typical White Rabbit Network [42].

2.4 Synchronization in White Rabbit

Fig. 2.6 presents the White Rabbit link delay scheme [56]. This scheme identifies the different types of delays involved in the precise evaluation of master to slave delay ($delay_{ms}$). This is done by taking into account the fixed master transmission (Δ_{txm}) and slave reception (Δ_{rxs}) delays and the transmission medium delay (δ_{ms}). The White Rabbit PTP synchronization technique evaluates the clock offset ($offset_{ms}$) and the $delay_{ms}$ between the Master and the Slave by a clock loopback technique. This technique measures the round trip phase ($phase_{mm}$) which is later combined with the coarse round trip delay value obtained by PTP to obtain a precise round trip delay ($delay_{mm}$) as explained in the Section 2.4.2. The technique is described by the following steps:

1. The Master's reference clock is encoded on the outgoing data to the Slave node.
2. The Slave recovers the clock from the received data stream, this recovered clock is delayed by the master to slave delay $delay_{ms} = \Delta_{txm} + \delta_{ms} + \Delta_{rxs}$.
3. The Slave shifts the phase of the recovered clock by the value $phase_s$ to obtain a phase compensated clock.
4. The Slave utilizes the phase compensated clock to encode the outgoing data.
5. The Master recovers the clock from the received data and measures the phase shift $phase_{mm}$ between its clock and recovered clock using a phase detector.

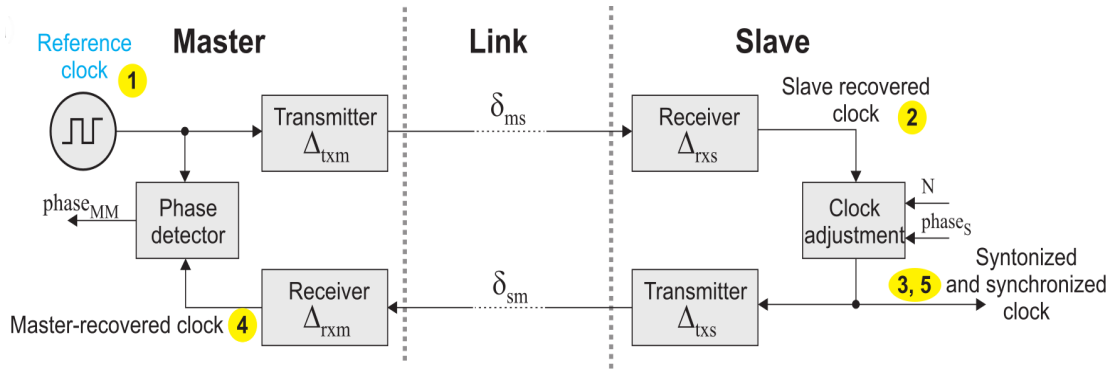


FIGURE 2.6: A White Rabbit link delay scheme [56].

During the clock adjustment process, the local oscillator of the Slave is locked to the recovered clock by the SoftPLL as depicted later in Fig. 2.16 and a variable delay $phase_s$ is introduced which allows a fine adjustment of the Slave oscillator's phase.

The $phase_s$ is the phase shift obtained from the clock offset computed from the PTP message exchange and the precise measurement of $phase_{mm}$. This process can be described by two subparts: **Initial synchronization** which determines the clock offset and $phase_s$ followed by the **Phase tracking** process which maintains the synchronization by tracking the $phase_{mm}$ and adjusts the $phase_s$ accordingly.

The following subsections describe the different steps in detail for the White Rabbit syntonization and synchronization process.

2.4.1 Syntonization

The first step is the establishment of a syntonized White Rabbit link carried out by Sync-E [56]. When the Slave is connected to the Master by a physical link (optical fiber), the Master sends an *Announce* message in search of a WR Slave and the WR Slave responds with a *Slave_present* message. If the Slave is not a WR device, then the syntonization process is terminated. Once the Master identifies a WR Slave at the other end of the link, it sends a *Lock* message and the Slave in response starts the clock recovery PLL and responds with a *Locked* message. Thus both the Master and the Slave clocks are at the same frequency but have different phases, so the syntonization is followed by a precise synchronization process.

2.4.2 Link Delay measurement

The White Rabbit synchronization process is based on two types of delay measurement for calculating the link delay as follows:

1. Coarse delay measurement

It is based on the two way message exchange mechanism of the PTP as described in Section 2.2.1. The two step message exchange process provides the

transmission and reception timestamps (t_1, t_2, t_3, t_4) which are used to calculate the coarse link delay.

2. Precise delay measurement

In this measurement the round trip phase shift ($phase_{mm}$) obtained by the DDMTD phase detector during the clock loopback technique is utilized to enhance the coarse timestamps measured by PTP. Out of the four PTP timestamps (t_1, t_2, t_3, t_4), only the reception timestamps are enhanced as they are produced in the clock domain asynchronous to the reference clock or the compensated clock. The precision of the PTP timestamps is enhanced beyond one clock cycle which is 8 ns, as the Gigabit Ethernet clock signal is at 125 MHz. A much detailed description can be found in [56].

The enhanced timestamps (t_{4p}, t_{2p}) are used to calculate the precise round trip delay using the PTP formula [56]:

$$delay_{mm} = (t_{4p} - t_1) - (t_3 - t_{2p}) \quad (2.6)$$

2.4.3 Link asymmetry evaluation

White Rabbit also addresses the different delay asymmetry sources contributing to the link latency. Fig. 2.7 shows the different types of delay asymmetries taken into account for a White Rabbit link.

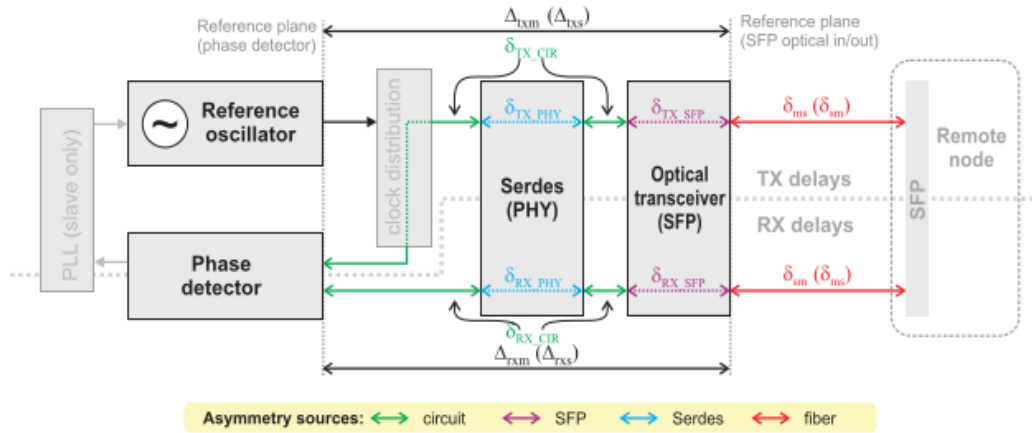


FIGURE 2.7: Delay asymmetries in a White Rabbit link [56].

The circuit asymmetry arises due to the propagation delay of electronic components and PCB traces. The optical emitters also introduce transmission and reception delay asymmetries. The PHY (SerDes) chips introduce transmission and reception delay asymmetries due to their internal structure. These represent the instrumental delay asymmetries. Another link asymmetry arises due to the different transmission

and reception wavelengths for a single fiber link.

The transmission and reception instrumental delay asymmetries for the Master/Slave device are expressed respectively as [56]:

$$\Delta_{tx(m/s)} = \delta_{TX(m/s)_PHY} + \delta_{TX_CIR(m/s)} + \delta_{TX_SFP(m/s)} \quad (2.7)$$

$$\Delta_{rx(m/s)} = \delta_{RX(m/s)_PHY} + \delta_{RX_CIR(m/s)} + \delta_{RX_SFP(m/s)} \quad (2.8)$$

These are obtained by performing the calibration procedure described in the WR calibration manual [57]. The method for PHY calibration and fiber propagation asymmetry are described in the following section.

1. Transceiver asymmetry (PHY calibration)

The transmission (TX) and reception (RX) latencies of a Gigabit Ethernet PHY Serializer/Deserializer (SerDes) circuit can be different each time the WR device is switched on or when the link is established. These latencies remain constant once the Phase locked loop/Clock Data Recovery is locked, thus requiring an initial PHY calibration when the WR link is set up. There are usually two types of PHY's which are commercially available. The first one is a separate chip and the second one is integrated inside the FPGA allowing internal TX/RX calibration using a bit-slip method. White Rabbit utilizes the latter one with Xilinx GTP SerDes. White Rabbit utilizes the DDMTD phase detector for PHY TX/RX calibration [56] presented in Fig. 2.8.

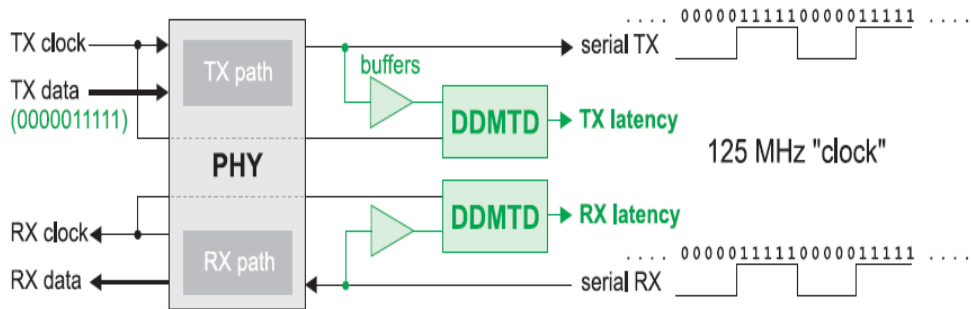


FIGURE 2.8: White Rabbit transceiver PHY calibration scheme [56].

For the TX calibration, a sequence of characters (1111100000) is sent to the TX path of the transceiver. This sequence generates a 125 MHz clock at the output of transceiver, which is fed to the DDMTD phase detector. The DDMTD measures the phase shift between the input and the output signals of the PHY transceiver. The RX calibration is done in a similar way.

The delay due to the SerDes chip consists of a fixed part and a variable part. This variable part is called as the bitslide value (ϵ) which is measured when the

WR link is established and is internally compensated for offset calculations. It can be obtained by the calibration procedure described in the manual [57].

2. The fiber propagation asymmetry

White Rabbit utilizes a single fiber and different wavelengths of propagation, for instance the recommended wavelengths for transmission and reception are 1490 nm and 1310 nm. For an optical fiber, the refractive index depends on the wavelength of propagation which results in different propagation delays for different wavelengths between the Master and the Slave. This gives rise to propagation delay asymmetry and the asymmetry coefficient α is defined in [56] as:

$$\alpha = \frac{\delta_{ms}}{\delta_{sm}} - 1 = \frac{n_{1490}}{n_{1310}} - 1 \quad (2.9)$$

where δ_{ms} is the Master to Slave transmission medium delay and δ_{sm} is the Slave to Master transmission medium delay and n is the refractive index of the fiber which may vary for different fiber manufacturers. Therefore, White Rabbit uses the measurements of the round-trip delay obtained from PTP two way mechanism $delay_{mm}$ and clock offset ($offset_{ms}$) measured with an oscilloscope in the laboratory for a more dependable calculation of the asymmetry coefficient. The value of α is then calculated by using the values of

$$delay_{mm} = \delta_{ms} + \delta_{sm} + \Delta \quad (2.10)$$

$$offset_{ms} = (\delta_{ms} - \delta_{sm})/2 \quad (2.11)$$

to obtain the equation [56]:

$$\alpha = \frac{delay_{mm} - \Delta + 2 \cdot offset_{ms}}{delay_{mm} - \Delta - 2 \cdot offset_{ms}} - 1 \quad (2.12)$$

where $\Delta = \Delta_{txm} + \Delta_{rxm} + \Delta_{txs} + \Delta_{rxs}$ is the sum of the fixed transmission and reception delays for the Master and the Slave. The fiber asymmetry is compensated separately in the Slave's PTP servo (described in the next section). This is valid for the case when the WR link utilizes a single fiber and different wavelengths of propagation (a bi-directional configuration). WR also supports a uni-directional setup utilizing dual fiber and a single wavelength of propagation, and for this setup a default α value of zero is usually used. Also, in this case the time offset would be due to the physical length imbalance of the dual fibers.

2.4.4 Clock offset evaluation

White Rabbit combines PTP with Sync-E, DDMDT phase detection and link asymmetry to achieve high performance. Having the values of the round trip delay $delay_{mm}$ (obtained by PTP) and the link asymmetry, the one way Master to Slave delay δ_{ms} is calculated by using the following equation [56]:

$$delay_{mm} = \delta_{ms} + \delta_{sm} + \Delta \quad (2.13)$$

Substituting for $delta_{sm}$ from equation 2.9 in the above equation, we obtain the value of one way Master to Slave transmission medium delay δ_{ms} in terms of α as:

$$\delta_{ms} = \frac{1 + \alpha}{2 + \alpha}(delay_{mm} - \Delta) \quad (2.14)$$

which accounts for the link asymmetry factor and the delay from master to slave is given as:

$$delay_{ms} = \delta_{ms} + \Delta_{txm} + \Delta_{rxs} = \frac{1 + \alpha}{2 + \alpha}(delay_{mm} - \Delta) + \Delta_{txm} + \Delta_{rxs} \quad (2.15)$$

and the master to slave offset is given by:

$$offset_{ms} = t_1 - t_{2p} - delay_{ms} \quad (2.16)$$

This value is then used by the WR Slave servo for synchronization, the detailed algorithm for the Slave's offset adjustment can be found in [56]. After the initial synchronization, the WR Slave periodically examines its offset to the master and updates the adjustments.

2.5 Unification of White Rabbit into PTP

White Rabbit is based on PTPv2 protocol and extends this standard with syntonization and PHY calibration. PTPv2 supports customization options such as the Type-Length-Value fields for Announce and Management messages [39] which allow the integration of White Rabbit messages. The message exchange flow for the WR-PTP combining the syntonization, transceiver calibration and synchronization is presented in Fig. 2.9 [56]. The WR messages are depicted in red. The first step is the set up of the syntonized WR link between the Master and the Slave as described in Section 2.4.1. After syntonization, the PHY calibration process is carried out as described above. With this step, a successful White Rabbit link is set up. The next step is the standard PTP two-step message exchange for the delay measurement and the Slave adjusts accordingly.

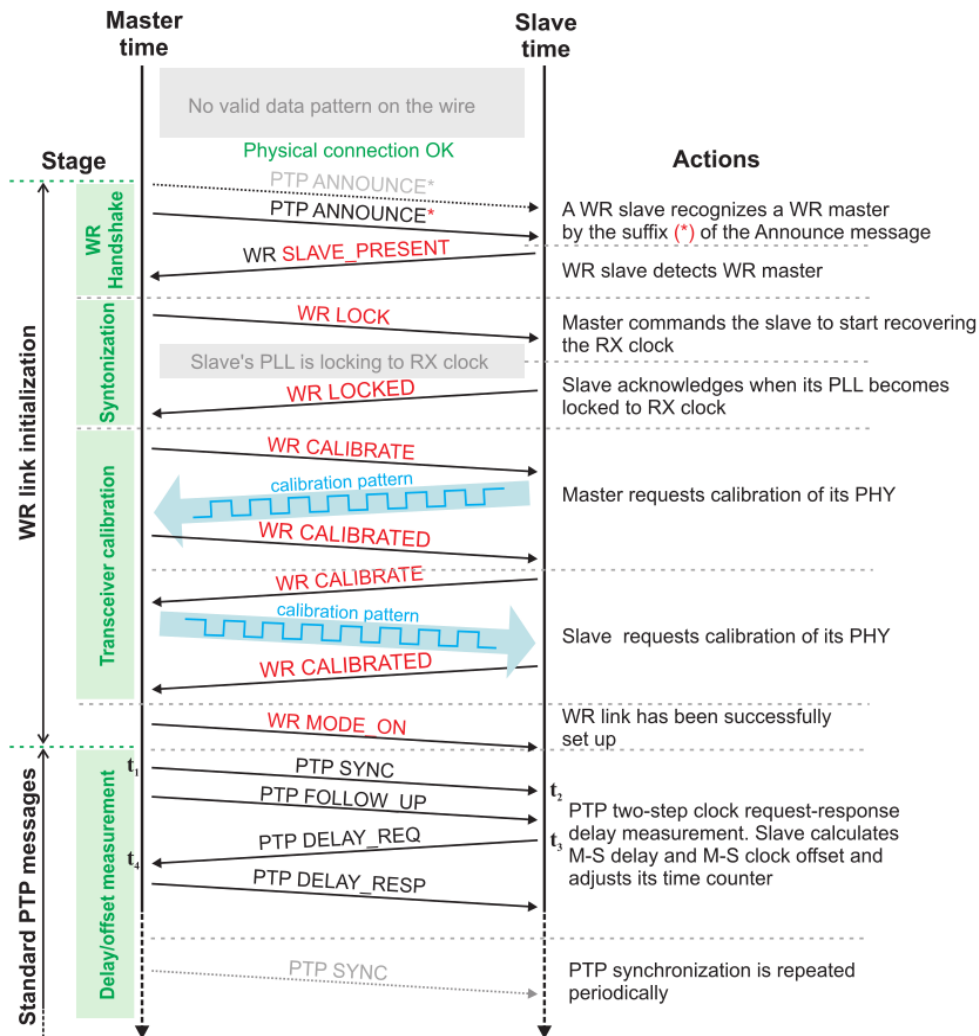


FIGURE 2.9: WR-PTP message exchange flow [56].

2.6 Components of a White Rabbit Network

A White Rabbit network consists of White Rabbit switches and White Rabbit nodes connected by optical fiber links. The following subsections introduce the different components and the physical medium for a White Rabbit network.

2.7 White Rabbit equipment

WR-PTP equipment is manufactured by at least two companies; Seven solutions [52] and CreoTech [58].

2.7.1 The White Rabbit Switch

The White Rabbit Switch (WRS) is the central component of a White Rabbit network providing precision timing [59]. The White Rabbit switch is a Gigabit Ethernet switch (IEEE802.1D Bridge [39]) compatible with PTP devices. It is a standalone

device providing 18 ports supporting both the Small form factor pluggable (SFP) optical transceivers connectors and copper connections, as displayed in Fig. 2.10. Each of the ports can be configured as a Slave, which receives time and frequency reference from the upper layer of the network or as a Master, which propagates the timing to the other switches or nodes in the underlying layer of the network. The WRS has two reference input connectors for 10 MHz and one pulse per second (PPS) signals from a Cesium atomic clock or a GPS Receiver and two output connectors for a Clock out and a PPS output.



FIGURE 2.10: A White Rabbit Switch (WRS) [59].

The WRS can be configured in one of the three modes:

- **Grandmaster mode:** In this mode, the WRS locks its internal local oscillator to the external 10 MHz and PPS reference signals. The Grandmaster WRS is the System timing Master of the White Rabbit network.
- **Boundary clock (BC) mode:** In the BC mode, the WRS serves as a Slave synchronized to the system timing master/Master of the White Rabbit network.
- **Free running master mode:** In this mode, the WRS utilizes its internal local oscillator as the reference clock.

We acquired four White Rabbit switches manufactured by Seven Solutions, two switches are from the hardware version 3.3 and other two are with the new hardware version 3.4. The 3.3 version WRS provides an output clock at 62.5 MHz whereas the new 3.4 version provides two clock outputs at 62.5 MHz and 10 MHz.

2.7.2 The White Rabbit Nodes

There are two types of WR nodes as follows:

1. **White Rabbit Simple PCI express Carrier (SPEC)** board hosts the White Rabbit PTP core (WRPC) responsible for the synchronization task and can hold

FPGA mezzanine cards (FMC) [60]. The board is a single port low cost end receiver and utilizes different FPGA and electronics as compared to the WRS. The SPEC board is a starting kit for White Rabbit technology. It can be used in two operation modes: it can be plugged into the PCI express port of a PC or can be deployed as an independent standalone device. The SPEC board is combined with a FMC-DIO (Digital Input/Output) card to provide external reference input signals and output signals as displayed in Fig. 2.11. It can be configured in any of the three modes - the Grandmaster, Slave and as a free running master as described for the WRS.

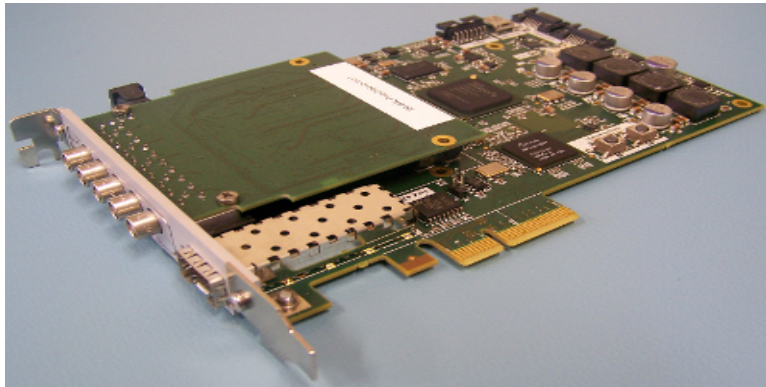


FIGURE 2.11: SPEC board hosting the five channel FMC card DIO [60].

2. **White Rabbit Zync embedded node (WR-ZEN)** is a novel versatile standalone unit providing WR timing features [61]. It is based on the Xilinx Zynq SoC technology and has a Processing System based on a dual core ARM processor that can run any conventional operating system like Linux unlike the SPEC board. It is optimized for delivering cost effective WR timing distribution. It is equipped with dual optical fiber connectors and Ethernet ports and FMC expansion connector. Fig. 2.12 illustrates the WR-ZEN board. It is basically an improved version of the previous WR node with faster FPGA and better electronics. It provides better performance due to its new clocking circuitry [62].

2.8 Optical emitters

White Rabbit utilizes small form factor pluggable (SFP) transceivers as optical emitters for the fiber link between the Master and the Slave nodes. A small form-factor pluggable (SFP) transceiver is a compact optical input/output transceiver widely used in telecommunications networks. SFP transceivers are widely used in communications standards including Synchronous optical networking (SONET) or Synchronous digital hierarchy (SDH), Gigabit Ethernet and fiber channel. They utilize Distributed feedback laser (DFB) technology and are available in a wide variety



FIGURE 2.12: The White Rabbit Zync embedded node (WR-ZEN) [61].

of CWDM and DWDM wavelengths. They are available in both Single fiber dual wavelength (Bi-directional) and Dual fiber single wavelength (Uni-directional) connectors. Their range varies from short distances of a few km to long range of about 150 km. We utilized both bi-directional and uni-directional SFPs for CWDM and DWDM wavelengths from different manufactures such as Fiberstore, Optospan and Axcen.



(A) Bi-directional single fiber SFP pair



(B) Uni-directional dual fiber SFP

FIGURE 2.13: Types of Small form factor pluggable (SFP) optical transceivers.

2.9 The transmission medium - Optical fibers

Optical fibers have been widely used for high bandwidth data services for telecommunication networks, industry and utility networks and for military applications. White Rabbit utilizes Optical fibers as the physical medium between the Master and the Slave node. It uses the single mode ITU G.652 commercial fiber. It is critical to discuss briefly some of the significant characteristics of Optical fibers such as attenuation, refractive index, and signal dispersion. Fig. 2.14 displays the optical attenuation as a function of the wavelength of propagation for silica fibers [63]. There are three windows for optical communication at 0.85, 1.31 and 1.55 μm respectively.

The first window is restricted to short distances due to high attenuation. The second window has relatively low loss and lies in the region of zero dispersion. For long distance communication, the third window wavelength $1.55 \mu\text{m}$ is widely used because it provides the lowest attenuation of 0.2 dB/km .

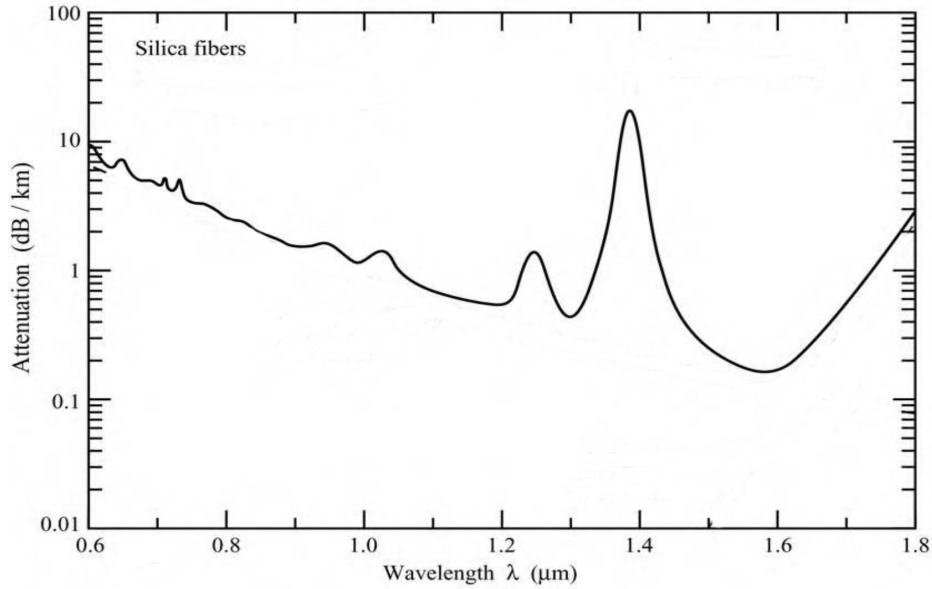


FIGURE 2.14: Optical attenuation variation with wavelength [63].

For a transparent bulky optical material, the refractive index is dependent on the wavelength of propagation as described by the Sellmeier equation [64] :

$$n(\lambda)^2 = A + \frac{B}{1 - C/\lambda^2} + \frac{D}{1 - E/\lambda^2} \quad (2.17)$$

where A, B, C, D, E are the Sellmeier coefficients and λ is the wavelength in micrometers.

Fig. 2.15 displays the variation of the refractive index with wavelength for silica fibers [63].

Another characteristic of Optical fibers is the Intradmodal dispersion as a result of material dispersion and waveguide dispersion. Material dispersion also known as Chromatic dispersion occurs due to the variation of index of refraction as a function of wavelength of propagation. The phase and the group refractive index are given as $n = c/v_{ph}$ and $n_{group} = c/v_{gr}$, where v_{ph} and v_{gr} are the phase and group velocities respectively. The phase refractive index is usually referred as the refractive index. The phase refractive index and the group index are related as $n_{group} = (n - \lambda \frac{dn}{d\lambda})$ [63].

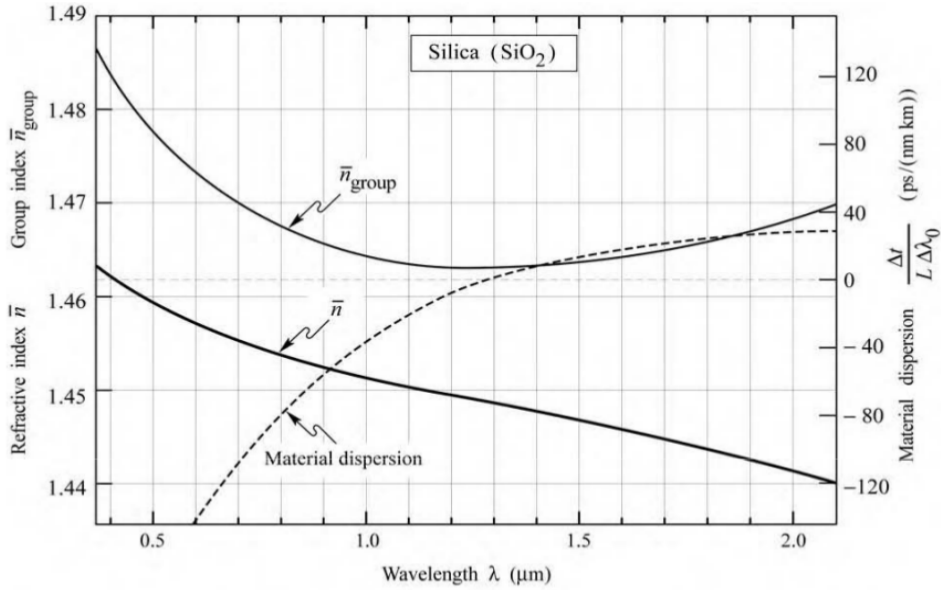


FIGURE 2.15: Refractive index, group index and material dispersion of silica fibers [63].

The propagation delay t for traversing a fiber of length L is expressed as [65]:

$$t = \frac{L}{c} \left(n - \lambda \frac{dn}{d\lambda} \right) \quad (2.18)$$

where c is the speed of light and n is the refractive index. Thus different wavelengths travel at different speeds following the same path.

The waveguide dispersion is the pulse spreading as the light propagates through the fiber. The optical power distribution for the fiber varies for different wavelengths, shorter wavelengths are more restricted to the core of the fiber while a large section of optical power at longer wavelengths propagates in the cladding. This spreading arises due to the difference in the core-cladding refractive index which gives rise to an optical power distribution in the fiber. The refractive index of the cladding is lower than the core, so the light propagating in the cladding travels faster than the light restricted to the core. The magnitude of the waveguide dispersion depends on the fiber design.

The Chromatic dispersion and pulse broadening for a single mode fiber are given by the following equations respectively [66]:

$$D(\lambda) = \frac{1}{L} \frac{d\tau}{d\lambda} \quad (2.19)$$

where τ is the propagation delay for a fiber of length L and dispersion is expressed in $ps/(nm.km)$.

$$\sigma = D(\lambda) L \sigma_\lambda \quad (2.20)$$

where σ_λ is the spectral linewidth of the optical source.

Fig. 2.15 shows the material dispersion of silica fibers as a function of wavelength for an optical fiber with zero dispersion at about 1310 nm. Determination of the refractive index for an optical fiber is a complicated process [67].

Chromatic dispersion affects both the accuracy and stability for time transfer. For accuracy, the value of the wavelength of propagation decides the contribution of the chromatic dispersion. For instance, the recommended optical setup for a White Rabbit link is Bi-directional utilizing a single fiber and different wavelength of propagation (1490/1310 nm pair). For this bi-directional configuration, a large differential chromatic dispersion arises due to the huge difference in the propagation wavelengths (180 nm difference) with zero chromatic dispersion for the 1310 nm wavelength. On the other hand, an uni-directional configuration utilizes dual fibers and single wavelength of propagation leading to comparatively much less chromatic dispersion, but can lead to a dramatic time offset due to the fiber length imbalance and hence inaccuracy. White Rabbit also supports the uni-directional configuration. For us, it is of great interest to utilize the uni-directional configuration in order to ensure compatibility with the existing active telecommunication networks and in addition benefit from the installed telecommunication equipment for long haul links.

Chromatic Dispersion also affects the time stability performance as studied in [68, 69, 70]. We study this effect in detail and we will show later in Chapter 4 that at short term, the finite spectral linewidth of the optical emitters governs the performance and the long term stability is influenced by the wavelength fluctuations of the optical emitters.

2.10 White Rabbit clocking Scheme

Fig. 2.16 shows the clocking scheme of the White Rabbit Switch 3.4 hardware version [71]. The local oscillator VCTCXO VM53S3 output signal at 25 MHz is multiplied by an external AD9516-4 phase locked loop to generate a signal at 62.5 MHz. The AD9516-4 is also a multi output clock distribution chip and is used for WR clock distribution. A set of clock outputs of the AD9516-4 are sent to the GTX transceiver for transmission by fiber links. One of the WR clock is fed to the SoftPLL, which is a digital implementation of a phase locked loop in an FPGA and a detailed description of the WRS SoftPLL can be found in [56].

The SoftPLL locks the local oscillator to the external reference signal in the Grandmaster mode or locks to the recovered clock from the Gigabit transceiver (GTX RX) when configured in Boundary clock mode. The locking is achieved by controlling

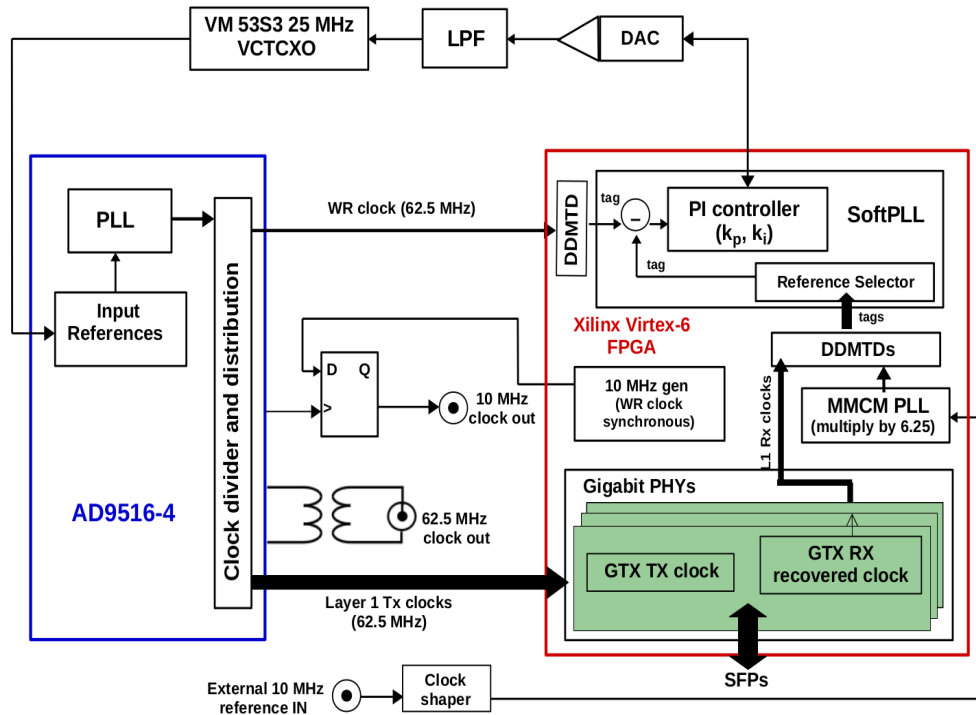


FIGURE 2.16: Clocking scheme of the White Rabbit switch hardware v3.4 (v3.3 lacks the 10 MHz clock output) [71].

the local oscillator by varying the Proportional (k_p) and Integrator (k_i) gains of the PI controller which utilizes the fine phase shift obtained by DDMTD phase detection. The output of the PI controller is then converted to an analog signal by a DAC, whose output is low pass filtered and fed to the local oscillator.

The external 10 MHz reference signal is multiplied to 62.5 MHz by a cascade of two phase locked loops called as the Mixed Mode Clock Managers (MMCM PLL). This multiplication is required because the SoftPLL operates at 62.5 MHz input clocks. These PLLs are noisy and their performance is described in detail in [71].

2.11 The potential performance limitations

Having discussed the WR clocking scheme, we can identify the potential performance limitations for a Grandmaster WRS and a Slave WRS from a basic system review analysis. Fig. 2.17 shows the free running phase noise power spectral density (PSD) of the local oscillator and for the external reference signal. The WRS SoftPLL locks the local oscillator to the external reference signal with a default bandwidth of locking set by the proportional and integrator gains of the PI controller. The phase noise PSD of the locked local oscillator for low Fourier frequencies comes from the external reference signal as the free running noise is compressed by the gain of the servo loop. The servo bump is visible at a frequency f_{lock} (denoted by the dashed

line).

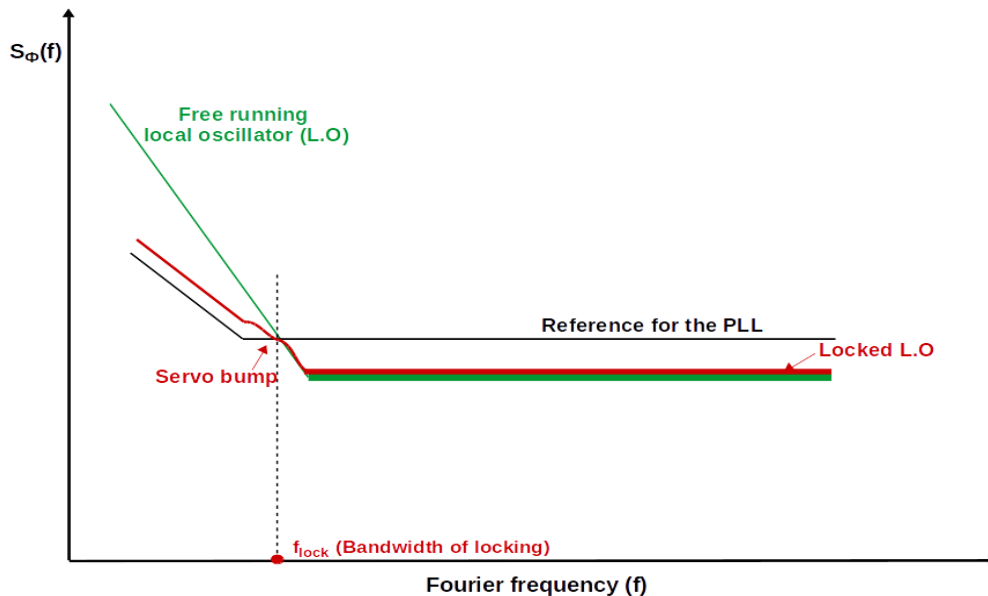


FIGURE 2.17: Illustration of a typical Phase noise power spectral density for a free running local oscillator, for the external reference signal and for the locked local oscillator.

For Fourier frequencies greater than the bandwidth of locking, the phase noise PSD of the locked local oscillator follows the curve for the free running local oscillator. The point where the transition from one source to another takes place (the bandwidth of locking) should be carefully chosen so as to achieve the least possible phase noise PSD.

The ideal performance is achieved when the phase detector is flawless. But in reality, we will have to take into account the noise contribution from the phase locked loop chain which results in higher noise when compared to the external reference signal. A detailed study of the performance and limitations of the WRS-DDMTD is described in [72]. From this analysis, the performance of a Grandmaster WRS would be mainly limited due to the quality of the local oscillator and the SoftPLL locking chain. In Chapter 3, we will perform a detailed analysis of Grandmaster's performance and focus on the Local Oscillator and SoftPLL contribution.

Further, we will identify the various performance limitations based on the system review for a Slave WRS, which is synchronized to the Grandmaster by an optical fiber link presented in Fig. 2.18. For the Slave WRS, there are other limiting factors. For the Slave, the reference clock is recovered from the fiber link by the Gigabit PHY transceivers. These transceivers consists of SerDes chips which contain PLL for the clock recovery process [56] and hence limit the Slave's performance. These could be the main instrumental limitations arising due to the Slave switch and will be studied

in Chapter 4 in case of long haul links.

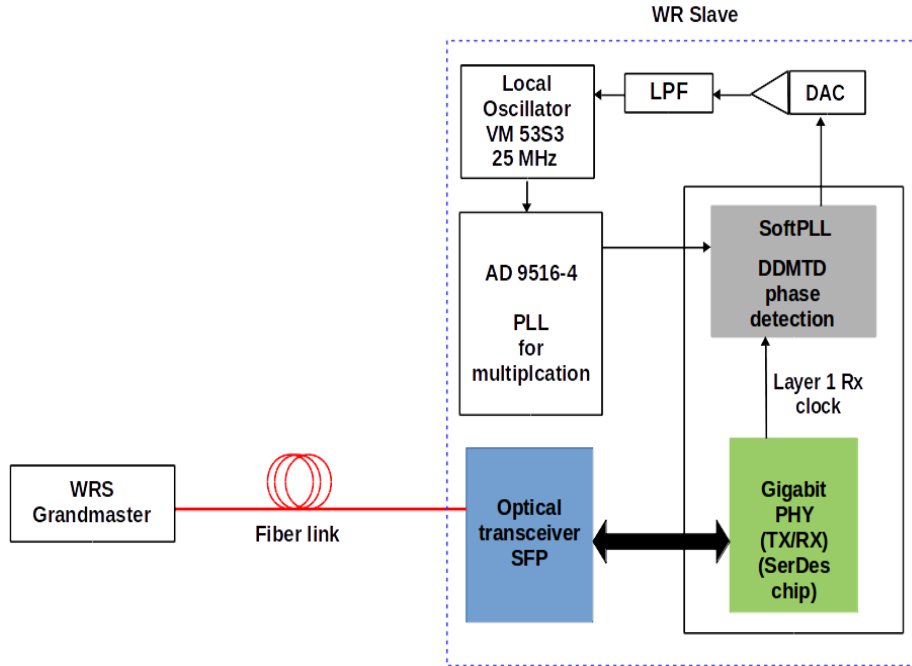


FIGURE 2.18: A WR Slave system review for studying its potential performance limitations [71].

Another very significant factor that may contribute to the limitation for a Slave's performance is the physical medium between the Master and the Slave which is the Optical fiber link. For any phase frequency servo system, the free running phase power spectral density is compressed by the finite gain G (proportional and integrator) of the loop and thus can be written as:

$$S_{locked} = G \cdot S_{free} \quad (2.21)$$

Newbury and co-workers studied the compressed phase noise PSD for an optical fiber link for coherent optical frequency transfer in [73], and the above equation then becomes:

$$S_{locked} = \frac{(2\pi f\tau)^2}{3} S_{fiber} \quad (2.22)$$

where f is the Fourier frequency, τ is the propagation delay for a fiber of length L . This equation describes the fundamental limitation for the compressed PSD due to the propagation delay and is described in detail in Chapter 4.

The free fiber propagation noise S_{fiber} arises due to the temperature fluctuations acting on both the physical length of the fiber and on the refractive index. It is a long term effect due to the day/night temperature fluctuations. The fiber thermal noise

is described intensively in Chapter 4.

Thus, we are able to identify the potential noise sources that could limit the performance of the Grandmaster and Slave White Rabbit switch. Fig. 2.19 displays these potential noise sources for a simple pictorial representation. At short term, the performance is dominated by the quality of the local oscillator. The available commercial quartz oscillators provide frequency stability in the range of 10^{-11} to 10^{-13} at one second of integration time and their cost increases linearly with the performance. For the Slave switch, chromatic dispersion may play a critical role at short term and the fiber thermal noise could restrict at long term. The acoustic fiber noise arising due to stress and vibrations on the optical fiber would not limit the stability performance [74]. Another contributing factor is due to the AD9516-4 chip used for White Rabbit clock distribution. The rms jitter of the output of the chip would be the ultimate limitation to the achievable performance [75].

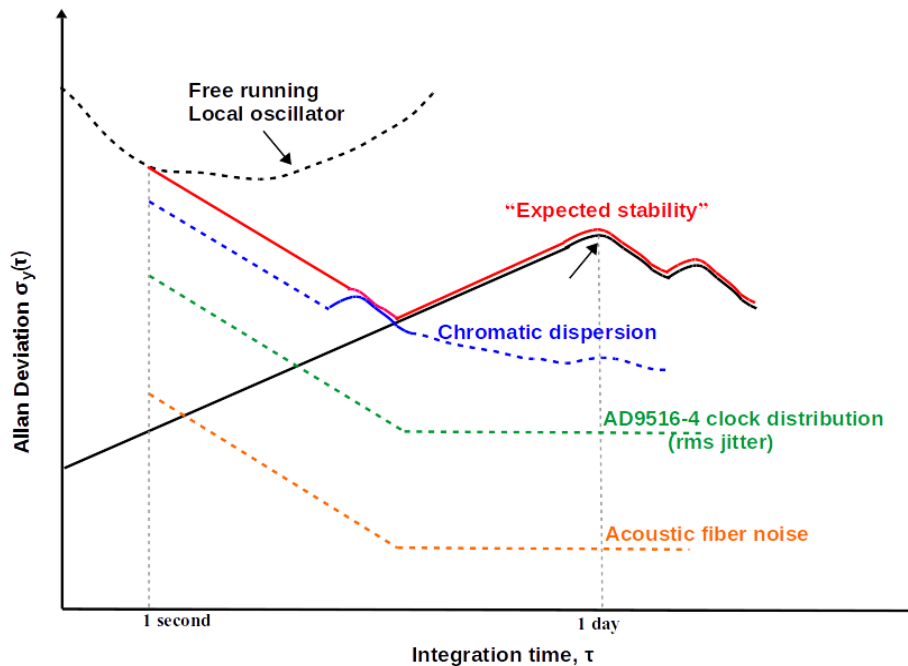


FIGURE 2.19: Pictorial representation of the potential noise sources that could limit the frequency stability performance of a typical Grandmaster and Slave White Rabbit Switch.

2.12 Outlook

We created an outline of the work to be undertaken. The first task was to study the default performances of the Grandmaster and Slave White Rabbit switches. Then, to test White Rabbit technology for time and frequency dissemination over mid range links and study its performance and limitations, and examine the scope for improving the default performances. Subsequently move on to realize long haul White

Rabbit links with an approach compatible with active telecommunication networks and study intensively its performance and limitations.

Chapter 3

Improving the White Rabbit Switch performance

3.1 Introduction

The first part of the chapter focuses on studying the default performance of the timing master of a WR network, called as the Grandmaster (GM) White Rabbit Switch. The performance limitations were identified and further work focused on improving its performance. Further, a White Rabbit link of mid-range length is introduced comprising of a Slave White Rabbit Switch synchronized to the Grandmaster WRS by an optical fiber link and different optical link configurations are studied. The tasks undertaken to improve the performance of the Slave WRS are presented and the frequency and time stability performances of the Slave are discussed.

3.2 The White Rabbit Switch in Grandmaster mode

The White Rabbit switch in the Grandmaster mode is the timing master for a White Rabbit network, so we began by studying the performance of the Grandmaster switch. In the Grandmaster mode, the WRS is locked to external 10 MHz and PPS (one pulse per second) reference signals (for example from a Cesium beam clock or from a GPS receiver) by the SoftPLL.

3.2.1 Experimental setup

The experimental setup to evaluate the performance of the Grandmaster WRS (GM) is presented in Fig. 3.1. We provided the switch with a 10 MHz reference signal derived by coherent division from the SYRTE H-Maser signal, amplified and distributed using a Frequency distribution amplifier in the laboratory. We also provided a PPS reference signal generated (SDI PPS generator), amplified and distributed in the laboratory with a TimeTech PPS 16 channel amplifier. The Power Spectral Density (PSD) of the GM clock was measured with a Microsemi Phase noise test set 5120A. The maximum input frequency for this device is 30 MHz but as the GM switch clock out signal is at 62.5 MHz, a frequency down conversion was performed. We down converted the 62.5 MHz signal to 10 MHz by utilizing a Mixer and a 72.5

MHz from the IFR frequency Synthesizer which was locked to the 10 MHz reference of the laboratory.

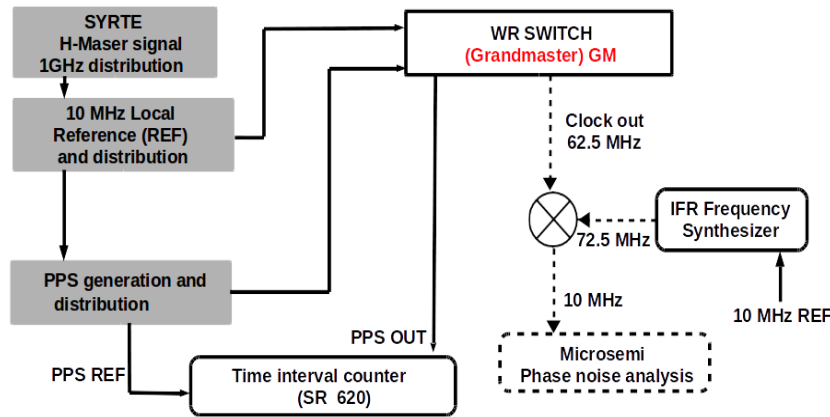


FIGURE 3.1: Experimental setup for GM switch performance analysis.

3.2.2 Phase noise power spectral density

Fig. 3.2 displays the phase noise power spectral density of the Grandmaster clock at 10 MHz (red curve). Fig. 3.2 also shows the phase noise power spectral density of the WR clock at 10 MHz for the free running mode in which the switch utilizes the internal local oscillator (configured as the free running Master). At 1 Hz Fourier frequency, we observed a PSD of -70 dBc/Hz with a default bandwidth of locking of about 20 Hz as exhibited by the servo bump. A much lower power spectral density can significantly improve the short term stability of the switch. This can be directly achieved by replacing with a better quality local oscillator which is considerably expensive or by modifying the SoftPLL bandwidth [71].

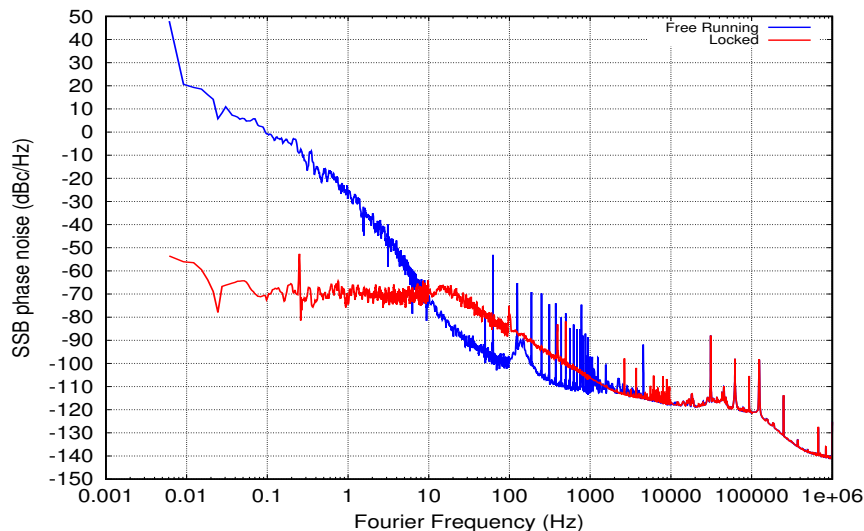


FIGURE 3.2: Phase noise power spectral density for the Grandmaster WR clock.

3.3 Improving the Grandmaster WRS performance

As described above, the default performance of the Grandmaster (GM) White Rabbit switch is suboptimal even if a high quality input signal is provided. We identified that the performance limitations are mainly due to the quality of the local oscillator and the phase and frequency lock chain of the WR SoftPLL. So, we focused on improving its performance and in this regard we studied the WR clocking scheme intensively and realized that there was scope of improvement. We discovered that there is a possibility to improve the short term stability significantly if a direct distribution of the external reference signal is performed. So with the help of the WR team at CERN, we implemented an improved approach by utilizing an external clock distribution mode for the AD9516-4 chip which is used for WR clock distribution. This mode allowed a direct distribution of an external reference clock signal by bypassing the internal local oscillator and the SoftPLL of the WRS. This improvement did not require any hardware change for the WRS and only a software modification was done. The software modification required an alteration of the configuration file for the multi-output clock distribution chip AD9516-4 and a recompilation of the FPGA binaries of the WRS was done. The WRS was then rebooted with these new binaries.

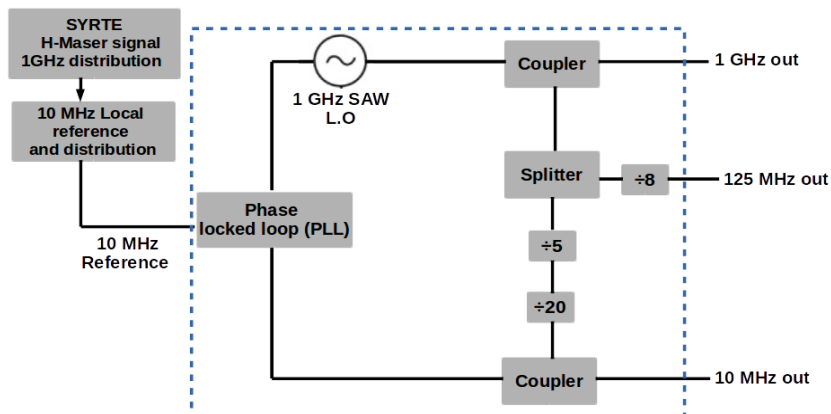


FIGURE 3.3: Schematic of the external 1 GHz local oscillator box.

Due to the internal frequency map of the WR switch, we provided a 125 MHz external reference signal as the input for the improved GM WRS. This signal was generated from a good quality 1 GHz local oscillator locked to the 10 MHz reference signal of the laboratory. Being a metrology laboratory with rich experience in good quality low phase noise oscillators, we chose a specific 1 GHz local oscillator HO4001-1 by RF Monolithics [76] at a reasonable cost. The frequency of this oscillator is stabilized by surface-acoustic-wave (SAW) technology. This results in excellent performance from a compact, rugged, oscillator operating at the fundamental frequency of 1000 MHz. In addition to this, it was our great interest to select a high frequency local oscillator in order to obtain lowest phase noise after division. Also, it was convenient to generate a 125 MHz signal from the 1 GHz local oscillator by

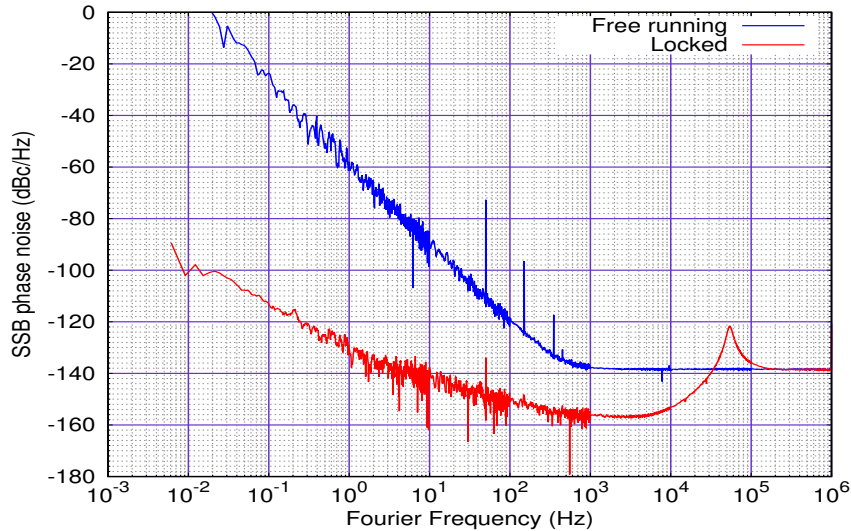


FIGURE 3.4: Phase noise power spectral density of the 10 MHz output signal of the 1 GHz local oscillator box.

simply dividing by 8. The Phase locked loop circuit for the 1 GHz local oscillator was developed in the laboratory and was enclosed in a box as displayed in Fig. 3.3. The 1 GHz local oscillator's output was coupled to a Splitter and the other output of the Coupler was made available as an output signal. One of the outputs of the Splitter was divided by 8 to generate a signal at 125 MHz which was used as the input signal for the improved GM WRS. The other output of the Splitter was first divided by 5 and then by 20 to generate a signal at 10 MHz. The output of the divider by 20 was coupled to provide a 10 MHz out signal which was fed to the phase locked loop circuit and the other 10 MHz output signal was fed to the GM switch, which is required for the normal booting procedure of the WRS (the reference signal for the improved WRS is the 125 MHz signal as described above.)

We measured the free running and locked (when the 1 GHz oscillator is locked to the 10 MHz reference of the laboratory) phase noise power spectral density of the 10 MHz out signal of the 1 GHz local oscillator box by Microsemi Phase noise test set 5120A, displayed in Fig. 3.4. For the locked mode, we observed a low phase noise PSD of -130 dBc/Hz with a servo bump at about 60 kHz which was later optimized by varying the proportional and integrator gains of the phase locked loop circuit.

3.3.1 Phase noise Power Spectral Density and Allan Deviation

The experimental setup for GM switch performance analysis is illustrated in Fig. 3.5. The Power Spectral Density (PSD) and Allan Deviation measurements of the GM clock were done with a Microsemi Phase noise test set 5120A. The GM switch clock out signal at 62.5 MHz was down converted to 10 MHz as described in the Section 3.2.1.

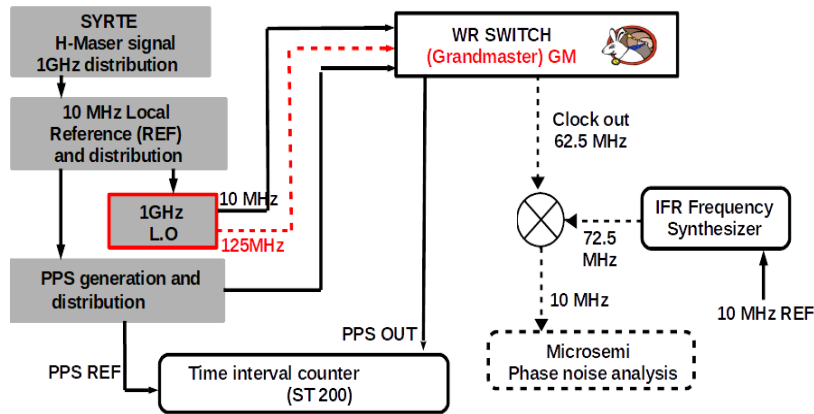


FIGURE 3.5: Experimental setup for the "improved" GM switch performance analysis.

Fig. 3.6 shows the Power Spectral density (PSD) of the down converted WR clock at 10 MHz for the default and the improved Grandmaster switch. For the improved case, about 25 dB lower phase noise is obtained at 1 Hz and about 40 dB lower phase noise at 10 Hz Fourier frequency. The bandwidth of locking has been increased by a factor of a thousand. The bandwidth of locking for the improved GM was controlled by the proportional and integrator gains of the phase locked loop of the 1 GHz local oscillator box and was optimized to 20 kHz as displayed in the Fig. 3.7.

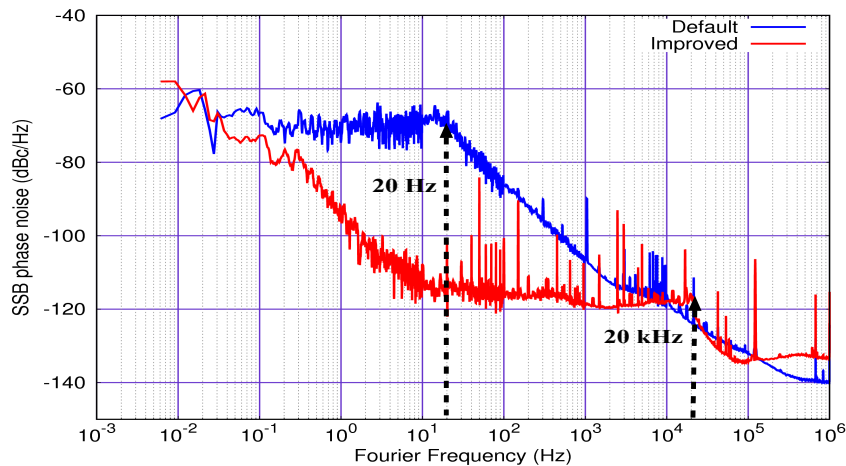


FIGURE 3.6: Phase noise power spectral density for default and improved Grandmaster WR clock.

The Allan deviation for the GM clock at 62.5 MHz for the improved and default case is displayed in Fig. 3.8. The frequency stability for the GM clock at 62.5 MHz was calculated by dividing the stability at 10 MHz by the factor 6.25. This improvement achieved an Allan Deviation of 4.9×10^{-13} at one second of integration time (NEQ BW=500 Hz) presented in Fig. 3.8, where the default performance (1.3×10^{-11} at one second of integration time at 62.5 MHz) has been improved by a factor of 26. The performance for the improved case is limited due to the noise floor of the

AD9516-4 chip used for the WR clock distribution as the external reference clock signal has even lower PSD as illustrated in Fig. 3.4.

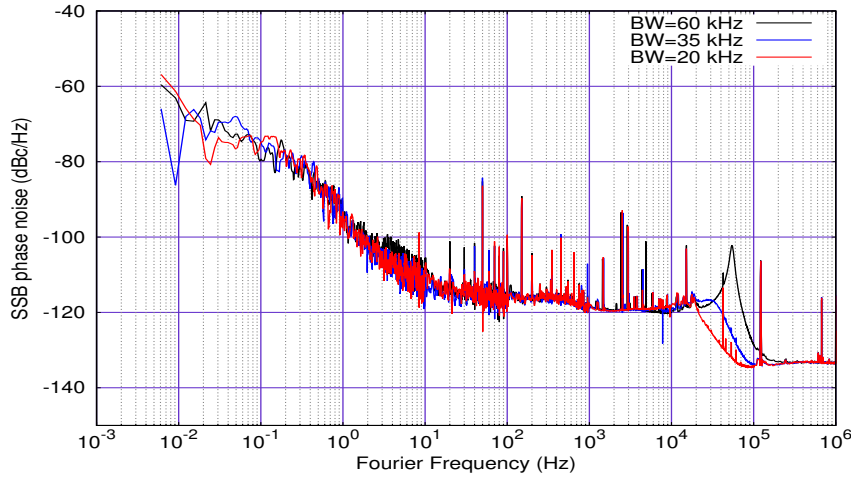


FIGURE 3.7: Phase noise power spectral density of the improved Grandmaster WR clock for PLL bandwidth optimization.

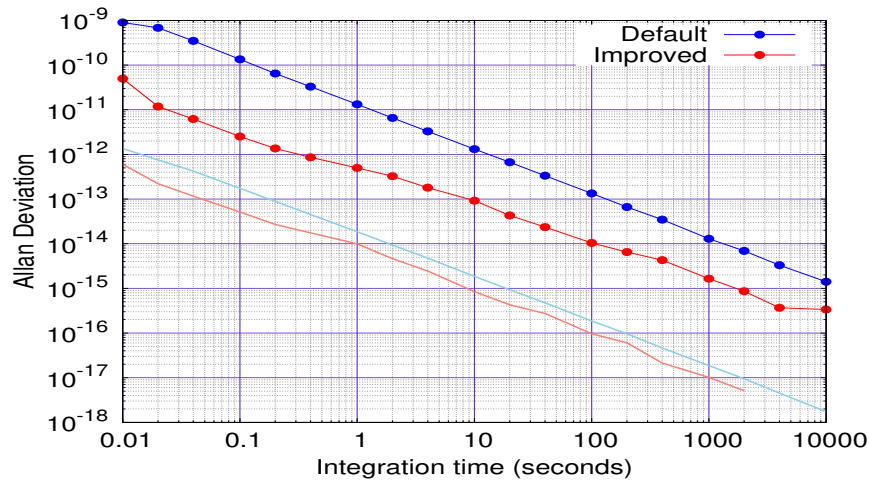


FIGURE 3.8: Allan Deviation (NEQ BW=500 Hz) for default and Improved Grandmaster WR clock (the solid light blue and red lines are their respective noise floors).

We notice that the Allan Deviation for the improved Grandmaster for NEQ BW=500 Hz (Fig. 3.8) and 50 Hz (Fig. 3.9) is equal because the phase noise PSD is constant for Fourier frequency range from 10 Hz to 20 kHz. Hence, the performance of the improved Grandmaster is not much affected by the bandwidth of measurement.

In Fig. 3.9, we compare our Improved Grandmaster with the enhanced White Rabbit version by OPNT, the Netherlands [77]. Their enhanced WRS consists of two modifications including the implementation of a low-jitter daughter board (developed by CERN [78]) along with a low noise clean-up oscillator. At one second of integration time, they achieve a stability of 4×10^{-12} averaging down to about $6 \times$

10^{-15} at 1000 s of integration time. We obtain better performance by one order of magnitude.

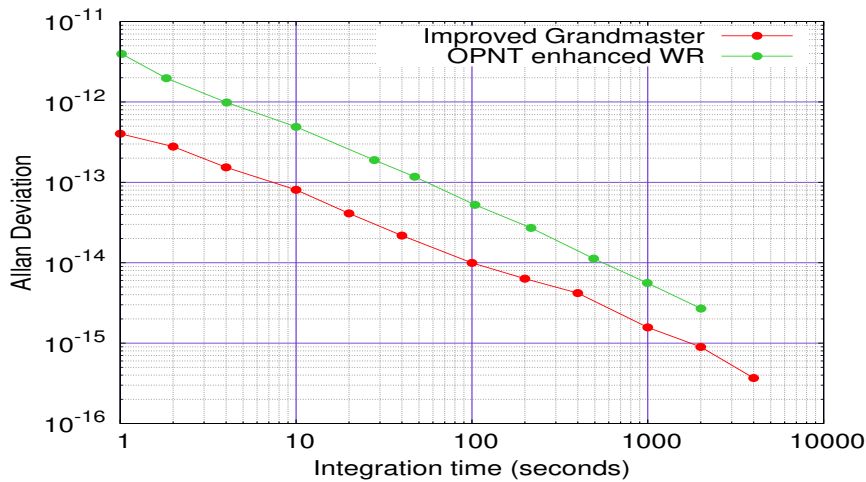


FIGURE 3.9: Comparison of Allan Deviation (NEQ BW=50 Hz) of our Improved Grandmaster WRS with OPNT enhanced WR.

3.3.2 Time Stability performance

The GM switch receives its notion of time from a reference PPS (Pulse per second) as described in Section 3.2.1. For the time stability analysis, we measure the time interval between the reference PPS and the PPS out of the GM switch by the time interval counter Physipus STS201. STS201 is a high performance time interval counter with a single shot resolution of about 300 fs by specification and was specially developed for the T2L2 project [79]. Fig. 3.10 illustrates the time interval data for about ten days of consecutive measurement. The peak to peak fluctuations are about 50 ps with no phase jumps observed over ten days of measurement.

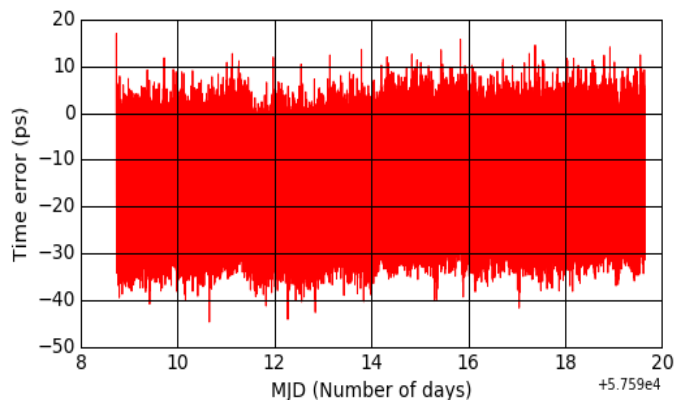


FIGURE 3.10: Phase data for the improved Grandmaster WRS (constant offset has been removed).

The time stability for the improved and default Grandmaster WRS is presented in the Fig. 3.11. At one second of integration time, the time stability for the improved case dropped down to 5.5 ps from the default value of 12 ps. The time stability for the default case attains the one picosecond level at 1000 seconds of integration time, whereas for the improved case it reaches the one picosecond level at short integration time of 30 seconds and remains below the picoseconds level for very long integration time (over one day).

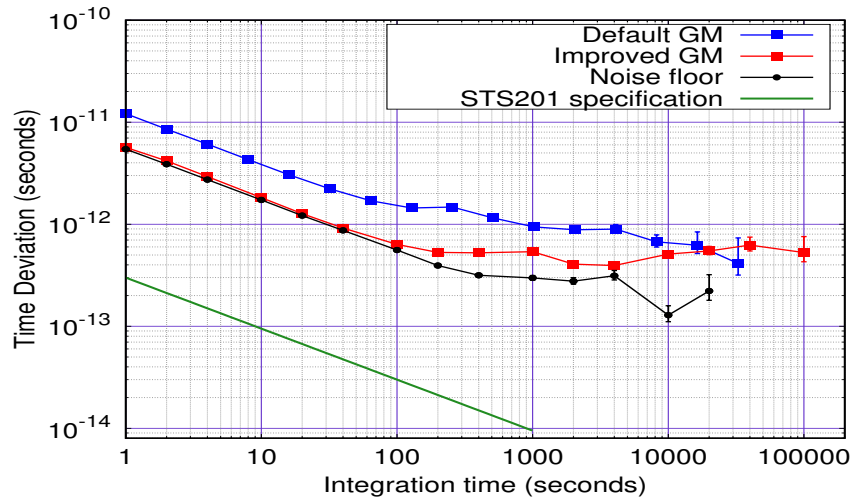


FIGURE 3.11: Time Deviation for default and Improved Grandmaster switch (Bandwidth of measurement = 1 Hz).

Such time stability performance demonstrates that the WRS has very low noise and very stable electronics. The short term limitation for the improved GM switch is mainly due to the PPS jitter due to the PPS generation and distribution in the laboratory. This is basically the noise floor of our measurement. The noise floor was calculated by measuring the time interval between two reference pulse per second pulses (PPS REF) out from the Timetech Pulse distribution unit with a pair of selected cables. We are not limited by the measuring instrument because the stability of the high performance STS201 counter according to the specification lies well below (by a factor of 18) the noise floor of our measurement. By comparing the time stability of the improved GM and the noise floor of our measurement we are able to observe the additive noise due to the GM switch. We observe that from 1 to 100 seconds of integration time, the performance of the improved GM hits the noise floor of our measurement thus illustrating ultimate performance. Hence it is very important to consider a high performance time interval counter to be able to observe the additive noise due to the GM switch. We would also like to comment that the default GM switch performance is very close to the resolution limitation of the time interval counter SR620 which is the most widely used counter in metrology laboratories.

3.4 Performance of a Slave White Rabbit Switch

In the last section, we described the first stage of a typical WR network, the Grandmaster WRS and discussed the work done to improve its performance. The second stage in a WR network is the Slave synchronized to the Grandmaster by an optical fiber link. Depending on the user requirements for a WR network, the Slave can be a White Rabbit switch or a White Rabbit node of the type SPEC-DIO or WR-ZEN (as explained in the last chapter).

3.4.1 Testing Optical link configurations

The recommended White Rabbit link configuration by CERN is the bi-directional setup which utilizes a single fiber and two different wavelength of propagation (1490 and 1310 nm). But it also supports the uni-directional setup utilizing dual fiber and a single wavelength of propagation as employed by the long haul White Rabbit link by the Finnish metrology laboratory VTT [43]. So we decided to perform a comparative study of the two possible optical link configurations for a White Rabbit link.

3.4.2 Experimental setup

The setup is illustrated in Fig. 3.12. We utilized two White Rabbit switches, two White Rabbit end nodes of the type SPEC, fiber spools and CWDM and DWDM small form factor pluggable optical transceivers (SFP). The default Grandmaster switch (GM) is the timing master of the White Rabbit network. The second switch, called the Master, was synchronized to the GM by a short uni-directional link of 14 m at 1541 nm. We then installed two links from the Master to two Slave SPEC boards numbered 1 and 2. The first slave SPEC1 was synchronized to the Master by a uni-directional link at the DWDM wavelength of 1541 nm using two 25 km fiber spools. These SFPs were long range SFPs with a specified range of 120 km. In order to avoid saturation of the optical receiver, we inserted a 15 dB attenuator in both the arms. This setup was referred to 'Bi-fiber'. The second Slave SPEC2 was synchronized to the Master by a bi-directional link using one 25 km fiber spool and utilized the 1490 and 1310 nm SFPs. This setup was referred to as 'Bi-color'.

Each of the Slave nodes outputs a PPS signal that was compared to the PPS reference signal of the laboratory. We used the time interval counter SR620 for the bi-fiber setup (SPEC1) and a high performance time interval counter STS201 for the bi-color setup. The two links were recorded simultaneously. Thus any variation of the reference signal and the first link from GM to Master is in common mode.

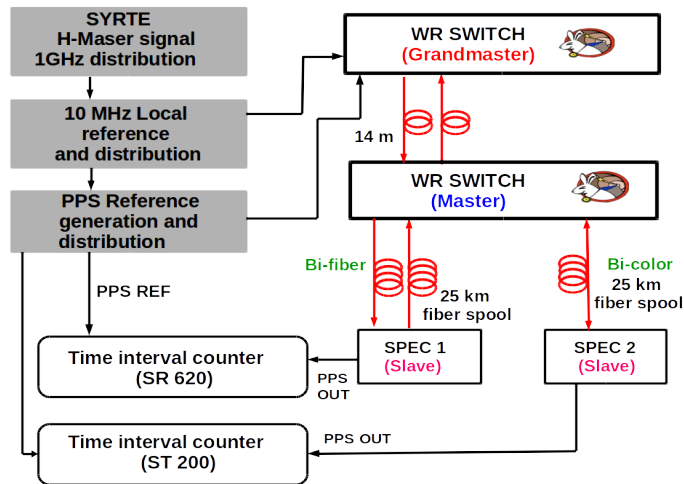


FIGURE 3.12: Experimental setup for comparison of uni-directional (Bi-fiber) and bi-directional (Bi-color) 25 km White Rabbit links.

3.4.3 Effect of Chromatic dispersion

One of the significant reasons to choose a specific optical link configuration among the two mentioned above is Chromatic Dispersion. Chromatic Dispersion is caused by the variation of the refractive index with the wavelength of propagation. This generates delays between different wavelength of propagation. The propagation delay t for a fiber of length L is given by the equation

$$t = \frac{n(\lambda)L}{c} \quad (3.1)$$

where where $n(\lambda)$ is the refractive index as a function of wavelength. The chromatic dispersion coefficient $D(\lambda)$ represents the variation of the delay with the wavelength:

$$D(\lambda) = \frac{1}{L} \frac{dt}{d\lambda} \quad (3.2)$$

Chromatic Dispersion affects both the accuracy and the stability of the time transfer. The accuracy of time transfer is mainly effected due to the difference in wavelength of propagation in the uni-directional and bi-directional links. In case of a bi-directional link, a large differential chromatic dispersion arises due to the huge difference in the propagation wavelengths. For instance, the recommended wavelengths for a single fiber link are 1490 and 1310 nm with a large wavelength difference of 180 nm with one wavelength (1310 nm) lying in the zero dispersion wavelength region giving rise to huge differential chromatic dispersion. On the other hand, a uni-directional link with same wavelength of propagation for the two way link, contributes much less to the chromatic dispersion. For the stability of time transfer at short term, the spectral linewidth of the optical emitter contributes to the chromatic dispersion.

So to estimate the magnitude of the contribution from Chromatic Dispersion, we first evaluate the effect on our 25 km fiber spools. To do so, we performed optical spectrum analysis of our emitters with an Optical Spectrum Analyzer Yokogawa AQ6370C using a resolution bandwidth of 20 pm. Fig. 3.13 and Fig. 3.14 display the optical power spectrum of the CWDM and DWDM SFPs in our laboratory. We observe that the spectrum of the 1310 nm emitter is extremely poor with many peaks over tens of nm. Using a Gaussian fit to the recorded spectra of the 1490 and 1541 nm SFPs, we measured linewidths of 32.1 pm and 23.6 pm over four second of measurement time respectively. These measured linewidths are just above the resolution of the Optical Spectrum Analyzer. The spectrum of the CWDM SFPs is clearly wider than that of the DWDM SFPs.

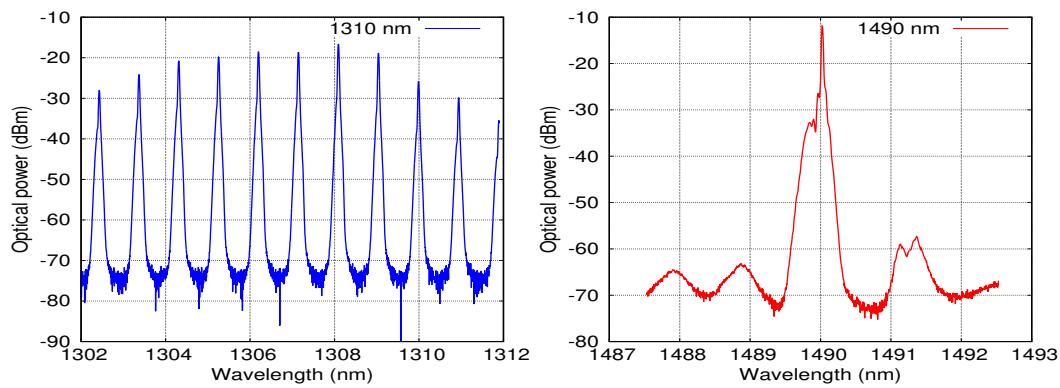


FIGURE 3.13: Optical spectrum of the 1310 and 1490 nm (Bi-directional) CWDM SFPs.

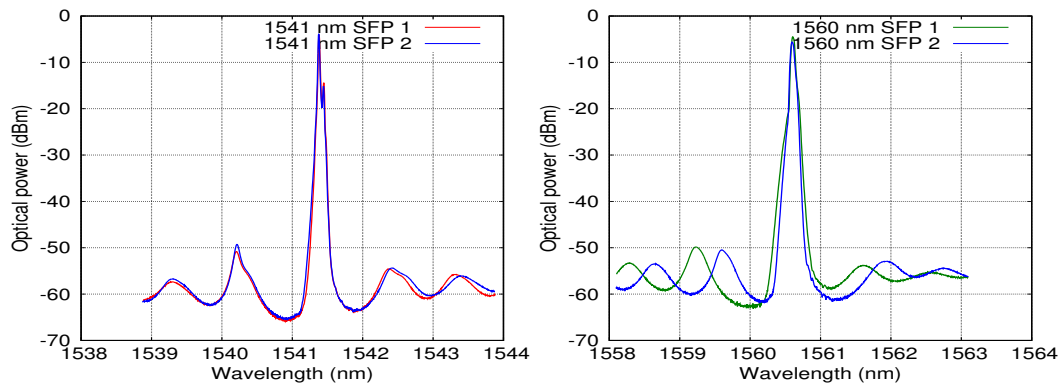


FIGURE 3.14: Optical spectrum of the 1541 and 1560 nm (Uni-directional) DWDM SFPs.

For SMF28 fiber the dispersion is equal to 17 ps/nm/km at 1550 nm and 13 ps/nm/km at 1490 nm [80]. We calculated the effect of Chromatic Dispersion using the equation 3.2 and the dispersion values stated above. We summarize the results for specified linewidth and for our measured linewidths for bi-directional and uni-directional WR link in the table 3.1.

25 km spools	1490/1310	1541
Wavelength difference (nm)	180	<0.5
Linewidth specified (nm)	3	<0.08
Instability associated to specification (ps)	515	25
Linewidth measured (nm, measurement time 4 s)	0.032	0.024
Instability@4s (ps)	5.5	7.3

TABLE 3.1: Comparison of the effect of Chromatic Dispersion on stability for commercial SFPs in two setups: a bi-color link using 1490/1310 nm emitters and a single fiber, and a bi-fiber link using the DWDM emitters at 1541 nm and dual fibers.

We observe a huge discrepancy between the specified and measured linewidth for the CWDM SFPs by a factor of about 90. For the DWDM SFPs, we observe a discrepancy factor of 3. The SFP manufacturers do not specify the measurement conditions (such as the resolution bandwidth and measurement time), which could possibly explain the deviation.

From Table 3.1, we notice that the calculated instability contribution for the CWDM SFP pair is less than the one for DWDM SFP. This can be explained by the fact that for the 1490/1310 pair, only 1490 nm contributes to the effect of chromatic dispersion as 1310 nm is the zero dispersion wavelength.

Chromatic Dispersion scales linearly with the length of the link and from the instability values reported here, it is clear that Chromatic Dispersion can play a significant and limiting role for long haul fiber links and the frequency stability of the optical emitters should be considered for links longer than 100 km. For extension to long haul links, the uni-directional configuration must be utilized to ensure compatibility with the telecommunication networks and to benefit from the installed backbone equipment. On the other hand for a bi-directional configuration, special bi-directional equipment would be required to be developed and installed on existing telecommunication networks. The only drawback of the uni-directional configuration is the fiber length imbalance which can lead to a dramatic time offset and hence inaccuracy.

3.4.4 Results

Fig. 3.15 displays about three days of phase data for the bi-fiber and bi-color setups showing peak to peak fluctuations of about 150 ps. We observe stable data sets with no de-locking from the Slave or Master side. The Overlapping Allan Deviation is

obtained from the time interval counter measurements. The Overlapping Allan Deviation is presented in Fig. 3.16. For both the setups, the frequency stability scales down as τ^{-1} and reaches the level of 10^{-15} at long integration time of 65000 seconds. We observe similar behavior for the bi-fiber and bi-color setups.

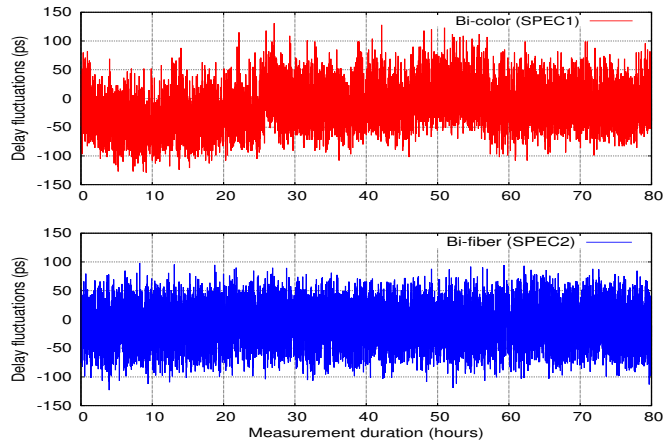


FIGURE 3.15: Phase data for the uni-directional (Bi-fiber) and bi-directional (Bi-color) setups.

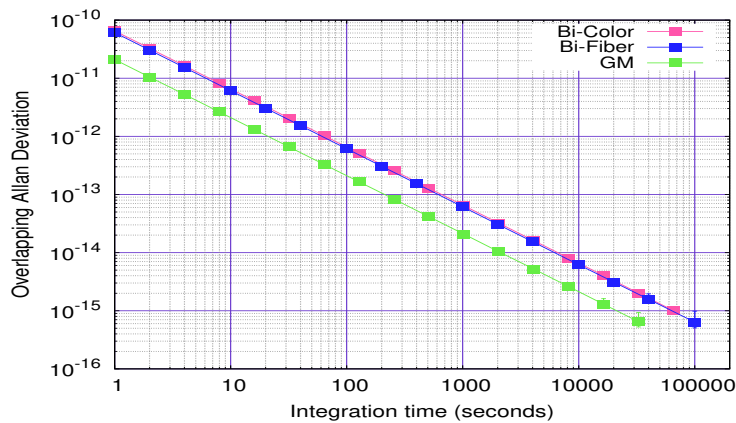


FIGURE 3.16: Overlapping Allan Deviation (calculated from phase data) for the unidirectional and bidirectional setups (Bandwidth of measurement = 1 Hz).

The time deviation is presented in the Fig. 3.17. We observe a time stability of 35 ps at one second of integration time for both the setups. The time stability reaches a minimum of about 2 ps at 1000 seconds of integration time after which it follows a rebound. With 25 km fiber spools, we expected a contribution of the chromatic dispersion to the instability of about 5-7 ps@4 s. At the current level of performance of White Rabbit, this effect was not detectable in our short-distance experiment in the laboratory and we observed similar behavior for the two setups [68].

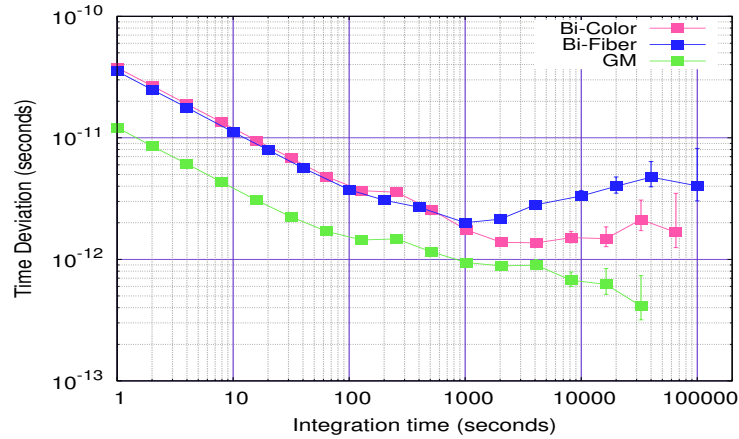


FIGURE 3.17: Time Deviation (calculated from phase data) for the unidirectional and bidirectional setups (Bandwidth of measurement = 1 Hz).

3.5 Improving the performance of a Slave WRS

We improved the performance of the timing master of a White Rabbit network. The next step towards advancement was to improve the performance of the Slave WRS. The Slave WRS uses the SoftPLL to lock the internal local oscillator to the clock recovered from the fiber link as described in the last chapter. The default bandwidth of locking is about 20 Hz. It was of great interest to study the effect of increased SoftPLL bandwidth, so we decided to perform bandwidth optimization to achieve better performance and followed the approach of M. Rizzi on his work on SoftPLL bandwidth variation [71].

3.5.1 Phase Locked Loops (PLL)

In this section, we briefly describe a typical Phase locked loop (PLL) circuit. Phase locked loops are utilized widely in communication systems for frequency locking. Fig. 3.18 displays the block diagram of a typical phase-locked loop. A PLL consists of three functional blocks: a voltage controlled oscillator (VCO), a phase detector (PD) and a loop filter. The phase detector generates an output voltage v_d proportional to the phase difference between the input signal (the reference signal) and the output of the VCO. In the locked state, the frequencies of the reference signal and the VCO's output signal are identical and the phase error between the reference signal and the VCO's output signal is zero (or remains constant). The phase detector output is referred as the error signal.

The loop filter filters out the AC components which have harmonic frequencies and is usually a passive low pass filter or an active power filter with an integration which can improve the stability of the PLL [81]. The loop filter's output v_c tunes the VCO. In Laplace domain, the output of the PD and the LPF are given respectively by the following equations [81]:

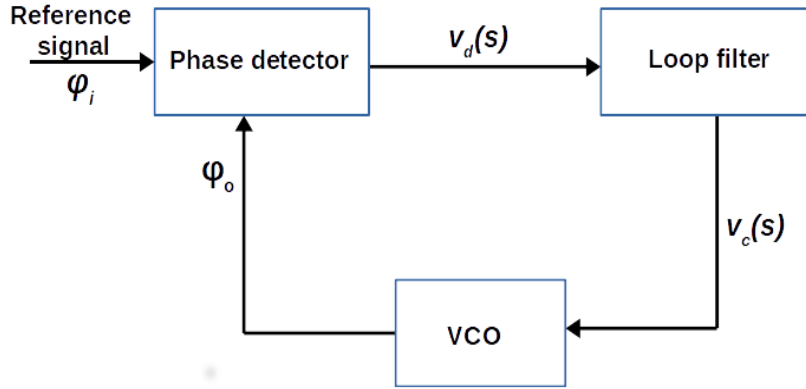


FIGURE 3.18: Block diagram of a typical phase locked loop [81].

$$v_d(s) = K_d(\phi_i(s) - \phi_o(s)) \quad (3.3)$$

where K_d is the detector gain.

$$v_c(s) = F(s) \cdot v_d \quad (3.4)$$

where $F(s)$ is the transfer function of the loop filter. A PLL is a closed loop system and a transfer function $H(s)$ which relates the reference signal to the VCO's output can be written as [81]:

$$H(s) = \frac{K_d K_{VCO} F(s)}{s + K_d K_{VCO} F(s)} \quad (3.5)$$

where K_{VCO} is the VCO gain and the transfer function for the error signal is defined as:

$$E(s) = 1 - H(s) = \frac{s}{s + K_d K_{VCO} F(s)} \quad (3.6)$$

Equation 3.5 represents the mathematical model of a PLL.

White Rabbit utilizes a SoftPLL (described briefly in Chapter 2 Section 2.10), in which the PLL function is realized by software. The phase error signal is fed to a PI controller which tunes the VCO by varying the proportional and integrator gains denoted by k_p and k_i respectively (Chapter 2 Fig. 2.16). A general PI controller has the transfer function:

$$K(s) = k_p + \frac{k_i}{s} \quad (3.7)$$

Variation of the PI gains is performed to minimize the phase error and thus achieve optimal response. In the next section, we describe the optimization of the PI gains of the SoftPLL of a Slave WRS in order to achieve best performance.

3.5.2 Experimental Setup

We built a uni-directional White Rabbit link of length 25 km using two White Rabbit Switches, fiber spools and Small form factor pluggable optical transceivers (SFP). We utilize a uni-directional configuration to ensure compatibility with the telecommunication network. The experimental setup is presented in Fig. 3.19. The improved GM switch is the timing master for the WR network. The Slave WRS is synchronized to the GM by a 25 km uni-directional link at 1541 nm.

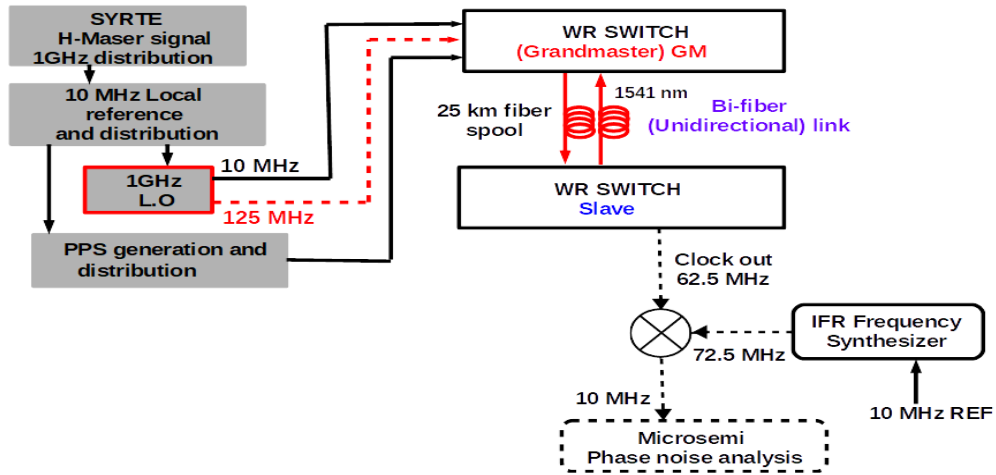


FIGURE 3.19: Experimental setup for a 25 km White Rabbit uni-directional link.

3.5.3 Phase locked loop Bandwidth variation

The two gain parameters of the Slave SoftPLL are the proportional gain (k_p) and the integrator gain (k_i). Our methodology of SoftPLL bandwidth (BW) optimization consists of two steps in order to obtain a set of optimized k_p and k_i . In the first step, the k_i parameter is held constant and k_p is varied to obtain an optimum value. Secondly, for this optimum value of k_p , k_i is varied to obtain an optimum value and then for this optimum k_i value, k_p is varied again and finally we obtain a set of optimized k_p and k_i . The optimization process of the proportional and integrator gains is an iterative loop.

We perform this method of k_p and k_i variation on the 25 km link described above. To see the effect of the k_p and k_i variation, we measure the phase noise power spectral density of the Slave clock for each variation. The Slave clock signal is down converted to 10 MHz as described in Section 3.2.1 and is measured by Microsemi Phase noise test set 5120A. To perform the gain parameter variation for the WRS, a software modification had to be done. This involves a reconfiguration of the gain parameter values in a specific file and recompilation was done to generate a new FPGA binary. The WRS default binary was then replaced by this new binary file and

the switch was rebooted.

The default values of k_p and k_i are 1100 and 30 respectively. We perform the first step of the SoftPLL BW optimization by choosing the default value of $k_i = 30$ and varying the k_p value from 100 to 8000. Fig. 3.20 presents the PSD of the Slave clock for a constant k_i value and different k_p values. For k_p values ranging from 100 to 4000, the SoftPLL is not locked and the single side band (SSB) phase noise is very high for low Fourier frequencies. Also, the servo bump of the loop is visible at about 20 Hz, which is the default BW of locking. With the increase of the proportional gain, it is seen that the magnitude of the servo bump is compressed accordingly. The SoftPLL locks for $k_p=8000$ value, but for Fourier frequencies between 100 Hz to 1 kHz, we observe that the PSD increased by almost 5 dB for higher values of k_p ranging from 2000 to 8000. So, $k_p=800$, a value not very far from the default value is chosen.

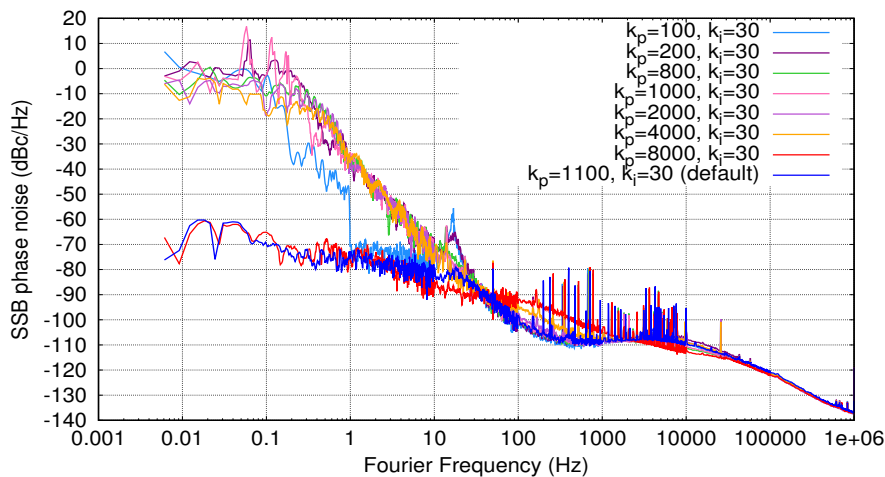


FIGURE 3.20: Power spectral density of the Slave clock for different k_p values for a constant $k_i = 30$.

In the second step, we vary the k_i value from 32 to 4000 for a constant value of $k_p=800$. Fig. 3.21 presents the different PSD curves obtained for different k_i values with fixed k_p . The plot depicts that the bandwidth of the locking increases with increase in the integrator gain as the servo bump shifts towards higher Fourier frequencies with increase in k_i , which is consistent with the PLL theory. For lower k_i values from 32 to 1024, we observe that the SoftPLL is not locked and the SSB phase noise is very high for low Fourier frequencies (less than 1 Hz). For $k_i=2048$ and 4000, the SoftPLL locks successfully compressing the free running noise of the local oscillator to about -70 dBc/Hz at 1 Hz of Fourier frequency. We attain about 250 Hz as the bandwidth of locking for $k_i=4000$ but the SSB phase noise increases by 10 dB at 1 Hz and increases significantly (about 40 dB for Fourier frequencies ranging from 10 Hz to 10 kHz) when compared to the default values. A high k_i value does indeed provide a higher bandwidth of locking but the SoftPLL is very noisy for Fourier frequencies from 10 Hz to 10 KHz, so the k_i value needs to be chosen carefully.

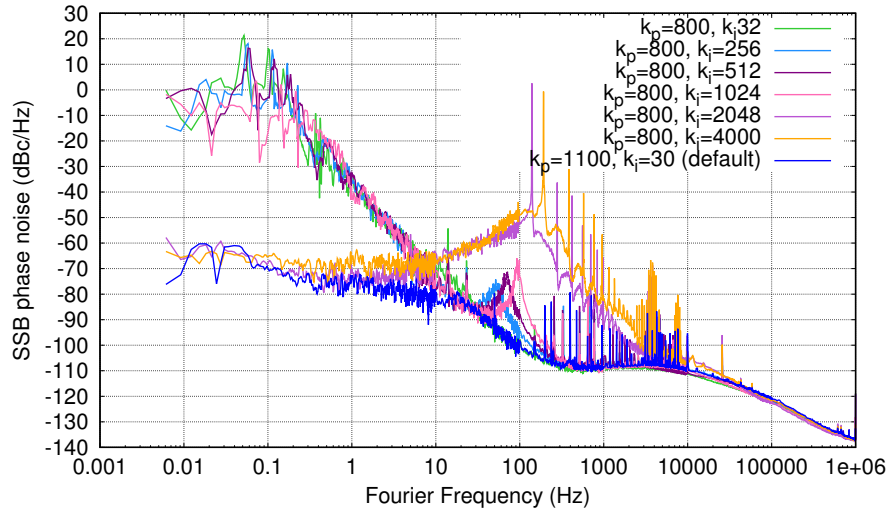


FIGURE 3.21: Power spectral density of the Slave clock for different k_i values for a constant $k_p = 800$.

Therefore, we chose a mid value for the integrator gain $k_i=300$ and perform a variation of k_p value from 100 to 2000. The phase noise power spectral density of the Slave clock is measured for each variation.

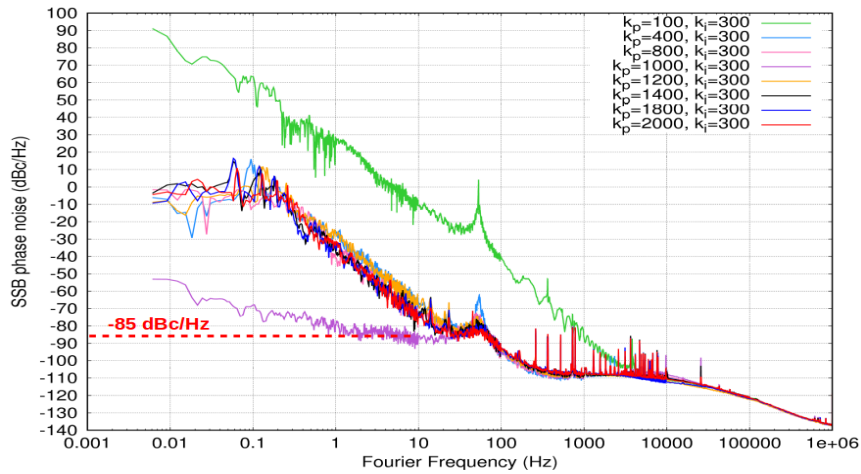


FIGURE 3.22: Power spectral density of the Slave clock for different k_p values for a constant $k_i = 300$.

The limitation for selecting a higher bandwidth of locking for the Slave arises mainly due to the noisy behavior of the SoftPLL for high Fourier frequencies. So, in our case of SoftPLL BW variation, we are not limited by the fundamental limit due to the propagation delay (τ) of the optical fiber link [73] (described in the last chapter). For a 25 km White Rabbit link, we calculate the maximum bandwidth limit according to the servo system formula ($1/4\tau$) [81] which is about 2 kHz, and it falls in the high Fourier frequency range. It is also important to consider that the bandwidth optimization method is most suitable for short and mid range links but for single span long haul links, a low bandwidth of locking is sufficient because the

bandwidth of locking decreases as the length of the link increases.

We studied intensively the behavior of the SoftPLL for variation of the proportional and integrator gains, and before performing the SoftPLL bandwidth optimization we increased the length of the WR link by a factor of 2 (as eventually we would study the performance of long haul WR links). The following subsection describes the SoftPLL bandwidth optimization for a mid range WR link.

3.5.4 A mid range White Rabbit link

We increase the length of the WR link by a factor of two and the setup for the 50 km uni-directional WR link is exactly the same as for the 25 km link except that we utilize 50 km fiber spools (2×25 km spool) for each arm. The experimental setup is illustrated in Fig. 3.23. The Slave WRS is synchronized to the improved GM switch by a 50 km uni-directional link at 1541 nm. The Slave clock signal is down converted to 10 MHz as described in the Section 3.2.1 and is measured by Microsemi Phase noise test set 5120A. First, we will discuss the SoftPLL BW optimization for this link and then discuss the frequency and time stability performances.

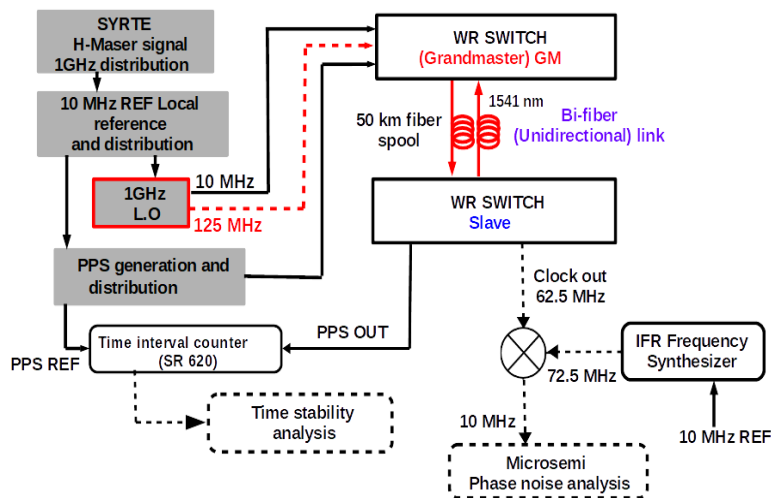


FIGURE 3.23: Experimental setup for a 50 km White Rabbit uni-directional link.

3.5.5 Phase locked loop bandwidth optimization

We utilize the optimized gain parameters as described in the Section above. Further, we fine tune the proportional gain for the integrator value $k_i=300$. Fig. 3.22 depicts the curves for different k_p for a constant value of $k_i=300$. The SoftPLL locks successfully only for one k_p value =1000 with noise compressed down to -85 dBc/Hz level for low Fourier frequencies (less than 10 Hz) with a servo bump at about 50 Hz. For the optimized set of values of $k_p=1000$ and $k_i=300$, a fine tuning of the k_p value is carried out. Fig. 3.24 displays the curves for the fine tuning of k_p value from 900 to

1100, all the curves overlap for the entire range of Fourier frequency. We also compare with the default $k_p=1100$ and $k_i=30$ values and observe that for the optimized set of $k_p=1000$ and $k_i=300$, the SSB phase noise is lower by 10 dB at 1 Hz Fourier frequency.

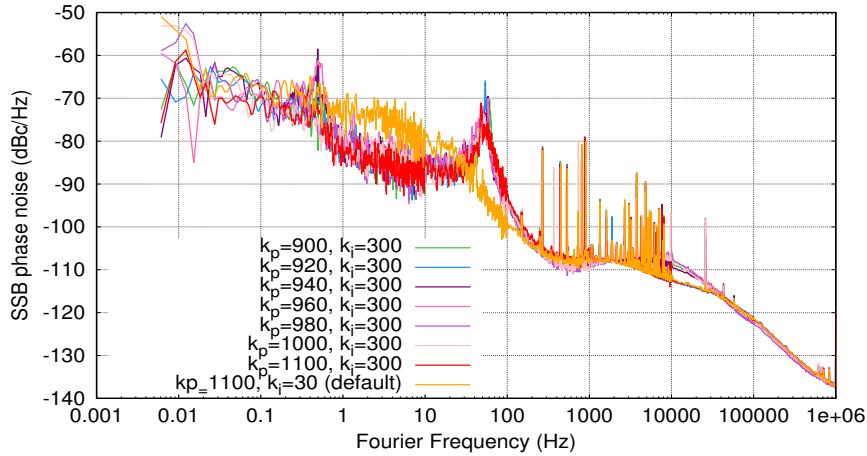


FIGURE 3.24: Power spectral density of the Slave clock for fine tuning of k_p values for a constant $k_i = 300$.

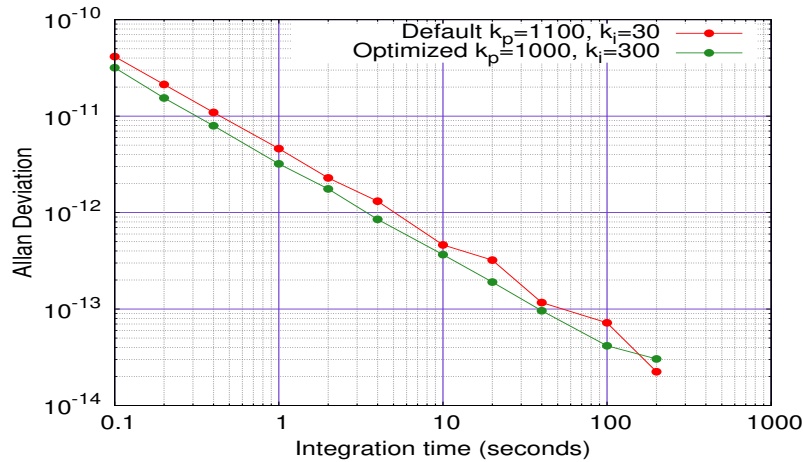


FIGURE 3.25: Allan deviation (NEQ BW=50 Hz) for the Slave switch for default and optimized gain parameters.

The Allan deviation of the down converted Slave clock at 10 MHz is also measured by Microsemi Phase noise test set 5120A. The frequency stability for the Slave clock at 62.5 MHz is calculated by dividing the stability at 10 MHz by the factor 6.25. Fig. 3.25 shows the Allan deviation (NEQ BW=50 Hz) for the Slave clock at 62.5 MHz with default and optimized gain parameters. At one second of integration time, the frequency stability falls down from the default value 4.6×10^{-12} to 3.1×10^{-12} for the optimized case (reduced by a factor of 1.44 as compared to the default case). It follows the same improvement for longer averaging times.

3.5.6 Frequency and Time stability performance

For the frequency and time stability analysis, we measure the time interval between the PPS out of the Slave switch and the reference PPS by the time interval counter SR620. Fig. 3.26 displays the time interval data for about three days of consecutive measurement. The peak to peak fluctuations are of about 120 ps with no phase jumps over the duration of measurement.

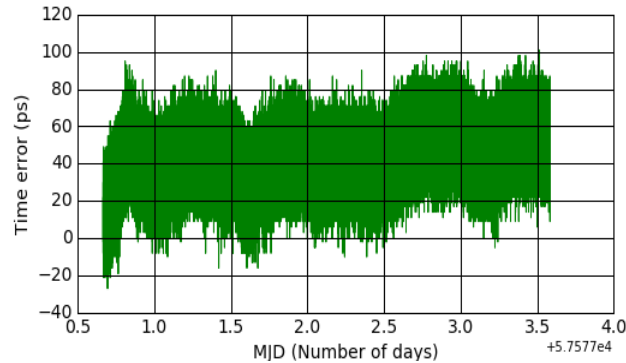


FIGURE 3.26: Phase data of the Slave WRS for the 50 km WR link (constant offset has been removed).

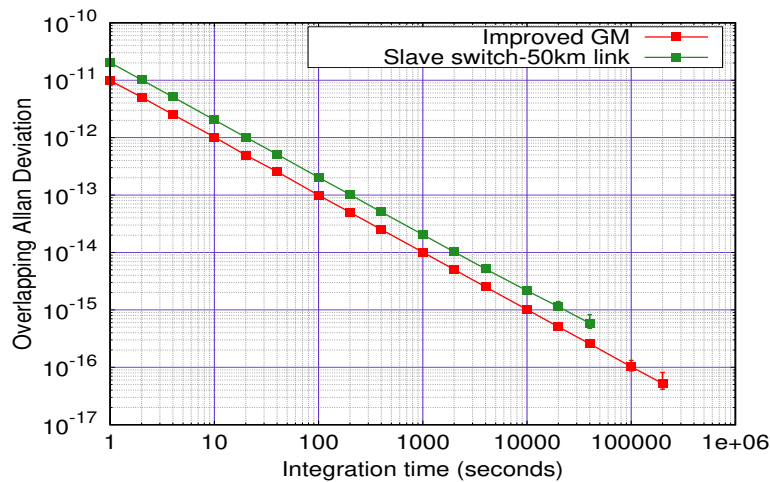


FIGURE 3.27: Frequency stability for a 50 km White Rabbit link.

The Overlapping Allan deviation for the Grandmaster switch and the Slave switch with increased bandwidth of 50 Hz is presented in the Fig. 3.27. For the Grandmaster WRS, we use the phase data of Fig. 3.10 for calculating the frequency stability, and we obtain a stability of 9.8×10^{-12} at one second of integration time (τ) and it scales down as τ^{-1} to 1.0×10^{-13} at 100 seconds of integration time and finally attains a stability of 1.0×10^{-16} at longer integration time of 100000 seconds. The short term stability is limited by the shot noise of the PPS generation and distribution in the laboratory (as described in Section 3.3.2).

For the Slave switch, the stability degrades by a factor of two when compared to the Grandmaster switch and we obtain a stability of 2.0×10^{-11} at one second of integration time, scaling down as τ^{-1} to 1.1×10^{-15} at 20000 seconds of integration time. Fig. 3.28 shows the time stability of the Slave switch which degrades by a factor of two as compared to the GM switch. At one second of integration time, the time stability is 11.7 ps and falls below the picoseconds level at about 300 seconds of integration time. It attains a minimum of 645 fs at 1000 seconds of integration time and then starts to degrade for longer averaging times due to the fiber thermal noise described in the next chapter.

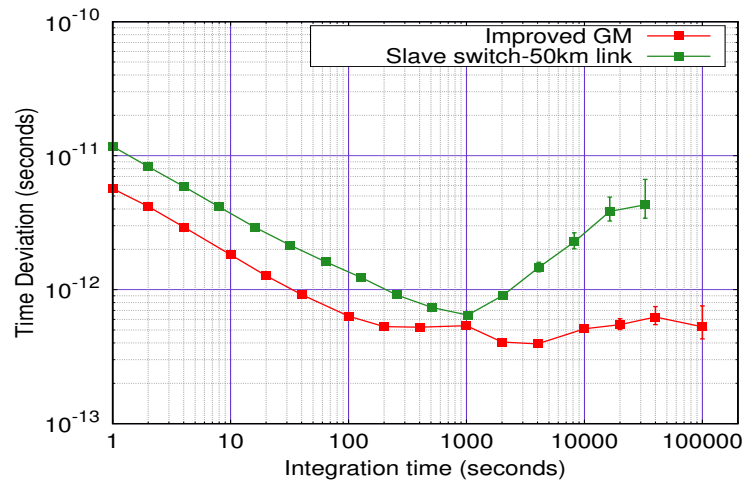


FIGURE 3.28: Time Deviation for a 50 km White Rabbit link.

3.6 The Local Oscillator performance

As discussed above, we found that a higher bandwidth of locking for the Slave switch results in a better performance and its performance is mainly limited by the quality of the local oscillator and the SoftPLL locking chain. We further decided to study the local oscillator performance. This work was done in collaboration with Seven solutions and University of Granada. We pick up the local oscillator signal (25 MHz) from the internal circuit of the WRS. We also pick up the error signal out of the SoftPLL of the Slave WRS synchronized to the improved GM switch by a 100 km uni-directional link (the experimental setup is similar to the Fig. 3.23 except for the length of the fiber spools). The Slave switch utilized increased bandwidth of locking of about 70 Hz obtained by optimization of the gain parameters as described in the subsection 3.5.3. The optimized gain parameter values are $k_p=1000$ and $k_i=500$.

We measure the PSD of the Slave output clock and the Local Oscillator (L.O) signal by Microsemi phase noise test set 5120A and convert them to Relative frequency noise displayed in Fig. 3.29. For Fourier frequencies (denoted by f) from 1 to 10 Hz,

the frequency noise of the L.O decreases by two decades due to the Random walk noise process with a slope of f^{-2} . From 10 to 100 Hz range, the noise goes down by one decade due to the Flicker frequency noise process with a slope f^{-1} . For Fourier frequency ranging from 100 to 1000 Hz, we see that the noise process is the white frequency with a slope of f^0 as the frequency noise remains constant for this decade. For the following decade from 1 kHz to 10 kHz, the noise increases by 20 dB because of the white phase noise with a slope of f^2 . It is clear that a higher bandwidth should be used to lock the local oscillator, preferably in the flat region from 100 to 1000 Hz (blue dashed line) as the minimum of the relative frequency noise lies at about 200 Hz. With a default bandwidth of locking of 20 Hz, we are not able to compress the high frequency noise (> 20 Hz) of the local oscillator and thus we need higher gain for noise compression.

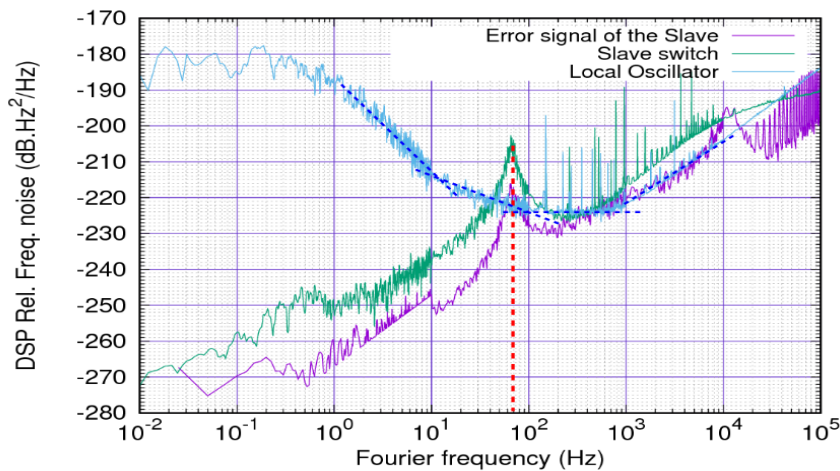


FIGURE 3.29: Relative frequency noise for the Slave switch, error signal of the Slave switch and for the local oscillator of the WRS.

We also record the error signal out of the SoftPLL of Slave WRS by an FFT analyzer and the voltage noise is converted to Relative frequency noise which is also displayed in Fig. 3.29. The frequency noise of the error signal for high Fourier frequencies ranging from 500 Hz to 10 kHz overlaps exactly with the frequency noise of the local oscillator proving that the error signal performance is limited by the local oscillator as expected. By comparison of the frequency noise of the Slave Switch and the error signal out of the Slave SoftPLL, we observe that the Slave Switch has excess of noise of about 10 dB at low Fourier frequencies (less than 100 Hz). This exhibits that there is still room for improving the Slave switch performance.

We also measure the internal 3.3 V power supply signal which powers the local oscillator of the Switch and the 5 V power supply signal used for the WR clock distribution chip AD9516-4 by an FFT analyzer. The voltage noise is converted into Relative frequency noise displayed in Fig. 3.30. We also convert the phase noise power

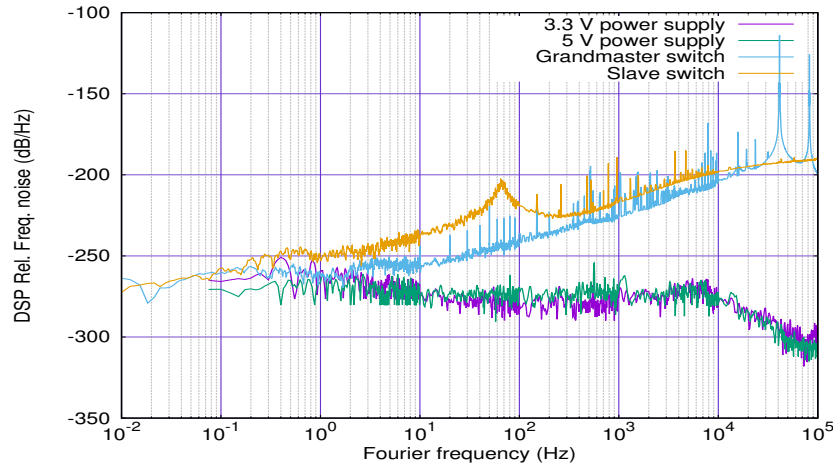


FIGURE 3.30: Relative frequency noise contribution from the 3.3 V and 5 V internal power supply, for the Grandmaster and the Slave switch.

spectral density of the Grandmaster clock (improved) and its Slave switch (synchronized by a 100 km uni-directional setup) to Relative frequency noise, which are displayed in Fig. 3.30. For very low Fourier frequency, the voltage noise of the power supply contributes to the frequency noise due to the dependence of the frequency output of the Local oscillator on the applied power supply voltage. We observe a convergence of the frequency noise of the improved GM switch and the 5 V power supply for low Fourier frequency of about 1 Hz. For the improved GM switch, as the local oscillator is bypassed, only the 5 V power supply signal contributes to the frequency noise for very low Fourier frequencies. Likewise, we observe a convergence of the frequency noise of the Slave WRS with the frequency noise of the 3.3 V power supply signal for low Fourier frequency from 0.1 to 1 Hz.

For both the power supplies, the frequency noise is at the level of -275 dB/Hz for higher Fourier frequency range, which does not limit the performance of the White Rabbit switches at high Fourier frequencies. We would also to comment that the WR switches utilize low noise power supplies.

3.7 Increasing the PTP message exchange rate

For the Slave WRS, we increased the bandwidth of locking to achieve better performance. Another factor whose frequency rate could be increased to attain better performance is the PTP message exchange rate between the Master and the Slave. As described in the last chapter, the Precision Time Protocol governs the clock synchronization process in White Rabbit. The protocol utilizes a two way message exchange process to calculate the clock offset between the master and the slave clocks. The

quality of the PTP synchronization depends on the exchange rate of the PTP messages. The lower the quality of the clock we want to recover, the higher the bandwidth of PTP message exchange. Recovering a high quality clock signal requires a very stable local oscillator in every Slave switch or an increase in the bandwidth of locking and a higher broadcast rate of PTP messages. The default rate of the PTP message exchange in WR is one packet per second (1 Hz). The IEEE 1588 standard [39] supports a maximum of 128 packets per second. Depending upon the application in a network, higher PTP traffic may interfere with other data traffic. In our case, we only had timing data in our network which allowed us to easily increase the PTP rate.

So we decided to perform a second improvement for the Slave by increasing the rate of the PTP message exchange. With the help of the WR team, a software modification was done to increase the PTP message exchange rate, which involved modification of a specific configuration file and recompilation of the WR-PTP implementation binary. The improved Grandmaster switch's default PTP binary was then replaced with the increased PTP rate binary, as the Master side governs the broadcast of the *Sync* messages and the Slave responds accordingly. Due to some limitation in the PTP implementation in White Rabbit, we could only set a maximum of 16 packets per second. We verified the increased PTP rate by the specific software command '*ptpdump*' available in the WRS tools. The output of this command was logged to a file and the PTP *Sync* messages were counted. We got 14 packets instead of 16, owing to the loss of two packets probably due to CPU overload. We were able to push the default PTP bandwidth from 1 Hz to 14 Hz.

We tested the effect of increased PTP rate on the performance of a Slave switch. We considered a Slave switch synchronized to the improved Grandmaster by a 100 km uni-directional link at 1541 nm. The experimental setup is similar to the Fig. 3.23 except that we utilized eight 25 km fiber spools for building the 100 km uni-directional link. We measured the time interval between the PPS out of the Slave switch and the reference PPS by the time interval counter SR620 for default and increased PTP rates. Fig. 3.31 displays the frequency stability comparison for the Slave WRS with default and increased PTP rates. We did not observe any improvement of the frequency stability with increased PTP rate, as for both the rates the frequency stability performance overlapped. No effect of the increased PTP rate is observable on the phase measurement. We further investigate its effect in the next Chapter.

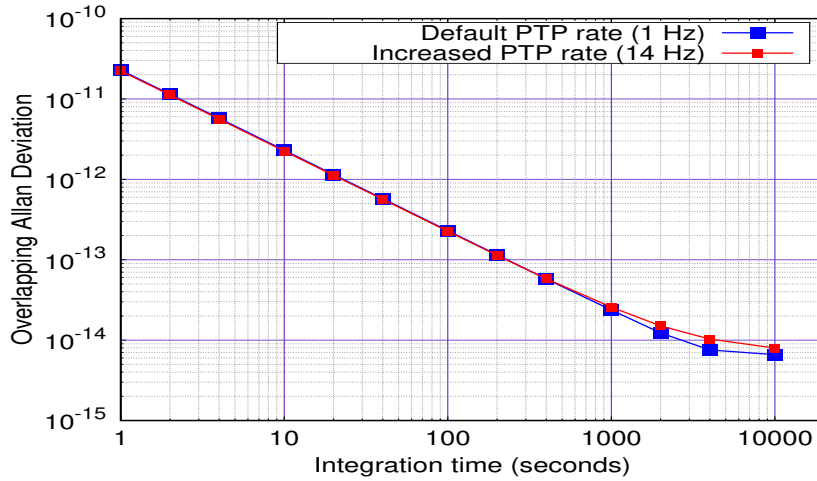


FIGURE 3.31: Frequency stability (calculated from phase data) comparison for default and increased PTP rate for the Slave WRS (100 km link).

3.8 Summary

This chapter focused on studying the default performance of the Grandmaster switch. Progressing further, the performance limitations were identified and an improvement method was discovered and tested successfully. We improved the short term stability for the Grandmaster switch from 1.3×10^{-11} to 4.9×10^{-13} at one second of integration time (NEQ BW=500 Hz). The time stability for the improved GM dropped down to 5.5 ps from the default value of 12 ps at one second of integration time. It attained the picoseconds level at short integration time of 30 seconds and remained below the picoseconds level for over one day of integration time.

Further, we compared two different optical configurations for a Slave switch and discussed its frequency and time stability performance and found that both the configurations give similar results for short links (up to 25 km). Our focus shifted towards improving the performance of a Slave synchronized to the improved GM switch. Two improvements were done for the Slave switch. The first one was to utilize a greater bandwidth of locking which allowed to compress the frequency noise of the local oscillator more effectively. The second improvement of increased PTP message exchange rate between the Master and the Slave switch did not yield any improvement in the stability performance calculated from the phase data. Further, we tested White Rabbit technology to disseminate time and frequency over mid-scale range to many users. In this regard, we realized a 50 km uni-directional setup to ensure compatibility with the telecommunication network. For this link, we obtained a frequency stability of 2.0×10^{-11} at one second of integration time, scaling down to 1.1×10^{-15} at 20000 seconds of integration time. The time stability for this link was 11.7 ps at one second of integration time and it dropped below the picoseconds level at about 300 seconds of integration time. It attained a minimum of 645 fs

at 1000 seconds of integration time.

The following table summarizes the main results of this chapter.

Performance	Default	Improved
Grandmaster WRS frequency stability @ 1 s (NEQ BW= 500 Hz)	1.3×10^{-11}	4.9×10^{-13}
Grandmaster WRS time stability @ 1 s (BW= 1 Hz)	12 ps	5.5 ps
Slave WRS SSB phase noise @ 1 Hz (50 km WR link)	-72 dBc/Hz	-82 dBc/Hz
Performance of a 25 km WR link (Bi-fiber)	@ 1 s	@ 1000 s
Frequency stability (BW= 1 Hz)	5×10^{-11}	6×10^{-14}
Time stability (BW= 1 Hz)	37 ps	2 ps
Performance of a 50 km WR link	@ 1 s	@ 1000 s
Frequency stability (BW= 1 Hz)	2×10^{-11}	1×10^{-14}
Time stability (BW= 1 Hz)	11.7 ps	645 fs

TABLE 3.2: Summary of the main results.

The local oscillator and internal power supply signals of the WRS were studied intensively. The objective of this study was to identify the limitations for the performance of the Slave and look for scope of improvement. We discovered that there is scope for two improvements. First, the performance can be improved by more noise compression which requires more gain and a higher rate of bandwidth of locking (optimum would be in the range of 100 to 500 Hz). This could be easily achievable with faster FPGAs. And also we notice that the error signal frequency noise is lower than the observed frequency noise of the Slave switch (by 10 dB) thus there is room for improvement. Second, a better power supply could possibly lower the influence at low frequency. This is possible to achieve but difficult for field situations where the equipment is housed in shelters in the countryside with significant temperature fluctuations.

Chapter 4

Towards long range time and frequency dissemination using White Rabbit

4.1 Introduction

Telecommunication span White rabbit links utilizing a Cascaded approach are introduced and their frequency and time stability performances are described. The different factors contributing to the short term and long term limitation for the time stability are described and discussed in detail. Further, a strategy to tackle such limitations is explained intensively. Lastly, the frequency and time stability performances of a long haul Cascaded 500 km White Rabbit link are described. The study demonstrates the achievable performances using White Rabbit over metropolitan area and long haul national scale links.

4.2 A realistic Telecommunication network span

The motivation is to realize a telecommunication span link for time and frequency dissemination to multiple users up to national scale. For an effective and cost cutting approach, deployment of White Rabbit must fit into the architecture of telecommunication networks particularly public networks such as the French network for Education and Research RENATER. Our main interest is to ensure compatibility with active telecommunication networks and to benefit from their installed telecommunication equipment (such as EDFAs). In this regard, we utilized a uni-directional configuration to build long haul WR links and also chose to utilize the central DWDM wavelength (1541 nm) widely used for telecommunication networks as one of the primary wavelengths along with CWDM wavelength emitters.

4.2.1 Experimental Setup

As national link spans are about 80-120 km long, we decided to build a 100 km White Rabbit link. We built a 100 km uni-directional link using two White Rabbit

Switches, a WR node of the type SPEC-DIO, fiber spools, an OADM (Optical add drop multiplexer) and small form factor pluggable (SFP) optical transceivers. The experimental setup is presented in Fig. 4.1. The improved Grandmaster switch is the timing master of the network. The two Slaves, a White Rabbit switch and the WR node SPEC-DIO are synchronized to the GM switch by a 100 km (8×25 km fiber spool) uni-directional link at 1541 nm and 1610 nm respectively. Both the SFPs are long range upto 120 km. An OADM is used at the transmitting and receiving side to multiplex and demultiplex the two wavelengths.

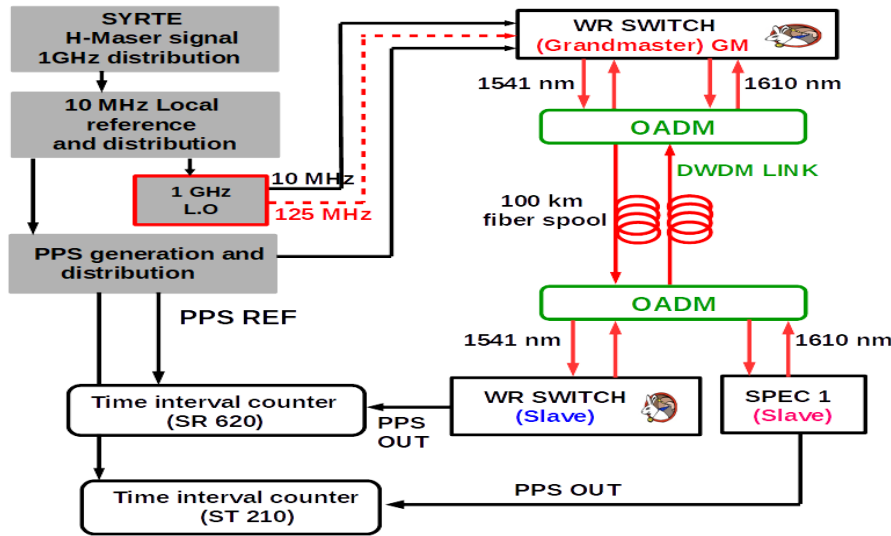


FIGURE 4.1: Experimental setup for a 100 km White Rabbit uni-directional link.

4.2.2 Phase locked loop Bandwidth optimization

The Slave switch bandwidth optimization was performed according to the methodology described in the last chapter. The Slave switch's output clock at 62.5 MHz was down converted to 10 MHz as described in the last Chapter section 3.2.1. The phase noise power spectral density of the down-converted Slave clock at 10 MHz was measured by the Microsemi Phase noise test set 5120A. The integrator gain for the 50 km WR link was optimized as $k_i=300$ (Chapter 3 section 3.5.4), so we test higher integrator gain values with proportional gain varying from 1000 to 8000. Fig. 4.2 shows the PSD curves for different k_i with corresponding k_p values. We observe that the servo bump shifted towards higher Fourier frequencies from 70 to 200 Hz for $k_i=500$ and $k_i=3200$ respectively. The SSB phase noise increases by 10 dB for Fourier frequencies ranging from 100 to 1 kHz for variation in k_i from 500 to 3200. For $k_i=3200$, we observe an overshoot due to excess of noise for $k_i=500$ and we clearly see the reduction in the noise as shown in Fig. 4.2. Hence, too high k_p and k_i values result in overshoot of noise and broadening of the curves.

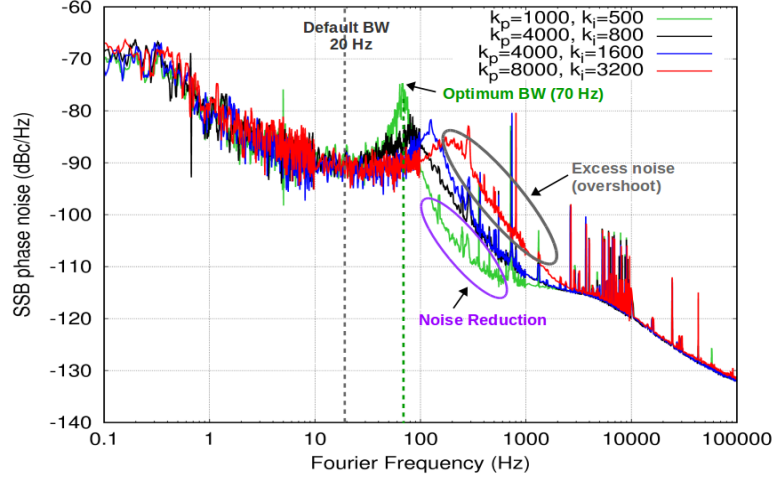


FIGURE 4.2: Phase noise power spectral density of the Slave clock for $k_p=4000$ and k_i values.

At 1 Hz Fourier frequency, the SSB phase noise overlaps for the different k_i values (500, 800, 1600, 3200) tested. So, we carefully analyze the Allan Deviation (NEQ BW=0.5 Hz) measured by Microsemi Phase noise test set 5120A. We calculate the Allan Deviation at 62.5 MHz by dividing the stability at 10 MHz by the factor 6.25 for the tested k_i values. We notice that with increasing k_i values, the short term stability degrades as presented in Fig. 4.3. We attain the best value for the frequency stability as 1.0×10^{-12} at one second of integration time for $k_i=500$ and $k_p=1000$. We chose the optimized set of gain parameters as $k_p=1000$ and $k_i=500$ with a bandwidth of locking of 70 Hz.

Gain values	Allan Deviation (NEQ BW=0.5 Hz) at 1 s
$k_p=1000, k_i=500$	1.0×10^{-12}
$k_p=4000, k_i=800$	1.1×10^{-12}
$k_p=4000, k_i=1600$	1.2×10^{-12}
$k_p=8000, k_i=3200$	1.4×10^{-12}

TABLE 4.1: Allan Deviation (62.5 MHz) at one second of integration time for the Slave clock for different k_p and k_i values.

4.2.3 Experimental results

Each of the Slaves outputs a PPS out signal and a time interval counter was used to measure the delay between the PPS out of the Slaves and the PPS REF signal as presented in Fig. 4.1. We used the time interval counter SR620 for the Slave switch and a high performance time interval counter STS201 for the SPEC slave. The experiment was performed under well controlled conditions and the two slaves were recorded simultaneously. Fig. 4.4 displays the phase data for the two Slaves for about nine days of consecutive measurement. The peak to peak fluctuations for both the Slaves

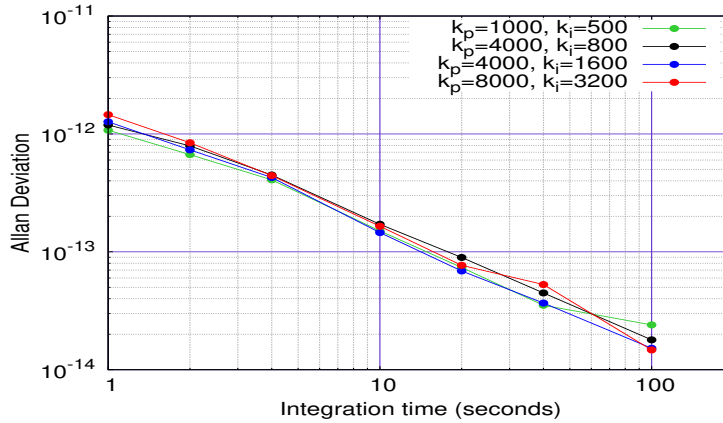


FIGURE 4.3: Allan Deviation of the Slave clock for different k_p and k_i values.

are of about 800 ps. For both the Slaves, we observe a periodic modulation of periodicity of about one day in the phase data. The phase data for the Slaves is highly correlated. This is probably due to the temperature variation as the period of the modulation is about one day. We also notice that the SPEC slave has a thicker phase trace than the Slave switch mainly due to its greater instrumental noise. The electronics for the White Rabbit switch is better than the low cost SPEC-DIO user node.

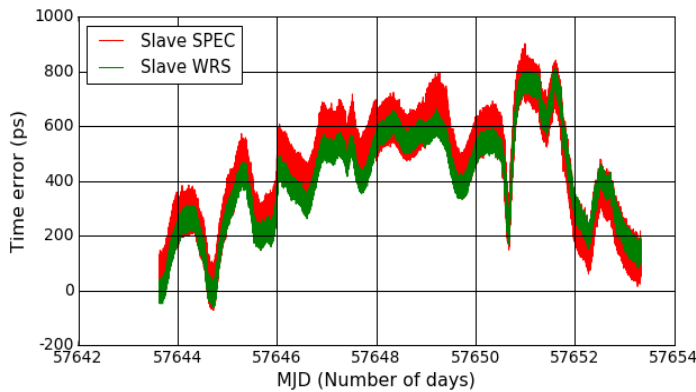


FIGURE 4.4: Phase data for the two Slaves (constant offset removed).

The Overlapping Allan Deviation for the 100 km WR link is presented in Fig. 4.5. The frequency stability for the GM switch scales down as τ^{-1} due to the white phase noise and reaches a value of 10^{-15} at 10000 seconds of integration time. The short term stability at one second of integration time for the Slave switch and SPEC is 2.2×10^{-11} and 5.3×10^{-11} respectively. For both the slaves, the stability scales down as τ^{-1} due to the white phase noise and reaches the level of 10^{-14} at about 4000 seconds of integration time. The GM depicts the performance of the WRS without any transmission (no fiber) and thus is a kind of noise floor with its frequency stability scaling down to 1.0×10^{-16} at 100000 seconds of integration time, but both the Slaves exhibit a bump with a maximum at 40000 seconds of integration time which

degrades their stability. This bump is a confirmation of the one day periodicity seen in Fig. 4.4. The bump is due to the fiber thermal noise explained in detail in the following subsection.

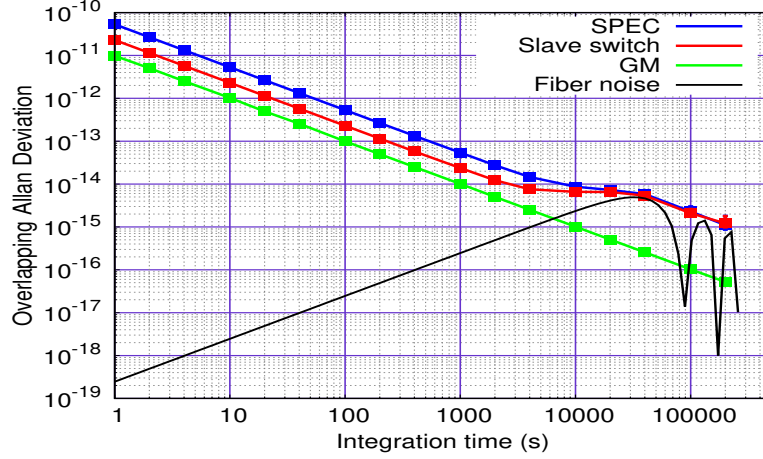


FIGURE 4.5: Overlapping Allan deviation (calculated from phase data) for the 100 km uni-directional WR link.

The time stability plot is presented in Fig. 4.6. We observe that the GM switch reaches 1 ps at 30 seconds of integration time and remains below the 1 ps level for longer integration time. The time stability at one second of integration time is 13 ps and 30 ps for the Slave switch and the SPEC slave respectively. The Switch and SPEC slave time stability initially scales down as $\tau^{-1/2}$ due to the white phase noise to a minimum value of 1.3 ps and 2.6 ps at 200 seconds of integration time respectively. Then the stability starts to degrade for longer averaging times due to the fiber thermal noise bump with a maximum at 40000 seconds of integration time which limits the time stability performance of both the Slaves to about 80 ps at long integration time of 100000 seconds. The degradation in stability arises from the coherent excitation of the fiber spools and exhibits a τ^1 behavior, where τ is the integration time.

4.2.4 Fiber thermal noise

In Fig. 4.4, we observe a periodic modulation of periodicity of about one day in the phase data for both the Slaves. This periodic modulation is due to the temperature fluctuations acting on the optical length of the fiber spools. The propagation delay τ for traversing a fiber of length L is given by $n.L/c$, where n is the refractive index of the fiber and c is the speed of light. Temperature variations act on the refractive index and the physical length of the fiber. We define the optical length of the fiber as the term $n.L$, the propagation delay change $\delta\tau$ is given by the equation [82]:

$$\frac{\delta\tau}{\delta T} = \frac{1}{c} \left[\frac{\delta n}{\delta T} L + n \frac{\delta L}{\delta T} \right] \quad (4.1)$$

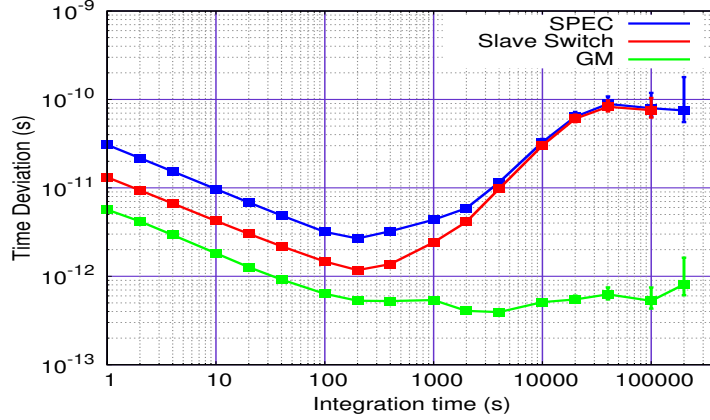


FIGURE 4.6: Time deviation (calculated from phase data) for the 100 km uni-directional WR link.

The propagation delay change occurs due to the refractive index variation δn , and fiber length variation δL with temperature change δT . The second term which is the fiber length change with temperature can be expressed as α , the thermal linear expansion coefficient for the fiber. The above equation can be expressed in terms of phase fluctuations by using the relation $\varphi(t) = x(t) 2\pi\nu$ [2], where $x(t)$ are the time fluctuations, ν is the carrier frequency and t is the time variable. The fiber thermal noise density is expressed as a function of the temperature change in [83] as follows:

$$\delta\varphi(t) = 2\pi\nu \frac{n(T_0)}{c} \left(\alpha_{SiO_2} + \frac{1}{n(T_0)} \frac{\delta n(T_0)}{\delta T} \right) \cdot \Delta T \quad (4.2)$$

where $n(T_0)=1.468$ is the refractive index, $\alpha_{SiO_2}=0.55 \times 10^{-6} K^{-1}$ is the thermal linear expansion coefficient, c is the speed of light, ΔT is the temperature variation and T_0 is the operating temperature. The second term inside the parenthesis is the thermo-optical coefficient equal to $7 \times 10^{-6} K^{-1}$ [84]. The above equation can be rewritten as:

$$\delta\varphi(t) = \gamma \cdot \Delta T \quad (4.3)$$

where γ is the first order phase-temperature coefficient. As calculated in [83], for the SMF 28 fiber specifications, $\gamma= 37$ fs/(K.m) for the carrier frequency at 194.4 THz (1542 nm) and at $T_0= 298$ K.

The periodic modulation arises from the day night cycle. This will induce a periodic modulation of temperature and thus of the propagation delay. The time period is quite stable and the amplitude is subject to day to day fluctuations. Such periodic modulation adversely affects the stability at long integration time [3]. We calculate the effect of the fiber thermal noise on the stability by the following equation [3]:

$$\sigma_y(\tau) = a \frac{\sin^2(\pi \times \tau \times f)}{(\pi \times \tau \times f)} \quad (4.4)$$

where a is the amplitude of the fluctuations and is assumed to be constant, $f=1/T$, T is the period of the periodic modulation which is equal to one day (86400 seconds) and τ is the integration time.

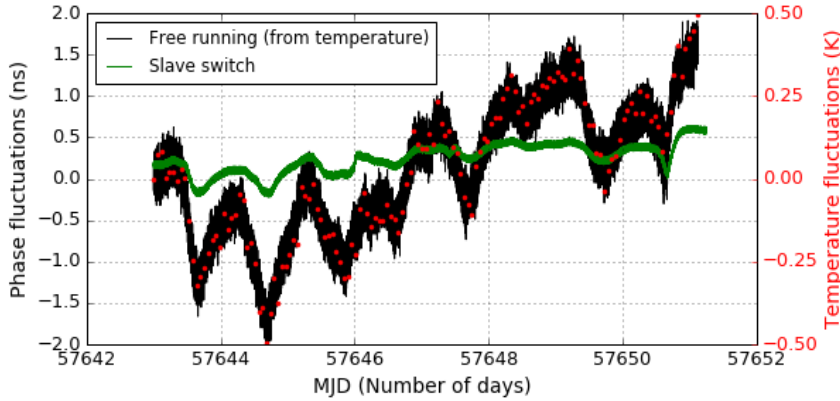


FIGURE 4.7: Ambient temperature variations experienced and recorded by the time interval counter STS201 and the calculated phase fluctuations. The green trace is the Slave switch data as in Fig. 4.4. We observe a compression factor of about 5 at half a day.

Fig. 4.7 shows the ambient temperature variations experienced by the time interval counter STS201 and were recorded by the STS201 simultaneously with the phase data. We observe peak to peak temperature fluctuations of about 0.8 K over nine days of measurement. We calculate a by using the thermal sensitivity of the fiber as 37 fs/(K.m) for a temperature variation of 0.8 K over the measurement time and for a link length of 100 km and we obtain a value equal to 2.96 ns. The calculated fiber thermal noise effect on stability according to the above equation is plotted in Fig. 4.5 as the black trace. We observe a bump in the frequency stability for both the Slaves with a maximum at 40000 seconds of integration time which confirms that the calculated fiber thermal noise agrees with the experimental results.

We also calculate the phase fluctuations from the temperature fluctuations using the relation 37 fs/(K.m) for a 100 km link. Fig. 4.7 displays these phase fluctuations and we refer them as the free running phase fluctuations as they are calculated directly from the temperature fluctuations. We observe peak to peak fluctuations of about 4 ns. These fluctuations can be used to calculate the free running fiber noise. Fig. 4.8 displays the free running fiber noise frequency stability and we observe a bump in the long term stability which confirms the presence of the bump observed for both the Slave switches.

We also plot the time error of the Slave switch in Fig. 4.7 depicted by the green trace (as in Fig. 4.4), these fluctuations are the compressed phase fluctuations (or we can say the in-loop phase fluctuations). We observe that these phase fluctuations are correlated to the temperature fluctuations. The free running phase fluctuations are

compressed approximately by a factor of 5.

We observe in Fig. 4.4 that the phase traces of the two Slaves overlap thus exhibiting noise correlation as expected as they are utilizing the same fiber spool bank and were recorded simultaneously. Thus the propagation noise arising due to the fiber spools is in common mode for the Slaves. Because of this, we could obtain the difference phase data by subtracting the phase data of SPEC and the Slave switch. By performing this subtraction, the effect of the common mode propagation noise due to the fiber spools cancels out and hence we should not observe the fiber thermal noise bump in the frequency stability performance. As an evidence of this fact, we calculate the frequency stability of the difference phase data. We compare the frequency stability of the SPEC slave, the Slave switch and the stability of their difference phase data in Fig. 4.8. The frequency stability for each of the Slaves degrades at long averaging time due to the fiber thermal noise bump. But as expected, the frequency stability calculated from the difference phase data did not exhibit any bump at long averaging time and the stability scales down to 9.6×10^{-16} at 100000 seconds of integration time.

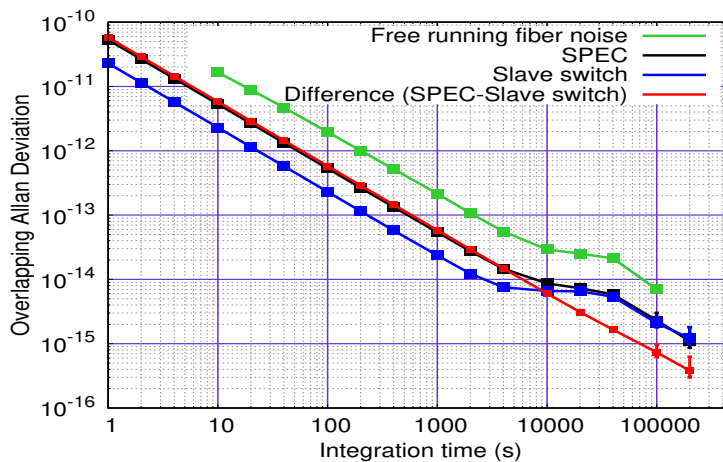


FIGURE 4.8: Overlapping Allan deviation (calculated from phase data) for the 100 km uni-directional WR link with evidence of the fiber thermal noise bump.

4.2.5 Limitations for the time stability performance

We focused on investigating the limitations of the time stability performance for the mid range White Rabbit link described above. We discovered two short term limitations for the time stability. The first short term limitation is due to the resolution of the Time interval counter. We utilized the most widely used time interval counter in the metrology laboratories, SR620 from Stanford Research Systems with a single shot resolution of 10 ps for the Slave switch. The single shot resolution of the time interval counter limits the time stability at one second of integration time (τ), which

averages down as $1/\sqrt{\tau}$ due to the white phase noise (shot noise). For the Slave switch's time stability presented in Fig. 4.9, we observe that the stability at one second of integration time lies very near to the limitation due to the time counter SR620 resolution. Thus for measuring few picoseconds of time stability, there is a stringent requirement for high performance time interval counters such as STS201 with a single shot resolution of 300 fs, which we utilized for the improved Grandmaster switch. The second short term limitation which plays a significant role for long haul fiber links is Chromatic dispersion which is described in detail in the following section.

The long term limitation for the time stability performance is the fiber thermal noise displayed in Fig. 4.9. As described in the Section 4.2.4, we observe that the time stability performance for the Slave degrades for long integration time exhibiting a bump due to the fiber thermal noise. The degradation in stability arises from the coherent excitation of the fiber spools and exhibits a τ^1 behavior, where τ is the integration time. For field application, we expect a $\sqrt{\tau}$ behavior for the degradation.

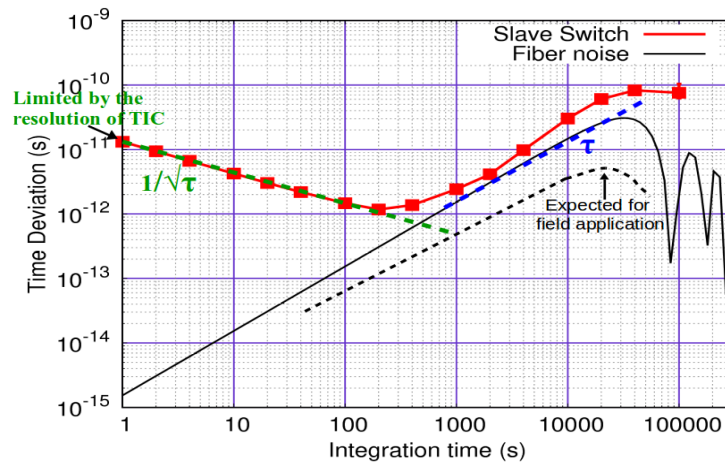


FIGURE 4.9: Limitations for the time stability (calculated from phase data) performance of the 100 km White Rabbit link.

4.3 Effect of Chromatic Dispersion

In the last Chapter Section 3.4.3, we noted that Chromatic Dispersion can play a significant and important role for the performance of long haul fiber links. The spectral linewidth of the optical emitters affects the short term stability.

We evaluate the effect of chromatic dispersion for the telecommunication span White Rabbit link described above. We calculate the limitation due to chromatic dispersion for the SMF28 fiber with a dispersion value equal to 17 ps/nm.km at 1550 nm [80] and the measured spectral linewidth for 1541 nm as 24 pm (as described in Chapter 3 Table 3.1). We calculate the value as $17 \text{ ps} \times 0.024 \times 100 \times$

$\sqrt{2}/2/C$, where C is the compression factor. The factor $\sqrt{2}$ arises due to the two way independent communication between the Master and the Slave. The division by 2 arises because the correction by the WR-PTP engine is calculated as half of the round trip time measured. If one considers $C=1$ for numerical application, we end up with about 29 ps, scaling linearly with the length of the fiber link.

In the following, we consider now a compression factor $C=3$ for the Slave as described in Section 4.2.4, and plot the result in Fig. 4.10. This calculated chromatic dispersion value scales down as $\tau^{-1/2}$ because the optical spectra of the SFPs has a Gaussian noise characteristic [85]. Fig. 4.10 displays the calculated limitation due to the chromatic dispersion to the short term time stability.

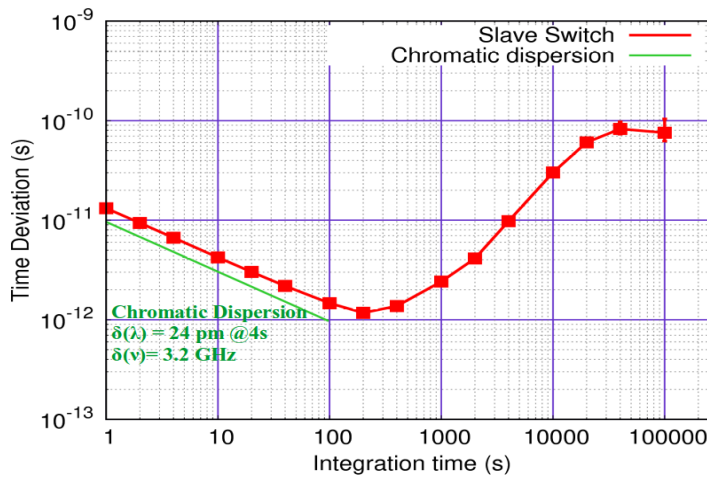


FIGURE 4.10: Chromatic dispersion contribution to the time stability performance of the Slave switch (100 km telecom span uni-directional link).

We expect a contribution of about 8.2 ps at 4 seconds of integration time which is very close to the observed time stability performance for the Slave switch. From the values reported above for the Chromatic dispersion contribution, it is clear that Chromatic dispersion can play a significant and limiting role for long haul fiber links with SFPs because it scales linearly with the length of the link as $17 \text{ ps} \times 0.024 \times L \times \sqrt{2}/2/C = 288 \text{ fs} \times L/C$ where L is the length of the fiber link.

For instance, if we calculate the chromatic dispersion limit taking into account the same spectral linewidth and assuming the same compression factor ($C=3$) for a single span White Rabbit link of 500 km as $17 \text{ ps} \times 0.024 \times 500 \times \sqrt{2}/2/C$, it is about 50 ps. This value clearly illustrates that the challenge is to limit the time stability performance to a few picoseconds level for long haul links ($L > 100 \text{ km}$) by reducing the effect of chromatic dispersion.

In the Netherlands, the OPNT group tested White Rabbit link (100 km) with CWDM and DWDM SFPs and they found that the link utilizing CWDM SFPs exhibited degradation in the frequency stability performance by about one order of magnitude from 500 seconds of integration time. [77].

4.4 Tackling Chromatic Dispersion

As explained in the last section, Chromatic dispersion is the main limitation for extension to long haul White Rabbit links with SFPs. With rich expertise of our group in coherent optical frequency transfer over long distance fiber links, we came up with a strategy of "Cascaded link approach" to tackle Chromatic dispersion. For any linear phase frequency servo system, the compressed power spectral density of the fiber phase noise is given by the equation [73]:

$$S_{locked}(f) = \frac{(2\pi f\tau)^2}{3} S_{free}(f) \quad (4.5)$$

where f is the Fourier frequency, τ is the delay of the loop and S_{free} is the free running fiber phase noise power spectral density.

According to the servo loop theory, the bandwidth of noise correction is limited to the value $1/4\tau$ [81, 73] which sets an upper limit to the above equation. For optical frequency transfer over fiber links, τ is limited by the travel time of the photon for a link of length L .

In the frame of optical frequency transfer over fiber links, from the above equation, one can anticipate that the bandwidth of correction decreases with decreasing L . Thus the performance of a long haul link can then be improved by dividing it into smaller subsections. For example, if a long haul link is subdivided into N number of equal parts, and taking into account that the free fiber noise scales as the length of the link, then the bandwidth of correction is increased by N . This is called the "Cascaded link approach" utilized for long haul optical frequency transfer [86]. Also, dividing a single span fiber link of length L into N number of sub spans results in less fiber noise (which scales linearly with the length of the link).

In case of implementation of White Rabbit for time and frequency dissemination over mid range links, we are by far not limited by the travel time through the optical fiber link but are limited by the default bandwidth of locking of the WRS SoftPLL, which can be optimized depending on the length of the link. For instance, let us compare the range of the fiber links with default and increased bandwidth of locking. The length of the link limited by the servo loop bandwidth of correction can be calculated as:

$$L = \frac{c\tau}{n} = \frac{c}{n(4f_{BW})} \quad (4.6)$$

where $n=1.468$ is the refractive index of fiber, c is the speed of light, $f_{BW}=1/4\tau$ is the bandwidth of correction (from servo loop theory limit) and τ is the propagation delay for a fiber of length L . Using the above equation, we can calculate the length for default (20 Hz) and increased bandwidth of locking (70 Hz) respectively as:

$$L_{20 \text{ Hz}} = \frac{2.99792458 \times 10^8}{1.468 \times 4 \times 20} = 2.5 \times 10^6 m \quad (4.7)$$

$$L_{70 \text{ Hz}} = \frac{2.99792458 \times 10^8}{1.468 \times 4 \times 70} = 729 \text{ km} \quad (4.8)$$

Thus from these values, we can clearly interpret that we are not limited by the travel time of the photon as the default bandwidth of locking of 20 Hz limits the the length of the optical fiber link to 3.5×10^6 m whereas the increased bandwidth limits the length to about 729 km.

The main advantage of using this cascaded approach for a long haul White Rabbit link is the reduction of the effect of chromatic dispersion because we earn by a factor N (number of spans). This is due to the fact that the noise related to Chromatic dispersion is smaller as the single span link undergoes division into smaller sub spans. For instance, we have less chromatic dispersion contribution as $L \rightarrow L/N$ which further implies $L/N \rightarrow \sigma_y/N$ (frequency stability per sub span improves by a factor of N).

4.5 Cascaded White Rabbit links using DWDM technique

We build long haul White Rabbit links by utilizing the cascaded approach to construct a set of experiments with multiples of 100 km (uni-directional) using the DWDM technique. This DWDM technique gives an advantage of using the same fiber link at different wavelength of propagation for consecutive cascaded stages. This allowed us to easily extend and realize long haul White Rabbit links in the laboratory.

4.5.1 Experimental Setup

We build a cascaded White Rabbit link using four White Rabbit Switches, fiber spools and CWDM and DWDM SFPs with dense wavelength division multiplexing technique. The improved Grandmaster switch (GM) is the timing master for the White Rabbit network. Fig. 4.11 presents the experimental schematic for the cascaded 300 km White Rabbit network.

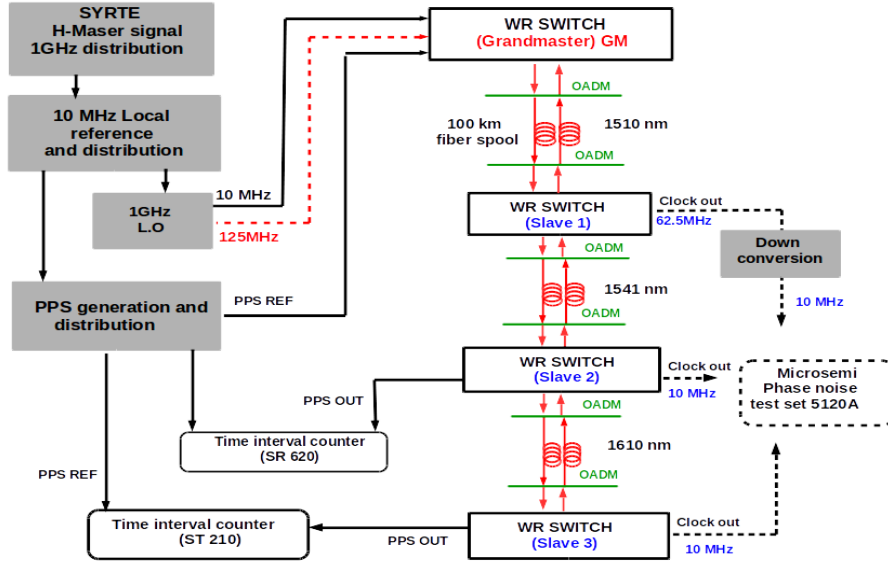


FIGURE 4.11: Experimental setup for the cascaded 300 km White Rabbit link.

The first span Slave switch (WRS 3.3v) is synchronized to the GM by a unidirectional link of 100 km (in total 8×25 km fiber spools) at 1510 nm. The second and third span Slave WRS utilize the same 100 km unidirectional link at 1541 nm and 1610 nm respectively. An OADM is used at the transmitting and receiving side to multiplex and demultiplex the three different wavelengths. As we utilize different hardware version of the White Rabbit Switches, it is important to mention that the first Slave is 3.3 version hardware with a clock output at 62.5 MHz which is down-converted to 10 MHz as described in the last Chapter Section 3.2.1. The other two Slaves switches are 3.4 version hardware with a clock output at 10 MHz.

4.5.2 Phase locked loop Bandwidth optimization for cascaded stages

Each of the Slave switch clock output is measured by Microsemi Phase noise test set 5120A. As the first Slave switch is synchronized to the GM by a 100 km unidirectional link, we simply choose the optimized gain parameters for the 100 km uni-directional link described in Section 4.2.2. We perform the variation of proportional and integrator gains for the Second and third span Slave switches.

As the second Slave switch is synchronized to the first Slave by the same span, we begin by testing the same optimized set of gain parameters as for the first Slave ($k_p=1000$ and $k_i=500$). Fig. 4.12 shows the PSD of the second Slave clock out at 10 MHz for $k_p=1000$ and $k_i=500$. We observe the servo bump of the phase locked loop at 70 Hz Fourier frequency with a very high magnitude of about -68 dBc/Hz due to excess of noise. To compress the magnitude of the servo bump, higher proportional gain values such as 8100 and 10000 are tested which resulted in compression

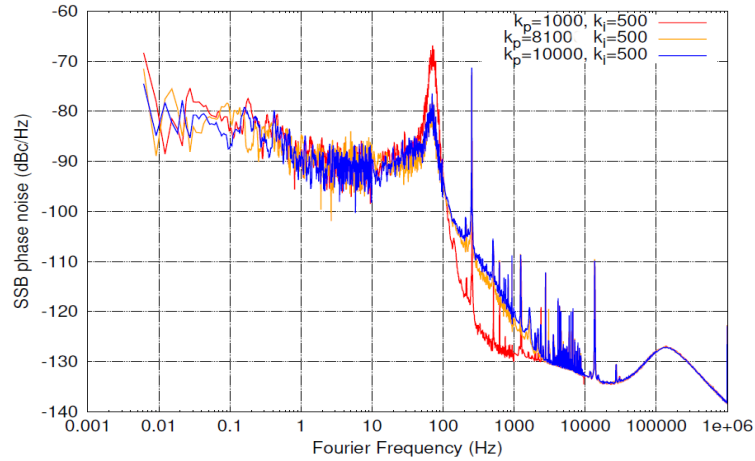


FIGURE 4.12: Phase noise power spectral density of the Second Slave clock for different k_p values with constant $k_i=500$.

by 12 dBc/Hz as seen in Fig. 4.12.

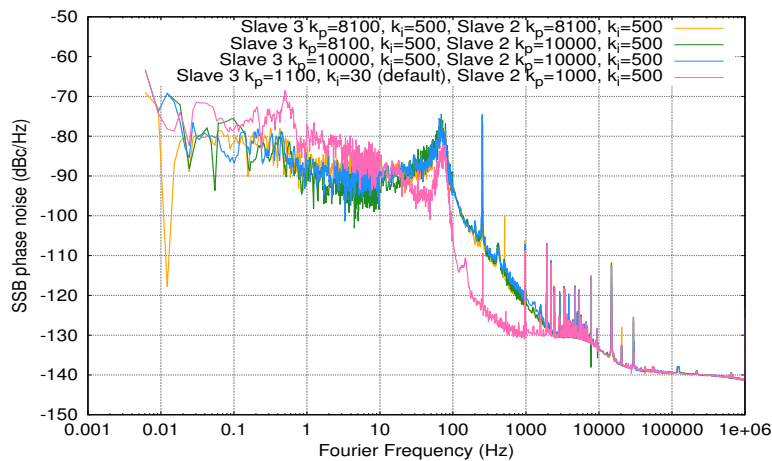


FIGURE 4.13: Phase noise power spectral density of the third Slave clock for default gain values and different k_p values for constant $k_i=500$.

Next, we test the above set of gain parameters (of the Second Slave) for the third Slave switch. Fig. 4.13 displays the PSD of the third Slave clock at 10 MHz for different gain parameters combined with k_p and k_i variation for the Second slave WRS. We also compare the PSD of the third Slave for default gain parameters with that for high gain parameters and we observe about 10 dBc/Hz lower phase noise for high gain parameters at 1 Hz Fourier frequency as displayed in Fig. 4.13.

To choose the optimized set of gain parameters for the Second and third Slaves, we also study the Allan Deviation (NEQ BW=5 Hz) measured by Microsemi Phase noise test set 5120A, presented in Fig. 4.14. We attain the best short term frequency stability of 3.2×10^{-12} at one second of integration time for $k_p=10000$ and $k_i=500$ for the Second slave along with $k_p=8100$ and $k_i=500$ for the third Slave switch. The

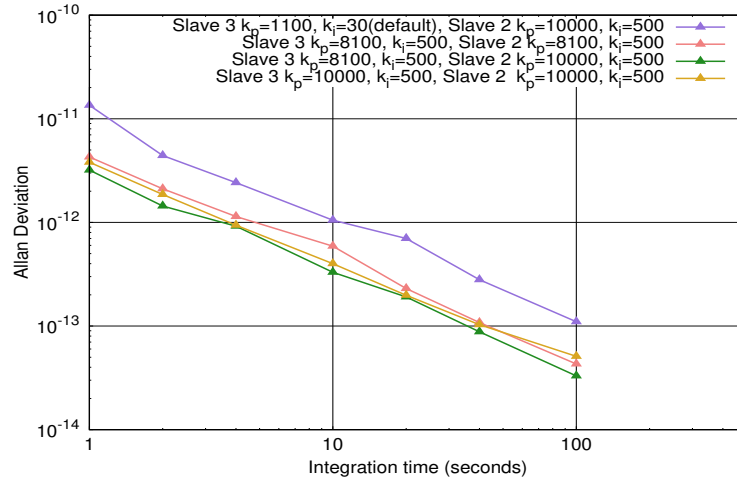


FIGURE 4.14: Allan Deviation (NEQ BW=5 Hz) for the third Slave clock for default gain values and higher k_p values for constant $k_i=500$.

optimized set of gain parameters for the cascaded stages are as $k_p=1000$ and $k_i=500$ for the first Slave switch, $k_p=10000$ and $k_i=500$ for the Second slave and $k_p=8100$ and $k_i=500$ for the third Slave switch with a bandwidth of locking of 70 Hz.

Table. 4.2 compares the optimized set of gain parameters for increasing link length. We observe that with increase in length from 50 km to 100 km, a bit higher integrator gain is required with approximately same proportional gain. For the cascaded stages of the 300 km White rabbit link, consecutive spans of equal lengths require much higher proportional gain with respect to the first cascaded stage for a selected value of the integrator gain. We report our experimental data in the table below and the evolution of proportional or integrator gains was not investigated further.

Link length (km)	Proportional gain (k_p)	Integrator gain (k_i)
50	1000	300
100	1000	500
200	10000	500
300	8100	500

TABLE 4.2: Comparison of the optimized set of gain parameters for increasing link length.

Fig. 4.15 displays the PSD of the cascaded 300 km White Rabbit network in a hierarchical manner beginning from the Grandmaster and the cascaded stages with optimized gain parameters. The clock output signals of the Grandmaster and the first Slave are at 62.5 MHz whereas for the second and third Slaves, the clock out signals are at 10 MHz. As the clock out signals are at different carrier frequencies, so we need to take into account a factor which is the logarithmic ratio of the two carrier frequencies for comparison of their phase noise power spectral densities. This factor

is equal to $20 \times \log(62.5/10)=15.9$ dB. This value is subtracted from the power spectral densities of the Grandmaster and the first Slave switch to compare with the following cascaded slave switches. At 1 Hz Fourier frequency, the PSD for the Grandmaster clock is -110 dBc/Hz, and for the following two cascaded Slave switches the PSD degrades by 10 dB and equals -100 dBc/Hz and -90 dBc/Hz at 1 Hz Fourier frequency respectively. The PSD for the last cascaded stage does not exhibit degradation and equals -90 dBc/Hz at 1 Hz Fourier frequency. The increased bandwidth of locking of 70 Hz is exhibited by the servo bump for each cascaded stage.

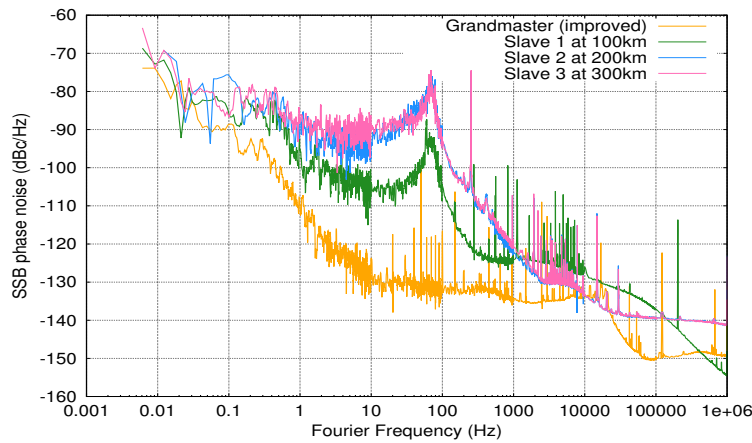


FIGURE 4.15: Phase noise power spectral density comparison for the cascaded stages.

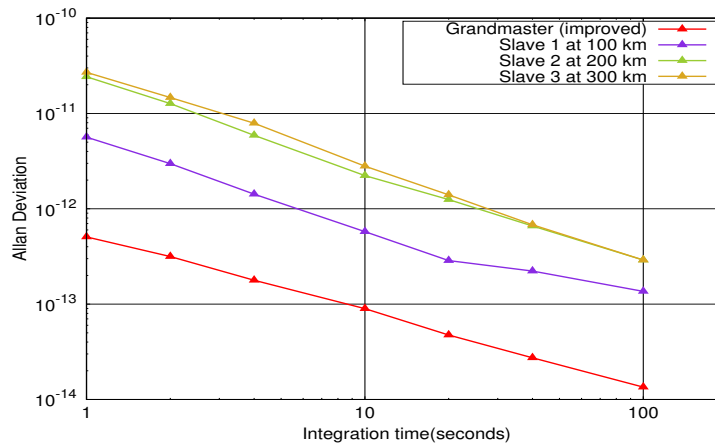


FIGURE 4.16: Allan Deviation (NEQ BW=500 Hz) for the cascaded stages.

Similar performance for the cascaded link can be observed in the time domain depicted by the Allan Deviation (NEQ BW=500 Hz) plot in Fig. 4.16. The Allan Deviation is also measured by Microsemi Phase noise test set 5120A. For the Grandmaster and Slave switches, we divide the frequency stability by the factor 6.25 to calculate their stability at 62.5 MHz. At one second of integration time, we obtain a short term stability of 4.9×10^{-13} for the GM switch and for the following two cascaded stages

at 100 and 200 km, the frequency stability degrades to 5.6×10^{-12} and 2.4×10^{-11} respectively. For the last cascaded stage at 300 km, we obtain a value of 2.7×10^{-11} at one second of integration time.

4.5.3 Frequency and time stability performance

Fig. 4.17 shows the phase data for the last two cascaded stages at 200 and 300 km length link. The peak to peak fluctuations are of about 350 ps for about four days of consecutive measurement.

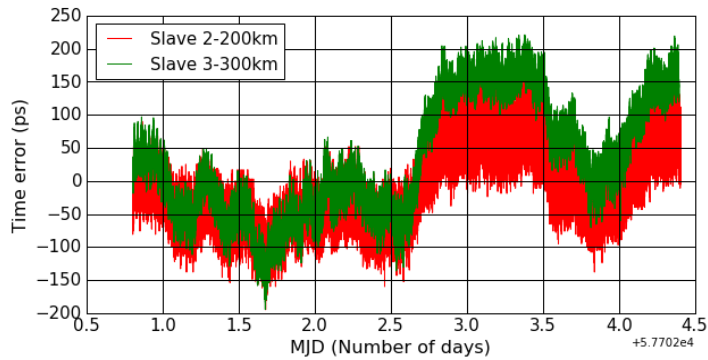


FIGURE 4.17: Phase data for the 200 and 300 km cascaded stages (constant offset removed).

As shown in the experimental setup, the time interval between the the reference PPS and PPS out of the Slave 2 and Slave 3 switches is measured by the time interval counters SR620 and STS201 respectively. The Overlapping Allan Deviation for the last two cascaded stages is presented in Fig. 4.18. At one second of integration time, we obtain a frequency stability of 3.4×10^{-11} and 1.3×10^{-11} for the 200 km and 300 km links respectively. We notice the short term stability at one second of integration for the 300 km link is lower when compared to the 200 km link, which is due to the fact that we utilize a high performance time interval counter with a single shot resolution of 300 fs for the measurement of the last cascaded stage and the evidence is described later in detail in Section 4.5.4.2.

The frequency stability for the 200 km link scales down as τ^{-1} due to the white phase noise and attains the value of 2.3×10^{-15} at 40000 seconds of integration time. For the 300 km link, the frequency stability scales down as τ^{-1} and then degrades due to a bump at 400 seconds of integration time and attains a value of 3.2×10^{-15} at 40000 seconds of integration time. This bump arises due to the effect of the perturbation due to the air conditioning system of the laboratory with a periodicity of about 1000 s due to the temperature variations as observed in [83].

The time stability for the cascaded stages is presented in Fig. 4.19. At one second of integration time, we obtain a time stability of 19 ps and 8 ps for the 200 and

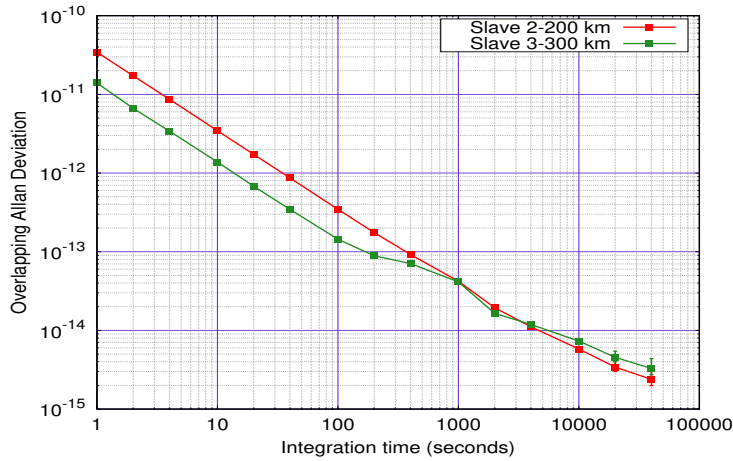


FIGURE 4.18: Overlapping Allan Deviation (calculated from the phase data) for the 200 and 300 km cascaded stages.

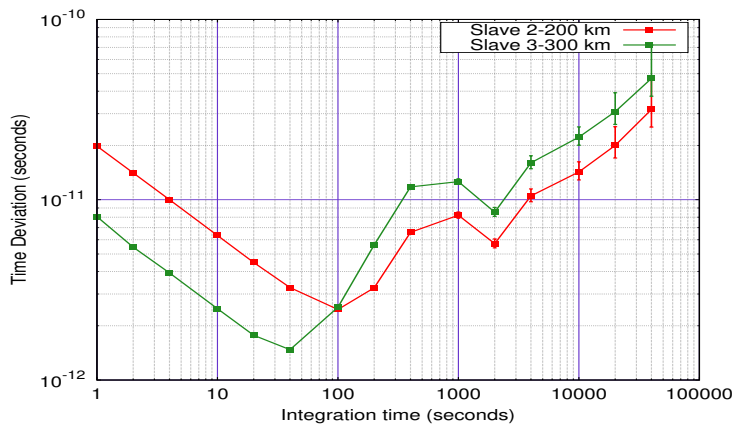


FIGURE 4.19: Time Deviation (calculated from the phase data) for the 200 and 300 km cascaded stages.

300 km links respectively. The time stability averages down due to the white phase noise and reaches a minimum of 2.4 ps at 100 seconds of integration time and 1.4 ps at 40 seconds of integration time for the 200 and 300 km links respectively. The time stability degrades due to the bump caused by the perturbation due to the air conditioning system as described above and attains a value of 20 and 30 ps at 20000 seconds of integration time for the 200 and 300 km links respectively.

4.5.4 Extension to a Cascaded 400 km White Rabbit link

The experimental setup is similar to the one described for the cascaded 300 km link with an addition of a fourth stage. The experimental setup is illustrated in Fig. 4.20. We utilize four White Rabbit switches and a user end receiver of the type WR-ZEN. We build a four span cascaded link of 400 km.

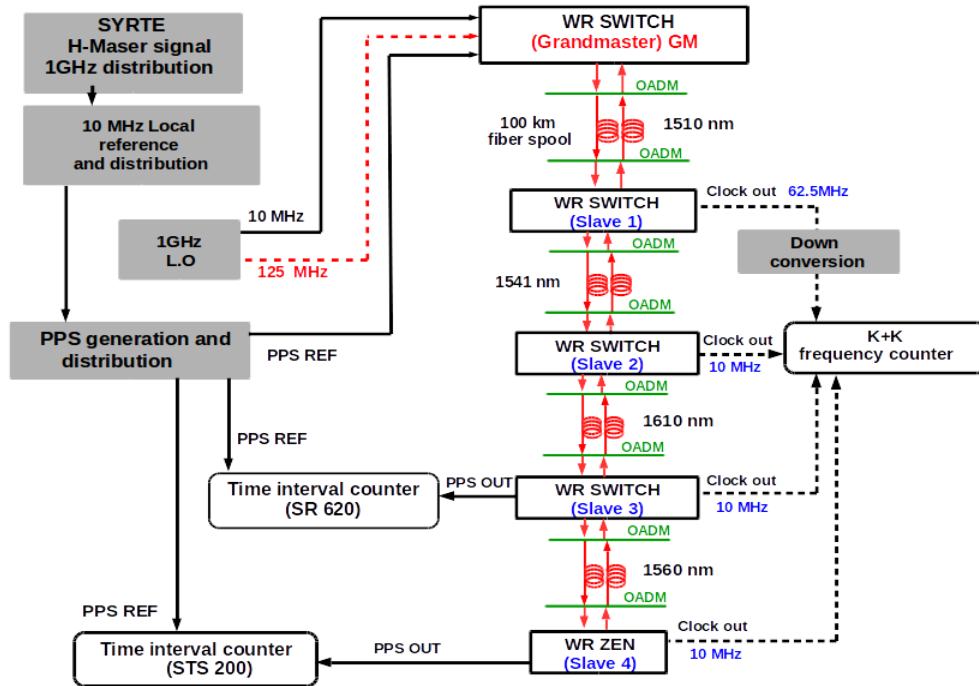


FIGURE 4.20: Experimental setup for the cascaded 400 km White Rabbit link.

The improved Grandmaster switch (GM) is the timing master for this White Rabbit network. Regarding the optical layer, all the Slaves utilize the same 2×100 km uni-directional fiber span and long range CWDM and DWDM SFPs. The first and the second Slaves use 1510 nm and 1541 nm respectively. The third and the fourth span utilize 1610 nm and 1560 nm respectively. An Optical add drop multiplexer (OADM) is used to multiplex and demultiplex the four different wavelengths.

The first Slave clock output is down-converted to 10.5 MHz using the down conversion process described in the last Chapter section 3.2.1. All the other Slaves output a 10 MHz signal. All the Slave clocks were recorded by a dead-time free phase and frequency counter K+K, operated in the Λ mode with one second gate time. It is significant to mention that the Allan Deviation calculated from the frequency data recorded in Λ and Π modes of the K+K frequency counter converge to the same value at longer integration time and thus exhibits good agreement as observed in the case of optical frequency transfer over a hybrid fiber link [87].

The time interval between the PPS reference of the laboratory and the PPS out of the Slave 3 switch and the user end node WR-ZEN was measured by time interval counter SR620 and the high performance STS201 respectively. Both the frequency and phase data were measured simultaneously.

4.5.4.1 Phase locked loop bandwidth optimization

As we basically extended the cascaded 300 km White Rabbit link by cascading further a user end node of the type WR-ZEN, the optimized gain parameters for the first three slaves as described in Section 4.4.3 were considered providing increased bandwidth of locking of 70 Hz. The end user node WR-ZEN utilized default bandwidth of locking of 20 Hz.

4.5.4.2 Frequency stability performance

The subplots of the Fig. 4.21 present the relative frequency deviation for each of the cascaded stages of the 400 km White Rabbit link respectively.

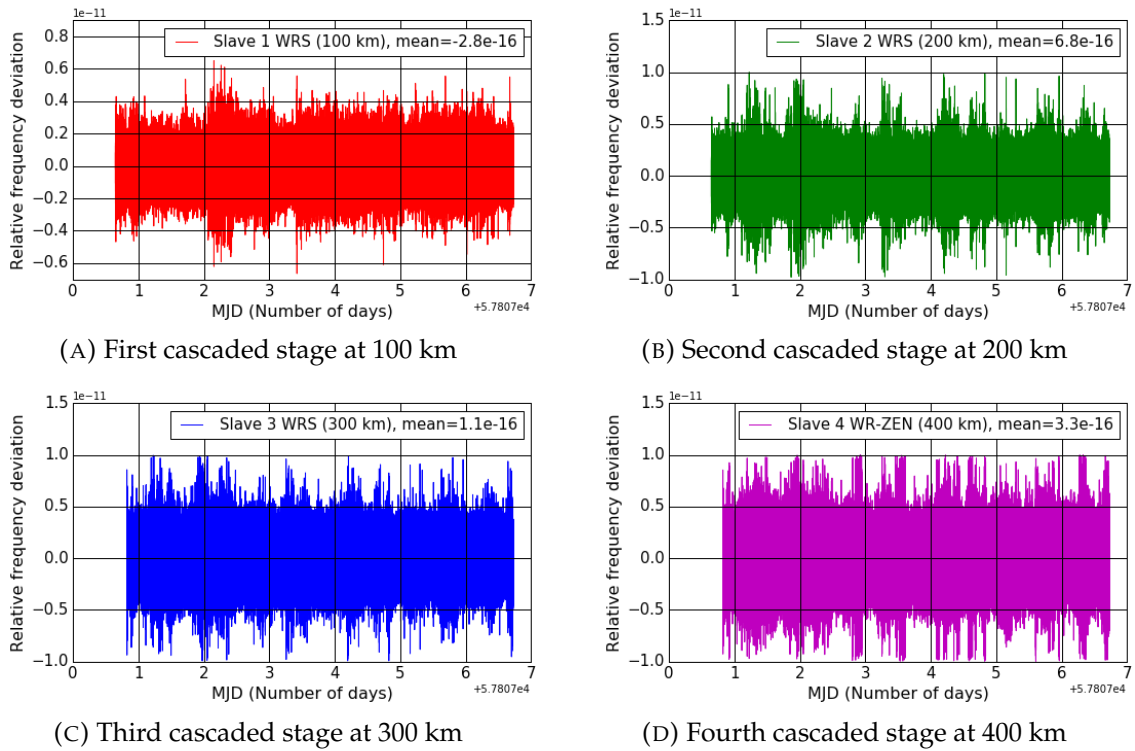


FIGURE 4.21: Relative frequency deviation for each of the cascaded stages of the 400 km cascaded White Rabbit link.

The peak to peak relative frequency deviations for the first cascaded stage are at the level of 1.0×10^{-11} . For the following cascaded stages, the peak to peak relative frequency deviations are at the level of about 2.0×10^{-11} . We assess the accuracy of the frequency transfer by calculating the mean of the relative frequency deviations from the carrier frequency for each of the Slaves. The mean value for each of the cascaded stages is -2.8×10^{-16} , 6.8×10^{-16} , 1.1×10^{-16} and 3.3×10^{-16} respectively. The mean value for each cascaded stage is below the statistical uncertainty of their

corresponding data sets. We did not observe any frequency shift within the statistical uncertainty.

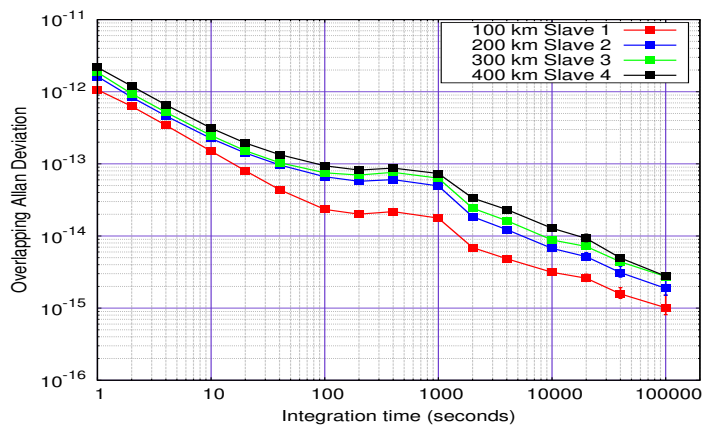


FIGURE 4.22: Overlapping Allan Deviation (calculated from frequency data) for the 400 km cascaded White Rabbit link.

The Overlapping Allan Deviation for the cascaded stages of the 400 km link is presented in Fig. 4.22. For the first span at 100 km, we obtain a frequency stability of 1.0×10^{-12} at one second of integration time. The stability for each consecutive span degrades as the distance of the link increased and we attain a value of 2.1×10^{-12} at one second of integration time for the 400 km link. The stability scales down as τ^{-1} initially due to the white phase noise but then starts to degrade due to a bump at about 300 seconds of integration time. This bump is explained in the Section 4.5.3. At 100000 seconds of integration time, the frequency stability for the 100 km span attains 1.0×10^{-15} and lies in the low region of 1.0×10^{-15} for the consecutive spans.

4.5.4.3 Time stability performance

Fig. 4.23 displays the phase data for the cascaded 300 km stage and for the end user node at 400 km for about seven days of consecutive measurement. The peak to peak fluctuations for both the cascaded stages are of about 900 ps.

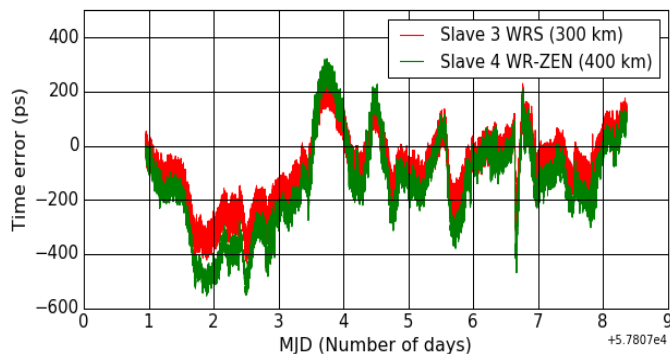


FIGURE 4.23: Phase data for the cascaded 300 km stage and for the user end node at 400 km (constant offset removed).

The time stability performance for the 300 km and 400 km cascaded stages is presented in Fig. 4.24. We obtain a time stability of 13 ps and 8.4 ps at one second of integration time for the 300 km and 400 km links respectively. For the 300 km link, the time stability scales down initially as $\tau^{-1/2}$ due to the white phase noise and attains a minimum value of 2.4 ps at 40 seconds of integration time. For the 400 km link, the time stability reaches a minimum of 1.6 ps at 40 seconds of integration time and then degrades due to a bump at about 400 seconds of integration time. This bump is explained in the Section 4.5.3. The time stability remains below 120 ps for long integration time and attains a value of 57 ps and 77 ps at 40000 seconds of integration time for the 300 km and 400 km links respectively.

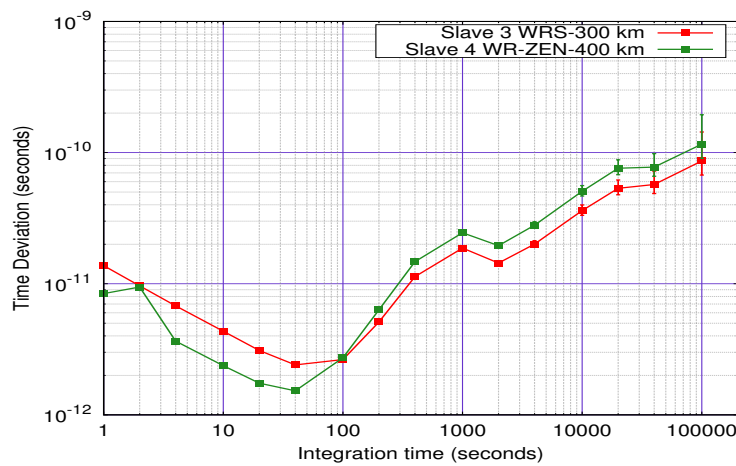


FIGURE 4.24: Time Deviation calculated from the phase data for the 300 km cascaded stage and for the user end node at 400 km.

We perform a test of the short term stability limitation due to the single shot resolution of the time interval counter utilized for the phase measurement. For this test, we record the time interval data for two cases. For the First case, Slave 3 and 4 utilize time interval counters SR620 and STS201 respectively for phase measurements and the second case is the counter swapping where these two counters are swapped for the Slaves while keeping rest of the setup similar to the first case.

Fig. 4.25 displays the phase data recorded for the two cases. The bottom figure displays the data for the counter swapped case. We clearly notice from these two figures that the thickness of the trace for the same Slave device is thinner when the high performance TIC STS201 is utilized for the phase measurement.

Fig. 4.26 displays the Overlapping Allan deviation for the Slave 3 and 4 for the two cases. We observe that the short term stability performance for each of the Slaves is better by a factor of 2 when the high performance counter STS201 is utilized. For the long term performance (> 1000 seconds of integration time), we observe that the shorter link has better performance than the longer one which is as expected.

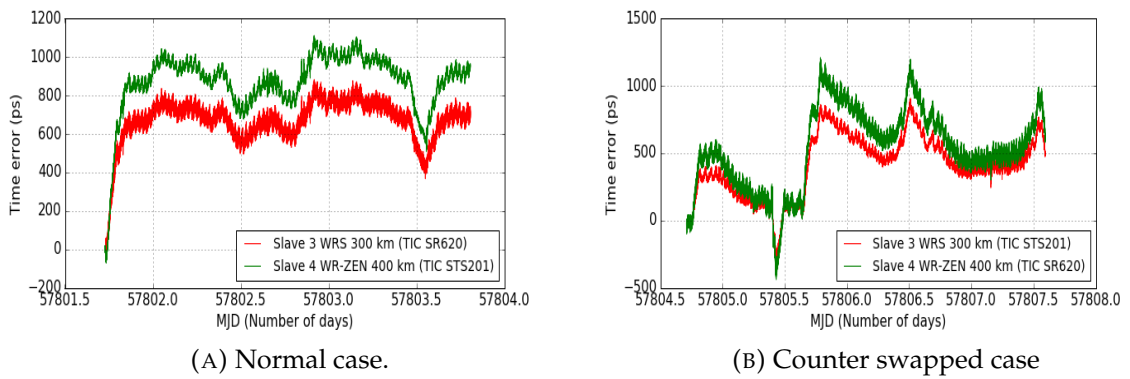


FIGURE 4.25: Phase data measurement for the 300 and 400 km cascaded link for the test of short term stability limitation.

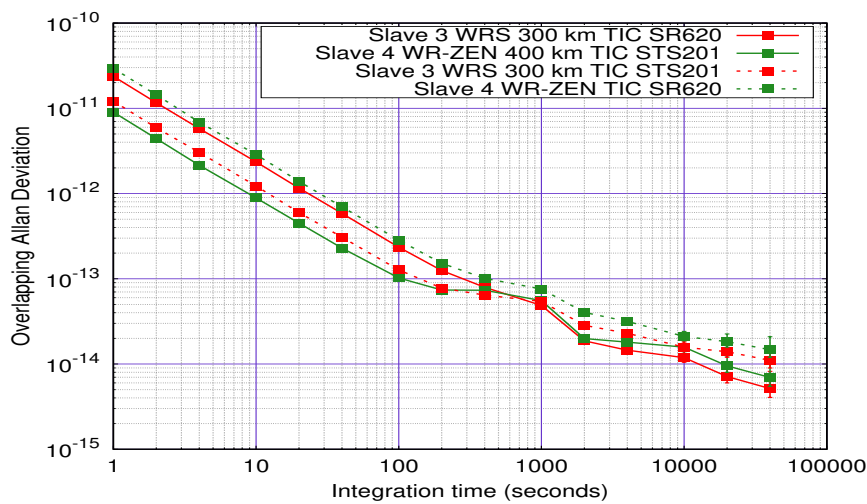


FIGURE 4.26: Comparison of Overlapping Allan Deviation (calculated from phase data) for the 300 and 400 km cascaded stages for counter swapped case.

The same effect is observed in the time stability comparison displayed in Fig. 4.27. For Slave 3, the time stability (solid and dashed red trace) at one second of integration time drops down from 13 ps to 7 ps for the high performance counter. We observe the same for Slave 4, the time stability drops down from 16 ps to 5 ps at one second of integration for the high performance counter. This clearly illustrates that the measured short term stability depends on the type of the time interval counter used (the short term stability is limited by the time interval counter and not by the WR link). The noise floor of the instrument used to assess the short term stability is not negligible any more as illustrated in Fig. 4.28 and is described below. This results in a stringent condition for the end user.

It is very interesting to compare the time stability performance calculated from the frequency data and the phase data. Fig. 4.28 shows the time stability for the cascaded 400 km link calculated from frequency and phase data along with the noise

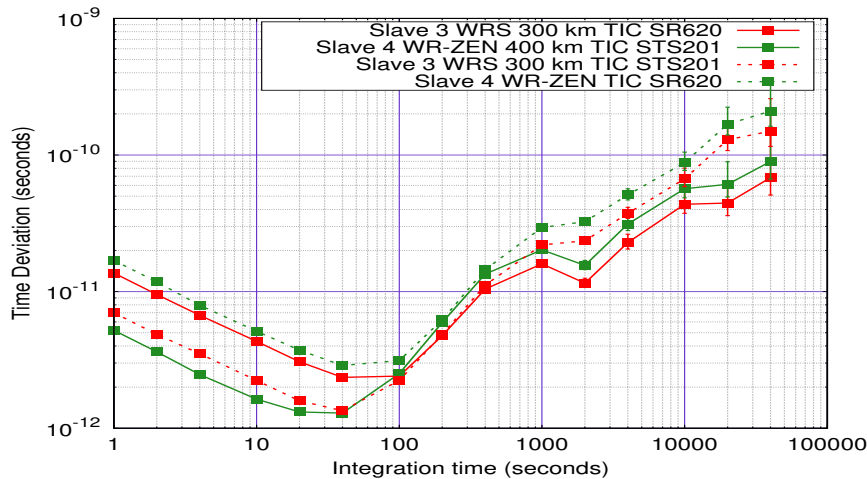


FIGURE 4.27: Comparison of Time Deviation (calculated from phase data) for the 300 and 400 km cascaded stages for counter swapped case.

floor for the PPS measurement. The noise floor of the PPS measurement is the limitation due to the PPS jitter arising from the PPS generation and distribution in the laboratory as described in the last Chapter, Section 3.3.2. In case of the time stability calculated from the frequency data, we actually observe that the time stability at one second of integration time is lower by a factor of 8 when compared with that of the phase data. This is due to the fact that the time stability calculated from phase data is limited by the noise floor due to the PPS generation and distribution in the laboratory. Also it is important to remember that we are not limited by the measuring instrument as we utilize a high performance time interval counter STS201 with a single shot resolution of 300 fs for the 400 km link. For integration time from 40 seconds onwards, we observe good agreement for the time stability performance calculated from frequency data and phase data.

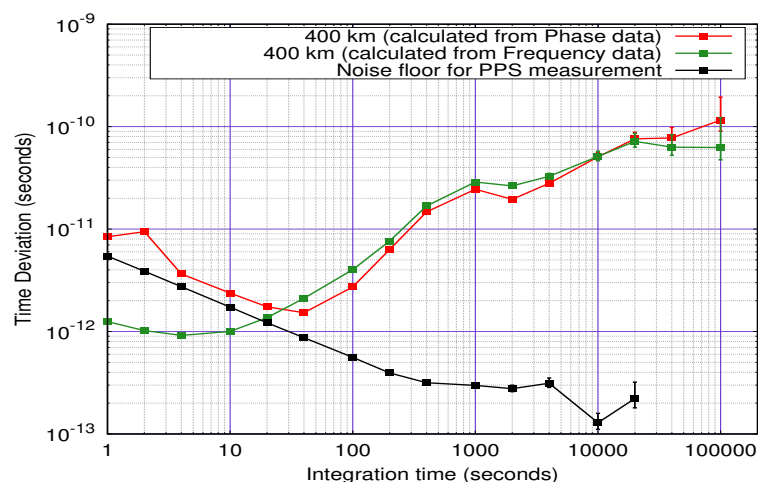


FIGURE 4.28: Time stability comparison for the frequency data and phase data for the 400 km cascaded link.

4.6 A long haul telecommunication span White Rabbit link

With an aim of time dissemination to multiple users using the active telecommunication networks, we further focused on realizing a realistic long haul telecommunication span White Rabbit link of 500 km using the "Cascaded approach" along with the DWDM technique.

4.6.1 Experimental setup

In the last section, we described a cascaded 400 km White Rabbit link by utilizing a uni-directional 100 km fiber span multiple times. We moved one step further by extending the 100 km span to 125 km to build a set of experiment with multiples of 125 km so that we could easily scale to 500 km. But the extension from 100 km to 125 km span was not easy as we faced the problem of Optical power attenuation because the long range SFPs (ranging from 100 to 130 km) were at the edge of the optical receiver sensitivity. Thus a thorough cleaning of the Optical fibers, Optical fiber connectors and SFPs was done. In addition to this, the setup was simplified in order to reduce the number of fiber patch cords resulting in less number of fiber connectors thus reducing optical losses.

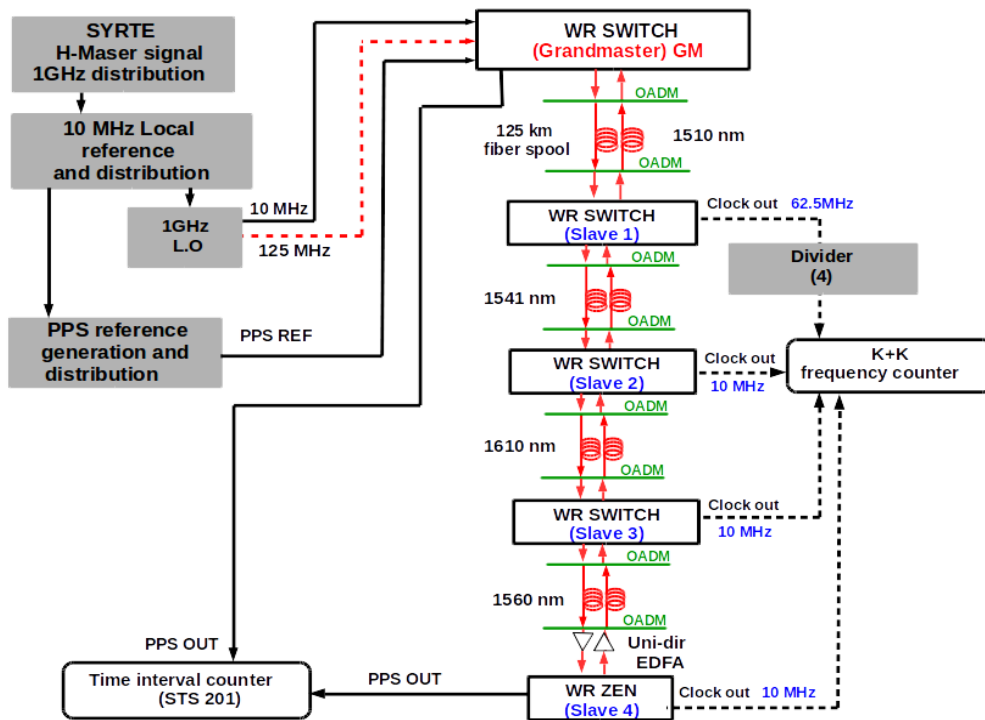


FIGURE 4.29: Experimental setup for the cascaded 500 km White Rabbit link.

The experimental setup is illustrated in Fig. 4.29. We build the first four span cascaded White rabbit link of 500 km [88]. The span utilized a uni-directional setup consisting of 2×125 km fiber spools (consisting in total of ten 25 km fiber spools).

We utilized four White Rabbit switches and a user end receiver of the type WR-ZEN. The improved Grandmaster switch (GM) is the timing master for the White Rabbit network. Regarding the optical layer, all the Slaves utilized the same 2×125 km uni-directional fiber span and long range CWDM and DWDM SFPs. The first and the second Slaves used 1510 nm and 1541 nm respectively. The third and the fourth span utilized 1610 nm and 1560 nm respectively. An Optical add drop multiplexer (OADM) was used to multiplex and demultiplex the four different wavelengths. For the last cascaded stage WR-ZEN, we utilized two uni-directional EDFAs (Erbium Doped Fiber Amplifier) to compensate for the strong losses.

All the Slaves output a 10 MHz signal except for the first Slave switch with a clock output at 62.5 MHz, which was divided by 4 for measurement by the K+K frequency counter. All the Slave clocks are recorded by a dead-time free phase and frequency counter K+K, operated in the Λ mode with one second gate time. The time interval between the PPS out of the Grandmaster WRS and the PPS out of the Slave 4 WR-ZEN was measured by the high performance STS201 respectively. The temperature of the experimental room was measured with a thermistor and was recorded with a datalogger Agilent 34972A. The wavelength of one of the SFPs at 1541 nm was measured by the Optical Spectrum Analyzer AQ6370C using a resolution bandwidth of 20 pm. All the measurements were done simultaneously.

We utilized increased bandwidth of locking of 70 Hz as for the cascaded 400 km link. In addition, we also utilized increased PTP rate of 14 Hz (as described in last chapter, section 3.7) between the Master and their corresponding Slaves.

4.6.2 Frequency stability performance

The subplots of the Fig. 4.30 present the relative frequency deviation for each of the cascaded stages of the 500 km White Rabbit link respectively. The peak to peak relative frequency deviations for the first cascaded stage are at the level less than 0.8×10^{-11} . For the following cascaded stages, the peak to peak relative frequency deviations are at the level of about 1.0×10^{-11} .

We assess the accuracy of the frequency transfer by calculating the mean of the relative frequency deviations from the carrier frequency for each of the Slaves. The mean value for each of the cascaded stages is -1.1×10^{-17} , -4.0×10^{-17} , -9.2×10^{-17} and -1.4×10^{-16} respectively. The mean value for each cascaded stage is below the statistical uncertainty of their corresponding data sets. We did not observe any frequency shift within the statistical uncertainty.

The Allan Deviation for the four span cascaded 500 km link is presented in Fig. 4.31. We obtain a frequency stability of 1×10^{-12} at one second of integration time. The stability for each span degrades as the length of the link increases

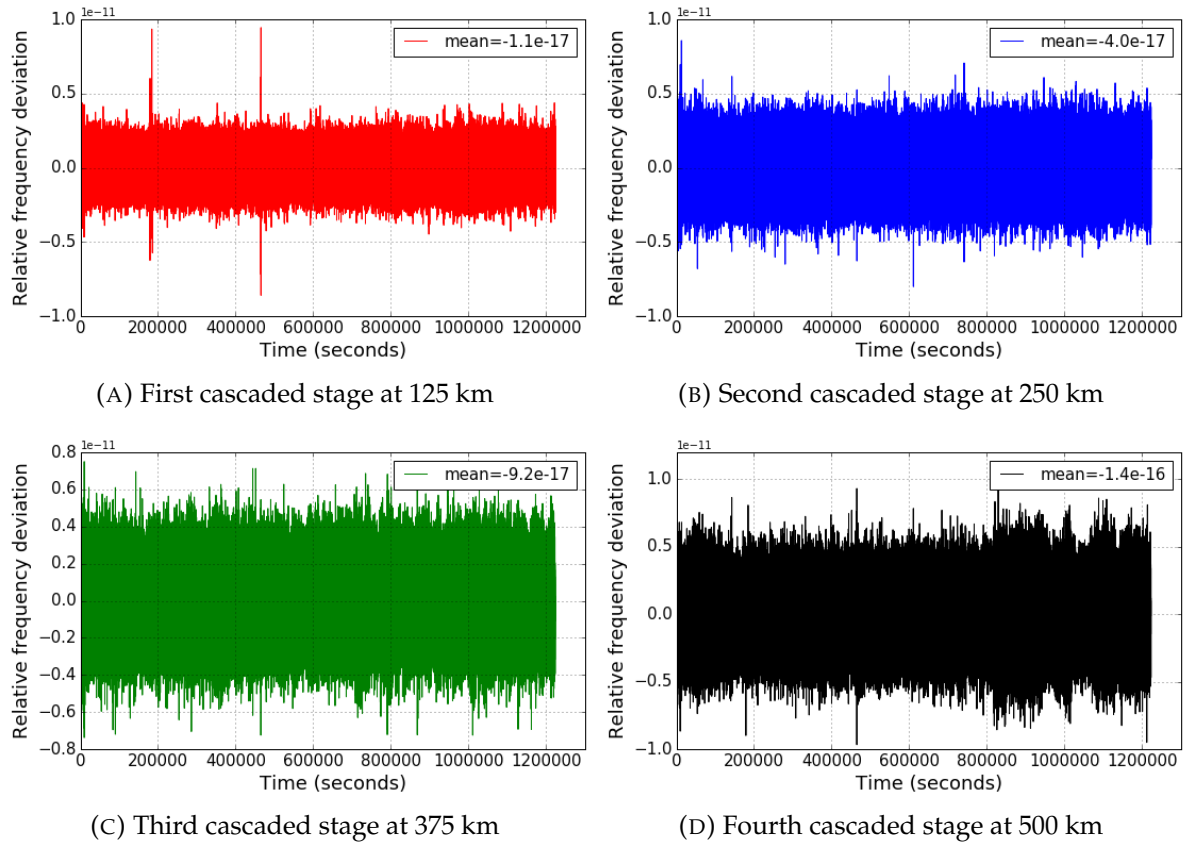


FIGURE 4.30: Relative frequency deviation for each of the cascaded stages of the 500 km White Rabbit link with increased PTP rate and increased BW of locking.

by 125 km each time, and we attain a stability of 2×10^{-12} at one second of integration time for the 500 km link. For each span, the stability degrades by a factor a little smaller than $\sqrt{2}$. The stability scales down as τ^{-1} in the beginning due to the white phase noise and then starts to degrade due to a bump at 20000 seconds of integration time. This bump arises due to the fiber thermal noise as described in the Section 4.2.4. The degradation in the frequency stability is due to the common temperature excitation of all the cascaded stages. At 200000 seconds of integration time, the frequency stability for the 125 km attains a value of 8×10^{-16} and lies in the low region of 1×10^{-15} for the consecutive stages. This fiber thermal noise is expected to be greatly reduced by a factor of five for the implementation on active telecommunication networks where the fiber is buried underground and thus experiences mild temperature fluctuations.

We also compare the frequency stability performance of the cascaded 500 km link with that of a good quality Oscilloquartz GPS receiver 5201. We observe similar short term stability of 2×10^{-12} at one second of integration time, but at long integration time of 1000 seconds our cascaded link exhibits better performance by two

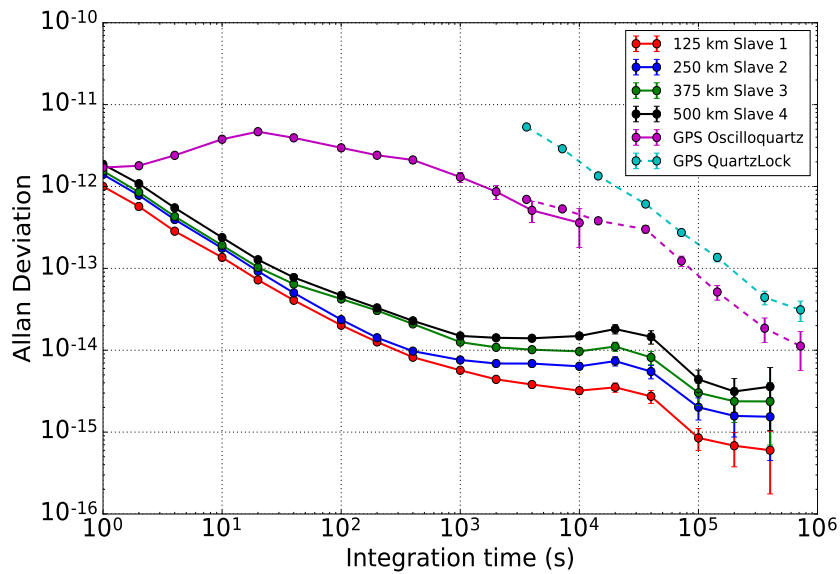


FIGURE 4.31: Allan Deviation for the 500 km cascaded White Rabbit link and comparison with different GPS receivers. Solid line depicts stability calculated from Frequency data, Dashed line depicts stability calculated from Phase data.

orders of magnitude. We also compare the performance with the widely used QuartzLock E8000 GPS disciplined frequency and time standard and we observe that at long term (from 1000 seconds of integration time) our cascaded link has better performance by almost two orders of magnitude. Thus, it clearly exhibits that White Rabbit technology surpasses the performance of commercial GPS systems.

From Fig. 4.31 we notice that WR attains a frequency stability of about 2×10^{-14} in about one hour of measurement time whereas the GPS systems reach the same level of performance after averaging down for more than a month. Such impressive short term performance of WR would be greatly advantageous for the application of Certification of local oscillators, with the user benefiting from just few hours of calibration time.

4.6.3 Time stability performance

The time interval data for the 500 km stage is presented as the blue trace in Fig. 4.32 for fifteen days of consecutive measurement. The peak to peak fluctuations are of about 2.5 ns. These time fluctuations show some limitation for the accuracy and for the stability performance.

Fig. 4.32 also displays the temperature fluctuations of about 2 K over the same

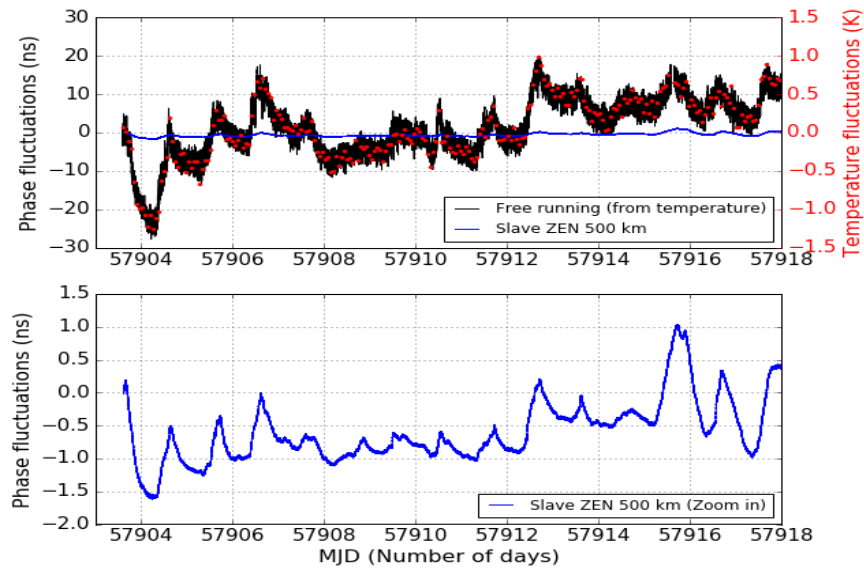


FIGURE 4.32: Top: Free running phase fluctuations calculated from the temperature fluctuations of the experimental room (constant offset removed for both), and the Slave ZEN phase fluctuations (blue trace). The blue trace is zoomed in the bottom figure. We observe a compression factor of about 20.

fifteen days of measurement. As described in Section 4.2.4, we calculate the free running phase fluctuations from the temperature fluctuations for a link length of 500 km and they are presented as the black trace in Fig. 4.32. We observe peak to peak free running phase fluctuations of about 45 ns over fifteen days of measurement.

We again clearly observe the correlation between the phase fluctuations of the Slave ZEN and the temperature fluctuations. We observe a periodic modulation in the phase data due to the temperature fluctuations acting on the optical length of the fiber spools (as described in the Section 4.2.4). The free running phase fluctuations are compressed approximately by a factor of 20. This is four times the compression factor for the 100 km link.

The time deviation plot is presented in Fig. 4.33 as the red trace. The time transfer stability for the 500 km cascaded link is 5 ps at one second of integration time and reaches a minimum of 1.2 ps at 20 seconds of integration time. The time stability degrades for longer averaging times and is limited due to the fiber thermal noise but still remains below the ns level.

We compare our lab experiment with two infield applications using the active telecommunication networks. The first one is a 950 km WR link by the Finnish metrology laboratory VTT between Espoo and Kajani in Finland [43], where the time stability has been scaled down to 500 km for easy comparison. The second one is a

540 km link by V. Smotlacha and co-workers for time transfer between metrology laboratories of Prague and Vienna (CESNET to BEV link) [89].

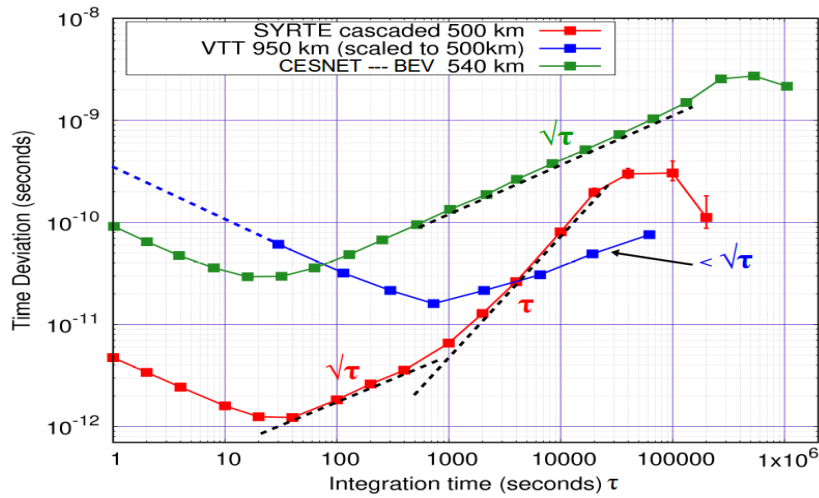


FIGURE 4.33: Time stability (calculated from phase data) for the cascaded 500 km White Rabbit link and comparison with infield applications.

For the CESNET to BEV link, the short term stability is limited by the link with significant contribution from the time interval counters (≈ 53 ps) and the actual link contribution would be approximately equal to 8.6 ps. The $\sqrt{\tau}$ behavior after 200 seconds of integration time is due to the clocks. For the VTT experiment data, the clock difference between UTC(MIKE) and HP 5071A (Cs clock) was removed, and the data represents the difference between the WR PPS and GPS-PPP. The published data begins at 200 seconds of integration time and the short term noise of the fiber is not revealed.

In comparison with these two infield applications, we have improved the time stability at one second of integration time by one to two orders of magnitude. For long term, the CESNET to BEV link exhibits the clock properties. The VTT link has a behavior better than $\sqrt{\tau}$, which may be due to the double difference procedure (WR-PPS - GPS-PPP) they follow. In our case, we observe a $\sqrt{\tau}$ behavior from 20 to 1000 seconds of integration time and then a τ slope behavior. We believe this is due to the our experimental conditions using fiber spools which experience coherent periodic excitation due to temperature in the laboratory. For long integration time, we expect to observe similar behavior as others if implemented on telecommunication networks.

Fig. 4.34 displays the time stability for each of the cascaded stages calculated from the frequency data described in the above section. For the first span at 125 km, we observe a time stability of 600 fs at one second of integration time and for the consecutive spans the time stability degrades as the length of the link increases and

attains a value of 1 ps at one second of integration time for the 500 km link. The time stability reaches a minimum of 400 fs at 10 seconds of integration time for the 125 km link and degrades by a factor of 1.2 approximately and attains a minimum of 700 fs at 10 seconds of integration time for the 500 km link. The rapid increase of the time stability is due to the common temperature excitation of all the cascaded stages. Comparing Fig. 4.33 and Fig. 4.34, we again observe that the time stability performance calculated from the frequency data is lower when compared to the time stability calculated from the phase data (as described in the Section 4.4.9), and it is better by a factor of 5 for the 500 km link.

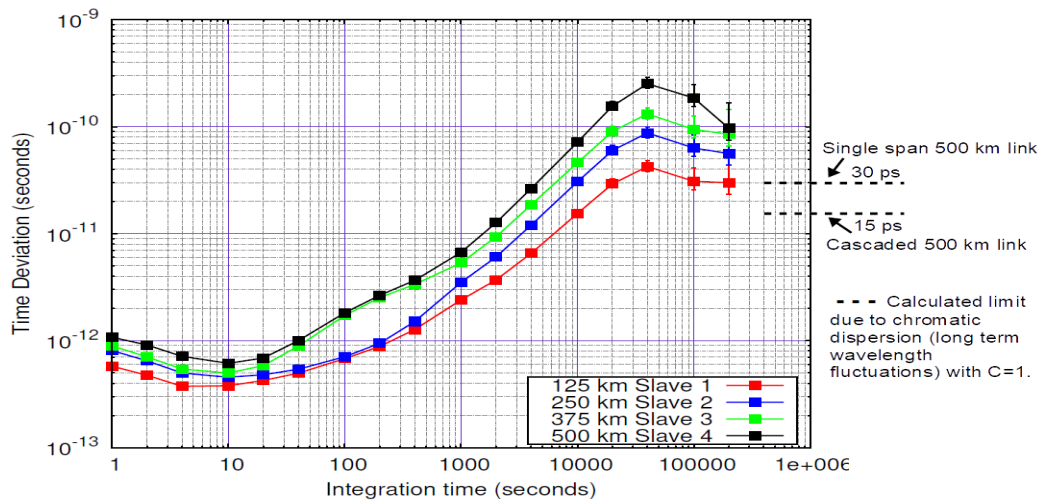


FIGURE 4.34: Time stability calculated from the frequency data for the cascaded 500 km White Rabbit link.

We were also interested to study the effect of long term wavelength fluctuations on the time stability performance. Fig. 4.35 displays the wavelength fluctuations of one of the SFPs at 1541 nm recorded simultaneously. We observe peak to peak fluctuations of 12 pm (1.5 GHz) and about 5 pm on average over fifteen days of consecutive measurement.

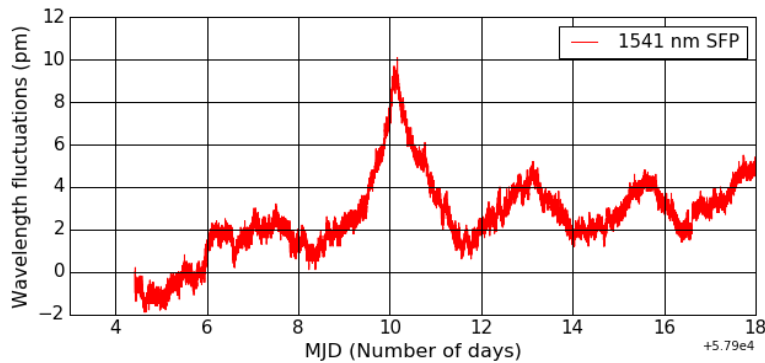


FIGURE 4.35: Wavelength fluctuations for the 1541 nm SFP (constant offset removed).

For the 500 km cascaded link, the magnitude of these long term wavelength fluctuations is calculated as $17 \text{ ps} \times 0.005 \times 125 \times \sqrt{N} \times \sqrt{2} / 2/C = 15/C \text{ ps}$ at about one day of integration time, where $N=4$ is the number of cascaded stages and C is the compression factor. This is a small contribution compared to fiber noise and at long term fiber noise will be dominant. For comparison, the long term wavelength contribution for a single span link of 500 km will be 4 times that of a 125 km link, as the effect of chromatic dispersion is proportional to length for a single-span link. Therefore, this effect will be 2 times larger than for the cascaded link, i.e. $30/C \text{ ps}$ at one day. These values are displayed in Fig. 4.34, for a compression factor $C = 1$.

4.6.4 Effect of reduced PTP rate

We had studied the effect of increased PTP rate on the frequency stability performance calculated from the phase data of a Slave switch in the last Chapter, Section 3.7 and found that there was no improvement in the performance.

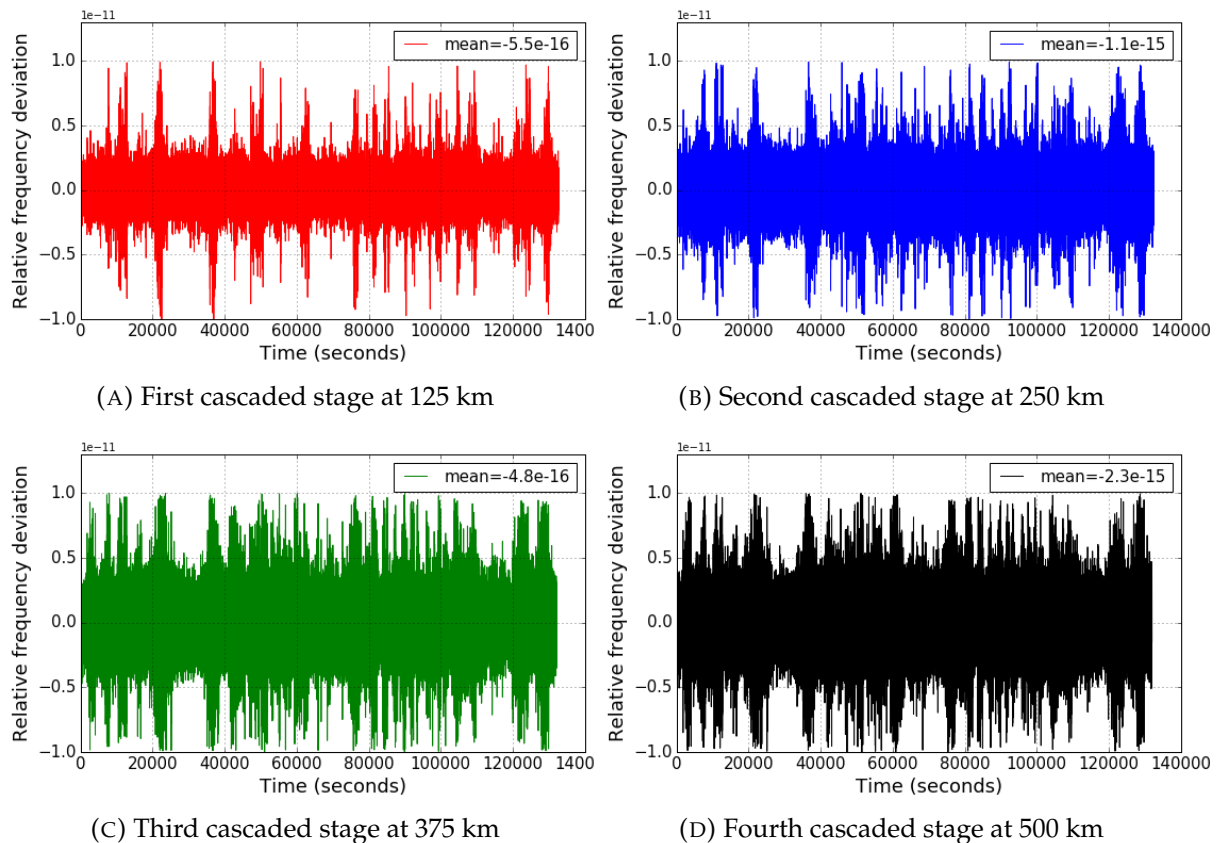


FIGURE 4.36: Relative frequency deviation for each of the cascaded stages of the 500 km White Rabbit link with default PTP rate.

We further wanted to investigate the effect of increased PTP rate by measuring the Slave clock signals. So we repeated the cascaded 500 km experiment with default PTP rate of 1 Hz for the Grandmaster and the consecutive cascaded stages

along with increased bandwidth of locking of 70 Hz for the Slaves.

Fig. 4.36 presents the relative frequency deviation for the cascaded stages of the 500 km link with default PTP rate. We compare the relative frequency deviations for the last stage WR-ZEN at 500 km with the one for increased rate in Fig. 4.30d. With default PTP rate we observe some spikes which are not present with the increased PTP rate. This clearly illustrates the significance of PTP bandwidth as the quality of the syntonization between the Master and the Slave depends on the rate of the PTP message exchange (as described in the last Chapter Section 3.7). A low quality clock signal would require a high PTP bandwidth. Thus, for the performance improvement, the Slave switch not only requires optimization of the PLL locking bandwidth but also requires increased PTP bandwidth.

We assess the accuracy of the frequency transfer by calculating the mean of the relative frequency deviations from the carrier frequency for each of the Slaves. The mean value for each of the cascaded stages is -5.5×10^{-16} , -1.1×10^{-15} , -4.8×10^{-16} and -2.3×10^{-15} respectively. The mean value for each cascaded stage is below the statistical uncertainty of their corresponding data sets. We did not observe any frequency shift within the statistical uncertainty. It is noticeable that the mean deviation to zero is about 50 times and 16 times higher with default PTP rate for the 125 km and 500 km stages respectively.

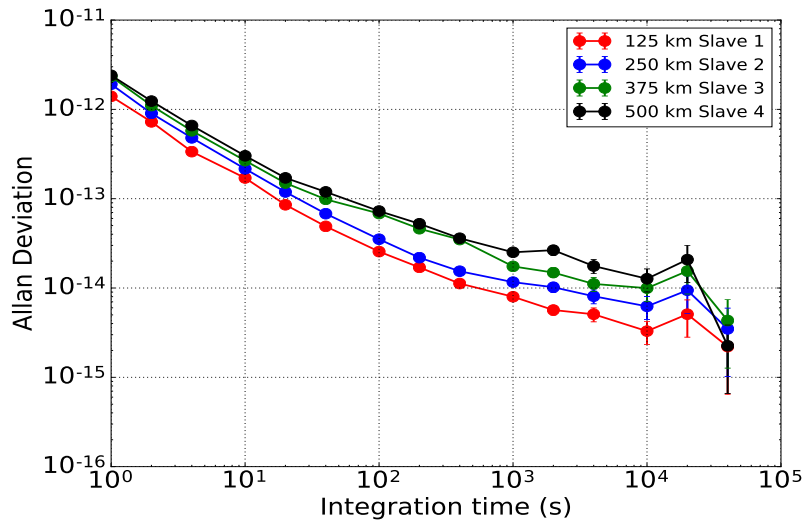


FIGURE 4.37: Allan Deviation (calculated from frequency data) for the 500 km cascaded White Rabbit link for default PTP rate.

Fig. 4.37 presents the Allan Deviation for the cascaded 500 km with default PTP rate. We compare the frequency stability with that of the increased PTP rate illustrated in Fig. 4.31. We observe that the frequency stability at one second of integration time for the 125 km span degrades for the default PTP case by a factor of 1.5.

We observe similar behaviour for the consecutive spans. It is significant to mention that we are able to observe the effect of increased PTP rate on the frequency stability performance calculated by the frequency data, because the frequency stability calculated from the time interval data is limited by the jitter due to PPS generation and distribution in the laboratory.

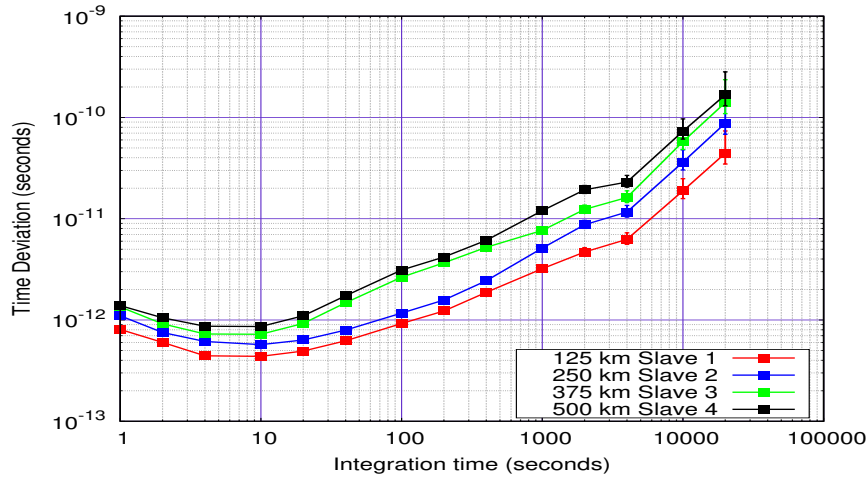


FIGURE 4.38: Time stability calculated from the frequency data for the cascaded 500 km White Rabbit link for default PTP rate.

The time stability calculated from the frequency data for the default PTP rate is presented in Fig. 4.38. Upon comparison with the time stability for the increased PTP rate (Fig. 4.34), we observe a degradation by a factor of 1.3 at one second of integration time for the 125 km span. We observe similar behavior for the consecutive stages. We conclude that increased PTP rate results in better performance.

4.6.5 Effect of reduced Bandwidth of locking

Next, we decided to reduce the bandwidth of locking to the default value of 20 Hz to study the performance of the cascaded 500 km WR link with a complete default configuration (default PTP rate and default bandwidth of locking).

We repeat the frequency measurement of the cascaded 500 km link. Fig. 4.39 presents the relative frequency deviation for the cascaded stages of the 500 km link with default bandwidth of locking. The mean value for each of the cascaded stages is -1.2×10^{-15} , -2.9×10^{-15} , -3.5×10^{-15} and -4.0×10^{-15} respectively. The mean value for each cascaded stage is below the statistical uncertainty of their corresponding data sets. We did not observe any frequency shift within the statistical uncertainty. It is noticeable that the mean deviation to zero is about 100 times and 28 times higher with default bandwidth of locking and default PTP rate for the 125 km and 500 km stages respectively.

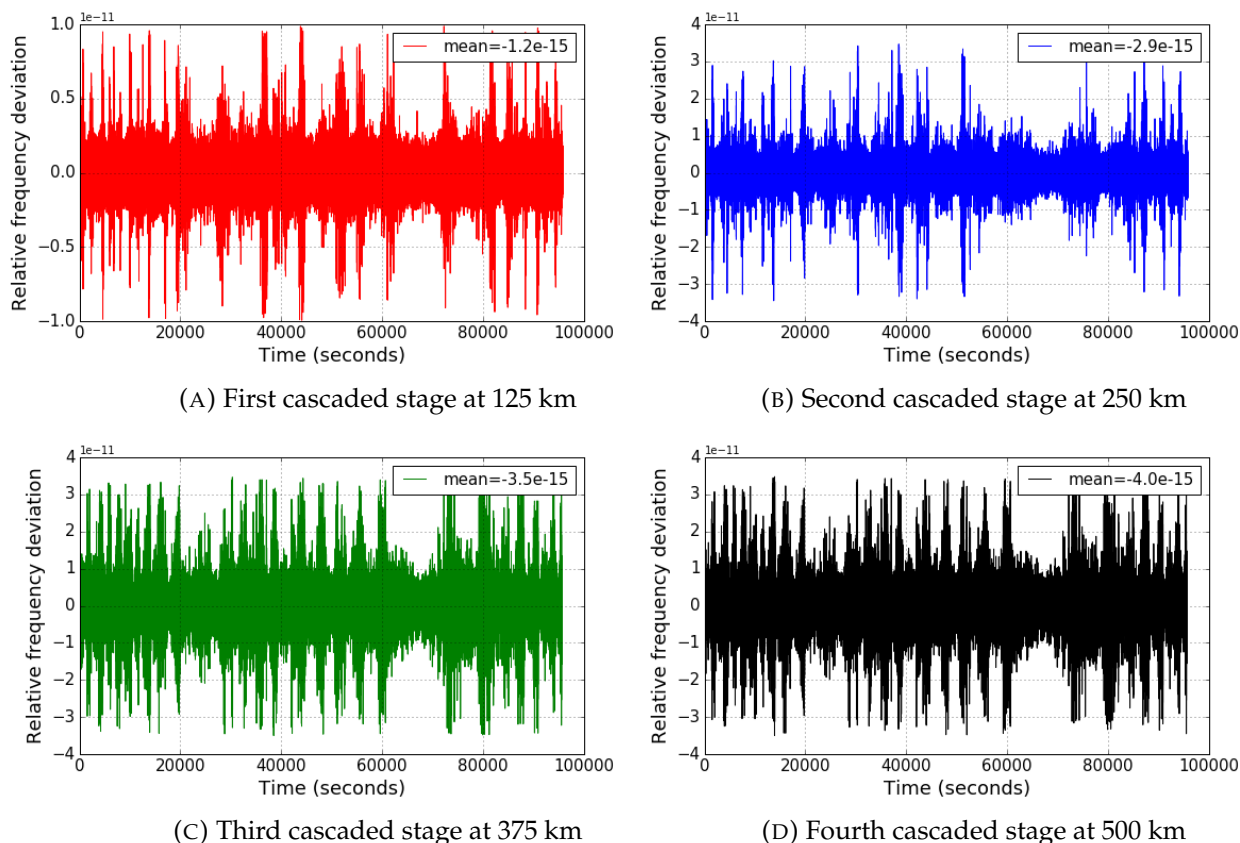


FIGURE 4.39: Relative frequency deviation for each of the cascaded stages of the 500 km White Rabbit link with default bandwidth of locking and default PTP rate.

We compare these relative frequency deviation with that for increased values presented in Fig. 4.30, and we observe that for each cascaded stage, the relative frequency deviation with default values increases by a factor of 2 approximately. This is clearly visible by observing the thickness of the relative frequency deviation trace for both the cases, which doubles for the default values exhibiting less compression of the noise. With reduced PTP rate, we observe the appearance of spikes in the relative frequency deviation data (Fig. 4.36) but the thickness of the trace (noise) is similar to the one with increased PTP rate.

Fig. 4.40 displays the Allan deviation for the cascaded 500 km with default bandwidth of locking and default PTP rate. When compared with the increased values, we notice that for the 125 km span the frequency stability at one second of integration time degrades by a factor of 1.5 and for the consecutive span, the frequency stability degrades by a factor of 1.7. For the last two cascaded stages, the frequency stability at one second of integration time degrades by a factor of 2.2.

The time stability calculated from the frequency data for the default bandwidth of locking is presented in Fig. 4.41. Upon comparison with the time stability for the

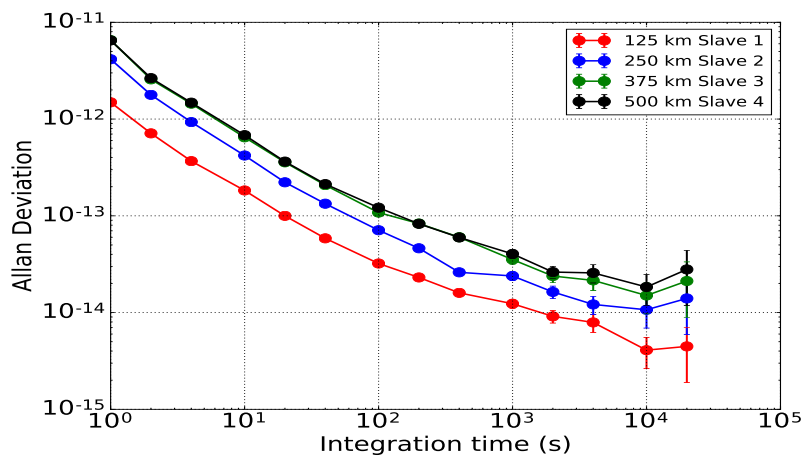


FIGURE 4.40: Allan Deviation (calculated from frequency data) for the 500 km cascaded White Rabbit link for default bandwidth of locking along with default PTP rate.

increased bandwidth of locking (Fig. 4.34), we observe a degradation by a factor of 1.4 at one second of integration time for the 125 km span. For the next stage, we observe a degradation by a factor of 2.5 at one second of integration time. For the third and fourth cascaded stages, we observe a degradation by a factor of about 3.5 at one second of integration time.

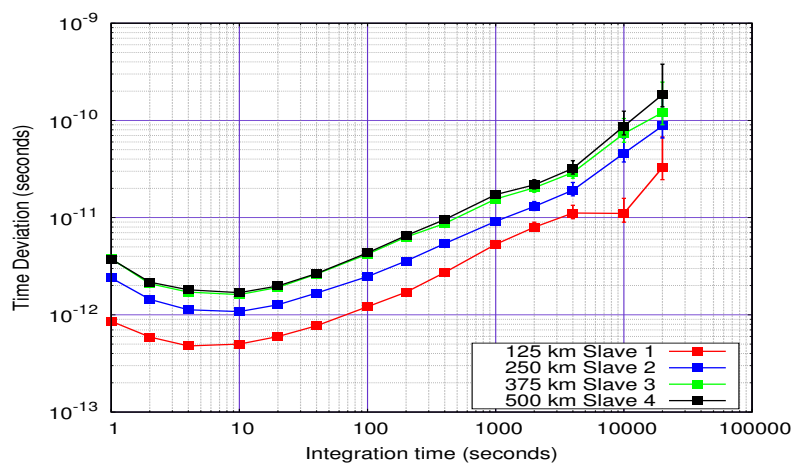


FIGURE 4.41: Time stability calculated from the frequency data for the cascaded 500 km White Rabbit link for default bandwidth of locking along with default PTP rate.

We also calculate the time stability from the time interval data measured simultaneously for the end node WR-ZEN with default configuration for the cascaded 500 km link. In Fig. 4.42, we compare with the time stability for increased values (from Fig. 4.33). We observe for the default configuration, a degradation in the short term stability by a factor of 2 at one second of integration time and from 1000 seconds onwards they both exhibit similar behavior.

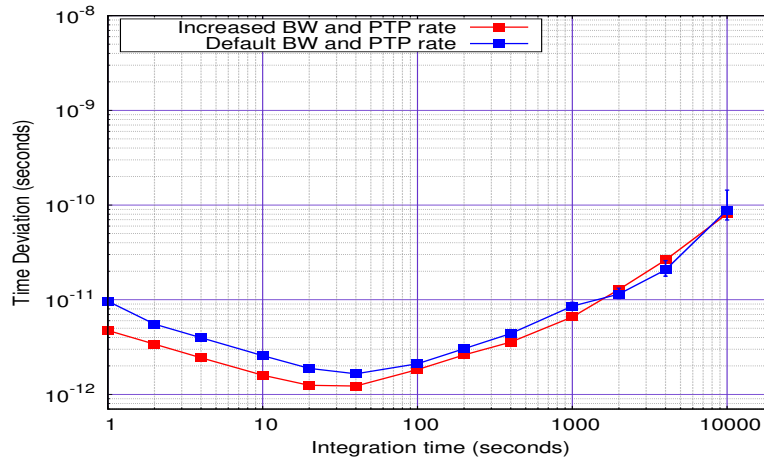


FIGURE 4.42: Time stability comparison calculated from phase data for the cascaded 500 km White Rabbit link for default bandwidth of locking along with default PTP rate.

4.7 A multi user 4x125 km White Rabbit link

4.7.1 Experimental Setup

We build a multi-user star configuration setup with three White Rabbit Slave switches and a WR node ZEN synchronized to the Grandmaster. The setup is similar to the cascaded 500 km link except that each of the Slaves is directly synchronized to the Grandmaster switch as displayed in Fig. 4.43. The clock output of each of the Slaves is measured by the K+K counter as described in Section 4.6.1.

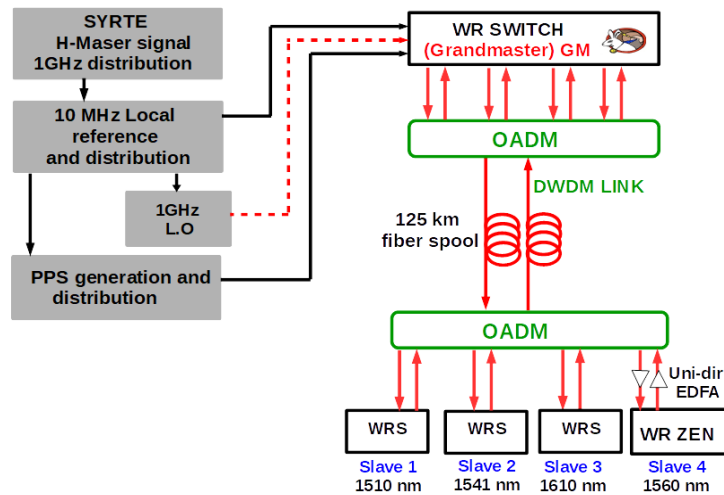


FIGURE 4.43: Experimental setup for the multi user 125 km White Rabbit link.

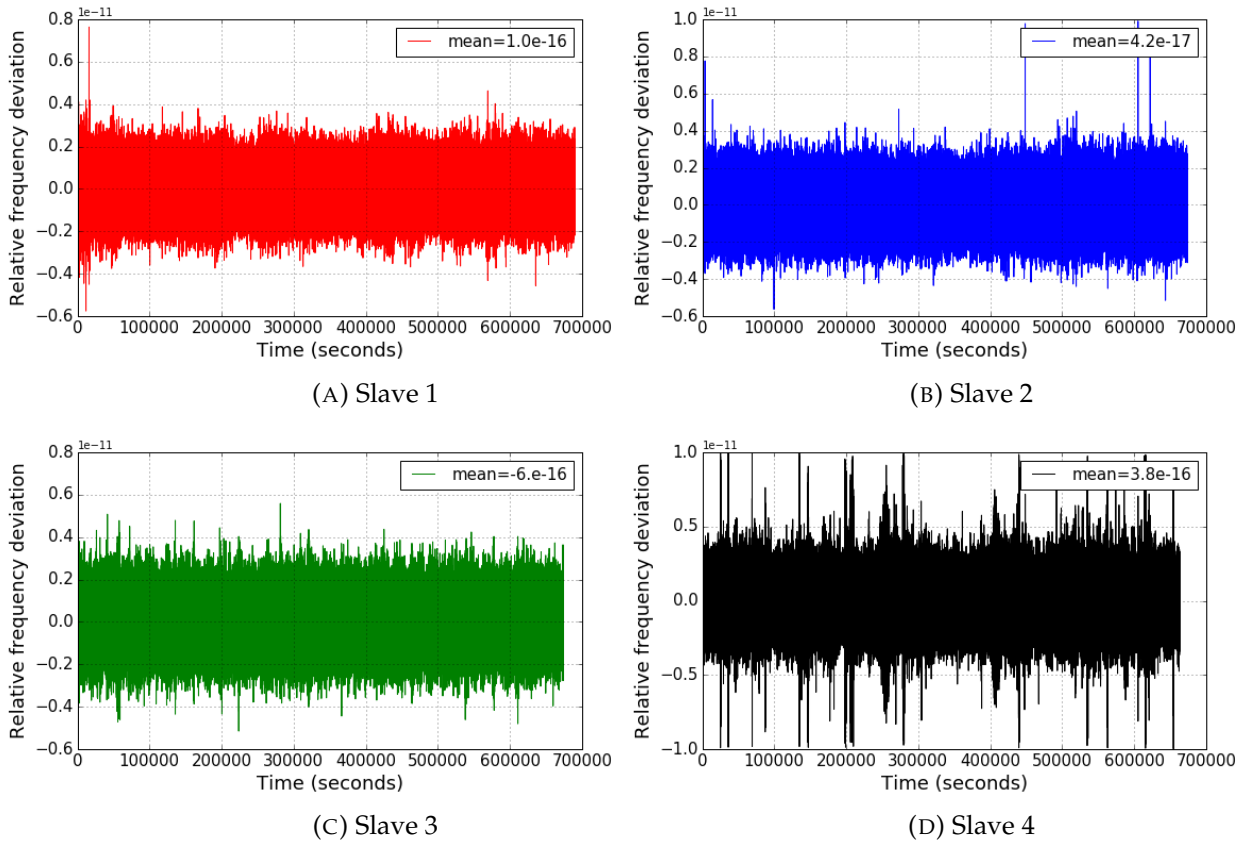


FIGURE 4.44: Relative frequency deviation for each of the Slaves at 125 km

4.7.2 Frequency and time stability performance

Fig. 4.44 presents the relative frequency deviation for the four Slaves each with a 125 km link length. The mean value for each of the Slaves is -1.0×10^{-16} , -4.2×10^{-17} , -6.0×10^{-16} and -3.8×10^{-16} respectively. The mean value for each cascaded stage is below the statistical uncertainty of their corresponding data sets. For the first three Slaves, we observe peak to peak relative frequency deviations of about 0.6×10^{-11} . But for the Slave ZEN, we observe a lot of spikes in the relative frequency deviation. We observe degradation in the mean value of Slave 1 and 3 when compared to Fig. 4.30.

The Allan deviation is presented in Fig. 4.45. The frequency stability at one second of integration time is 9.3×10^{-13} , 1×10^{-12} , 1×10^{-12} and 1.4×10^{-12} for each of the Slaves respectively. For Slave 1 and 2, the frequency stability curves almost overlap, with the fiber thermal noise limiting the stability performance at long term. But strangely, we do not observe a similar behavior in the case of Slave 3 and 4. Their short term performance starts to degrade at about 100 s of integration time due to a bump. As all the Slaves utilize the same fiber spool and are synchronized to the same Grandmaster, one expects them to exhibit the same behavior.

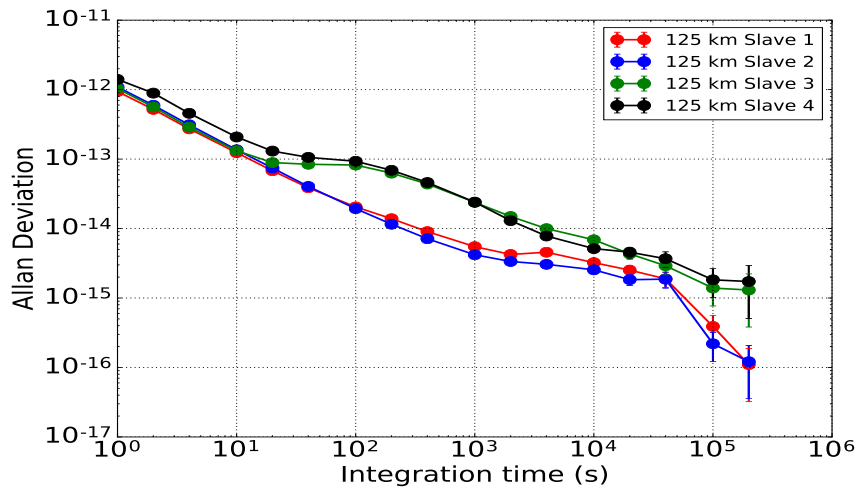


FIGURE 4.45: Allan Deviation (calculated from frequency data) for the multi-user 4x125 km White Rabbit links.

But for Slave 3 and 4, we observe a bump, which might be due to the overload of the PTP traffic for the Grandmaster switch. In the default operation mode of the White Rabbit Switch, it utilizes 1 Hz PTP rate for each of the 18 ports, which results in a complete bandwidth of 18 Hz. In our improved case, we synchronize four Slaves each with a 14 Hz PTP rate for each of the four ports utilized. So, the performances of Slave 1 and 2 are almost similar which suggests that the WRS could handle the load of increased PTP rate for these ports, but for Slave 3 and 4, the CPU was overloaded with increased PTP traffic and we observe a degradation in their stability performances.

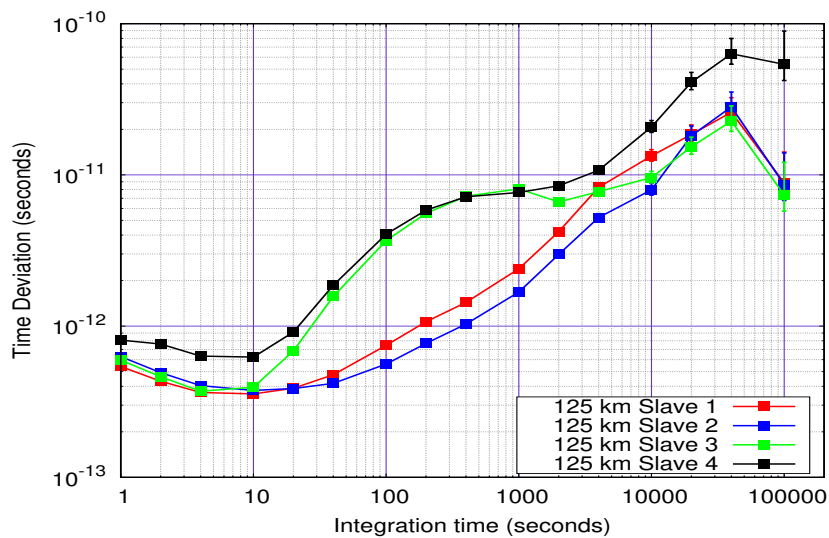


FIGURE 4.46: Time Deviation calculated from frequency data for the multi-user 4x125 km White Rabbit links.

Fig. 4.46 displays the time stability. At one second of integration time, we attain

a time stability of about 600 fs for Slave 1,2,3 and about 800 fs for Slave 4. The time stability performance degrades for Slave 3 and 4 as observed in the frequency stability performance.

4.8 Conclusion

We have demonstrated high performance long haul White Rabbit links using a cascaded approach for time and frequency dissemination. We identified the short term and long term limitations for the time stability performance of long haul White Rabbit links, which are summarized in Fig. 4.47.

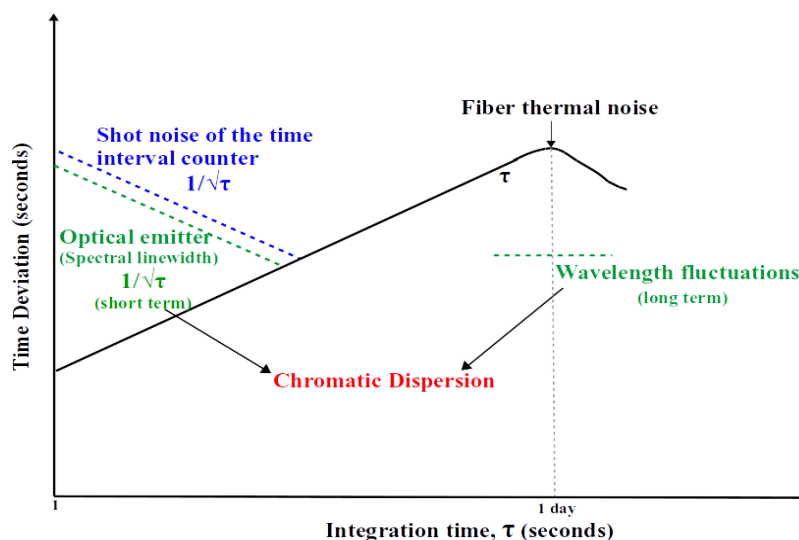


FIGURE 4.47: Pictorial representation of the short term and long term limitations for time stability performance of a long haul White Rabbit link.

By this study, we conclude that the uni-directional configuration is fully endorsed by White Rabbit and it supports both CWDM and DWDM SFPs. We tested links with 1510, 1541, 1560, 1610 nm providing the same level of performance. We used high performance K+K frequency counter and time interval counter STS201 for frequency and time interval measurements and if a user requires the demonstrated level of performance then there is a rigorous requirement of utilization of such high performance instruments. Upon comparison of time stability performance calculated from frequency and phase data, we discovered that PPS generation and distribution in the laboratory is the limitation at short term as we observed convergence between them from 1000 s of integration time.

We utilized a "Cascaded approach" to tackle the problem of Chromatic Dispersion for building long haul White Rabbit links. The short term limitation is due to

the finite spectral linewidth of the optical emitters. The long term wavelength fluctuations are not a limitation for our experiments done on fiber spools but will become a more significant contribution in the field. The Cascaded approach resulted in frequency stability degradation for each of the cascaded stages by a factor approximately equal to $\sqrt{2}$ instead of 2.

Our cascaded 500 km link outperforms the good quality GPS systems Oscilloquartz 5201 and QuartzLock E8000 by two orders of magnitude at long term. We have demonstrated high performance cascaded long haul White Rabbit links for time and frequency dissemination ensuring compatibility with active telecommunication network topology. With the achieved level of performance, White Rabbit provides an eligible and scalable technique to compare industrial atomic clocks at regional and national scales.

White Rabbit links (uni-directional)	Integration time	
	1 s	10000 s
100 km Slave WRS OADEV	2.2×10^{-11}	6.5×10^{-15}
100 km Slave WRS TDEV @ 1 s (BW= 1 Hz)	13 ps	30 ps
Cascaded 300 km WR link		
200 km cascaded stage OADEV	3.4×10^{-11}	5.7×10^{-15}
300 km cascaded stage OADEV	1.3×10^{-11}	7.3×10^{-15}
200 km cascaded stage TDEV	19 ps	14 ps
300 km cascaded stage TDEV	8 ps	22 ps
Cascaded 400 km WR link		
100 km cascaded stage OADEV*	1.0×10^{-12}	3.1×10^{-15}
200 km cascaded stage OADEV*	1.6×10^{-12}	6.7×10^{-15}
300 km cascaded stage OADEV*	1.8×10^{-12}	8.8×10^{-15}
400 km cascaded stage OADEV*	2.1×10^{-12}	1.2×10^{-14}
300 km cascaded stage TDEV	13 ps	35 ps
400 km cascaded stage TDEV	8 ps	51 ps
Cascaded 500 km WR link		
125 km cascaded stage (WRS) ADEV*	1.0×10^{-12}	3.2×10^{-15}
250 km cascaded stage (WRS) ADEV*	1.4×10^{-12}	6.4×10^{-15}
375 km cascaded stage (WRS) ADEV*	1.5×10^{-12}	9.7×10^{-15}
500 km cascaded stage (WR-ZEN) ADEV*	1.8×10^{-12}	1.5×10^{-14}
125 km cascaded stage (WRS) TDEV*	576 fs	15 ps
250 km cascaded stage (WRS) TDEV*	808 fs	30 ps
375 km cascaded stage (WRS) TDEV*	892 fs	45 ps
500 km cascaded stage (WRS) TDEV*	1 ps	71 ps
500 km cascaded stage (WR-ZEN) TDEV	5 ps	80 ps
Effect of reduced PTP rate		

125 km cascaded stage (WRS) ADEV*	1.4×10^{-12}	3.3×10^{-15}
250 km cascaded stage (WRS) ADEV*	1.9×10^{-12}	6.2×10^{-15}
375 km cascaded stage (WRS) ADEV*	2.3×10^{-12}	1.0×10^{-14}
500 km cascaded stage (WR-ZEN) ADEV*	2.4×10^{-12}	1.2×10^{-14}
125 km cascaded stage (WRS) TDEV*	806 fs	18 ps
250 km cascaded stage (WRS) TDEV*	1.1 ps	36 ps
375 km cascaded stage (WRS) TDEV*	1.3	57 ps
500 km cascaded stage (WRS) TDEV*	1.3 ps	73 ps
Effect of reduced Bandwidth of locking		
125 km cascaded stage (WRS) ADEV*	1.4×10^{-12}	4.1×10^{-15}
250 km cascaded stage (WRS) ADEV*	4.1×10^{-12}	1.0×10^{-14}
375 km cascaded stage (WRS) ADEV*	6.5×10^{-12}	1.5×10^{-14}
500 km cascaded stage (WR-ZEN) ADEV*	6.5×10^{-12}	1.8×10^{-14}
125 km cascaded stage (WRS) TDEV*	859 fs	11 ps
250 km cascaded stage (WRS) TDEV*	2.3 ps	45 ps
375 km cascaded stage (WRS) TDEV*	3.7	73 ps
500 km cascaded stage (WRS) TDEV*	3.7 ps	87 ps
Mutli-user 4 x 125 km WR link		
Slave 1 (WRS) ADEV*	9.4×10^{-13}	3.2×10^{-15}
Slave 2 (WRS) ADEV*	1.1×10^{-12}	2.5×10^{-15}
Slave 3 (WRS) ADEV*	1.0×10^{-12}	6.9×10^{-15}
Slave 4 (WR-ZEN) ADEV*	1.4×10^{-12}	5.1×10^{-15}
Slave 1 (WRS) TDEV*	540 fs	13 ps
Slave 2 (WRS) TDEV*	628 fs	7.9 ps
Slave 3 (WRS) TDEV*	596 fs	9.5 ps
Slave 4 (WR-ZEN) TDEV*	807 fs	20 ps

TABLE 4.3: Summary of the main results. ADEV-Allan Deviation, ODAEV- Overlapping ADEV, TDEV- Time deviation. * the stability is calculated from K+K frequency counter data, else the stability is calculated from time interval counter data.

Chapter 5

Deployments

5.1 Introduction

In this chapter, we describe two White Rabbit link setups for time and frequency dissemination.

5.2 A short range in-campus dissemination network

We initiate short range time dissemination using White Rabbit inside the campus of Paris Observatory. We build a short range bi-directional White Rabbit link from the UTC room of SYRTE to our laboratory. For this purpose, optical fibers were installed linking the two rooms. We set up the Grandmaster WRS in the UTC room. The experimental setup is described in Fig. 5.1.

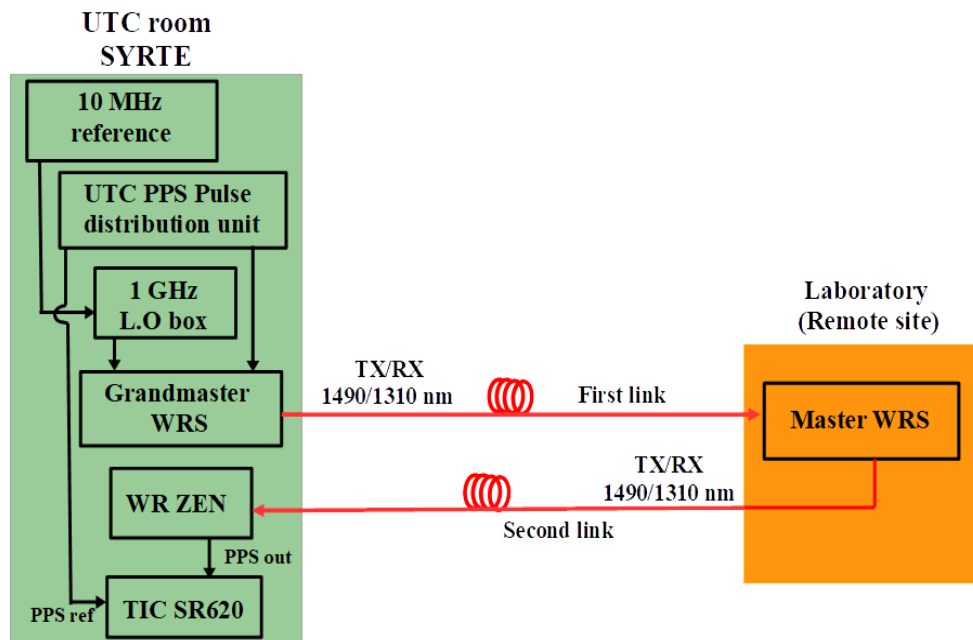


FIGURE 5.1: Experimental setup of the UTC room to Laboratory White Rabbit link.

We build a bi-directional link from UTC room to our laboratory with a "Master" switch synchronized to the Grandmaster in UTC room and we refer this as the first link.

As the Master switch is at a remote place, we build another link from our laboratory back to the UTC room (loop back). A WR-ZEN slave in UTC room is synchronized to the Master switch in our laboratory as shown in Fig. 5.1 and we refer this as the second link. Both the links are bi-directional utilizing separate optical fibers of approximately the same physical length (~ 400 m) as they are in the same bundle. We utilize the SFP pair 1490/1310 nm for both the links. The second link is particularly built for calibration purpose described in the next Chapter.

5.3 A mid range suburban WR link using dark fiber network

We build a mid range sub-urban White Rabbit link connecting our laboratory to LPL (Laboratoire de Physique des Lasers), University Paris 13, utilizing the local telecommunication network. Fig. 5.2 displays the experimental setup. This is a 43 km dark fiber link with a uni-directional setup. The link utilizes the DWDM wavelength of 1541 nm. The Grandmaster switch is the time reference for the link. We utilize the White Rabbit node of the type SPEC as a Slave at the LPL side. An Optical Add Drop Multiplexer is used at both the sides to multiplex/demultiplex the White Rabbit signal on the telecommunication network.

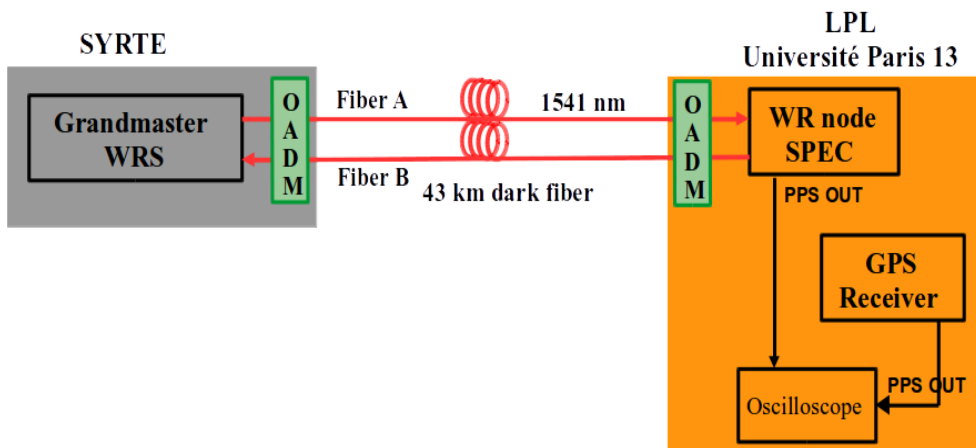


FIGURE 5.2: A 43 km suburban telecommunication network White Rabbit link between SYRTE and LPL (Université Paris 13), Paris.

As this is a private link, it is tested for a calibration technique described in the following Chapter.

Chapter 6

Time Accuracy

6.1 Introduction

Time accuracy is the combined uncertainty (Statistic and Systematic) of the time offset between the reference timescale and the local timescale. The statistical uncertainty is given by the Time Deviation, and as shown in the previous chapter it can be made largely below 100 ps. The dominant term is the Systematic uncertainty. Systematic time shift occurs from differential instrumental delays, non reciprocal propagation delays, and eventually other fundamental terms depending on the topology of the link (for instance the Sagnac effect [8, 9]).

Time calibration is a challenging task due to the various types of delays associated with a time transfer method. For instance, relative calibration determines the delay between a reference device to the local device, which involves evaluating the instrumental delays arising due to the equipment and the delay due to the propagation channel. If the reference and local devices are at the same place, then it is *relatively* easy to perform calibration. But if they are at remote sites, then certainly calibration becomes more difficult. For instance, GPS calibration among European laboratories at a few nanosecond level requires huge efforts and precise techniques [90, 91].

If we now focus on the propagation term, the inaccuracy of the time transfer is dictated by the optical length difference between the two paths (forward and backward).

In case of a bi-directional link using a single fiber, the fiber physical length is the same, but the large index difference results in huge optical length difference. For instance, the 180 nm wavelength difference for the recommended 1490/1310 nm pair induces a time shift of about 30 ns for a 25 km link (as described in Chapter 3 Section 3.4.3). WR-PTP can perform internal transmission and reception delay calibrations, as described in Chapter 2. WR can compensate for the delay asymmetry arising due to different wavelengths of propagation for a bi-directional link, provided that the asymmetry factor is well known (by calibration) and that the asymmetry is constant.

Calibration methods for a bi-directional White Rabbit link are described and documented in the White Rabbit Calibration manual [57], and these were applied here in a metrology laboratory.

The challenge I address in this thesis is to measure the asymmetry of a deployed uni-directional White Rabbit link.

For a uni-directional link using the same wavelength on the two fibers, the wavelength difference between the two SFPs is small (Chapter 3 Section 3.4.3) with chromatic dispersion contribution to path asymmetry at the level of about 100 ps (Chapter 3 Section 3.4.3). Hence, the main term arises from the physical fiber length imbalance, including the optical length difference contribution from the optical amplifiers set up in the field. It can induce a time shift of several microseconds. In the case of a link on a telecommunication backbone, the main issue is to find methods for accurate determination of the link asymmetry.

In addition to this, we should mention that for a long range time transfer link, the variations of the propagation delay (due to temperature variations) can vary by a few hundred of ns [43, 92] and can range up to microseconds for several months of integration over a 1000 km link. These fluctuations are largely rejected by the WR discipline, and the residual delay fluctuations can be made smaller than 1 ns on the long term (> 3 months). This contribution can be neglected for an uncertainty budget at the ns level. But we have to keep in mind that it cannot be neglected anymore if one aims at a lower uncertainty level.

In this chapter, I will first describe a preliminary study I conducted for accuracy, which is about testing the repeatability of the results after connection/disconnection of the link and checking deterministic instrumental delays. Then I describe the calibration of two fiber spools by forcing asymmetry in a uni-directional White Rabbit link. Further, I will describe three different techniques to calibrate a deployed White Rabbit link for different configurations: Wavelength swapping technique for a short range bi-directional link, Fiber swapping technique for a mid range uni-directional link in field, and a Dual wavelength technique for a long range uni-directional link with spools.

6.2 Calibration of fiber spools using White Rabbit

We consider a short range experiment to calibrate a 25 km fiber spool. We consider a Slave WRS synchronized to the Grandmaster (GM) WRS by a uni-directional link of 5 m at 1541 nm displayed as step 1 in Fig. 6.1. As we have a uni-directional link, we refer the fiber link from the Grandmaster to the Slave switch as the *up link* and

the fiber link from the Slave to Grandmaster as the *down link*.

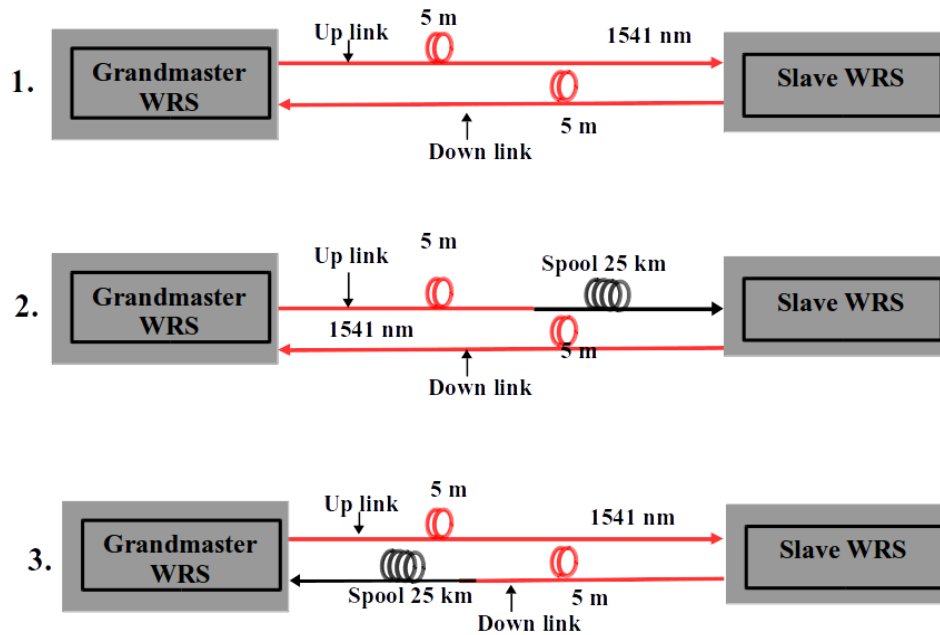


FIGURE 6.1: Experimental setup for the calibration of the fiber spool.

6.2.1 Calibration: A sensitive task

At first, we demonstrate the variation of the accuracy obtained with a simple short White Rabbit link depicted in step 1 of Fig. 6.1. We study the variation of the delay between the reference PPS and the PPS out of the Slave (measured by TIC SR620) by connecting and disconnecting the link. Fig. 6.2 shows the bar chart of the variation of the delay (offset has been removed) for 20 repetitions of connection and disconnection of the link. We observe fluctuations of a few tens of ps with an average value of -15 ps (depicted by the blue line) and a standard deviation of 0.029 ns. The blue lines depict the values as $(-15 \text{ ps} \pm 0.029 \text{ ns})$.

We clearly observe that a simple connection and disconnection of the fiber link can result in tens of picoseconds variation in time accuracy proving calibration is a sensitive task. But as these variations are small they can be neglected in many cases.

6.2.2 Calibration by forcing asymmetry in a uni-directional link

We develop a calibration technique by forcing asymmetry in a balanced uni-directional link. For a uni-directional link, asymmetry can be forced either in the up link or in the down link. We utilize the original calculation procedure for determining the propagation delay of a fiber described in [57]. Originally, the calibration method is

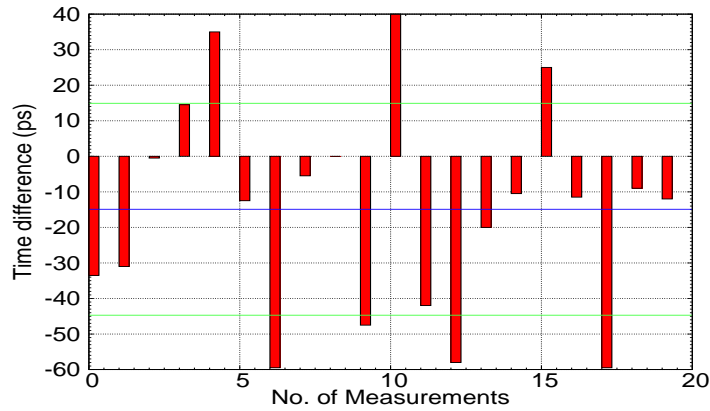


FIGURE 6.2: Variation of the delay (offset has been removed) for connecting/disconnecting the fiber link.

implemented on a bi-directional White Rabbit link.

Before we initiate the experiment it is important to set some parameters for the measurement as described in the calibration manual [57]. As described in Chapter 2 (Section 2.4.3), the measured round trip time is the sum of the fixed instrumental delays (TX, RX) and the propagation delay of the fiber. As initially none of them are known, we set the transmission and reception delays, the alpha parameter to be equal to zero for both the switches used in the experiment. As the transmission and reception delays are set to zero, the bitslide values (defined in [57]) are reported as the reception delays (RX) for GM (ϵ_{GM}) and Slave WRS (ϵ_S).

The following three steps describe the forced asymmetry technique for the experimental setup displayed in Fig. 6.1:

1. For step 1, we synchronize a Slave WRS to the Grandmaster WRS by a 5 m uni-directional link. Once synchronized, we note down the round trip time (RTT_1) and the bitslide values (ϵ_{GM1} , ϵ_{S1}) reported by the White Rabbit monitoring software.

This gives the reference point for the measurement process. We will then measure differential delays compared to this initial time delay. This is actually a usual procedure, both at SYRTE and for the WR calibration.

2. Next, we add a 25 km fiber spool to the existing *up link* of the 5 m uni-directional link. Once synchronized we note down the round trip time (RTT_2) and the bitslide values (ϵ_{GM2} , ϵ_{S2}). The original procedure for a bi-directional link is similar till this step, but as we utilize a uni-directional setup, we have two links (up link and down link) as options to add the fiber spool.

3. In step 3, we add the same 25 km fiber to the existing *down link* of the 5 m uni-directional link and we write down the round trip time (RTT_3) and the bitslide values ($\varepsilon_{GM3}, \varepsilon_{S3}$).
4. We subtract the bitslide values from the round trip delay for the above steps as follows:

$$RTT'_1 = RTT_1 - \varepsilon_{GM1} - \varepsilon_{S1} \quad (6.1)$$

$$RTT'_2 = RTT_2 - \varepsilon_{GM2} - \varepsilon_{S2} \quad (6.2)$$

$$RTT'_3 = RTT_3 - \varepsilon_{GM3} - \varepsilon_{S3} \quad (6.3)$$

where the values for step 2 and 3 should be equal as we utilize the same fiber spool. The following table lists the values of RTT and bitslide values measured for the above steps repeated 20 times:

RTT_1 (ns)	$\varepsilon_{GM1}, \varepsilon_{S1}$ (ns)	RTT_2	$\varepsilon_{GM2}, \varepsilon_{S2}$ (ns)	RTT_3 (ns)	$\varepsilon_{GM3}, \varepsilon_{S3}$ (ns)	RTT'_1 (ns)	RTT'_2 (ns)	RTT'_3 (ns)
1016.234	8.0, 11.2	125276.561	8.0, 12.0	125278.916	7.2, 15.2	997.034	125256.561	125256.516
1017.815	5.6, 15.2	125264.533	5.6, 2.4	125259.711	0.0, 3.2	997.015	125256.533	125256.511
1001.826	1.6, 3.2	125266.976	1.6, 8.8	125269.351	7.2, 5.6	997.026	125256.576	125256.551
1008.191	5.6, 5.6	125263.744	5.6, 1.6	125280.515	10.4, 13.6	996.991	125256.544	125256.515
1023.399	12.8, 13.6	125272.567	12.8, 3.2	125271.767	14.4, 0.8	996.999	125256.567	125256.567
1004.234	6.4, 0.8	125262.992	6.4, 0.0	125262.939	6.4, 0.0	997.034	125256.592	125256.539
1005.047	8.0, 0.0	125275.74	8.0, 11.2	125277.305	10.4, 10.4	997.047	125256.54	125256.505
1020.24	12.8, 10.4	125278.184	12.8, 8.8	125259.729	1.6, 1.6	997.04	125256.584	125256.529
1002.611	4.0, 1.6	125266.163	4.0, 5.6	125280.539	14.4, 9.6	997.011	125256.563	125256.539
1006.664	0.0, 9.6	125258.138	0.0, 1.6	125263.717	0.8, 6.4	997.064	125256.538	125256.517
1016.24	12.8, 6.4	125280.539	12.8, 11.2	125277.345	13.6, 7.2	997.04	125256.539	125256.545
1006.642	2.4, 7.2	125270.116	2.4, 11.2	125280.51	13.6, 10.4	997.042	125256.516	125256.51
1022.654	15.2, 10.4	125279.718	15.2, 8.0	125282.874	12.8, 13.6	997.054	125256.518	125256.474
1011.423	0.8, 13.6	125263.718	0.8, 6.4	125282.882	14.4, 12.0	997.023	125256.518	125256.482
1011.418	2.4, 12.0	125272.514	2.4, 13.6	125265.317	1.6, 7.2	997.018	125256.514	125256.517
1005.052	0.8, 7.2	125257.319	0.8, 0.0	125274.109	11.2, 6.4	997.052	125256.519	125256.509
1007.426	4.0, 6.4	125263.686	4.0, 3.2	125282.073	10.4, 15.2	997.026	125256.486	125256.473
1026.653	14.4, 15.2	125274.883	14.4, 4.0	125260.444	1.6, 2.4	997.053	125256.483	125256.444
1005.032	5.6, 2.4	125268.513	5.6, 6.4	125276.479	14.4, 5.6	997.032	125256.513	125256.479
1003.431	0.8, 5.6	125269.292	0.8, 12	125265.286	7.2, 1.6	997.031	125256.492	125256.486

TABLE 6.1: The measured round trip time (RTT) and bitslide values for Step 1, 2, 3.

We calculate the propagation delay for the fiber spool as follows:

$$\delta_{1spool} = RTT'_2 - RTT'_1 \quad (6.4)$$

where the fiber spool was added in the up link and for the down link case we have the following:

δ_{1spool} (ns)	δ_{2spool} (ns)	Length calculated using δ_{1spool} (m)	Length calculated using δ_{2spool} (m)
124259.527	124259.482	25065.313	25065.304
124259.518	124259.496	25065.311	25065.307
124259.550	124259.525	25065.318	25065.313
124259.553	124259.524	25065.318	25065.312
124259.568	124259.568	25065.321	25065.321
124259.558	124259.505	25065.319	25065.309
124259.493	124259.458	25065.306	25065.299
124259.544	124259.489	25065.317	25065.305
124259.552	124259.528	25065.318	25065.313
124259.474	124259.453	25065.302	25065.298
124259.499	124259.505	25065.307	25065.309
124259.474	124259.468	25065.302	25065.301
124259.464	124259.420	25065.300	25065.291
124259.495	124259.459	25065.307	25065.299
124259.496	124259.499	25065.307	25065.307
124259.467	124259.457	25065.301	25065.299
124259.460	124259.447	25065.300	25065.297
124259.430	124259.391	25065.294	25065.286
124259.481	124259.447	25065.304	25065.297
124259.461	124259.455	25065.300	25065.299

TABLE 6.2: The calculated propagation delay for the fiber spool 1 from step 2,3 and the corresponding calculated length of the fiber spool.

$$\delta_{2spool} = RTT'_3 - RTT'_1 \quad (6.5)$$

In Table 6.2, as expected we observe that the calculated propagation delay values for the fiber spool are same at a level of tens of ps whether the fiber spool is added to the *up link* or the *down link*.

In Table 6.2, we obtain the length of the fiber spool (δ_{1spool}) in ns as 124259.503 ns \pm 0.040 ns. Knowing the propagation delay of the fiber spool, we can estimate the length of the fiber spool using the relation $\tau = n.L/c$ where n is the refractive index for the optical fiber, c is the speed of light and L is the length of the fiber. Using this relation, the length calculated from the propagation delay values δ_{1spool} , δ_{2spool} and $n=1.4682$ is listed in Table 6.2. The mean of the length of the fiber spool calculated from δ_{1spool} , δ_{2spool} is same and is equal to 25065.3 m with a standard deviation of 0.008 m, reflecting the very small difference observed in the time domain. The length of the fiber spool reported by the manufacturer is 25300 m and this value differs from the calculated value by about 1.0%. It illustrates that the effective refraction index is not accurately known, and depends indeed on the strain on the fiber.

We also measure simultaneously the time interval between the GM PPS and PPS out of the Slave switch with the time interval counter SR620 for the Step 1, 2, 3 for each repetition. Let us denote the time interval counter reading (TIC) for each of the Step 1, 2, 3 as TIC_1 , TIC_2 and TIC_3 respectively. The following table summarizes

the time interval readings.

TIC_1 (ns)	TIC_2 (ns)	$TIC_3 \times (-1)$ (ns)	TIC'_2 (ns)	$TIC'_3 \times (-1)$ (ns)
1.223	62130.854	62128.684	62129.631	62129.907
1.240	62130.865	62128.673	62129.625	62129.913
1.188	62130.881	62128.657	62129.693	62129.845
1.204	62130.862	62128.662	62129.658	62129.866
1.221	62130.868	62128.665	62129.647	62129.886
1.207	62130.895	62128.649	62129.688	62129.856
1.242	62130.862	62128.673	62129.62	62129.915
1.226	62130.857	62128.665	62129.631	62129.891
1.213	62130.881	62128.659	62129.668	62129.872
1.237	62130.857	62128.654	62129.620	62129.891
1.242	62130.830	62128.632	62129.588	62129.874
1.223	62130.854	62128.659	62129.631	62129.882
1.232	62130.868	62128.632	62129.636	62129.864
1.226	62130.881	62128.616	62129.655	62129.842
1.245	62130.868	62128.640	62129.623	62129.885
1.218	62130.816	62128.621	62129.598	62129.839
1.204	62130.835	62128.630	62129.631	62129.834
1.226	62130.840	62128.630	62129.614	62129.856
1.223	62130.857	62128.616	62129.634	62129.839
1.213	62130.827	62128.643	62129.614	62129.856

TABLE 6.3: Time interval counter readings for Step 1, 2, 3 for Spool 1.

For the balanced 5 m uni-directional link, we observe a time offset (TIC_1) of 1.2 ns between the Grandmaster and the Slave. We observe that for Step 2 (when the fiber spool is added in the *up link*), the time interval counter reading TIC_2 is positive and time offset is 62.1 μ s. We calculate the quantity $TIC'_2 = TIC_2 - TIC_1$, as we did in equation 6.4. This quantity reflects the time shift due to the fiber spool added in the *up link*, and we expect to observe a time shift of about 62 μ s (as half of the spool length in ns (δ_{1spool}) in Table 6.3) because we force asymmetry in the link by a 25 km fiber spool. Thus, the value TIC'_2 gives the contribution to the asymmetry of the link due to the 25 km fiber spool.

For Step 3, we add the fiber spool in the *down link* which is the opposite to Step 2, so we again expect to observe a time shift of about 62 μ s. As expected, we observe a time shift of about 62.1 μ s (as half of the spool length in ns (δ_{2spool}) in Table 6.3) but with a negative sign. The negative sign is due to the fact that the asymmetry was forced in the *down link*. We calculate the quantity $TIC'_3 = TIC_3 - TIC_1$, as we did in equation 6.5. This quantity reflects the negative asymmetry introduced in the link due to the 25 km fiber spool.

So we observe that the forced asymmetry for a WR link is reflected in the time interval reading and the magnitude of the asymmetry is positive if the asymmetry is introduced in the *up link* and it is negative when forced in the *down link*.

RTT_1 (ns)	$\varepsilon_{GM1}, \varepsilon_{S1}$ (ns)	RTT_2	$\varepsilon_{GM2}, \varepsilon_{S2}$ (ns)	RTT_3 (ns)	$\varepsilon_{GM3}, \varepsilon_{S3}$ (ns)	RTT'_1 (ns)	RTT'_2 (ns)	RTT'_3 (ns)
1001.845	3.2,1.6	125566.272	3.2,11.2	125573.447	10.4,11.2	997.045	125551.872	125551.847
1008.245	0.0,11.2	125564.629	0.0, 12.8	125572.618	10.4,10.4	997.045	125551.829	125551.818
1018.634	11.2,10.4	125566.281	11.2, 3.2	25566.234	13.6, 0.8	997.034	125551.881	125551.834
1006.66	8.8,0.8	125563.909	8.8, 3.2	125570.295	3.2, 15.2	997.06	125551.909	125551.895
1020.266	8.0,15.2	125570.298	8.0, 10.4	125566.3	10.4, 4.0	997.066	125551.898	125551.9
1009.841	8.8,4.0	125572.693	8.8, 12.0	125561.482	8.0, 1.6	997.041	125551.893	125551.882
1003.423	4.8,1.6	125570.269	4.8, 13.6	125575.064	10.4,12.8	997.023	125551.869	125551.864
1023.451	13.6,12.8	125569.491	13.6, 4.0	125567.162	13.6, 1.6	997.051	125551.891	125551.962
1013.058	14.4,1.6	125575.931	14.4, 9.6	125567.935	3.2, 12.8	997.058	125551.931	125551.935
1013.824	4.0,12.8	125558.357	4.0, 2.4	125570.329	7.2, 11.2	997.024	125551.957	125551.929
1011.446	8.8,5.6	125571.921	8.8, 11.2	125564.728	3.2, 9.6	997.046	125551.921	125551.928
1012.233	5.6,9.6	125569.476	5.6, 12.0	125563.913	8.0, 4.0	997.033	125551.876	125551.913
1002.646	1.6,4.0	125566.312	1.6, 12.8	125563.923	9.6, 2.4	997.046	125551.912	125551.923
1014.659	15.2,2.4	125571.092	15.2, 4.0	125563.901	8.0, 4.0	997.059	125551.892	125551.901
1005.026	4.0,4.0	125555.881	4.0, 0.0	125560.682	5.6, 3.2	997.026	125551.881	125551.882
1015.442	15.2,3.2	125579.066	15.2, 12.0	125556.683	1.6, 3.2	997.042	125551.866	125551.883
1005.818	5.6,3.2	125566.329	5.6, 8.8	125575.92	8.8, 15.2	997.018	125551.929	125551.92
1024.227	12.0,15.2	125574.328	12.0, 10.4	125561.525	2.4, 7.2	997.027	125551.928	125551.925
1004.262	0.0,7.2	125565.505	0.0, 13.6	125559.929	4.0, 4.0	997.062	125551.905	125551.929

TABLE 6.4: The measured round trip time (RTT) and bitslide values for Step 1, 2, 3 for Spool 2.

$\delta_{1spool2}$ (ns)	$\delta_{2spool2}$ (ns)	Length calculated using $\delta_{1spool2}$ (m)	Length calculated using $\delta_{2spool2}$ (m)
124554.827	124554.802	25124.880	25124.875
124554.784	124554.773	25124.872	25124.869
124554.847	124554.800	25124.884	25124.875
124554.849	124554.835	25124.885	25124.882
124554.832	124554.834	25124.881	25124.882
124554.852	124554.841	25124.885	25124.883
124554.846	124554.841	25124.884	25124.883
124554.840	124554.911	25124.883	25124.897
124554.873	124554.877	25124.890	25124.890
124554.933	124554.905	25124.902	25124.896
124554.875	124554.882	25124.890	25124.891
124554.843	124554.880	25124.883	25124.891
124554.866	124554.877	25124.888	25124.890
124554.833	124554.842	25124.881	25124.883
124554.855	124554.856	25124.886	25124.886
124554.824	124554.841	25124.880	25124.883
124554.911	124554.902	25124.897	25124.895
124554.901	124554.898	25124.895	25124.895
124554.843	124554.867	25124.883	25124.888

TABLE 6.5: The calculated propagation delay for the fiber spool from step 2,3 and the corresponding calculated length of the fiber spool for Spool 2.

We repeat the entire process for another fiber spool (Spool 2) of length 25 km. The round trip time and bitslide values are listed in Table 6.4. The length is calculated from the propagation delay values $\delta_{1spool2}$, $\delta_{2spool2}$ and $n=1.4682$ is listed in Table 6.5. We obtain the length of the fiber spool 2 ($\delta_{1spool2}/\delta_{2spool2}$) in ns as 124554.854 ns \pm 0.033 ns.

The mean of the length of the fiber spool 2 calculated from $\delta_{1spool2}$, $\delta_{2spool2}$ is same and is equal to 25124.8 m with a standard deviation of 0.007 m respectively. The length of the fiber spool reported by the manufacturer is 25936 m and this value differs from the calculated value by about 3.2%. We also measure the time interval counter readings as we did for Spool 1 and they are listed in the Table 6.6.

TIC_1 (ns)	TIC_2 (ns)	$TIC_3 \times (-1)$ (ns)	TIC'_2 (ns)	$TIC'_3 \times (-1)$ (ns)
1.226	62278.543	62276.354	62277.317	62277.580
1.194	62278.548	62276.378	62277.354	62277.572
1.226	62278.564	62276.389	62277.338	62277.615
1.202	62278.543	62276.386	62277.341	62277.588
1.221	62278.562	62276.375	62277.341	62277.596
1.215	62278.570	62276.359	62277.355	62277.574
1.226	62278.537	62276.351	62277.311	62277.577
1.234	62278.575	62276.392	62277.341	62277.626
1.218	62278.586	62276.383	62277.368	62277.601
1.221	62278.562	62276.389	62277.341	62277.610
1.188	62278.589	62276.397	62277.401	62277.585
1.242	62278.567	62276.386	62277.325	62277.628
1.261	62278.564	62276.373	62277.303	62277.634
1.213	62278.586	62276.370	62277.373	62277.583
1.215	62278.551	62276.386	62277.336	62277.601
1.237	62278.567	62276.375	62277.330	62277.612
1.267	62278.613	62276.416	62277.346	62277.683
1.234	62278.581	62276.405	62277.347	62277.639
1.229	62278.567	62276.400	62277.338	62277.629

TABLE 6.6: Time interval counter readings for Step 1, 2, 3 for Spool 2.

In this calibration technique, we have access to the time delay measurements and by a differential method we can accurately measure the delay of the spool, which is equivalent to its optical length at a given wavelength.

6.3 Wavelength swapping technique

This technique involves swapping the pair of wavelengths for two parallel bi-directional links with a topology that the second link loops back to the reference site. Such a topology gives access to the reference signals for time delay measurements. Let us consider the first bi-directional link with a transmission wavelength as 1490 nm and the reception wavelength as 1310 nm, and this link results in a time offset δ between the reference PPS and the PPS out of the Slave switch. If we utilize the same transmission and reception wavelengths for the second bi-directional link, then we expect a similar time offset value contribution and expect the delay between the reference PPS and the PPS out of the second Slave would be 2δ . This is true if the second link is in succession to the first one and both the links have approximately same physical lengths and same TX/RX wavelengths, which will result in addition of the time offsets as δ (due to first link) + δ (due to second link).

Another case can be when the transmission and reception wavelengths are as 1490 nm and 1310 nm respectively for the first link and we swap the transmission and reception wavelengths for the second link (1310 nm and 1490 nm as transmission and reception wavelengths respectively). Then for this case, we expect to observe a cancellation of the time offsets since their magnitude is almost equal but the second link with swapped TX/RX wavelength results in a negative contribution. This will reduce the effect of asymmetry due to the wavelength pairs to a minimum.

6.3.1 Implementation and Results

We test this technique on the short range UTC to laboratory WR link described in the last Chapter. As this is a private link, we can perform this wavelength swapping technique. For convenience, the experimental setup is represented again in the Fig. 6.3.

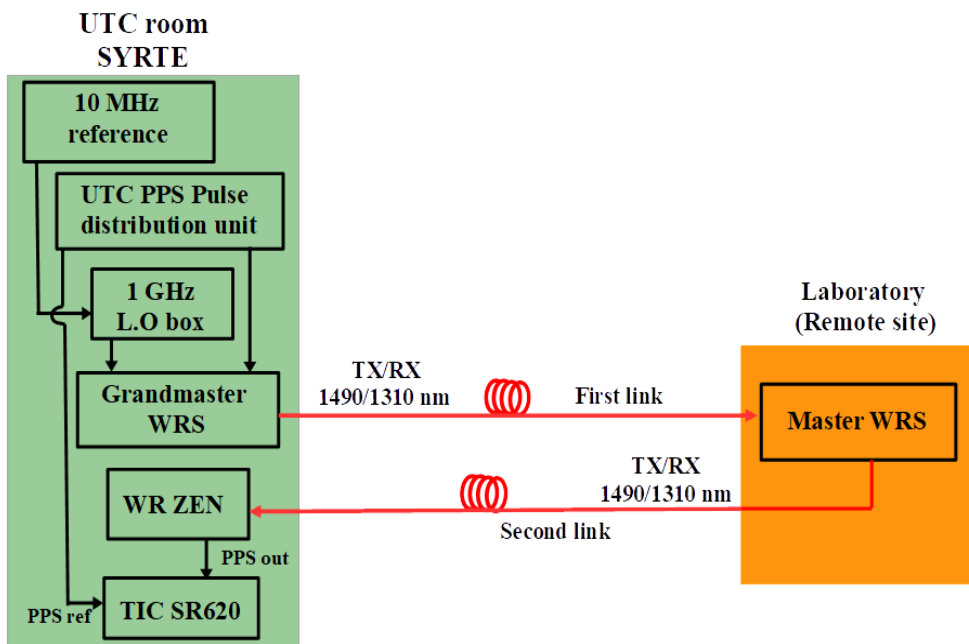


FIGURE 6.3: Experimental setup of the UTC room to Laboratory White Rabbit link.

It is important to mention again that both the links are bi-directional utilizing separate optical fibers of approximately the same physical length as they are part of the same bundle.

The delay between the PPS reference and the PPS out of the Grandmaster switch (δ_{gm}) and the PPS out of the Slave ZEN ($\delta_{slaveZEN}$) are measured with a SR620 time

interval counter (values are averaged over 100 points). With these two measurements, one can perform a differential measurement to obtain the delay between the Grandmaster and the Slave ZEN as follows:

$$\delta_{gm} = PPS_{ref} - PPS_{gm} \quad (6.6)$$

$$\delta_{SlaveZEN} = PPS_{ref} - PPS_{SlaveZEN} \quad (6.7)$$

$$\delta = \delta_{SlaveZEN} - \delta_{gm} = PPS_{gm} - PPS_{SlaveZEN} \quad (6.8)$$

With a differential measurement, we have an advantage of canceling out the contribution arising due to the cables provided we use the same set of cables for both the delay measurements.

We obtain $\delta_{gm} = 61.798$ ns with a standard deviation of 9 ps. The following table summarizes the $\delta_{SlaveZEN}$ and its corresponding standard deviation (σ), δ values for different TX/RX wavelengths combinations for the two bi-directional links:

Case no.	TX/Rx wavelength (nm) for first link	TX/RX wavelength (nm) for second link	$\delta_{SlaveZEN}, \sigma$	δ
Case 1	1490/1310	1490/1310	62.415 ns, $\sigma = 9$ ps	616 ps
Case 2	1490/1310	1310/1490	61.837 ns, $\sigma = 11$ ps	39 ps

TABLE 6.7: Wavelength swapping of the two links and corresponding variation of δ values.

From Table 6.7, for Case 2 we observe that the δ value is small (tens of ps) which is what we expected as the TX/RX wavelength pairs are opposite for the two links. This shows that the asymmetry due to the wavelength pairs is reduced. These preliminary measurements demonstrate that capability of measuring the change in delay when the wavelengths pairs are swapped. It demonstrates the principle of the wavelength swapping technique but we can not interpret the measurement numbers precisely because the instrumental delay calibration was not performed.

6.4 Fiber swapping technique

This technique can be utilized to estimate the asymmetry of an uni-directional WR link. A uni-directional setup utilizes dual fibers, which provides the possibility of swapping the dual fibers at both the ends of the link. Once synchronized, one measures the time offset between a reference PPS and the PPS out of the Slave. Then, the dual fibers of the link are swapped at both the ends and the time offset is remeasured. The difference between the two time offset measurements (for the normal

and the swapped cases) gives the asymmetry of the uni-directional link.

6.4.1 Implementation and Results

We implement this technique on the mid range sub-urban WR link described in the last Chapter. As this is a dark fiber link, we can easily perform the fiber swapping technique. For convenience, the experimental setup is represented again in the Fig. 6.4.

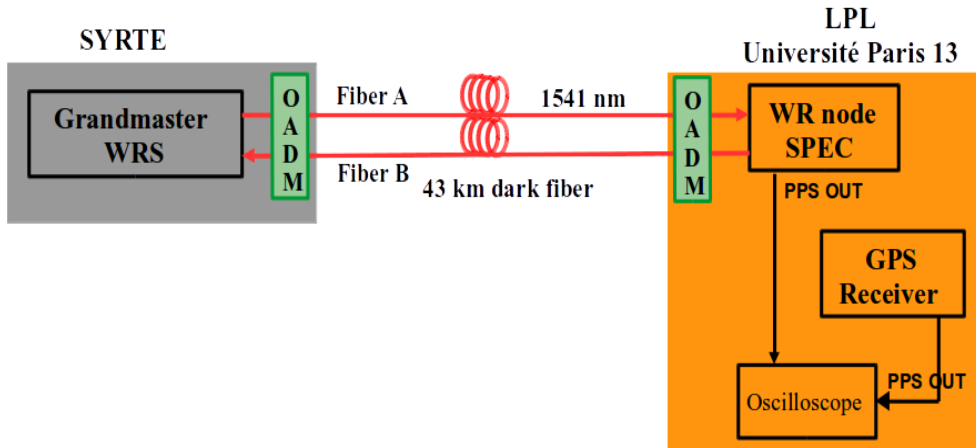


FIGURE 6.4: A 43 km sub-urban active telecommunication network White Rabbit link between SYRTE and LPL (Université Paris 13), Paris.

As the WR Slave node SPEC is at a remote site (at LPL), we consider the PPS out of a low cost GPS receiver as the local time reference. The GPS receiver is not calibrated. The Slave WR node SPEC is synchronized to the Grandmaster WRS at SYRTE by a 43 km uni-directional link. We measure the offset between the PPS out of the low cost GPS receiver and the PPS out of the SPEC by an oscilloscope for two cases. The first case is the normal setup as described in Fig. 6.4 with the dual fibers labeled as Fiber A and B respectively and the measured offset value is $\tau=870$ ns. The second case is when these two fibers are swapped at both sites and the offset is remeasured as $\tau_{swap}=914$ ns. The difference between these two values gives the asymmetry of the link:

$$asymmetry = \tau_{swap} - \tau = 44 \text{ ns} \quad (6.9)$$

We obtain an asymmetry of 44 ns for the 43 km link. This asymmetry contributes a systematic offset of 22 ns to the PPS out of the Slave if uncorrected. The accuracy of this technique does not depend on the calibration in time of the GPS receiver. The only thing that matters is that the local oscillator of the GPS receiver is well disciplined on a frequency standard. As the measurement time for the swapping technique can be done in typically 20 minutes, the requirements on the accuracy

and stability of the local oscillator are easy to match: typically, even 10^{-10} frequency stability at one second with 10 Hz bandwidth and accuracy of 10^{-12} are enough. In practice, it means that a sufficient warm up time has to be respected before performing the calibration.

This method is simple to implement but cannot be realized on an active telecommunication network because the networks don't permit to swap the fiber (cf. RX/TX architecture). Therefore, this method can be implemented only in a private network or for a dark fiber approach.

6.5 Dual wavelength technique

We test a new variational method to estimate the asymmetry of a uni-directional White Rabbit link. This method involves a differential measurement approach by operating two White Rabbit links at different wavelengths over the same optical fiber link using the DWDM technique. This variational method is based on the two way message exchange process of PTP. Fig. 6.5 illustrates the two way PTP scheme for the two Slaves synchronized at different wavelengths. The PTP timestamp values for the two Slaves are denoted as t_1, t_2, t_3, t_4 and t'_1, t'_2, t'_3, t'_4 respectively.

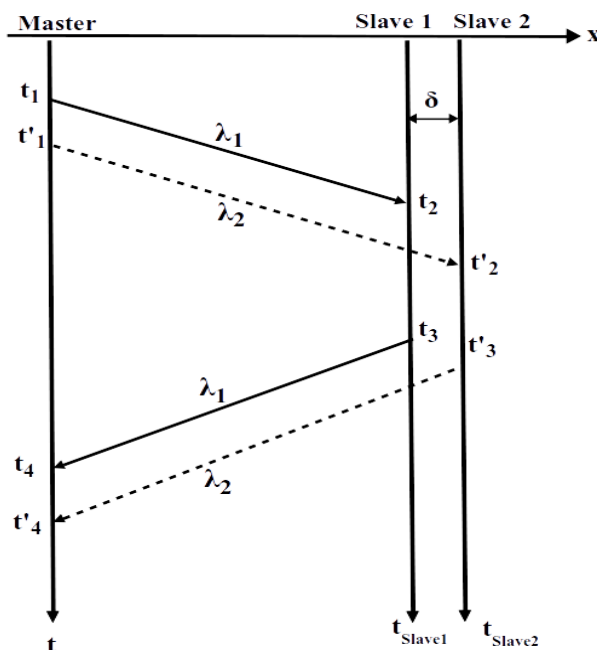


FIGURE 6.5: The two way PTP scheme for dual wavelength technique.

As already discussed in Chapter 2, the propagation delay for a fiber is a function of the wavelength given as $n(\lambda).L/c$, where the product $n(\lambda).L$ is the optical length of the fiber with physical length L . Let us denote the optical lengths for the Slave 1 (at λ_1) as l_1 and l_2 for the dual fibers (Master to Slave and Slave to Master fiber paths)

respectively. Similarly for the Slave 2 (at λ_2), we denote the optical lengths as l'_1 and l'_2 for the dual fibers respectively.

Since we have different Slave WRSs, their time scales are different. The difference between their timescales is denoted by δ as displayed in Fig. 6.5. To align the time scales of the two Slaves, we utilize a time interval measurement. We measure the time interval between the reference PPS and the PPS out of the two Slaves respectively and subtract these values to obtain the time scale offset (δ) between the two Slaves. With the knowledge of the δ value, we can simply add or subtract this value from the t'_2 value for Slave 2 to be aligned to Slave 1 depending upon the situation whether Slave 2 is in advance or in delay with respect to Slave 1.

The ideal two way PTP scheme for the Slaves is presented in Fig. 6.6. For the ideal case, the first requirement is that the transmission times are equal for both the Slaves that is $t_1 = t'_1$. The second requirement is that the two Slaves are part of the same White Rabbit switch so that we attain minimum timescale difference and minimum instrumental delay difference. The Fig. 6.5 is redrawn with the aligned time scales and is presented in Fig. 6.6.

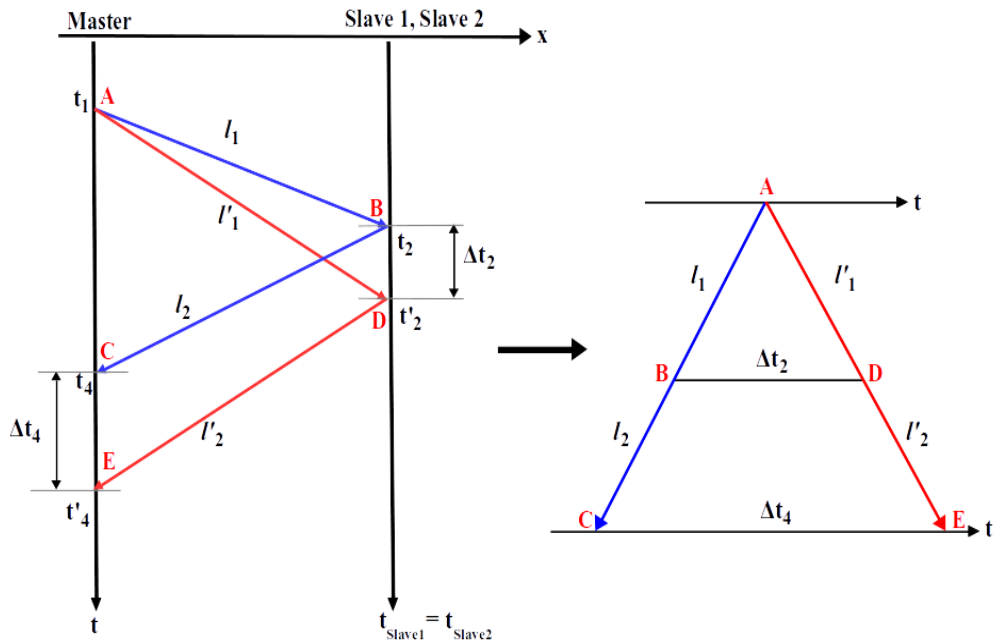


FIGURE 6.6: The two way PTP scheme for dual wavelength technique with Thales theorem representation.

For simplicity, we assume that the Slave transmits the message to the Master at a time $t_3 = t_2$. With the above requirements and this assumption, one can use the Thales theorem [93] to explain the two way PTP message exchange for the two Slaves displayed in Fig. 6.6. The Thales theorem states that if a straight line is drawn parallel to one of the sides of a triangle, then it cuts the other sides of the triangle

(or these produced) proportionally. The PTP scheme is redrawn into a triangle and according to this theorem, the following equation holds:

$$\frac{AB}{AC} = \frac{AD}{AE} \quad (6.10)$$

The above equation gives:

$$\frac{l_1}{l_1 + l_2} \Big|_{\lambda_1} = \frac{l'_1}{l'_1 + l'_2} \Big|_{\lambda_2} \quad (6.11)$$

The above equation holds because the optical lengths are proportional to the physical lengths L_1 and L_2 of the dual fibers in the uni-directional setup. The propagation delay of the two Slaves operating at different wavelengths will be different. The expected difference in the one way propagation delay for the Slaves synchronized at different wavelengths (denoted by τ) is given by the equation [94]:

$$\delta\tau = \frac{(n(\lambda_{1510}) - n(\lambda_{1610})) \cdot L}{c} \quad (6.12)$$

where $n(\lambda)$ is the group refractive index for the optical fiber. The difference between the group index at 1510 nm and 1610 nm can be calculated from the group index graph described in Fig. 2.15 in Section 2.9 of Chapter 2. The group index increases as the wavelength of propagation increases beyond 1510 nm. The difference between the group index values at 1510 nm and 1610 nm is given by the slope of the graph as 5×10^{-4} . Thus, one can calculate the expected propagation delay difference between the Slaves for a link length of 125 km by using the above equation and we obtain a value of 208 ns.

The Slaves synchronized at different propagation wavelengths implies that the time of arrival (t_2 and t'_2) of the packets for the two Slaves will be different as depicted in Fig. 6.6. We expect the difference between the corresponding t_2 values of the two Slaves to be equal to the value calculated above which is 208 ns. We consider Δt_2 as the difference between the t_2 timestamp values for both the Slaves as:

$$\Delta t_2 = t_2 - t'_{2a} \quad (6.13)$$

where $t'_{2a} = (t'_2 \pm \delta)$ represents the aligned timescale of the Slave 2 to Slave 1 as described above. It is also significant to observe that the transmission times (t_1 and t'_1) for each of the Slaves are different (in an ideal case, we would require that the transmission times are synchronized as displayed in Fig. 6.6). So we take into account the difference of the transmission timestamps and the above equation is rewritten as:

$$\Delta t_2 = t_2 - t'_{2a} - (t_1 - t'_1) \quad (6.14)$$

The above equation can be rearranged as:

$$\Delta t_2 = (t_2 - t_1) - (t'_{2a} - t'_1) \quad (6.15)$$

where the quantity $(t_2 - t_1)$ is the one way propagation delay for Slave 1 and $(t'_{2a} - t'_1)$ is the one way propagation delay for Slave 2 and Δt_2 can be estimated as the difference of the one way propagation delays of Slave 1 and 2. The one way propagation delays include the instrumental delays and so we need to correct for these delays by subtracting the transmission and reception (TX/RX) delays for the Master, Slave 1 and Slave 2. Let us represent the transmission delay of the Master and the reception delay of the Slave 1 as tx_m, rx_m and tx_s, rx_s and the same set for the Slave 2 is denoted by tx'_m, rx'_m and tx'_s, rx'_s . The above equation is rewritten as:

$$\Delta t_{2c} = (t_2 - t_1 - tx_m - rx_s) - (t'_{2a} - t'_1 - tx'_m - rx'_s) \quad (6.16)$$

Let us denote the round trip time reported by the Slave 1 and 2 as RTT and RTT' respectively. These round trip values include the transmission and reception delays values, the corrected values of the round trip time for the Slave 1 and Slave 2 respectively are obtained as follows:

$$RTT_c = RTT - (tx_m + rx_s + tx_s + rx_m) \quad (6.17)$$

$$RTT'_c = RTT' - (tx'_m + rx'_s + tx'_s + rx'_m) \quad (6.18)$$

Then with the differential measurement of t_2 timestamps and the round trip time measurement, one can estimate the asymmetry of the uni-directional link. We define β as the ratio of Δt_{2c} to the difference of the round trip time of Slave 1 and Slave 2:

$$\beta = \frac{\Delta t_{2c}}{(RTT_c - RTT'_c)} \quad (6.19)$$

where β represents the asymmetry as it is the ratio of the difference in the one way propagation delay for the two Slaves to the difference of their round trip time. The value of alpha for a purely symmetric uni-directional link would be 0.5. Any deviations from the symmetric value would reflect the asymmetry of the link which is given by the quantity as $\beta_0 = 0.5 - \beta$. Using the value of β_0 one can calculate the expected time offset to the reference timescale by the following equation:

$$\text{expected time offset} = (0.5 - \beta) \frac{nL}{c} \quad (6.20)$$

for a fiber link of length L .

6.5.1 Implementation and Results

We describe the implementation by the experimental setup displayed in Fig. 6.7. Two WRS Slave 1 and 2 are synchronized to the Grandmaster switch by a uni-directional link of 125 km at 1510 nm and 1610 nm respectively using the DWDM technique. An optical add drop multiplexer is used at both the ends to multiplex and demultiplex the two wavelengths.

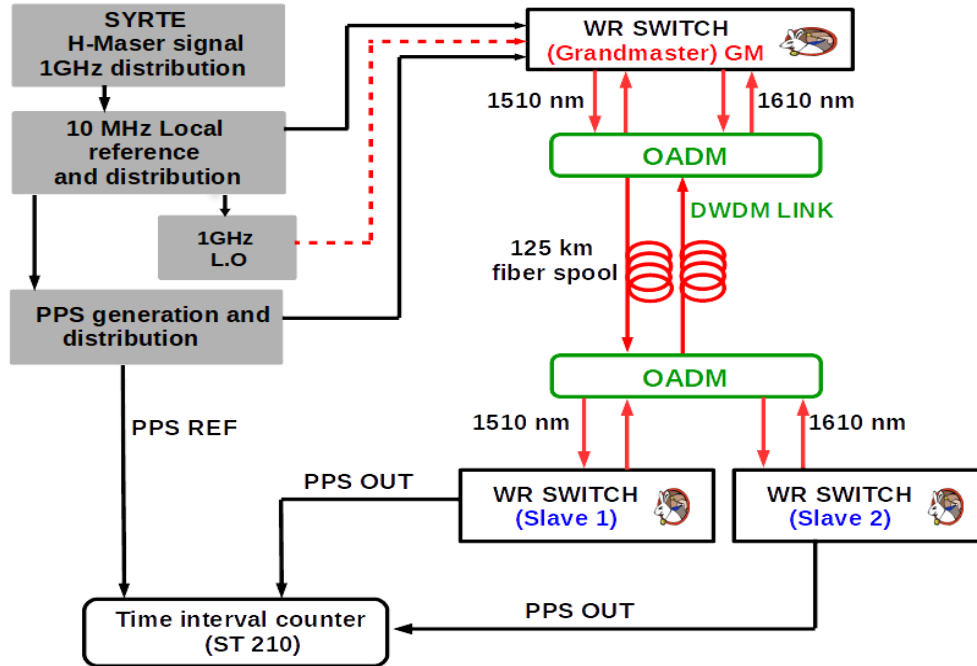


FIGURE 6.7: Experimental setup for a 125 km White Rabbit uni-directional link for two Slave WRS.

We log the PTP timestamps and the round trip time (RTT) for both the Slaves simultaneously every second. Simultaneous to the timestamp logging we also measure the time interval between the reference PPS and the PPS output of both the Slaves by a high performance time interval counter ST201. We collect the data for about 16 days of consecutive measurement.

To calculate β from the logged data, we need to perform two tasks. The first is the synchronization of the PTP timestamp data for the Slaves, which is done by matching the MJD of each of the data sets for the Slave. For the second task, this synchronized dataset of the timestamps is synchronized with the time interval data for both the Slaves.

The time interval counter measures the delay between the reference PPS and the PPS out of the both the Slaves. Let us denote the time interval counter (TIC) readings for the Slave 1 and Slave 2 as TIC_{Slave1} and TIC_{Slave2} respectively and are given as follows:

$$TIC_{Slave1} = \text{offset}_{Slave1} + \text{fluc}_{Slave1} \quad (6.21)$$

$$TIC_{Slave2} = \text{offset}_{Slave2} + \text{fluc}_{Slave2} \quad (6.22)$$

where the TIC reading is the sum of the offset value ($\text{offset}_{Slave1/2}$) and the fluctuations from this offset (fluc_{Slave1}). The measured offset value are as $\text{offset}_{Slave1} = 497.725$ ns and $\text{offset}_{Slave2} = 496.038$ ns. The difference of the above equations gives the time offset (δ) between the two Slaves as:

$$\delta = 1.687 \text{ ns} + (\text{fluc}_{Slave1} - \text{fluc}_{Slave2}) \quad (6.23)$$

As described above, to align the timescales of the two Slaves we need to take into account this time offset value. We observe that Slave 1 is delayed by 1.687 ns with respect to the Slave 2, therefore for our calculations, we add the δ value to the timescale of Slave 2 for synchronization with Slave 1.

The default transmission and reception delay values reported by the WR monitoring software of Slave 1 and 2 were used for calculations. For Slave 1 the values are $tx_m=224.634$ ns, $rx_s=235.797$ ns, $tx_s=224.083$ ns, $rx_m=240.799$ ns and for Slave 2 $tx'_m=224.749$ ns, $rx'_s=226.197$ ns, $tx'_s=224.082$ ns, $rx'_m=240.051$ ns.

Fig. 6.8 shows the fluctuations of the round trip time for both the Slaves. For each of the Slaves, an offset of $1247.164165 \mu s$ and $1247.604656 \mu s$ has been removed respectively. Further, the RTT trace for Slave 2 has been shifted by 2 ns for clarity. We observe clearly that the fluctuations are correlated as both the Slaves utilize the same fiber spools. We observe peak to peak fluctuations of 6 ns over 16 days of consecutive measurement.

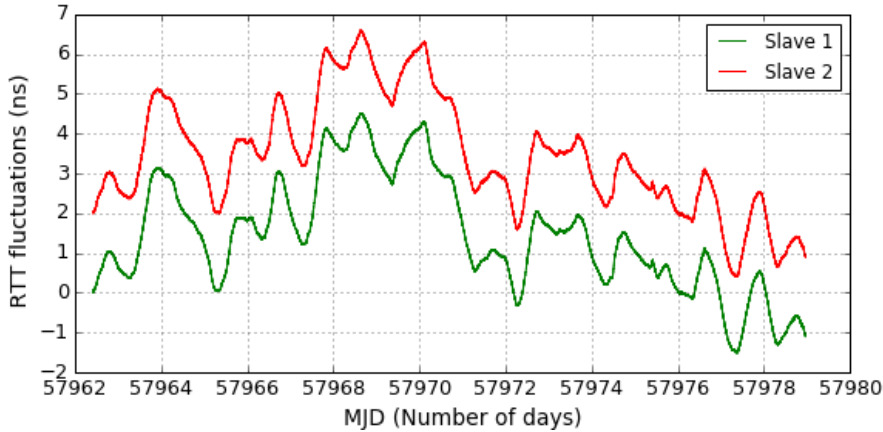


FIGURE 6.8: Round trip time fluctuations for both the Slaves over 16 days of measurement (offset has been removed for both). The trace for Slave 2 has been shifted by 2 ns for clarity.

Fig. 6.9 displays the fluctuations of the difference of the RTT for Slave 2 and Slave 1. An offset of 440.490 ns has been removed. We observe peak to peak fluctuations of about 200 ps over 16 days of measurement.

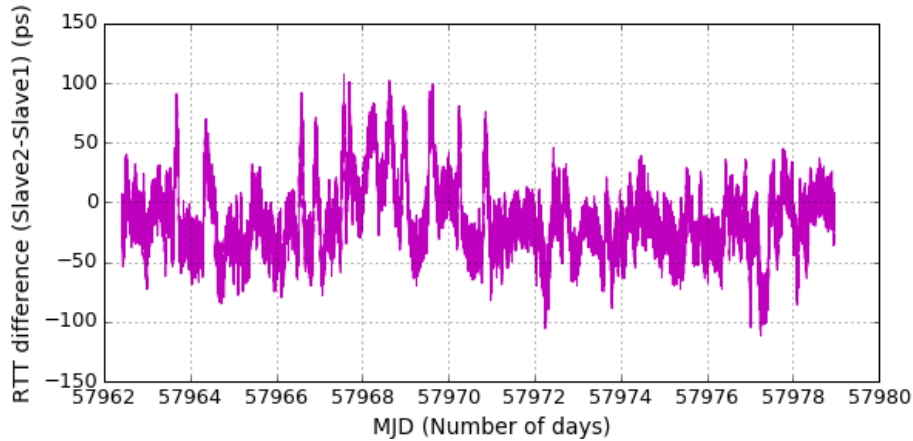


FIGURE 6.9: Fluctuations of the round trip time difference Slave2-Slave1 (offset has been removed).

We calculate the value of β by equation 6.19 and Fig. 6.10 shows the fluctuations of β over 16 days of consecutive measurement and we observe peak to peak fluctuations of about 2×10^{-4} and we obtain a mean value = 0.49630 shown by the red line.

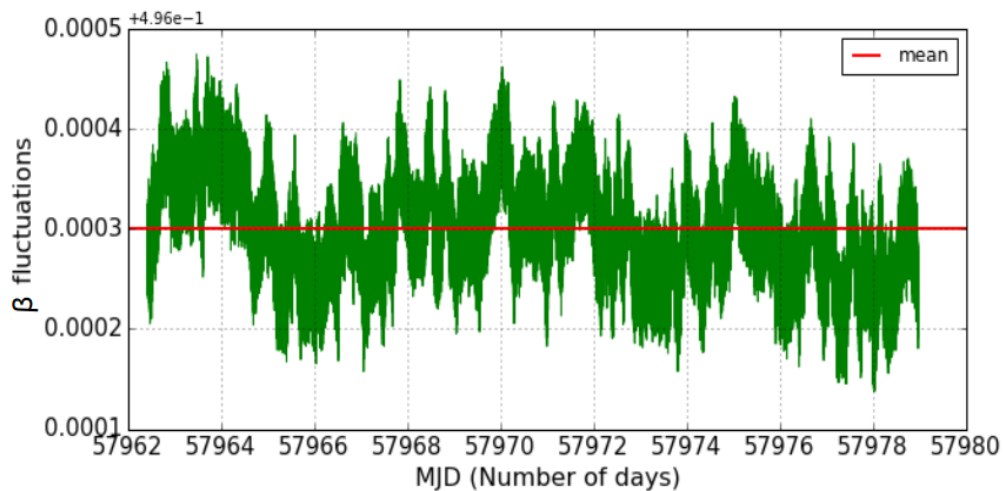


FIGURE 6.10: Fluctuations of β over 16 days of measurement.

The long term β fluctuations can be converted into a time shift, which gives an estimate of how much the accuracy can vary over a given period of time. The time shift with β fluctuations of 2×10^{-4} for a link of length 125 km with a propagation delay of about 625 μs is $2 \times 10^{-4} \times 625 \mu s = 1.25$ ns.

We calculate the expected time offset for the Slaves taking into account the calculated asymmetry of the link using the equation 6.20 with $n=1.4682$ and $L=125$ km and we obtain a value $2.2 \mu s$. This value is 4 times higher than the observed offset value for the Slaves (about 500 ns for both the Slaves given by $\text{offset}_{\text{Slave}1/2}$ values). This clearly illustrates that to reach accuracy at the ns level we need to calibrate carefully the instrumental delays at the scale of few hundred of picoseconds. With our current experiment using the default calibration of the transmission and reception delays, we cannot distinguish between the fiber length asymmetry and the instrumental delay asymmetry. Thus what we calculate is the total asymmetry of the link. It is also important to note that the default instrumental delays do not include the SFP calibration. Hence, without proper SFP calibration our method results in an accuracy in the range of few microseconds. We expect that with an instrumental delay calibration with a few hundred of picoseconds precision, our method could achieve tens of ns of asymmetry measurement accuracy.

We conclude that with our method, one can obtain accuracy in the range of few microseconds with statistical uncertainty of 1 ns or lower depending upon the long term integration time. With a careful calibration of the instrumental delays one can improve the accuracy performance of this dual wavelength technique. One of the advantages of this technique is that it is compatible with the telecommunication network topology.

6.6 Summary

The chapter focused on testing different techniques for time calibration of White Rabbit links (uni-directional and bi-directional links). We began with an initial study addressing calibration of delays as a sensitive task. We observed that the delay fluctuates by few tens of picoseconds for a simple connection/disconnection of the fiber link. Then, we performed Calibration of fiber spools (25 km) by forcing asymmetry in an uni-directional White Rabbit link. This study provided calibration of the length of the fiber spools in terms of delay with a standard deviation of 40 ps.

The rest of the chapter describes three different techniques for time calibration of a White Rabbit link for three different configurations. We performed the Wavelength swapping technique for a short pair of bi-directional White Rabbit link built inside the campus of the Observatory. This method involved measurement of time delay before and after swapping the transmission and reception wavelengths of a pair of bi-directional links (the second bi-directional link was looped back to the initial site for delay measurements with respect to the reference signal). With this method, we observed that opposite pairs of transmission and reception wavelengths reduce the asymmetry (due to the difference in Tx/Rx wavelengths). We demonstrated the

principle of the method along with the measurement capabilities and one needs to perform instrumental delay calibration to interpret the preliminary results.

The second method was the Fiber swapping technique which was performed on a 43 km sub-urban uni-directional WR link between the Observatory and LPL (University Paris 13). This method utilized a low cost GPS receiver as the reference signal at the remote site for delay measurements. The delay is measured at the remote site before and after swapping the two fibers of the uni-directional link and the difference of these delays gives the asymmetry of the link. We obtained a difference of 44 ns which contributes a systematic offset of 22 ns to the PPS out of the Slave WRS at the remote site if uncorrected. This method is very simple to implement but cannot be utilized on active telecommunication networks because fiber swapping is not permitted by the networks.

We developed and tested a new technique; the Dual wavelength technique for a 100 km uni-directional link built using fiber spools in the laboratory. The method utilizes two Slave WRSs synchronized to the Grandmaster WRS by the same 100 km uni-directional link at different wavelengths (1510 nm and 1610 nm respectively) by using the wavelength division multiplexing technique. The asymmetry of the link can be evaluated by recording the PTP timestamps and round trip time (RTT) measurements performed simultaneously for both the Slaves. The principle of this method is based on Chromatic Dispersion, which results in a time difference between the timescales of the two Slaves (due to the difference in propagation wavelengths over the same fiber link). With this method, we achieved four times the observed value. This discrepancy arises as we utilized default instrumental delay calibration. This method could achieve ns level accuracy for calibration of instrumental delays with a few hundreds of picoseconds precision. One of the benefits of this method is that it is compatible with the telecommunication network architecture.

Chapter 7

Conclusion

7.1 Summary

The thesis work was divided into several stages with each chapter reporting on the progress during the PhD. The first stage focused on studying the performances of the White Rabbit equipment (White Rabbit Switch and White Rabbit nodes), testing different White Rabbit network topologies (for 25 km link), and identifying the performance limitations with an outlook for improvement. The next stage improved the performance of the Grandmaster White Rabbit switch by a factor of 25 approximately by direct distribution of the reference clock and the Slave's performance was improved by utilizing increased bandwidth of locking by performing SoftPLL bandwidth optimization. These improvements did not require any hardware modification, only a software modification was done with no expense. We studied the performance of a mid range White Rabbit link of 50 km. All the links were built in the laboratory using fiber spools.

Progressing further, we studied the performance of a telecommunication span White Rabbit link using uni-directional configuration ensuring compatibility with the telecom network. We discovered that for long range links, chromatic dispersion (due to the wavelength stability of the optical emitters (SFPs) and the properties of C-band telecom single mode fiber) can limit the short term performance, while the long term performance is limited by fiber thermal noise. To tackle chromatic dispersion, we utilized the 'Cascaded approach' to build long haul links with multiples of 100 and 125 km links using the DWDM technique. We built the first four span cascaded 500 km White Rabbit link in the laboratory and demonstrated high performance with a frequency stability of 2×10^{-12} at one second of integration time averaging down to a few 10^{-15} in about one day. We expect that the effect of fiber thermal noise will be reduced by about one order of magnitude in field application. The accuracy for frequency dissemination is at the level of 10^{-16} and is below this level for links smaller than 500 km. We attained a time stability of 5 ps at short term and it remained below 1 ns for longer averaging times.

I show in this thesis that, at the range of 500 km the short term performance

is dominated by chromatic dispersion. The achieved short term stability is state of the art. To attain performance beyond that, would require a change of the optical emitters for non ITU-standard emitters (such as OEM DFB laser stabilized in temperature). This is certainly doable, and is indeed done for some experiments, but it restricts, by a matter of fact, the access to fiber networks (public and private) and the potential impact of WR-PTP for industry and commercial sectors.

With such performances, White Rabbit enables frequency dissemination at a regional and national scale and at a scale of small European countries with better frequency stability performance of two orders of magnitude at long term than GNSS based methods. Such level of performance greatly meets the requirements of industry and civil applications. However, it is very important to keep in mind that such level of performance is only achievable if the end user utilizes high performance instruments (Frequency counters and Time interval counters) and the user should be careful to exploit such high quality White Rabbit signals. With the White Rabbit switch consisting of 18 ports, scalability to multiple users can be achieved without compromising its performance

Further we focused on time accuracy. For time accuracy for a dedicated fiber link, the fiber swapping technique was performed on a suburban dark fiber link. For short range in campus dissemination, we demonstrated the principle of Wavelength swapping technique and demonstrated the measurement capability. We tested a dual wavelength method for long range links compatible with telecommunication network topology which achieved a time accuracy of a few microseconds. We pointed out that careful calibration of the instrumental and optical emitter delays is mandatory for a time calibration at a few tens of ns level.

The central question of this thesis is to assess whether a method compatible with telecommunication architecture can meet the performances of GNSS based methods. We can now answer this question, with distinctions between time and frequency, and distinction between metropolitan/regional scale and long-haul scale.

At metropolitan and regional scale, i.e. for uni-directional and bi-directional White Rabbit links, we demonstrate in this thesis that, yes, frequency dissemination by White Rabbit can compete and even surpass the performances of GNSS. For long haul links, using uni-directional configuration and DWDM SFPs, the answer is also 'yes', if one is concerned about frequency stability and accuracy.

Regarding time accuracy, WR-PTP on a LAN is certainly better than industrial grade GNSS receiver to disseminate time over an industrial facility or a campus, provided that a single mode fiber network is used. For long links, and comparable work effort from the staff, we obtained results worse than what can be achieved with

an industrial grade GNSS receiver, and our answer is therefore 'no'. But we would like to add to this negative answer 'for the time being', believing that technical solutions will be found in near future.

7.2 Perspectives

We believe there is still scope for further improvements. First concerning the Slave, more gain would be required to compress the fiber thermal noise. This could be attained by increasing the SoftPLL bandwidth. Another factor could be to further increase the PTP rate for operation. However, it must be clear that this solution would mean changing the FPGA, or even undergo a deeper re-design of the board to support larger computational speed and share of the tasks allocated to the FPGA, micro-controllers, and automated servo loops.

The local oscillator on-board of the White Rabbit switches could be replaced by a more stable component. This issue is not trivial, as several manufacturing constraints has to be fulfilled together, as volume, power consumption, voltage power supply and footprint. Quite complete reviews were done at CERN by Mattia Rizzi and reported on the White Rabbit wikipedia [78], but new products are available monthly and technological monitoring must be carried on. For instance silicon-based devices don't show better performance at the time being for the frequency of interest, but if one looks at the progress made over a decade in this field of research, one can get some reasonable optimism for White Rabbit.

The PPS output could be improved to be a better representation of the WR time as it is physically defined inside the FPGA. Work is underway at CERN, NIKHEF, LAL/IN2P3 (to name only a few), in order to improve the electronic board, either with better selection of components (buffers, GTX, serializer/deserializer, phase comparator, clock fan out), with better functional design (clock frequency, phase lock loops, DDMTD design, etc), or change in the circuitry (insertion of micro controllers, DDS, etc).

Internal and dynamic time calibration could be performed. Work is also underway, especially at Nikhef in the frame of the ASTERICS project, for much better time calibration and self-calibration methods. Redundant topologies are also under study, with recent work published by University of Granada. The work towards higher resiliency and the use of redundant topology can be directly beneficial for the implementation of our Dual wavelength method as the time scale at the Slave side would be *de facto* in common mode for the two wavelengths.

Last but not least, remote control and monitoring is available at the present time for a single device, but there is no tool to supervise and monitor a network. This

work will be undertaken within the WRiTE project, recently funded by EURAMET as a joint research program with about 10 partners including INRIM, VSL, VTT, NIKHEF, SevenSol, OPNT and OP/LNE-SYRTE.

In this thesis, we just begin testing some methods for estimating the accuracy of time transfer using White Rabbit. From the experiences reported here, we can conclude that accurate time transfer over a LAN is certainly doable with White-Rabbit. Given proper calibration methods, ns-accuracy can be reached and kept for at least several weeks. We perform the first trial of a possible in-field calibration method using dual wavelength technique over 125 km link (using fiber spools). This experiment shows that reaching ns accuracy over multi-user WR network will not be that easy. In our view, time calibration for multiple users at long range with reasonable efforts still remains a challenge and a fully open question.

Appendix A

Publications

Time transfer over a White Rabbit network

Namneet Kaur, Philip Tuckey, and Paul Eric Pottie

LNE-SYRTE, Observatoire de Paris, PSL Research University, CNRS, Sorbonne Universités,
UPMC Univ. Paris 06, 61 avenue de l'Observatoire,
75014 Paris, France
namneet.kaur@obspm.fr

Abstract—We started experiments with White Rabbit at LNE-SYRTE for time and frequency dissemination to a large number of users over long haul telecommunication networks. We consider in this paper preliminary work performed on fiber spools, and comparing two situations, one link with one optical fiber and two colors, and a second link with two fibers and a single wavelength. We present preliminary results showing time deviation down to 1 ps at 1000 seconds and Allan deviation as low as 10^{-15} for about 10000 seconds, for both configurations. We discuss the effect of chromatic dispersion on long haul time transfer regarding stability and accuracy. Finally, we outline our plan for future work.

Keywords—White Rabbit, Long haul time and frequency dissemination, Chromatic dispersion

I. INTRODUCTION

Over the last fifteen years, optical fiber links have been intensively studied for frequency dissemination. They have demonstrated frequency transfer with uncertainties below 10^{-17} over several hundred km [1 and references therein]. Today optical fiber links are the most accurate way for comparing remotely located atomic clocks [2]. Time transfer was by comparison less intensively studied. After seminal work by Jefferts *et al.* [3], using SONET or SDH frames, relatively few experiments were carried out over the following decade as Global Navigation Satellite System (GNSS) solutions fulfilled most needs. However weaknesses of GNSS solutions, such as their vulnerability to jamming or spoofing, but also the increasing need for accurate and secure time dissemination for critical applications, have led to renewed interest for this research [4]. There has been an increasing demand for access to precise time and frequency standards in areas such as telecommunication, navigation, internet, metrology for industry and for scientific applications.

Time and frequency transfer over optical fiber links has emerged as an excellent alternative to GNSS based methods. Several studies are being undertaken all over the world for large scale time dissemination [6-10]. The main objective of our study is to disseminate time (and frequency) to multiple users (typically hundreds of users) over long haul telecom fiber links with time accuracy in the range of one microsecond at worst to about one nanosecond. We initiated for that purpose an experiment with White Rabbit technology.

II. WHITE RABBIT

A. Introduction

White Rabbit (WR) is a multi-laboratory, multi-company collaboration for the development of an Ethernet based network ensuring sub-nanosecond synchronization and

deterministic data transfer [5]. It was initiated at CERN in 2008 as a potential successor for the General Machine timing system. It was developed for providing accurate time synchronization for CERN's accelerator complex consisting of particle detectors such as ATLAS, ALICE and others. White Rabbit technology is based on PTP (Precision time protocol) using Synchronous Ethernet and Digital Dual-Mixer Time Difference (DDMTD) phase detection. It demonstrates sub-nanosecond time stability and synchronization of arrays of instruments over 10 km scale networks [6].

B. White Rabbit for precise time transfer on long haul fiber links

In view of the timing capabilities of WR, several studies have focused on precise time and frequency transfer using White Rabbit in the last two years. Two experiments were built. The first one is a time transfer experiment between Espoo and Kajaani, where WR is carried on a dark C-band channel over an active Dense Wavelength Division Multiplexing network of the Finnish University Research Network (FUNET). The link length is 950 km. Including a large number of compensation dispersion spools and unidirectional EDFAs, the VTT group demonstrated standard deviation in time as low as 20 ps at 1000 seconds integration time, probably limited by the local GPS receiver in Kajaani for long integration time [7]. The second experiment connects VSL to VuA and NiKhef with a bi-directional link of 2×137 km. WR is carried by SURFNet on their active telecommunication network on the Coarse Wavelength Division Multiplexing band. This experiment achieved a time stability of 10 ps at 1000 seconds integration time [7]. Finally these two experiments recently presented an accuracy budget below 8 ns using two quite different approaches [7].

III. WHITE RABBIT AT SYRTE

We are following the approach of VTT, and our work focuses on using WR for accurate long haul time dissemination compatible with active telecommunication networks, using unidirectional configurations, long range small form factor pluggable (SFP) optical transceivers and dense wavelength division multiplexing (DWDM) technology.

We present here the preliminary work we have performed in the laboratory, with two white rabbit switches and two end-node receiver (SPEC-boards). To study the role of chromatic dispersion we use fiber spools and several sets of SFP emitters. We describe in the next section our experimental White Rabbit network setup, expectations on the role of chromatic dispersion, and the experimental results.

A. Experimental Setup

The experimental setup is illustrated in Figure 1. We have two White Rabbit Switches (WRS) and two White Rabbit nodes of type SPEC-DIO [5]. The Grandmaster White Rabbit Switch (GM) is frequency and phase locked to a local 10 MHz reference (from a SYRTE H-Maser signal) and a one pulse per second reference (PPS REF) of the laboratory. This switch provides the timing reference for the entire White Rabbit network. The second switch, called the Master, is synchronized to the GM by a short unidirectional link of length comprised between 14 m and 25 km. This realizes an architecture close to the one that could be implemented in the future on an active network.

We then installed two links from the Master to the slave White Rabbit nodes #1 and #2. First the unidirectional link utilizes two fiber spools with approximately equal lengths. We work with a single wavelength of about 1541 nm. The SFPs are from the same manufacturer. They are long range SFPs with a specified range of 120 km. In order to avoid saturation of the receiver, we insert in both arms a 15 dB attenuator. This link is referred to as “bi-fiber”.

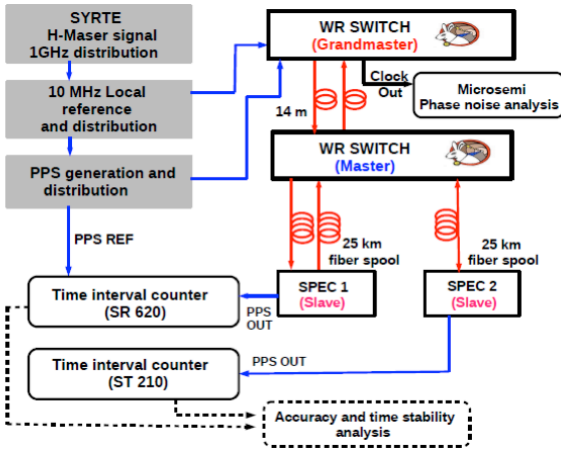


Figure 1. Experimental setup

The second slave node, SPEC2, is synchronized to the Master switch over a bidirectional link using one 25 km fiber spool. We work with bi-color SFPs, at 1310 and 1490 nm. The uplink was at 1490 nm and the down link at 1310 nm. This setup is referred to as “bi-color”.

Time is transferred from the Grandmaster to the Master and then to the slaves in a hierarchical manner using a cascaded topology network. Each of the switches and nodes outputs a PPS signal that may be compared with the PPS time reference signal. A time interval counter (TIC) measures the delay between the PPS REF signal from the Pulse Distribution Unit (PDU) and the PPS out of the slave boards. We use an SR620 for the bi-fiber configuration (SPEC1), and a high performance time interval counter Phusipus ST201 [13-14] for the bi-color configuration (SPEC2). The experiment is performed under well controlled environmental conditions. The two links to the end-nodes are used and recorded simultaneously. Thus any

variation of the reference signal and the first link from GM to Master is in common mode.

B. Effect of Chromatic Dispersion

Chromatic Dispersion is caused by the variation of the refractive index with wavelength. This generates delays between the wavelengths and broadens the transmission pulse as it propagates along the fiber. The propagation delay t for a fiber of length L is given by the equation

$$t = \frac{n(\lambda)L}{c} \quad (1)$$

where $n(\lambda)$ is the refractive index as a function of wavelength λ , given by the Sellmeier equation

$$n^2(\lambda) = 1 + \frac{B_1\lambda^2}{\lambda^2 - C_1} + \frac{B_2\lambda^2}{\lambda^2 - C_2} + \frac{B_3\lambda^2}{\lambda^2 - C_3} \quad (2)$$

where $B_{1,2,3}$ and $C_{1,2,3}$ are experimentally determined Sellmeier coefficients (note that these are not accurately known). The chromatic dispersion coefficient D is defined as:

$$D(\lambda) = \frac{1}{L} \frac{dt}{d\lambda} \quad (3)$$

$D(\lambda)$ represents the variation of the delay with the wavelength. For SMF28 fiber the dispersion is equal to 17 ps/nm/km at 1550 nm and 13 ps/nm/km at 1490 nm [18].

25 km spools	1310/1490	1541
Wavelength difference (nm)	180	<.5
Time shift (ns)	30.8	<0.1
Linewidth (nm, as specified)	3	0.08
Instability associated to specification (ps)	515	25
Linewidth (nm, measured 4s measurement time)	0.032	0.024
Instability @4s (ps)	5.5	7.3

Table 1. Comparison of the effect of chromatic dispersion on stability and time offset for a link using commercial SFPs in two situations: a bi-color link using 1310/1490nm emitters and a single fiber, and a bi-fiber link using DWDM long range emitters @ 1541 nm and two fibers.

Chromatic dispersion affects both the accuracy and the stability of the time transfer. We evaluate the order of magnitude of the effect on our 25 km spools. To do so, we perform optical spectrum analysis of our emitters with a spectrum analyzer Yokogawa AQ6370C, using a resolution bandwidth of 2pm. We observe that the spectrum of emission of 1310 emitters are extremely poor, with many peaks over tens of nm. Using a gaussian fit to the recorded spectra of the SFPs at 1490 nm and 1541 nm we measured linewidths of 32.1

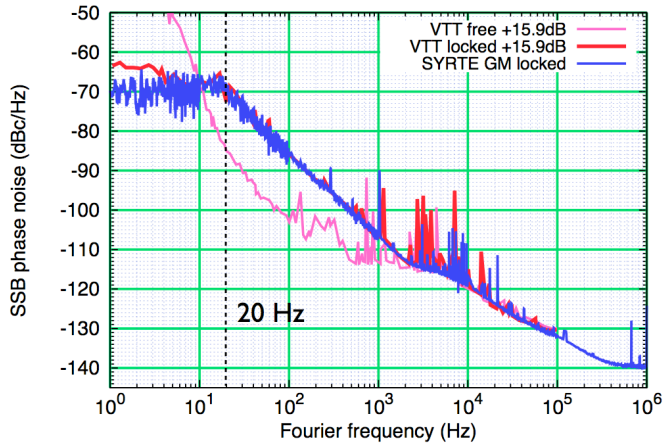


Figure 2. Power spectral density of the White Rabbit switch clock output in locked and free running modes, showing the results of this work and the previous measurements by A. Wallin of VTT [17].

pm and 23.6 pm respectively over 4 s measurement time. The spectrum of the CWDM SFPs is clearly wider than that of the DWDM SFPs. A better measurement campaign should still be carried out with a better resolution and better control of the bandwidth of measurement. We summarize in the table 1 the results of the evaluation of the effect of chromatic dispersion for a WR link, in both the uni-directional and bi-directional configurations, using the linewidth specifications of the SFPs and our measured linewidths. It is important to keep in mind that the chromatic dispersion scales linearly with the length of the link. From the values reported here, it is clear that chromatic dispersion plays an important and limiting role for long haul fiber links with SFPs, and that care must be taken on the frequency stability of the emitters for links longer than 100 km.

C. Results

The Power Spectral Density (PSD) of the phase noise of the Grandmaster for free-running and locked modes is evaluated using a Microsemi Phase test set 5120A. The result is presented in Figure 2. The PSD measured for the 62.5 MHz clock output is approximately -70 dBc/Hz below the locking frequency of about 20 Hz. Much lower phase noise could be achieved by improving the local oscillator of the master switch and by improving the PLL bandwidth [16]. We plot for comparison the result of a similar measurement performed by A. Wallin of VTT [17]. The two data sets are in perfect agreement, when taking into account the frequency ratio between the two outputs of our respective white rabbit switches (10 MHz at VTT and 62.5 MHz at SYRTE).

The time transfer performance to the slave outputs is obtained from the TIC measurements. Figure 3 displays a few days of phase data for the bi-fiber and bi-color data set, showing peak-peak fluctuations of about 150 ps. We observe very stable long data sets with almost no phase drift (typically a few $10^{-17}/s$). We also observe occasional phase glitches, such as the one shown in Figure 3, for which the reasons remain unknown. The time deviation plot is presented in Figure 4. We observe that the TDEV reach a minimum of about 1-2 ps at 1000 s, after which the TDEV follows a rebound. This TDEV

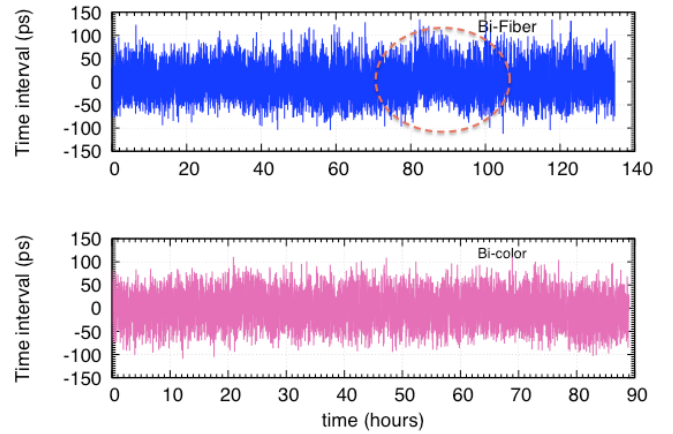


Figure 3. Time intervals raw data using the bi-fiber and the bi-color end-node modules. The time offset were removed.

minimum is 5 times lower than the previously reported value.. WR technology is improving fast, and we now have off the shelf devices whose performance approaches the resolution limit of time interval counters such as the SR620.

The Allan deviation is presented in Figure 5. It scales down as τ^{-1} , and becomes smaller than 10^{-15} at 65000 s of integration time. We also perform a measurement with 50 km of fiber spools between the master and the slave, with the uni-directional setup and with the SR620 TIC. We observe a similar TDEV, even slightly better. Figures 4 and 5 summarize all of the measurements done.

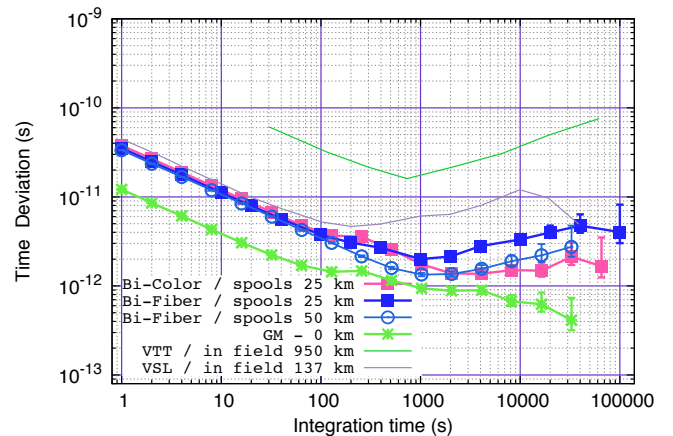


Figure 4. Time deviation for the unidirectional and bidirectional links.

With 25-km fiber spools we expect a contribution of the chromatic dispersion to the instability of about 5-7 ps @ 4 s. At the present level of performance of White Rabbit, this effect is not detectable in the our short-distance experiment in the laboratory, and we observe similar behaviors for the two configurations.

IV. CONCLUSION

We tested a White Rabbit solution to disseminate time to many users. We performed preliminary tests in the laboratory using a complete WR architecture comprising two white rabbit switches and two end nodes. We measured the time deviation of the end nodes compared to the laboratory reference using the

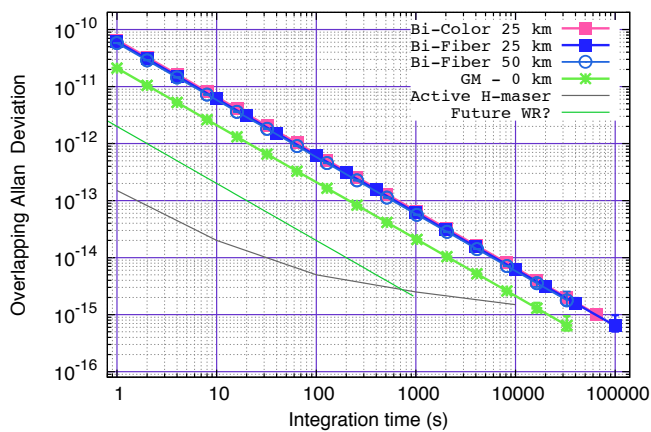


Figure 5. Overlapping Allan deviation for unidirectional and bidirectional link setup.

two popular link configurations: a unidirectional link using one wavelength and two fibers, and a bidirectional link using two colors and one fiber. The links were built using 25 km fiber spools. We obtained very similar performances for these two links over this short distance. We obtained a time deviation of about a picosecond at 1000 seconds of integration time, which is about 5 times better than the previously reported value. We also obtained an overlapping Allan deviation of 10^{-15} at 65000 seconds under well controlled laboratory conditions. For long haul links of length greater than 100 km, the unidirectional configuration must be utilized to ensure compatibility with telecom networks and benefit from the installed backbone equipment. The first challenge to overcome, in order to limit the time deviation to the level of a few tens of ps at short integration times, is to control and reduce the effect of chromatic dispersion. The second drawback of the DWDM approach is that the fiber path length imbalance can lead to a dramatic time offset and hence inaccuracy if the lengths are not accurately measured. The challenge here is to measure accurately the one-way propagation delay. Pseudo-ranging methods as employed in GNSS, based on the autocorrelation of pseudo-random codes, seem to be a promising technique [8,15]. The practical implementation of such techniques in White Rabbit is still an open question that needs to be addressed in order to reach high timing accuracy.

REFERENCES

[1] O. Lopez, F. K  f  lian, H. Jiang, A. Haboucha, A. Bercy, F. Stefani, B. Chanteau, A. Kanj, D. Rovera, J. Achkar, C. Chardonnet, P.-E. Pottie, A. Amy-Klein, G. Santarelli, "[Frequency and time transfer for metrology and beyond using telecommunication network fibres](#)", *Comptes Rendus Physique*, 16 (5), pp. 459-586 (2015)

[2] C. Lisdat, G. Grosche, N. Quintin, C. Shi, S.M.F. Raupach, C. Grebing, D. Nicolodi, F. Stefani, A. Al-Masoudi, S. D  rscher, S. H  fner, J.-L. Robyr, N. Chiodo, S. Bilicki, E. Bookjans, A. Koczwara, S. Koke, A. Kuhl, F. Wiotte, F. Meynadier, E. Camisard, M. Abgrall, M. Lours, T. Legero, H. Schnatz, U. Sterr, H. Denker, C. Chardonnet, Y. Le Coq, G. Santarelli, A. Amy-Klein, R. Le Targat, J. Lodewyck, O. Lopez, P.-E. Pottie, "A clock network for geodesy and fundamental science," <http://arxiv.org/ftp/arxiv/papers/1511/1511.07735.pdf>

[3] S. R. Jefferts, M. A. Weiss, J. Levine, S. Dilla and T. E. Parker, "Two-way time transfer through SDH and SONET systems," *European Frequency and Time Forum* (1996), pp. 461-464. DOI: 10.1049/cp:19960095

[4] M. Weiss, J. Eidson, C. Barry, D. Broman, L. Goldin, B. Iannucci, E.A. Lee and K. Stanton. [Time-Aware Applications, Computers, and Communication Systems \(TAACCS\)](#). NIST Tech Note 1867, (2015).

[5] P. Krehlik, L. Sliwczynski, L. Buczek, M. Lipinski, "Fiber-Optic Joint Time and Frequency Transfer With Active Stabilization of the Propagation Delay", *IEEE Trans. Instrum. Meas.*, vol. 61, no. 10, pp. 2844-2851, (2012).

[6] G Wu, L. , H. Zhang, J. Chen., "High-precision two-way optic-fiber time transfer using an improved time code", *Rev. Sci. Instruments* 85(11):114701 (2014); G. Wu, J.g Hu, H. Zhang, and J. Chen, "Distributed high-precision time transfer through passive optical networks " *Optical Engineering* 53(9), 096113 (2014)

[7] E.F. Dierikx, A.E. Wallin, T. Fordell, J. Myyry, P. Koponen, M. Merimaa, T.J. Pinkert, J.C.J. Koelemeij, H.Z. Peek and R. Smets, "White Rabbit Precision Time Protocol on Long Distance Fiber Links ", *IEEE Transactions on Ultrasonics, Ferroelectrics, and Frequency Control* In press, TUFFC, DOI: 10.1109/TUFFC.2016.2518122

[8] N. Sotiropoulos, C. M. Okonkwo, R. Nuijts, H. de Waardt, and J. C. J. Koelemeij Delivering 10 Gb/s optical data with picosecond timing uncertainty over 75 km distance *Optics Express* 21(26), pp. 32643-32654 (2013) doi: [10.1364/OE.21.032643](https://doi.org/10.1364/OE.21.032643)

[9] V. Smotlacha, A. Kuna and W. Mache, "Time transfer using fiber links," *EFTF-2010 24th European Frequency and Time Forum*, Noordwijk, 2010, pp. 1-8. DOI: 10.1109/EFTF.2010.6533650

[10] S.-C. Ebenhag, P. O. Hedekvist, K. Jaldehag, C. Rieck, Time transfer between UTC(SP) and UTC(MIKE) using frame detection in fiber-optical communication networks, *Precise Time and Time Interval Meeting (PTTI'11)*, Long Beach, Ca, 2011-11-14

[11] White Rabbit. <http://www.ohwr.org/projects/white-rabbit>.

[12] M. Lipinski, T. Wlostowski, J. Serrano, and P. Alvarez, "White rabbit: a PTP application for robust sub-nanosecond synchronization," *Proc. of the International IEEE Symposium on Precision Clock Synchronization for Measurement Control and Communication (ISPCS)*, 2011. <http://ieeexplore.ieee.org/stamp/stamp.jsp?tp=&arnumber=6070148>

[13] E. Samain et al., "Time Transfer by Laser Link - T2L2: Current status and future experiments", *IFCS proceeding 2011*, DOI: 10.1109/IFCS.2011.5977854.

[14] ST201,PHUSIPUS integration,8 ALLEE BELLEVUE, 06460 SAINT VALLIER DE THIEY, FRANCE

[15] L. Sliwczynski, P. Krehlik, A. Czubla, L. Buczek, and M. Lipinski, "Dissemination of time and RF frequency via a stabilized fibre optic link over a distance of 420 km," *Metrologia* 50, 133 (2013).

[16] M. Rizzi, 9th WR Workshop, talks available at <http://www.ohwr.org/projects/white-rabbit/wiki/Mar2016Meeting>

[17] <http://www.ohwr.org/projects/white-rabbit/wiki/Mikes>; see also http://www.anderswallin.net/2014/11/white-rabbit-switch-pps-output-test/wrs_tdev_2014-11-26/ TDEV data from the 20th November 2014

[18] *ITU-T Rec. G.652* <https://www.itu.int/rec/>

Time and frequency transfer over a 500 km cascaded White Rabbit network

Namneet Kaur, Florian Frank, Paul-Eric Pottie, Philip Tuckey
 LNE-SYRTE, Observatoire de Paris, PSL Research University
 CNRS, Sorbonne Universites, UPMC Univ. Paris 06
 Paris 75014, France
 Email: namneet.kaur@obspm.fr

Abstract—We perform experiments with White Rabbit for time and frequency dissemination over long distance optical fiber links. We consider a unidirectional link setup to ensure compatibility with active telecommunication networks and build the first four-span 500 km cascaded White Rabbit link, using commercial White Rabbit equipment and improved software parameters. We demonstrate a frequency transfer stability at the level of 2×10^{-15} at 200 000 s of integration time. The time transfer stability reaches a minimum of 1.2 ps at 20 seconds of integration time. Finally, we compare our results with infield applications and discuss the limitations of the performance.

I. INTRODUCTION

Over the last few years, optical fiber links for frequency and time dissemination have evolved rapidly demonstrating frequency transfer with uncertainties (well) below 10^{-17} over several hundred km (see [1] and references therein). Currently, the most accurate way of comparing remotely located atomic clocks is by the means of optical frequency transfer by coherent fiber links [2]. Besides such highly demanding applications, there has been an increasing demand for fiber access to precise time and frequency standards in areas such as telecommunication, navigation, Internet, metrology for industry and some scientific applications with lower stability and accuracy requirements, and much larger scalability to many users. Indeed many methods for time and frequency transfer over optical fiber links have emerged as excellent alternatives to Global Navigation Satellite System (GNSS) based methods. Today, a very promising direction for time transfer over optical fiber links is the implementation of White Rabbit - Precision Time Protocol (WR - PTP) technology on long range networks [3], [4].

II. WHITE RABBIT-PRECISION TIME PROTOCOL

A. White Rabbit for precise time and frequency transfer

Two time transfer experiments were performed on active telecommunication networks during the last two years. The first experiment by VTT is a 950 km link between Espoo and Kajaani in Finland, where WR is carried over an active Dense Wavelength Division Multiplexing (DWDM) network of the Finnish University Research network. They demonstrated time stability as low as 20 ps at 1000 seconds of integration time [3]. The second experiment is a 2×137 km link between VSL and Nikhef, The Netherlands. WR is carried by SURFnet

on their active telecommunication network on a Coarse Wavelength Division Multiplexing band. They achieved a time stability of 10 ps at 1000 seconds of integration time [3]. These two experiments recently presented an accuracy budget below 8 ns using two different approaches for calibration.

Our work focuses on using WR for accurate long haul time and frequency dissemination, compatible with active telecommunication networks, targeting multiple users, with time accuracy in the range of one microsecond to about one nanosecond for achieving performances competitive with GPS time service.

III. IMPROVING THE WHITE RABBIT SWITCH PERFORMANCE

We study first the performance of a White Rabbit Switch (WRS v3.3) in Grandmaster mode (in which the switch locks to an external reference). We observe suboptimal performance, shown by the phase noise spectral density (PSD) of the Grandmaster WR clock of -70 dBc/Hz at 1 Hz and an Allan Deviation of 1.3×10^{-11} at 1 second of integration time (NEQ BW=500 Hz), illustrated in Fig. 1 and 2 respectively, even if a very high quality signal is provided to the Grandmaster. This excess of noise is due to the phase and frequency lock of the local oscillator on the reference signal. This non optimal lock has repercussion on the whole frequency chain in a WR link. With the help of CERN, we implement a modified version of the configuration file, so that direct clocking of the multi-output clock distribution chip (AD9516-4) is enabled. In order to obtain the lowest relative frequency stability given that phase noise is constant, it is of interest to work at a higher frequency. For some practical reasons related to the frequency map inside the WR switch, we provided the WR switch with a 125 MHz input signal, generated by dividing a 1 GHz H-maser signal by 8. We also provided the switch with a 10 MHz input signal derived by coherent division from the same 1 GHz signal.

Fig. 1 shows the PSD of the WR clock for the default and the improved Grandmaster WRS. The PSD and Allan Deviation measurement are done with a Microsemi Phase test set 5120A. For the improved case, about 20 dB lower

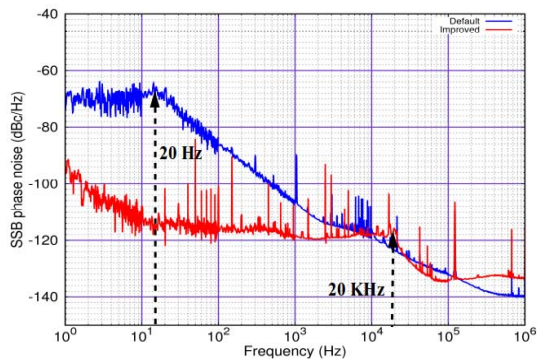


Fig. 1. Phase noise power spectral density for default and improved Grandmaster WR clock.

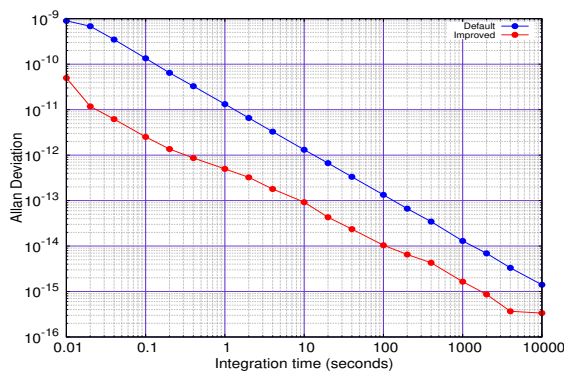


Fig. 2. Allan Deviation for default and Improved Grandmaster WR clock.

phase noise is obtained at 1 Hz and the bandwidth has been increased by a factor of a thousand. This improvement achieved an Allan deviation of 4.9×10^{-13} at 1 second of integration time (NEQ BW=500 Hz) as illustrated in Fig. 2. The performance limitation for the improved case is mainly due to the noise floor of the AD9516-4 used for the WR clock distribution as the external reference clock signal has even lower PSD (-110 dBc/Hz at 1 Hz).

For a Slave WRS synchronized to the Grandmaster WRS through a fiber link, we cannot use the same trick. The SoftPLL is used to lock the internal local oscillator to the clock recovered from the fiber link. The default servo bandwidth for the slave is about 20 Hz. To achieve better performance, the PLL bandwidth (BW) parameters are varied [5]. We consider a Slave WRS synchronized to the Grandmaster WRS by a 100 km uni-directional fiber link (i.e. utilizing dual fiber and the same wavelength of propagation in the two directions) at 1541 nm, with more than three times greater bandwidth of locking. Fig. 3 shows the relative frequency noise of the Slave clock with an increased bandwidth of 70 Hz. Fig. 3 also depicts the frequency noise of the free running local oscillator of the WRS and it is clear that a higher bandwidth should be used to lock the local oscillator, as the minimum of the relative frequency noise lies at about 200 Hz. We also record the error signal out of

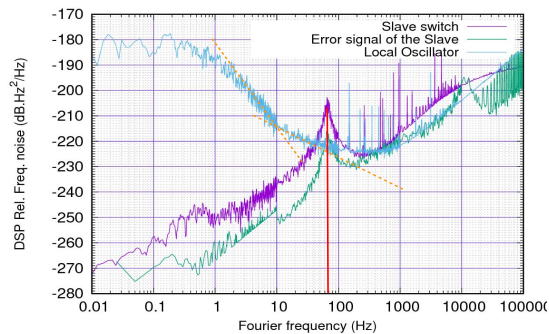


Fig. 3. Relative frequency noise for the Slave clock, the free running Local Oscillator and the error signal of the slave switch.

the SoftPLL of the slave WRS by an FFT analyser and the voltage noise is then converted to frequency noise which is also displayed in Fig. 3. By comparing the frequency noise of the Slave switch and the error signal out of the Slave PLL, we observe that the slave switch has an excess of noise of about 10 dB at low frequencies (less than 100 Hz). This shows that there is still room for improving the Slave switch performance.

Chromatic dispersion affects both the accuracy and the stability (short term) of time transfer as described in [6]. In a WR link, we use small form factor pluggable optical transceivers (SFP). We observed that the line-width is about 3 GHz in 0.25 Hz bandwidth of measurement for SFPs operated in the C-band. As chromatic dispersion scales linearly with the length of the link, it plays a significant and limiting role for long haul fiber links with SFPs, and the frequency stability of the emitters needs to be taken into account for links longer than 100 km. To tackle the limitation due to chromatic dispersion for long haul links, we employ a cascaded approach described in the following section, and tried a faster rate of communication between the master and the slave.

IV. A CASCADED 500 KM WHITE RABBIT LINK

We build the first four span 500 km uni-directional White Rabbit link using fiber spools, long range SFPs and dense wavelength division multiplexing technique. We describe the experimental setup and the results for the cascaded White Rabbit link in this section.

A. Experimental Setup

The experimental setup is illustrated in Fig. 4. We build a four span cascaded WR link of 500 km. Each span is 125 km long. We are using four White Rabbit switches and one WR-ZEN as end-receiver. All these equipments were manufactured by SevenSolutions [7]. The four 10 MHz outputs are recorded simultaneously by a dead-time free phase and frequency counter K+K, operated in Λ mode with 1-s gate time. For time transfer, the Grandmaster also receives a Pulse per second (PPS) generated (SDI PPS generator), amplified and distributed in the laboratory with a TimeTech PPS 16 channels amplifier. Time is transferred from the Grandmaster

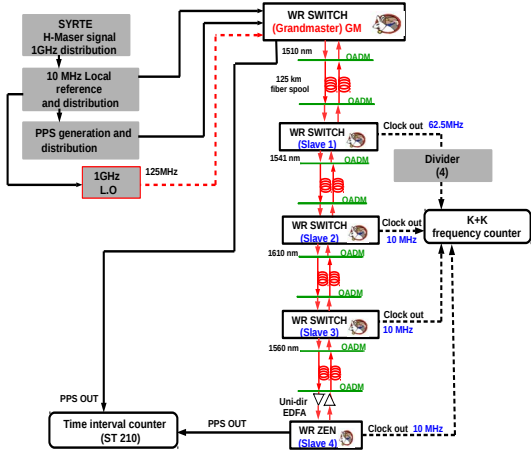


Fig. 4. Experimental Setup for the 500 km cascaded WR link.

to the Boundary Switches and finally the slave (end receiver) in a hierarchical manner using a cascaded approach. Each of the slaves outputs a PPS (Pulse per second) signal that may be compared with the PPS of the Grandmaster or with another output of the PPS amplifier using time interval counters. In the experimental data presented below, we were using a Physipus ST201 [8] to measure the time interval between the output PPS of the GM and the output PPS of the ZEN end-receiver. The ST201 is a high performance time interval counter with a single shot resolution of about 300 fs. The temperature of the experimental room was measured with a thermistance and recorded with a datalogger (Agilent 34972A). All the measurements were done simultaneously.

Regarding the optical layer, all the slave WRS utilize a 2×125 km uni-directional fiber link and long range SFPs in the C-band or OSC channels close to the C-Band. The first and the second span use 1510 nm and 1541 nm respectively. The third and the fourth span use 1610 nm and 1560 nm respectively. We are using OADMs (optical add drop multiplexer) to multiplex these four wavelengths. For the last stage, we use two uni-directional EDFAs to compensate for stronger losses.

In addition, we also modified configuration files of the switch to increase the PTP rate. We set the PTP rate to be 16 per seconds, but observe by logging an effective 14 packets per seconds rate. All the slave switches utilize increased bandwidth of locking of 60 Hz and the increased PTP rate.

B. Results

To show the impact of the PTP rate increase, we present the relative frequency deviation for the last slave WR-ZEN (clock out 10 MHz) at 500 km in the two situations, with standard PTP rate (Fig. 5) and the increased PTP rate (Fig. 6). With standard PTP rate we observe some spikes which are not

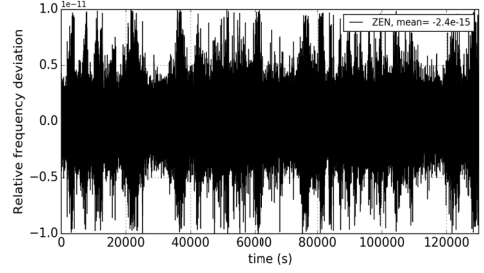


Fig. 5. Relative frequency deviations for WR-ZEN clock out with default PTP rate.

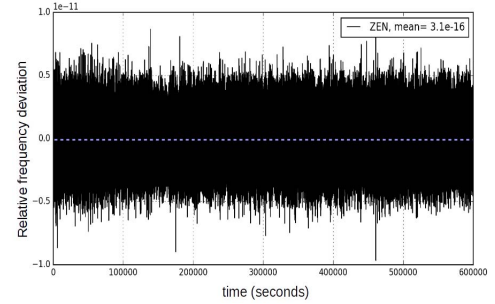


Fig. 6. Relative frequency deviations for WR-ZEN clock out with increased PTP rate.

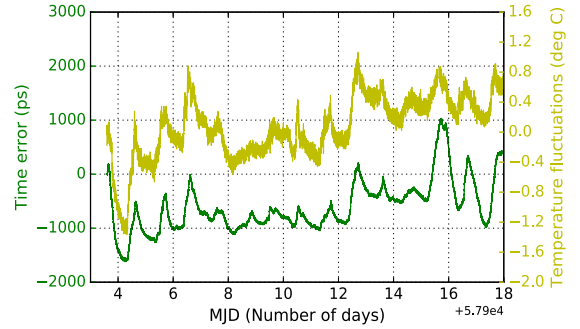


Fig. 7. Phase data for WR-ZEN and the temperature fluctuations of the experimental room (constant offset removed for both).

present with the increased PTP rate. With increased rate, peak to peak relative frequency deviations are at the level of 0.5×10^{-11} . The mean of the frequency data is 3×10^{-16} , which is below the statistical uncertainty of the data set. It is noticeable that the mean deviation to zero is about 7 times higher with the standard PTP rate.

Fig. 7. illustrates the time interval data for eighteen days of consecutive measurement for WR-ZEN. The peak to peak fluctuations are about 2.5 ns. These time fluctuations show some limitation for the accuracy and the frequency stability. Fig. 7 also shows the temperature fluctuations of about 0.8 K over the same eighteen days of measurement. We clearly see the correlation between the phase fluctuations and the temperature fluctuations. We observe a periodic modulation in the phase data, which is due to the temperature fluctuations

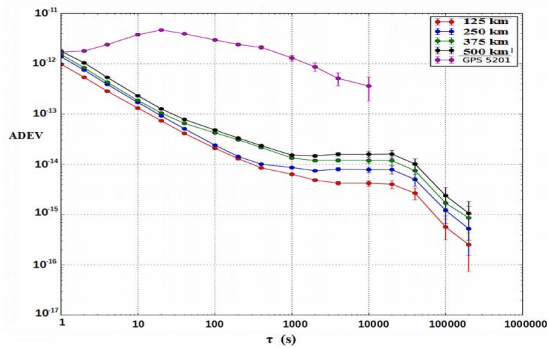


Fig. 8. Allan Deviation for the cascaded 500 km WR link and comparison with GPS Receiver.

acting on the optical length of the fiber. This periodic modulation adversely affects the stability at long integration time [9]. The wavelength variations were measured at 1541 nm, and were found to be 15 pm peak to peak. They are also correlated to the temperature fluctuations.

The Allan deviation (ADEV) for the cascaded stages of the 500 km link is presented in Fig. 8. For the first span at 125 km, we obtain a frequency stability of 1×10^{-12} at one second of integration time. The stability for each span degrades as the length of the link increases, and we attain a value of 2×10^{-12} at one second of integration time for the 500 km link. The stability degrades for each span by a factor a little smaller than $\sqrt{2}$. The stability scales down as τ^{-1} initially and then degrades showing a bump with a maximum at about 20000 seconds of integration time. The bump arises from the fiber thermal noise as the fiber is subject to temperature fluctuations with a sensitivity of 37 fs/(K.m) [10]. At 200000 seconds of integration time, the frequency stability for 125 km span attains 8×10^{-16} and lies in the low region of 1×10^{-15} for the consecutive spans. This fiber noise bump is expected to be greatly reduced by a factor of five for the implementation on active telecommunication networks where the fiber is buried underground. We also compare the frequency stability of the cascaded 500 km WR link with a good quality GPS receiver 5201 and we observe similar short term stability of 2×10^{-12} at 1 second of integration time, but for long integration time (at 1000 seconds) our cascaded WR link has better performance by almost two orders of magnitude.

The time deviation plot is presented in Fig. 9. We compare our lab experiment with two infield applications using the active telecommunication networks. The first one is a 950 km WR link by the Finnish metrology lab VTT between Espoo and Kajani in Finland [3], where the time stability has been scaled down to 500 km for easier comparison. The second one is a 540 km link by V. Smotlacha and co-workers for time transfer between the metrology labs of Prague and Vienna [11]. The time transfer stability for the 500 km cascaded link is 5.5 ps at one second of integration time and reaches a

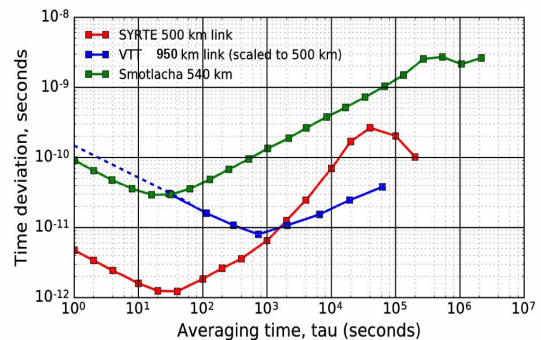


Fig. 9. Time Deviation for the 500 km White Rabbit link and comparison with infield applications.

minimum of 1.2 ps at 20 seconds of integration time. The time stability degrades for long averaging times due to the thermal fiber noise but still remains below the ns level. The rapid increase of the TDEV is due to the common temperature excitation of all the cascaded stages. In comparison, we have improved the time stability at one second of integration by more than one order of magnitude. For longer averaging time, we expect to observe a similar behavior as in [3], [11] if implemented on active telecommunication networks.

V. CONCLUSION

We studied White Rabbit technology for long range time and frequency dissemination. We optimized the White Rabbit Switch operating conditions to achieve better performance. We improved the short term stability of the Grandmaster White Rabbit switch from 1.8×10^{-11} to 4.9×10^{-13} (NEQ BW=500 Hz) at one second of integration time. We utilized three times greater bandwidth of locking for the boundary WRS. We built the first four-span 500 km cascaded link using fiber spools and evaluated its performance for long range time and frequency dissemination. We demonstrated a frequency transfer stability at the level of 2×10^{-15} over one day of integration time. We do not observe any frequency shift within the statistical uncertainty. The time stability at one second of integration time is 5.5 ps and it reached a minimum of 1.2 ps at 20 seconds of integration time. The limitations for the performance are chromatic dispersion (optical emitter stability) at short integration time and fiber thermal noise for long integration time. In further work, we are studying practical solutions to be implemented in field for determining time accuracy.

ACKNOWLEDGMENT

The authors would like to thank Javier Diaz, Rafa Rodriguez, J. Gabriel Ramirez at Seven Solutions and Felipe Torres González at University of Granada for their collaboration and help. We would also like to thank people involved in the WR project for their continuous stimulations and sharing issues through the mailing list, and to thank especially Javier Serrano, Alessandro Rubini, T. Włostowski, and Mattia Rizzi at CERN for their help and support. This work was supported

by the LABEX Cluster of Excellence FIRST-TF (ANR-10-LABX-48-01), within the Program 'Investissements d'Avenir' operated by the French National Research Agency (ANR) and by Bpifrance under the SCP Time project.

REFERENCES

- [1] O. Lopez, F. Kéfélian, H. Jiang, A. Haboucha, A. Bercy, F. Stefani, B. Chanteau, A. Kanj, D. Rovera, J. Achkar, C. Chardonnet, P.-E. Pottie, A. Amy-Klein, G. Santarelli, "Frequency and time transfer for metrology and beyond using telecommunication network fibres", *Comptes Rendus Physique*, 16 (5), pp. 459-586 (2015).
- [2] Lisdat, C. et al. "A clock network for geodesy and fundamental science", *Nat. Commun.* 7:12443 doi: 10.1038/ncomms12443 (2016).
- [3] E.F. Dierikx, A.E. Wallin, T. Fordell, J. Myyry, P. Koponen, M. Merimaa, T.J. Pinkert, J.C.J. Koelmeij, H.Z. Peek and R. Smets, "White Rabbit Precision Time Protocol on Long Distance Fiber Links", *IEEE Transactions on Ultrasonics, Ferroelectrics, and Frequency*, DOI: 10.1109/TUFFC.2016.2518122 (2016).
- [4] J. Serrano et al., "The White Rabbit project", IBIC2013, Oxford, UK, 2013.
- [5] M. Rizzi talk, 9th WR Workshop, talks available at <http://www.ohwr.org/projects/white-rabbit/wiki/Mar2016Meeting>
- [6] N. Kaur, P. Tuckey and P. E. Pottie, "Time transfer over a White Rabbit network", 2016 European Frequency and Time Forum (EFTF), York, 2016, pp. 1-4. doi: 10.1109/EFTF.2016.7477793
- [7] White Rabbit Switch <http://www.ohwr.org/projects/white-rabbit/wiki/Switch>, White Rabbit ZEN node <http://sevensols.com/index.php/products/wr-zen-board/>
- [8] ST201, <http://sigmatime.fr>, Sigmatime, PHUSIPUS integration, 8 allée Bellevue, 06460 SAINT VALLIER DE THIEY, FRANCE
- [9] Pierre Urich, Stabilité des Oscillateurs ultra-stables, Journées X-ENS-UPS de Physique 9 mai 2007, http://softs.polytechnique.fr/departements/physique/colloques/pdf/2007/Urich_Pierre_X-ENS-UPS2007.pdf
- [10] L. G. Cohen and J. W. Fleming, Effect of temperature on transmission in lightguides, *Bell Syst. Tech. J.* 58, 945951 (1979).
- [11] V. Smotlacha, A. Kuna and W. Mache, "Time transfer using fiber links", EFTF-2010 24th European Frequency and Time Forum, Noordwijk, 2010, pp. 1-8. DOI:10.1109/EFTF.2010.6533650.

Bibliography

- [1] Micheal Lombardi. “Fundamentals of Time and Frequency”. In: *CRC Press LLC* (2002). URL: <https://tf.nist.gov/general/pdf/1498.pdf>.
- [2] W J Riley. *Handbook of Frequency Stability Analysis*. Vol. 31. 1. U.S. Department of Commerce, National Institute of Standards and Technology, 1994. ISBN: 3-01-975305-8. DOI: [10.1016/0148-9062\(94\)92706-5](https://doi.org/10.1016/0148-9062(94)92706-5).
- [3] Pierre Uhrich. “Stabilité des Oscillateurs ultra-stables”. In: *Journées X-ENS-UPS de Physique* (2007), pp. 1–41. URL: http://softs.polytechnique.fr/departements/physique/colloques/pdf/2007/Uhrich_Pierre_X-ENS-UPS2007.pdf.
- [4] D B Sullivan et al. “Characterization of clocks and oscillators”. In: *NIST Tech. Note 1337* (1990), N–N. URL: <http://tf.nist.gov/general/pdf/868.pdf>.
- [5] J. Guena et al. “Progress in atomic fountains at LNE-SYRTE”. In: *IEEE Transactions on Ultrasonics, Ferroelectrics, and Frequency Control* 59.3 (Mar. 2012), pp. 391–409. ISSN: 0885-3010. DOI: [10.1109/TUFFC.2012.2208](https://doi.org/10.1109/TUFFC.2012.2208).
- [6] B. J. Bloom et al. “An optical lattice clock with accuracy and stability at the 10⁻¹⁸ level”. In: *Nature* 506.7486 (Jan. 2014), pp. 71–75. ISSN: 0028-0836, 1476-4687. DOI: [10.1038/nature12941](https://doi.org/10.1038/nature12941). URL: <http://www.nature.com/doifinder/10.1038/nature12941> (visited on 01/11/2018).
- [7] Fritz Riehle. “Towards a redefinition of the second based on optical atomic clocks”. en. In: *Comptes Rendus Physique* 16.5 (June 2015), pp. 506–515. ISSN: 16310705. DOI: [10.1016/j.crhy.2015.03.012](https://doi.org/10.1016/j.crhy.2015.03.012). URL: <http://linkinghub.elsevier.com/retrieve/pii/S1631070515000638> (visited on 01/08/2018).
- [8] G Sagnac. “L'éther lumineux démontré par l'effet du vent relatif d'éther dans un interféromètre en rotation uniforme”. In: *C. R. Acad. Sci.* 157 (1913), p. 708. URL: <http://zelmanov.ptep-online.com/papers/zj-2008-07.pdf>.
- [9] Guido Rizzi and Matteo Luca Ruggiero. “A Direct Kinematical Derivation of the Relativistic Sagnac Effect for Light or Matter Beams”. en. In: *General Relativity and Gravitation* 35.12 (Dec. 2003), pp. 2129–2136. ISSN: 0001-7701, 1572-9532. DOI: [10.1023/A:1027345505786](https://doi.org/10.1023/A:1027345505786). URL: <https://link.springer.com/article/10.1023/A:1027345505786>.
- [10] Micheal Lombardi et al. “Time and Frequency Measurements Using the Global Positioning System”. In: *The International journal of metrology* (2001). URL: <https://tf.nist.gov/general/pdf/1424.pdf>.

- [11] Judah Levine. "A review of time and frequency transfer methods". In: *Metrologia* 45.6 (Dec. 2008), S162–S174. ISSN: 0026-1394, 1681-7575. DOI: [10.1088/0026-1394/45/6/S22](https://doi.org/10.1088/0026-1394/45/6/S22). URL: <http://stacks.iop.org/0026-1394/45/i=6/a=S22?key=crossref.360059c91167a7da12869fe7f911d0f8>.
- [12] M. Weiss et al. "Ionospheric models and measurements for common-view time transfer". In: *Proceedings of the 2002 IEEE International Frequency Control Symposium and PDA Exhibition (Cat. No.02CH37234)*. 2002, pp. 517–521. DOI: [10.1109/FREQ.2002.1075938](https://doi.org/10.1109/FREQ.2002.1075938).
- [13] P. Defraigne and G. Petit. "Time transfer to TAI using geodetic receivers". en. In: *Metrologia* 40.4 (2003), p. 184. ISSN: 0026-1394. DOI: [10.1088/0026-1394/40/4/307](https://doi.org/10.1088/0026-1394/40/4/307). URL: <http://stacks.iop.org/0026-1394/40/i=4/a=307> (visited on 07/19/2018).
- [14] G. Petit and Z. Jiang. "Precise Point Positioning for TAI computation". In: *2007 IEEE International Frequency Control Symposium Joint with the 21st European Frequency and Time Forum*. May 2007, pp. 395–398. DOI: [10.1109/FREQ.2007.4319104](https://doi.org/10.1109/FREQ.2007.4319104).
- [15] J. M. Dow, R. E. Neilan, and G. Gendt. "The International GPS Service: Celebrating the 10th anniversary and looking to the next decade". In: *Advances in Space Research. Satellite Dynamics in the Era of Interdisciplinary Space Geodesy* 36.3 (Jan. 2005), pp. 320–326. ISSN: 0273-1177. DOI: [10.1016/j.asr.2005.05.125](https://doi.org/10.1016/j.asr.2005.05.125). URL: <http://www.sciencedirect.com/science/article/pii/S0273117705007684>.
- [16] A Bauch et al. "Comparison between frequency standards in Europe and the USA at the 10^{-15} uncertainty level". In: *Metrologia* 43.1 (Feb. 2006), pp. 109–120. ISSN: 0026-1394, 1681-7575. DOI: [10.1088/0026-1394/43/1/016](https://doi.org/10.1088/0026-1394/43/1/016). URL: <http://stacks.iop.org/0026-1394/43/i=1/a=016?key=crossref.5950df7509be12052c447717e2c7bc1e>.
- [17] Andreas Bauch. "Time and frequency comparisons using radiofrequency signals from satellites". en. In: *Comptes Rendus Physique* 16.5 (June 2015), pp. 471–479. ISSN: 16310705. DOI: [10.1016/j.crhy.2015.02.006](https://doi.org/10.1016/j.crhy.2015.02.006). URL: <http://linkinghub.elsevier.com/retrieve/pii/S1631070515000201> (visited on 01/15/2018).
- [18] D. W. Hanson. "Fundamentals of two-way time transfers by satellite". In: *Proceedings of the 43rd Annual Symposium on Frequency Control*. May 1989, pp. 174–178. DOI: [10.1109/FREQ.1989.68861](https://doi.org/10.1109/FREQ.1989.68861).
- [19] Olivier Lopez et al. "Frequency and time transfer for metrology and beyond using telecommunication network fibres". In: *Comptes Rendus Physique* 16.5 (June 2015), pp. 531–539. URL: <https://hal.archives-ouvertes.fr/hal-01176012>.

- [20] S. Droste et al. "Optical-Frequency Transfer over a Single-Span 1840 km Fiber Link". en. In: *Physical Review Letters* 111.11 (Sept. 2013). ISSN: 0031-9007, 1079-7114. DOI: [10.1103/PhysRevLett.111.110801](https://doi.org/10.1103/PhysRevLett.111.110801). URL: <https://link.aps.org/doi/10.1103/PhysRevLett.111.110801>.
- [21] C. Lisdat et al. "A clock network for geodesy and fundamental science". En. In: *Nature Communications* 7 (Aug. 2016), p. 12443. ISSN: 2041-1723. DOI: [10.1038/ncomms12443](https://doi.org/10.1038/ncomms12443). URL: <https://www.nature.com/articles/ncomms12443>.
- [22] J. Guéna et al. "First international comparison of fountain primary frequency standards via a long distance optical fiber link". en. In: *Metrologia* 54.3 (2017), p. 348. ISSN: 0026-1394. DOI: [10.1088/1681-7575/aa65fe](https://doi.org/10.1088/1681-7575/aa65fe). URL: <http://stacks.iop.org/0026-1394/54/i=3/a=348>.
- [23] P. Delva et al. "Test of Special Relativity Using a Fiber Network of Optical Clocks". In: *Physical Review Letters* 118.22 (June 2017), p. 221102. DOI: [10.1103/PhysRevLett.118.221102](https://doi.org/10.1103/PhysRevLett.118.221102). URL: <https://link.aps.org/doi/10.1103/PhysRevLett.118.221102>.
- [24] Jacopo Grotti et al. "Geodesy and metrology with a transportable optical clock". In: *arXiv:1705.04089 [physics]* (May 2017). arXiv: 1705.04089. URL: <http://arxiv.org/abs/1705.04089>.
- [25] Krehlik Przemyslaw and Sliwczynski Lukasz. "Fiber-optic time distribution with the autonomous calibration of dispersion-induced offset". In: *IEEE*, Apr. 2016, pp. 1–2. ISBN: 978-1-5090-0720-2. DOI: [10.1109/EFTF.2016.7477760](https://doi.org/10.1109/EFTF.2016.7477760). URL: <http://ieeexplore.ieee.org/document/7477760/>.
- [26] J.-F. Cliche and B. Shillue. "Applications of control Precision timing control for radioastronomy maintaining femtosecond synchronization in the atacama large millimeter array". In: *IEEE Control Systems Magazine* 26.1 (Feb. 2006), pp. 19–26. ISSN: 0272-1708. DOI: [10.1109/MCS.2006.1580149](https://doi.org/10.1109/MCS.2006.1580149). URL: <http://ieeexplore.ieee.org/document/1580149/>.
- [27] L. Sliwczynski et al. "Remote synchronization of atomic clocks". In: *IEEE*, May 2016, pp. 1–3. ISBN: 978-1-5090-2214-4. DOI: [10.1109/MIKON.2016.7492092](https://doi.org/10.1109/MIKON.2016.7492092). URL: <http://ieeexplore.ieee.org/document/7492092/>.
- [28] Cecilia Clivati et al. "A coherent fiber link for very long baseline interferometry". In: *IEEE Transactions on Ultrasonics, Ferroelectrics, and Frequency Control* 62.11 (Nov. 2015), pp. 1907–1912. ISSN: 0885-3010. DOI: [10.1109/TUFFC.2015.007221](https://doi.org/10.1109/TUFFC.2015.007221). URL: <http://ieeexplore.ieee.org/document/7321699/>.
- [29] Sascha W. Schediwy et al. "Stabilized microwave-frequency transfer using optical phase sensing and actuation". en. In: *Optics Letters* 42.9 (May 2017), p. 1648. ISSN: 0146-9592, 1539-4794. DOI: [10.1364/OL.42.001648](https://doi.org/10.1364/OL.42.001648). URL: <https://www.osapublishing.org/abstract.cfm?URI=ol-42-9-1648>.

- [30] Yabai He et al. “Long-distance telecom-fiber transfer of a radio-frequency reference for radio astronomy”. EN. In: *Optica* 5.2 (Feb. 2018), pp. 138–146. ISSN: 2334-2536. DOI: [10.1364/OPTICA.5.000138](https://doi.org/10.1364/OPTICA.5.000138). URL: <https://www.osapublishing.org/abstract.cfm?uri=optica-5-2-138>.
- [31] Olivier Lopez et al. “Simultaneous remote transfer of accurate timing and optical frequency over a public fiber network”. In: *2013 Joint European Frequency and Time Forum and International Frequency Control Symposium, EFTF/IFC 2013* (2013), pp. 474–476. ISSN: 09462171. DOI: [10.1109/EFTF-IFC.2013.6702214](https://doi.org/10.1109/EFTF-IFC.2013.6702214).
- [32] M. Rost et al. “Time transfer through optical fibers over a distance of 73 km with an uncertainty below 100 ps”. In: *arXiv:1209.4467 [physics]* (Sept. 2012). arXiv: 1209.4467. URL: <http://arxiv.org/abs/1209.4467>.
- [33] M. Lessing et al. “Frequency comb-based time transfer over a 159 km long installed fiber network”. In: *Applied Physics Letters* 110.22 (May 2017), p. 221101. ISSN: 0003-6951. DOI: [10.1063/1.4984144](https://doi.org/10.1063/1.4984144). URL: <http://aip.scitation.org/doi/full/10.1063/1.4984144>.
- [34] P. Krehlik et al. “Fiber-Optic Joint Time and Frequency Transfer With Active Stabilization of the Propagation Delay”. In: *IEEE Transactions on Instrumentation and Measurement* 61.10 (Oct. 2012), pp. 2844–2851. ISSN: 0018-9456. DOI: [10.1109/TIM.2012.2196396](https://doi.org/10.1109/TIM.2012.2196396).
- [35] L. Sliwczynski and P. Krehlik. “Multipoint joint time and frequency dissemination in delay-stabilized fiber optic links”. In: *IEEE Transactions on Ultrasonics, Ferroelectrics, and Frequency Control* 62.3 (Mar. 2015), pp. 412–420. ISSN: 0885-3010. DOI: [10.1109/TUFFC.2014.006773](https://doi.org/10.1109/TUFFC.2014.006773). URL: <http://ieeexplore.ieee.org/document/7055436/>.
- [36] Przemyslaw Krehlik et al. “ELSTAB—Fiber-Optic Time and Frequency Distribution Technology: A General Characterization and Fundamental Limits”. In: *IEEE Transactions on Ultrasonics, Ferroelectrics, and Frequency Control* 63.7 (July 2016), pp. 993–1004. ISSN: 0885-3010. DOI: [10.1109/TUFFC.2015.2502547](https://doi.org/10.1109/TUFFC.2015.2502547). URL: <http://ieeexplore.ieee.org/document/7332966/> (visited on 01/07/2018).
- [37] David L. Mills. *Computer network time synchronization: the Network Time Protocol on Earth and in space*. 2nd ed. Boca Raton, FL: CRC Press, 2011. ISBN: 978-1-4398-1463-5.
- [38] *The OSI Model Layers from Physical to Application*. URL: <https://www.lifewire.com/layers-of-the-osi-model-illustrated-818017>.
- [39] Technical Committee. “IEEE Standard for a Precision Clock Synchronization Protocol for Networked Measurement and Control Systems”. In: *IEEE Std 1588-2008 (Revision of IEEE Std 1588-2002)* (2008), pp. 1–300. DOI: [10.1109/IEEESTD.2008.4579760](https://doi.org/10.1109/IEEESTD.2008.4579760).

- [40] S.R. Jefferts et al. "Two-way time and frequency transfer using optical fibers". In: *IEEE Transactions on Instrumentation and Measurement* 46.2 (Apr. 1997), pp. 209–211. ISSN: 00189456. DOI: 10.1109/19.571814. URL: <http://ieeexplore.ieee.org/document/571814/>.
- [41] Sven-Christian Ebnehag et al. "Measurements and Error Sources in Time Transfer Using Asynchronous Fiber Network". In: *IEEE Transactions on Instrumentation and Measurement* 59.7 (July 2010), pp. 1918–1924. ISSN: 0018-9456, 1557-9662. DOI: 10.1109/TIM.2009.2028214. URL: <http://ieeexplore.ieee.org/document/5280272/>.
- [42] Javier Serrano et al. "The White Rabbit project". In: *IBIC 2013*. Japan, 2013, pp. 93–95. URL: https://www.ohwr.org/attachments/2528/IBIC2013_WR.pdf.
- [43] Erik F. Dierikx et al. "White Rabbit Precision Time Protocol on Long-Distance Fiber Links". In: *IEEE Transactions on Ultrasonics, Ferroelectrics, and Frequency Control* 63.7 (July 2016), pp. 945–952. ISSN: 0885-3010. DOI: 10.1109/TUFFC.2016.2518122. URL: <http://ieeexplore.ieee.org/document/7383303/>.
- [44] *BIPM - WGATFT*. URL: <https://www.bipm.org/en/committees/cc/wg/wgatft.html>.
- [45] *Open Hardware Repository | Wiki | WRpublications*. URL: <https://www.ohwr.org/projects/white-rabbit/wiki/wrpublications>.
- [46] Javier Serrano. *OHR WR users*. 2017. URL: <https://www.ohwr.org/projects/white-rabbit/wiki/WRUsers>.
- [47] Jason Allnutt et al. *Timing Challenges in the Smart Grid*. Tech. rep. NIST SP 1500-08. Gaithersburg, MD: National Institute of Standards and Technology, Jan. 2017. DOI: 10.6028/NIST.SP.1500-08. URL: <http://nvlpubs.nist.gov/nistpubs/SpecialPublications/NIST.SP.1500-08.pdf>.
- [48] Jose Luis Gutierrez-Rivas et al. "White Rabbit HSR: a seamless sub-nanosecond redundant timing system with low-latency data capabilities for Smart Grid". In: *IEEE Transactions on Industrial Informatics* (2017), pp. 1–1. ISSN: 1551-3203, 1941-0050. DOI: 10.1109/TII.2017.2779240. URL: <http://ieeexplore.ieee.org/document/8125717/> (visited on 03/08/2018).
- [49] D. P. Venmani et al. "On the role of network synchronization for future cellular networks: an operator's perspective". In: *IEEE Communications Magazine* 54.9 (Sept. 2016), pp. 58–64. ISSN: 0163-6804. DOI: 10.1109/MCOM.2016.7565273.
- [50] *ESMA*. URL: <https://www.esma.europa.eu/>.
- [51] *MiFID II : NPLTime® : Products & Services : Commercial Services : National Physical Laboratory*. URL: <http://www.npl.co.uk/commercial-services/products-and-services/npltime/mifid-ii/>.

- [52] Seven Solutions. *Seven Solutions, Synchronization and Deterministic Timing*. URL: <http://sevensols.com/>.
- [53] Maclej Lipiński et al. "White rabbit: A PTP application for robust sub-nanosecond synchronization". In: *IEEE International Symposium on Precision Clock Synchronization for Measurement, Control, and Communication, ISPCS (2011)*, pp. 25–30. ISSN: 19490305. DOI: [10.1109/ISPCS.2011.6070148](https://doi.org/10.1109/ISPCS.2011.6070148).
- [54] J. L. Ferrant et al. "Synchronous ethernet: a method to transport synchronization". In: *IEEE Communications Magazine* 46.9 (Sept. 2008), pp. 126–134. ISSN: 0163-6804. DOI: [10.1109/MCOM.2008.4623717](https://doi.org/10.1109/MCOM.2008.4623717).
- [55] *ITU-T in brief*. URL: <https://www.itu.int/en/ITU-T/about/Pages/default.aspx>.
- [56] T Wlostowski. "Precise time and frequency transfer in a White Rabbit network". PhD Thesis. Warsaw University of Technology, 2011. URL: <https://www.ohwr.org/attachments/622/mgr.pdf>.
- [57] Grzegorz Daniluk. *White Rabbit calibration*. en. 2015. URL: <https://www.ohwr.org/documents/213> (visited on 01/27/2018).
- [58] *CreoTech*. URL: <http://creotech.pl/en/home/>.
- [59] *Open Hardware Repository | Wiki | SPEC*. URL: <https://www.ohwr.org/projects/spec/wiki>.
- [60] *Open Hardware Repository | White Rabbit - Overview*. URL: <https://www.ohwr.org/projects/white-rabbit>.
- [61] Javier Diaz. *White Rabbit ZEN Boards | sevensolutions*. 2016. URL: <http://sevensols.com/index.php/products/wr-zen-board/>.
- [62] Miguel Jiménez-López et al. "WR-ZEN: Ultra-accurate synchronization SoC based on zynq technology". In: *2016 European Frequency and Time Forum, EFTF 2016 (2016)*, pp. 0–3. DOI: [10.1109/EFTF.2016.7477790](https://doi.org/10.1109/EFTF.2016.7477790).
- [63] E. F. Schubert. *Light-Emitting Diodes*. 2006. ISBN: 978-0-521-86538-8. DOI: [10.1017/CB09780511790546](https://doi.org/10.1017/CB09780511790546).
- [64] Gorachand Ghosh. "Sellmeier coefficients and dispersion of thermo-optic coefficients for some optical glasses". In: *Applied Optics* 36.7 (1997), p. 1540. ISSN: 0003-6935. DOI: [10.1364/AO.36.001540](https://doi.org/10.1364/AO.36.001540). URL: <https://www.osapublishing.org/abstract.cfm?URI=ao-36-7-1540>.
- [65] Kyle Cochrane et al. "Wavelength-dependent measurements of optical-fiber transit time, material dispersion, and attenuation". EN. In: *Applied Optics* 40.1 (Jan. 2001), pp. 150–156. ISSN: 2155-3165. DOI: [10.1364/AO.40.000150](https://doi.org/10.1364/AO.40.000150). URL: <https://www.osapublishing.org/ao/abstract.cfm?uri=ao-40-1-150> (visited on 03/06/2018).
- [66] Gerd Keiser. *Optical Fiber communication*. McGraw-Hill Education, 2014. ISBN: 978-981-4575-69-0. URL: <https://books.google.fr/books?id=0wBfngEACAAJ>.

- [67] He Wen et al. "Measurements of the Birefringence and Verdet Constant in an Air-Core Fiber". In: *Journal of Lightwave Technology* 27.15 (Aug. 2009), pp. 3194–3101. ISSN: 0733-8724, 1558-2213. DOI: 10.1109/JLT.2008.2009546. URL: <http://ieeexplore.ieee.org/document/4838862/>.
- [68] N. Kaur, P. Tuckey, and P. E. Pottie. "Time transfer over a White Rabbit network". In: *2016 European Frequency and Time Forum (EFTF)*. Apr. 2016, pp. 1–4. DOI: 10.1109/EFTF.2016.7477793.
- [69] Łukasz Śliwczyński, Przemysław Krehlik, and Marcin Lipiński. "Optical fibers in time and frequency transfer". In: *Measurement Science and Technology* 21.7 (July 2010), p. 075302. ISSN: 0957-0233, 1361-6501. DOI: 10.1088/0957-0233/21/7/075302. URL: <http://stacks.iop.org/0957-0233/21/i=7/a=075302?key=crossref.5090936e280242cad1473de767396c14>.
- [70] Wei Chen et al. "Joint time and frequency dissemination network over delay-stabilized fiber optic links". In: *IEEE Photonics Journal* 7.3 (June 2015). arXiv: 1501.05403, pp. 1–9. ISSN: 1943-0655. DOI: 10.1109/JPHOT.2015.2426874. URL: <http://arxiv.org/abs/1501.05403> (visited on 02/28/2018).
- [71] Mattia Rizzi. *White Rabbit Switch performance in Grandmaster mode*. Tech. rep. 2016, p. 20. URL: <https://www.ohwr.org/documents/475>.
- [72] Mattia Rizzi. *DDMTDreport*. Tech. rep. 2017. URL: https://www.ohwr.org/attachments/4928/DDMTD_report_final.pdf.
- [73] N. R. Newbury, P. A. Williams, and W. C. Swann. "Coherent transfer of an optical carrier over 251 km". en. In: *Optics Letters* 32.21 (Nov. 2007), p. 3056. ISSN: 0146-9592, 1539-4794. DOI: 10.1364/OL.32.003056. URL: <https://www.osapublishing.org/abstract.cfm?URI=ol-32-21-3056>.
- [74] C. N. Pannell, J. D. C. Jones, and D. A. Jackson. "The effect of environmental acoustic noise on optical fibre based velocity and vibration sensor systems". en. In: *Measurement Science and Technology* 5.4 (1994), p. 412. ISSN: 0957-0233. DOI: 10.1088/0957-0233/5/4/015. URL: <http://stacks.iop.org/0957-0233/5/i=4/a=015>.
- [75] Analog Devices. *AD9516-4 datasheet*. URL: <http://www.analog.com/media/en/technical-documentation/data-sheets/AD9516-4.pdf>.
- [76] Compact General-purpose Oscillator. "1000.0 MHz SAW Oscillator". In: (2008), pp. 2–3. URL: <https://media.digikey.com/pdf/DataSheets/MurataPDFs/H04001-1.pdf>.
- [77] C. van Tour and J. C. J. Koelemeij. *Sub-Nanosecond Time Accuracy and Frequency Distribution through White Rabbit Ethernet*. Tech. rep. 2017. URL: https://library.nrao.edu/public/memos/ngvla/NGVLA_22.pdf.
- [78] Mattia Rizzi. *OHR White Rabbit low jitter*. 2016. URL: <https://www.ohwr.org/projects/wr-low-jitter/documents>.

- [79] Etienne Samain et al. "T2L2 : Ground to ground time transfer". In: *EFTF 2012 - 2012 European Frequency and Time Forum, Proceedings*. 2012, pp. 36–40. ISBN: 978-1-4673-1924-9. DOI: [10.1109/EFTF.2012.6502328](https://doi.org/10.1109/EFTF.2012.6502328).
- [80] Digital Systems. "G.652 (11/2016)". In: (2016). URL: <https://www.itu.int/rec/T-REC-G.652-201611-I/en>.
- [81] Roland E Best. *Phase Locked Loops*. English. OCLC: 958578974. Blacklick, USA: McGraw-Hill Professional Publishing, 2007. ISBN: 978-0-07-159521-6. URL: <http://public.eblib.com/choice/publicfullrecord.aspx?p=4656788>.
- [82] L. G. Cohen and J. W. Fleming. "Effect of temperature on transmission in light-guides". In: *The Bell System Technical Journal* 58.4 (Apr. 1979), pp. 945–951. ISSN: 0005-8580. DOI: [10.1002/j.1538-7305.1979.tb03328.x](https://doi.org/10.1002/j.1538-7305.1979.tb03328.x).
- [83] Fabio Stefani et al. "Tackling the limits of optical fiber links". In: *Journal of the Optical Society of America. B, Optical Physics* 32 (2015), pp. 787–797. DOI: [10.1364/JOSAB.32.000787](https://doi.org/10.1364/JOSAB.32.000787).
- [84] Qiyang Chen and Ping Lu. "Fiber Bragg Gratings and Their Applications as Temperature and Humidity Sensors". In: *Atomic, Molecular and Optical Physics: New Research* (2008), pp. 235–260. URL: <http://citeseerx.ist.psu.edu/viewdoc/download?doi=10.1.1.555.1123&rep=rep1&type=pdf>.
- [85] C. F. Dietrich. *Uncertainty, calibration, and probability: the statistics of scientific and industrial measurement*. 2nd ed. The Adam Hilger series on measurement science and technology. Bristol ; Philadelphia: A. Hilger, 1991. ISBN: 978-0-7503-0060-5.
- [86] Olivier Lopez et al. "Cascaded multiplexed optical link on a telecommunication network for frequency dissemination". EN. In: *Optics Express* 18.16 (Aug. 2010), pp. 16849–16857. ISSN: 1094-4087. DOI: [10.1364/OE.18.016849](https://doi.org/10.1364/OE.18.016849). URL: <https://www.osapublishing.org/abstract.cfm?uri=oe-18-16-16849>.
- [87] Dan Xu et al. "Studying the fundamental limit of optical fiber links to the 10⁻²¹ level". EN. In: *Optics Express* 26.8 (Apr. 2018), pp. 9515–9527. ISSN: 1094-4087. DOI: [10.1364/OE.26.009515](https://doi.org/10.1364/OE.26.009515). URL: <https://www.osapublishing.org/oe/abstract.cfm?uri=oe-26-8-9515> (visited on 04/04/2018).
- [88] N. Kaur et al. "Time and frequency transfer over a 500 km cascaded White Rabbit network". In: *2017 Joint Conference of the European Frequency and Time Forum and IEEE International Frequency Control Symposium (EFTF/IFCS)*. July 2017, pp. 86–90. DOI: [10.1109/FCS.2017.8088808](https://doi.org/10.1109/FCS.2017.8088808).
- [89] Vladimir Smotlacha and Alexander Kuna. "Two-way optical time and frequency transfer between IPE and BEV". In: *IEEE*, Apr. 2012, pp. 375–378. ISBN: 978-1-4673-1923-2 978-1-4673-1924-9 978-1-4673-1922-5. DOI: [10.1109/EFTF.2012.6502405](https://doi.org/10.1109/EFTF.2012.6502405). URL: <http://ieeexplore.ieee.org/document/6502405/> (visited on 01/08/2018).

- [90] P. Uhrich et al. "Use of two traveling GPS receivers for a relative calibration campaign among European laboratories". In: *2015 Joint Conference of the IEEE International Frequency Control Symposium the European Frequency and Time Forum*. Apr. 2015, pp. 643–648. DOI: [10.1109/FCS.2015.7138927](https://doi.org/10.1109/FCS.2015.7138927).
- [91] G. D. Rovera et al. "Link calibration against receiver calibration time transfer uncertainty when using the Global Positioning System". In: *2014 European Frequency and Time Forum (EFTF)*. June 2014, pp. 455–458. DOI: [10.1109/EFTF.2014.7331534](https://doi.org/10.1109/EFTF.2014.7331534).
- [92] ohwrMIKES. *Open Hardware Repository | Wiki | Mikes*. URL: <https://www.ohwr.org/projects/white-rabbit/wiki/Mikes>.
- [93] Thales Theorem. *Thales' Theorem*. URL: <https://www.cut-the-knot.org/Curriculum/Geometry/GeoGebra/ThalesTheorem.shtml>.
- [94] S. Siu et al. "Time/phase synchronization distribution over Optical Transport Network(OTN)". In: *2013 IEEE International Symposium on Precision Clock Synchronization for Measurement, Control and Communication (ISPCS) Proceedings*. Sept. 2013, pp. 24–28. DOI: [10.1109/ISPCS.2013.6644758](https://doi.org/10.1109/ISPCS.2013.6644758).

Résumé

Dans cette thèse, notre objectif est de développer une approche de transfert de temps et de fréquence multi-utilisateurs, compatible avec les réseaux de télécommunications et compétitive avec la distribution de temps par GNSS. Nous nous intéressons donc aux méthodes pour les réseaux à commutation par paquets, comme le NTP (Network Time Protocol) et le PTP (Precision Timing Protocol). Nous nous concentrons également sur les liaisons “unidirectionnelles”, où les signaux aller et retour entre les nœuds de réseau se propagent sur des fibres distinctes, non au sein d’une même fibre (liaisons “bidirectionnelles”). En particulier, nous utilisons une méthode appelée White Rabbit PTP (WR). Développée au CERN, basée sur PTP, utilisant l’ethernet synchrone et d’autres techniques pour atteindre des performances élevées, WR réalise une stabilité du temps sous-nanoseconde pour la synchronisation d’instruments sur des réseaux à l’échelle de 10 km. Nous sommes particulièrement intéressés par l’extension de cette méthode pour la distribution de références au niveau régional ou national, sur des liaisons allant jusqu’à 1000 km. Nous étudions d’abord les performances de l’équipement réseau White Rabbit, en particulier le commutateur White Rabbit. Nous y apportons diverses améliorations: sur le verrouillage du commutateur grand maître à la référence externe, améliorant ainsi sa stabilité à court terme de plus d’un ordre de grandeur; sur la bande passante de verrouillage du commutateur esclave; et en augmentant le débit des messages PTP entre les commutateurs maître et esclave. Nous étudions ensuite les liaisons WR moyennes et longues distances. Nous construisons un lien unidirectionnel de 100 km en utilisant des bobines de fibres dans le laboratoire. Nous découvrons que la performance à court terme est limitée par la dispersion chromatique de la fibre, tandis que la performance à long terme est dégradée par le bruit thermique. Pour limiter l’effet de la dispersion chromatique sur les liaisons longue distance, nous proposons l’utilisation d’une approche en cascade. Nous réalisons un lien en cascade de 500 km, à nouveau avec des bobines de fibres. Nous utilisons le multiplexage en longueur d’onde dense pour construire ce lien par des passages multiples à travers des bobines plus courtes. Nous obtenons une stabilité de transfert de fréquence de 2×10^{-12} à une seconde de temps d’intégration et de 4×10^{-15} en un jour, limitée par le bruit thermique à long terme. Nous obtenons une stabilité temporelle de 5 ps à une seconde de temps d’intégration, diminuant jusqu’à un minimum de 1,2 ps à 20 secondes et restant inférieure à une nanoseconde pour des durées plus longues. Ces performances sont similaires à court terme, et deux ordres de grandeur meilleures à long terme, qu’un récepteur GPS de bonne qualité. Nous nous attendons à ce que les fluctuations thermiques et donc l’effet du bruit thermique des fibres soient réduits d’un facteur d’environ cinq pour les installations sur le terrain. Enfin, nous faisons des études préliminaires sur l’étalonnage en temps des liaisons WR. Le principal défi est de mesurer l’asymétrie de longueur optique entre les deux fibres utilisées pour le transfert des signaux aller et retour. Nous démontrons une technique d’échange de fibres, en utilisant une liaison suburbaine White Rabbit sur fibre noire. Nous décrivons et testons ensuite une nouvelle méthode variationnelle pour l’étalonnage, impliquant une méthode de mesure différentielle basée sur l’exploitation de deux liaisons WR à différentes longueurs d’onde sur la même liaison.

Abstract

In this thesis our objective is to develop a scalable network time and frequency transfer approach, providing multi-user dissemination, compatible with large telecommunication networks and competitive with GNSS-based time distribution. Therefore we are concerned with methods for use in packet-based networks, like the Network Time Protocol (NTP) and Precision Timing Protocol (PTP). We also concentrate on “unidirectional” links, where the forward and backward signals between network nodes propagate over separate fibers, not within the same fiber (“bidirectional” links). In particular we use a method called White Rabbit PTP (WR). This is a novel technology developed at CERN, based on PTP while using Synchronous Ethernet and other techniques to achieve high performance. It demonstrates sub-nanosecond time stability and synchronization of arrays of instruments over 10 km scale networks. We are particularly interested in extending this method for large scale distribution of references at regional or national level, over links of up to 1000 km. We first study extensively the default performances and limitations of White Rabbit network equipment, in particular the White Rabbit switch. We make various improvements to its operation: on the locking of the grandmaster switch to the external reference, thus improving its short-term stability by more than an order of magnitude; optimizing the locking bandwidth of the slave switch; and increasing the PTP messaging rate between master and slave switches. We then study medium and long-distance WR links. We construct a 100 km, unidirectional link using fiber spools in the laboratory. We discover that the short-term performance is limited by chromatic dispersion in the fiber, while the long-term performance is degraded by the influence of temperature variations on the fiber. To limit the effect of chromatic dispersion for long-haul links, we propose the use of a cascaded approach. We realise a national scale, cascaded, 500 km link, again utilizing fiber spools. We use Dense Wavelength Division Multiplexing methods to construct this link by multiple passages through shorter spools. We achieve a frequency transfer stability of 2×10^{-12} at one second of integration time and 4×10^{-15} at one day, limited by thermal noise in the long term. We achieve a time stability of 5 ps at one second of integration time, decreasing to a minimum of 1.2 ps at 20 seconds and remaining below one nanosecond for longer averaging times. These performances are similar in the short term, and two orders of magnitude better in the long term, than good quality GPS receivers. We expect thermal fluctuations and therefore the effect of fiber thermal noise to be suppressed by a factor of approximately five for installations in the field. Finally we make preliminary investigations of time calibration of WR links. The main challenge here is to measure the optical length asymmetry between the two fibers used for signal transfer in the forward and backward directions. We demonstrate a fiber swapping technique, using a mid range, suburban White Rabbit link over dark fiber. We then describe and test a new variational method for calibration, involving a differential measurement method based on operating two WR links at different wavelengths over the same optical fiber link.

Keywords: Diffusion à long terme du temps et des fréquences, White Rabbit PTP, Liens de fibre optique. Long range time and frequency dissemination, White Rabbit PTP, Optical fiber links.